

Christian-Albrechts-Universität zu Kiel
Institut für Theoretische Physik und Astrophysik



DISSERTATION
ZUR ERLANGUNG DES AKADEMISCHEN GRADES
DOCTOR RERUM NATURALIUM
DER MATHEMATISCH-NATURWISSENSCHAFTLICHEN FAKULTÄT
DER CHRISTIAN-ALBRECHTS-UNIVERSITÄT ZU KIEL

**Solving the Two-time
Kadanoff-Baym Equations.
Application to Model Atoms and Molecules**

VORGELEGT VON
KARSTEN BALZER
GEB. AM 03.09.1980 IN KIEL

KIEL, AUGUST 2011

This work was typeset in L^AT_EX.

Figures were created using  *Asymptote*, the vector graphics language, mathematica, the technical computing software, and  gnuplot, the portable command-line driven graphing utility.

PACS numbers that have overlap with the contents of this work:

02.70.Dh, 05.10.-a, 05.30.-d, 31.15.-p, 31.15.B-, 31.15.V-, 31.15.X-, 31.50.Bc, 32.30.-r, 32.80.Rm, 73.21.-b, 78.67.-n

LISTE DER GUTACHTER:

Prof. Dr. Michael Bonitz
Institut für Theoretische Physik und Astrophysik,
Christian-Albrechts-Universität zu Kiel,
Leibnizstrasse 15,
24098 Kiel,
Germany

Prof. Dr. Stefan Heinze
Institut für Theoretische Physik und Astrophysik,
Christian-Albrechts-Universität zu Kiel,
Leibnizstrasse 15,
24098 Kiel,
Germany

Prof. Dr. Robert van Leeuwen
Department of Physics,
Nanoscience Center,
P.O. Box 35 (Y5),
40014 University of Jyväskylä,
Finland

DATUM DER MÜNDLICHEN PRÜFUNG: 12. Oktober 2011

Dedicated to my beloved wife Božena.

Abstract

The method of nonequilibrium Green functions (NEGFs) constitutes a solid framework to describe closed and open quantum systems. It captures situations far from equilibrium including arbitrary perturbations *and* correlations—effects higher than first order in the binary interactions. On the contrary, in the absence of external fields, it reduces to the imaginary-time Matsubara formalism. The abilities (and successes) of the method originate from its self-consistency and the conserving character of many-body approximations that are introduced by diagram technique. On this account, NEGFs have, now for a long time, brought insight into the dynamics of nuclear matter, non-ideal quantum gases and (semiconductor) plasmas. However, applications to localized, finite and strongly interacting systems have emerged only within the recent decade.

The dynamical properties follow from quantum kinetic equations—the two-time Kadanoff-Baym equations for the one-particle NEGF—the numerical solution of which is the central topic of this thesis. The non-Markovian structure of these equations thereby inhibits an unlimited, gradual propagation of the nonequilibrium Green function: Any self-consistent, future dynamics of the system is tightly linked to the (complete) past by non-local self-energies. Further, the success in obtaining solutions is being diminished if the system under investigation is *not* isotropic or inhomogeneous and, in addition, the spatial topology (e.g., the charge carrier or spin density) needs to be resolved in time. On top of this, small isolated systems are generally not candidates showing fast decoherence which offers little hope for smooth and well-damped integration kernels.

Despite these difficulties, the thesis at hand is devoted to the computation of the two-time NEGF for finite, closed systems of which ensembles of electrons bound by nuclei forming atoms or molecules are the most natural representatives. Here, in the spirit of the well-studied one-dimensional helium atom, the electron dynamics in model atoms and molecules is addressed in *ab initio* fashion.

To render calculations possible in the first place,

- (i) a novel hybrid representation of the NEGF is introduced based on the conception of finite elements (FE) and the discrete variable representation (DVR), and
- (ii) a parallel algorithm is developed that allows for an efficient, well scalable distributed-memory computation of the full two-time Green function.

The first point attributes plenty of flexibility and makes the method readily adjustable to different Hamiltonians avoiding the need to, by hand or in intricate numerical manner, calculate the whole bunch of matrix elements of one- and two-particle operators. Also, in consequence, it drastically simplifies the evaluation of self-energies. The second point makes the NEGF approach ready

for large-scale, high-performance computing facilities, the resources (of computer power: mainly memory!) of which are indispensable for (some of) the calculations presented.

The applicability of the developed methods is demonstrated *inter alia* on the basis of helium, beryllium, hydrogen and lithium hydride modeled in one spatial dimension whereby electron-electron correlations are treated in the second(-order) Born approximation. After a thorough discussion on the self-consistent ground states, the thesis focuses on the electron dynamics in the linear response regime as well as in the presence of strong external fields. Overall, to assess the performance of the second Born approximation, the results are compared to the Hartree-Fock approximation, on the one hand, and to the exact solution of the time-(in)dependent Schrödinger equation, on the other hand. In addition, aiming at the possibility of extended time-dependent calculations, the behavior of the generalized Kadanoff-Baym ansatz is discussed.

Kurzfassung

Diese Kurzfassung ist eine Übersetzung des englischen Abstracts von Seite i.

Die Methode der Nichtgleichgewicht-Greenfunktionen (NGGF) stellt ein robustes Verfahren dar, um sowohl abgeschlossene als auch offene Quantensysteme zu beschreiben. Es erlaubt die Betrachtung der Vielteilchendynamik unter dem Einfluss von Korrelationen – Effekten von höherer als zweiter Ordnung in der Wechselwirkung – *und* beliebiger Störungen fern vom Gleichgewicht. In Abwesenheit externer Felder reduziert sich die Theorie dagegen auf den imaginärzeitlichen Matsubara Formalismus. Die Stärken (und die Erfolge) der Methode liegen in ihrer Selbstkonsistenz und in der Möglichkeit diagrammatische Vielteilchennäherungen einzuführen, die makroskopische Erhaltungssätze erfüllen. Diesen Eigenschaften ist es zu verdanken, dass NGGFen erfolgreich zur Beschreibung von Kernmaterie, nichtidealen Quantengasen und (Halbleiter-)Plasmen verwendet werden. Anwendungen auf endliche, lokalisierte und stark wechselwirkende Systeme sind jedoch erst innerhalb der letzten zehn Jahre erfolgt.

Die dynamischen Eigenschaften folgen aus quantenkinetischen Gleichungen – den zweizeitigen Kadanoff-Baym Gleichungen für die Einteilchen-NGGF –, deren numerische Lösung zentraler Gegenstand dieser Arbeit ist. Die nicht-Markovsche Struktur verhindert dabei eine unbegrenzte, schrittweise Propagation der Nichtgleichgewicht-Greenfunktion: Jede selbstkonsistente, zukünftige Entwicklung des Systems ist durch nichtlokale Selbstenergien streng mit seiner (gesamten) Vorgeschichte verknüpft. Weiter erschwert wird die Lösung, wenn das zu untersuchende System *nicht* isotrop oder inhomogen ist, so dass zusätzlich die räumliche Topologie (z.B. die Ladungs- oder Spindichte) aufgelöst werden muss. Überdies hinaus weisen kleine, isolierte Systeme generell große Kohärenzzeiten auf, was wenig Hoffnung zur Annahme von glatten und deutlich gedämpften Stoßintegralen bietet.

Trotz dieser Schwierigkeiten beschäftigt sich die vorliegende Dissertation mit der Berechnung der zweizeitigen NGGF von endlichen, abgeschlossenen Systemen. Im Sinne des wohl untersuchten eindimensionalen Heliumatoms wird die Elektronendynamik in Modellatomen und -molekülen aufgegriffen. Die Beschreibung erfolgt dabei *ab initio*.

Um die Rechnungen überhaupt zu ermöglichen, wird

- (i) eine neuartige Hybriddarstellung der NGGF angewendet, die auf der Idee von finiten Elementen (FE) und der diskreten Variablendarstellung (DVR) beruht, und

-
- (ii) wird ein paralleler Algorithmus entwickelt, der eine effiziente, gut skalierbare Berechnung der vollen zweizeitigen Greenfunktion unter Berücksichtigung von verteiltem Speicher erlaubt.

Die FE-DVR-Darstellung ist dabei leicht übertragbar auf unterschiedliche Systeme und Wechselwirkungen, ohne dass die Matrixelemente von Ein- und Zweiteilchenoperatoren jedes Mal in komplizierter Weise neu berechnet werden müssen. Außerdem lässt sich eine drastische Vereinfachung der Selbstenergien erzielen. Der zweite Punkt ermöglicht die Nutzung von Hoch- und Höchstleistungsrechnersystemen, deren Ressourcen (in Computerleistung: hauptsächlich Speicher!) unabdingbar sind für (einige) der durchgeführten Rechnungen.

Die Anwendbarkeit der entwickelten Methoden wird unter anderem für Helium, Beryllium, Wasserstoff und Lithiumhydrid gezeigt, wobei sich die Elektronen in einer Raumdimension bewegen und Elektron-Elektron-Korrelationen in der zweiten Bornschen Näherung behandelt werden. Nach einer sorgfältigen Diskussion der selbstkonsistenten Grundzustände beschäftigt sich die vorliegende Arbeit mit der Elektronendynamik sowohl im Linear Response Bereich als auch unter dem Einfluss starker externer Felder. Dabei werden die Resultate einerseits mit der Hartree-Fock-Näherung verglichen und andererseits der exakten Lösung der zeit(un)abhängigen Schrödinger-Gleichung gegenübergestellt, um die Güte der zweiten Bornschen Näherung zu untersuchen.

Contents

Abstract	i
Kurzfassung	iii
1 Introduction	1
1.1 Electron Correlations	1
1.2 Two-time Kadanoff-Baym Equations; Overview and Motivation	2
1.3 Thesis Outline	7
I Theory	9
2 Quantum Statistical Mechanics	11
2.1 Quantum Statistical Averages	11
2.2 Dynamics of Creation and Annihilation Operators	13
2.3 Nonequilibrium Green Functions (NEGFs)	14
2.3.1 Definitions	14
2.3.2 The Kadanoff-Baym Equations	15
2.3.3 The Dyson Equation; Equilibrium Limit	18
2.3.4 Matrix Formulation and Properties	20
2.4 Summary	23
II Numerical Methods	25
3 Representation of the Nonequilibrium Green Function	27
3.1 Electron Spin Variables	28
3.2 The Finite Element-Discrete Variable Representation (FE-DVR)	29
3.2.1 General Idea and Fields of Application	29
3.2.2 Definitions	31

3.2.3	FE-DVR Basis Functions	33
3.3	FE-DVR Hamiltonian; Matrix Elements and Self-energies	34
3.3.1	Single-particle Energy	35
3.3.2	Interaction Energy	38
3.3.3	Lowest-order Self-energies	38
3.4	Summary	40
4	Solving the Two-time Kadanoff-Baym Equations	43
4.1	Method of Propagation	44
4.1.1	Preparation of Initial States	44
4.1.2	Full Two-time Propagation of the NEGF	46
4.2	Advanced Code Parallelization and Performance	50
4.2.1	Distribution of Memory	51
4.2.2	Inter-process Communications; Algorithm Overview	53
4.2.3	Performance Tests	55
4.3	The Generalized Kadanoff-Baym (GKB) Ansatz	57
4.4	Summary	59
III	Application to Model Atoms and Molecules	61
5	Model Description of Atoms and Molecules	63
5.1	Introduction	63
5.2	Model Hamiltonian for Atoms and Molecules; Observables	65
5.2.1	General Remarks	67
5.2.2	A brief Overview on Strong-field Phenomena	70
5.3	Summary	73
6	Equilibrium Properties and Nonequilibrium Behavior	75
6.1	Electronic Ground State Properties	75
6.1.1	Properties of He, Be, H ₂ , H ₃ ⁺ , and LiH	76
6.2	Nonequilibrium Behavior in External Fields	84
6.2.1	Linear Response Properties of He	85
6.2.2	Ultra-violet Field-induced Electron Dynamics in He and LiH	89
6.3	Revisiting Few-electron Spectra	93
6.3.1	Approximate Excitation Level	97
6.3.2	One- and Multi-electron Transitions	97
6.4	Summary	102
7	Conclusions	105

A	The Gauss-Lobatto Quadrature Rule	111
B	Two-time Propagation of the NEGF; Algorithm and Tests	113
C	The GKB Ansatz; Retarded/Advanced Green Function and Algorithm	119
D	Supplement Tables	123
	Bibliography	125
	List of the Author's Publications	141
	Acknowledgements	145
	Curriculum Vitae	147
	Selbständigkeitserklärung	149

Introduction

The long-range Coulomb interactions between charge carriers—mainly between electrons, protons¹, and electrons and protons—are responsible for the rich, multi-faceted nature of the world we are living in and we are a part of. Together with the non-pointlike quantum behavior of the particles and the spin statistics theorem², the attractive and repulsive interactions lead to the diverse (atomic and electronic) structure of all condensed matter [Koh99], the origin of which is associated with the formation of individual atoms and molecules. For an extended solid, for instance, the ensemble of internal interactions clearly determines whether it is electrically conducting, semiconducting or constitutes an insulator. Furthermore, the interactions mediate thermodynamic and/or structural phase transitions, participate in the physical and chemical properties of (quantum) liquids, gases and plasmas, and lead to the existence of "exotic" quasiparticles such as (indirect) excitons³ or Cooper (BCS⁴) pairs [Coo56] which, as composite bosons, can form Bose-Einstein condensates [Ket02, CW02] and induce superfluidity [Leg99] and superconductivity [Ann04].

1.1 Electron Correlations

All phenomena mentioned in the paragraph above arise in the nonrelativistic framework of a specific quantum many-body problem, where the particles are correlated. Thereby, in general, the term "correlated" means that the particles interact, among one another and with the environment, via electromagnetic forces and spin (for the study of atomic and molecular systems—apart from the property of mass⁵ itself—all gravitational forces can be neglected). However, in quantum many-body theory, the term "correlations" is often used more specifically: It covers those parts of the interactions that cannot be incorporated into an independent particle model. In perturbation theory, this finds its equivalent in the separation of the mean-field (Hartree-Fock or Slater-determinant)

¹In the presence of neutrons, protons are usually bound into positively charged atomic nuclei by the residual strong forces. To form protons and neutrons, the strong interaction of the standard model binds together quarks.

²For fermions, this is expressed by the Pauli exclusion principle (Pauli blocking).

³Quasiparticles of an electron and a hole (being spatially separated), e.g., Ref. [BFB11].

⁴Named after the Bardeen-Cooper-Schrieffer theory.

⁵The mass of the particles is, of course, essential for the transport properties.

approximation for the system's total wave function and post-Hartree-Fock methods as, e.g., provided by the Møller-Plesset formalism [SO96]. Whereas the former method assumes that each particle interacts only with the charge distribution due to the other particles⁶, the latter allow for systematic corrections of this oversimplified conception.

Regarding atomic and molecular physics [DE06], correlation effects are responsible for the fact that already two-electron atoms have a rich electronic structure (for an overview, see Ref. [TRR00]) and reveal very complex (ionization) dynamics when being exposed to strong external fields, e.g., [WSD⁺94, BF99]. Thereby, the presence of dynamic correlations drastically limits the direct numerical solution of the time-dependent Schrödinger equation. Currently, the quantum mechanical treatment of atomic systems with more than two electrons in full dimensionality, i.e., the treatment of systems beyond the hydrogen molecule, is not feasible without further approximations. Nevertheless, this does not diminish the fundamental interest in electron-electron correlation effects. On the contrary, due to the emergence of intense and ultra-short laser pulses [BK00, KI09] as well as novel experimental techniques that allow us to probe electron correlations in a time-dependent fashion [UMD⁺97, KGU⁺04, UUS⁺07], there exists an increasing demand for detailed theoretical investigations and *ab initio* modeling. In order to satisfy this demand, e.g., multi-configuration techniques [CZK⁺05, HB11, HLM11] are used to approximate the solution of the time-dependent Schrödinger equation.

However, it is also reasonable to further develop methods that are not based on the many-body wave function and, instead, allow for a reduced description of interacting quantum many-body systems. Following this intention, we, in this thesis, apply the method of nonequilibrium Green functions. Electron-electron correlations, thereby, manifest themselves in non-Markovian, i.e., memory effects (retardation).

1.2 Two-time Kadanoff-Baym Equations; Overview and Motivation

Being developed about 50 years ago, the two-time (Keldysh-)Kadanoff-Baym equations [KB62, Kel65a] for the (one-particle) nonequilibrium Green function (NEGF) offer a solid, microscopic approach to the description of interacting quantum many-body systems far from equilibrium⁷. The pioneering works of *L.V. Keldysh*, *G. Baym*, and *L.P. Kadanoff* have been successfully considered in many contexts, and beyond a great collection of peer-reviewed articles, the interdisciplinary conferences "Progress in Nonequilibrium Green's functions I-IV" held in Rostock (September 1999), Dresden (August 2002), Kiel (August 2005), and Glasgow (August 2009) as well as the eponymous Proceedings, published as,

(I) M. Bonitz (Ed.) (World Scientific, Singapore, 2000),

(II) M. Bonitz and D. Semkat (Eds.) (World Scientific, Singapore, 2003),

⁶Some degree of correlation may be attributed to exchange effects.

⁷For two very recent theory reviews by *N.J.M. Horing* and *T. Kita*, see Refs. [Hor10] and [Kit10].

(III) M. Bonitz and A. Filinov (Eds.), J. Phys.: Conf. Ser. **35**, 011001-012023 (2006), and

(IV) M. Bonitz and K. Balzer (Eds.), J. Phys.: Conf. Ser. **220**, 001-042 (2010),

witness, that NEGF methodologies, in general, and the Kadanoff-Baym equations, in particular, are of still growing interest in many fields of research. Today, "routine" applications of the method can be found in quantum transport theory [RS86], in semiconductor optics and electronics [HJ96], in plasma physics [KSK05] and, respectively, in nuclear and high-energy physics [BM90]. Thereby, the broad spectrum of applications is attributed to the general framework on which the nonequilibrium Green functions and their equations of motion are based on: Quantum field theory and quantum statistical mechanics.

The Kadanoff-Baym equations (KBE) are integro-differential equations for the one-particle NEGF $\mathcal{G}(1, \bar{1})$, which, with space-time coordinates⁸ $1 = (\vec{r}, t)$ and $\bar{1} = (\vec{r}, \bar{t})$, appears as a two-time generalization of the reduced (one-particle) density matrix⁹. Without going into details here (this is the objective of Chapter 2 of this thesis), the KBE read,

$$\begin{aligned} \left(i \frac{\partial}{\partial t} - \hat{h}^{(1)}(1) \right) \mathcal{G}(1, \bar{1}) &= \delta_{\mathcal{C}}(1 - \bar{1}) + \int_{\mathcal{C}} d2 \Sigma[\mathcal{G}](1, 2) \mathcal{G}(2, \bar{1}) , \\ \left(-i \frac{\partial}{\partial \bar{t}} - \hat{h}^{(1)}(\bar{1}) \right) \mathcal{G}(1, \bar{1}) &= \delta_{\mathcal{C}}(1 - \bar{1}) + \int_{\mathcal{C}} d2 \mathcal{G}(1, 2) \Sigma[\mathcal{G}](2, \bar{1}) , \end{aligned} \quad (1.1)$$

where both times t and \bar{t} , and, on the right hand side, the delta function as well as the integral are defined on the complex Keldysh contour \mathcal{C} . Further, the operator $\hat{h}^{(1)}$ incorporates the single-particle plus mean-field energy, and correlations enter via the two-time self-energy functional $\Sigma[\mathcal{G}](1, \bar{1})$, which (on different levels of many-body perturbation theory) can be constructed by Feynman diagram techniques and has to be convolved with the nonequilibrium Green function.

Pioneering work on the numerical solution of the two-time Kadanoff-Baym equations (1.1) is due to *P. Danielewicz* [Dan84a], who in Ref. [Dan84b] has applied the NEGF method to heavy-ion collisions. Thereby, at high beam energies, the modeled dynamics has been studied in the direct Born approximation¹⁰, and comparisons to the (single-time) Boltzmann dynamics have shown that the KBE approach produces notably superior results. About a decade later, the work of *Danielewicz* has been confirmed and extended to lower energies and densities by *H.S. Köhler* [Kö95, KM01], and additional nuclear matter applications including relativistic effects have been presented, see, e.g., the works of *C. Greiner et al.* [GWR94] and *P. Božek* [Bož97].

In the field of dense, correlated electron gases and non-ideal plasmas¹¹, nonequilibrium Green functions are used by many authors—inter alia by *W. Schäfer* [Sch96], *M. Bonitz* [BKS⁺96], *R. Binder* [BKBK97], *N.H. Kwong* [KBBK98], *D. Semkat* [SKB99, KSB05] and *H.S. Köhler* [KKY99].

⁸In general, the vector \vec{r} may also include the spin.

⁹For the definition of $\mathcal{G}(1, \bar{1})$, see Eq. (2.12) in Chapter 2.

¹⁰Here, $\Sigma[\mathcal{G}](1, \bar{1})$ is of third order in \mathcal{G} .

¹¹Here, we refer to, both, the general one-component plasma (e.g., the hydrogen plasma) and the electron-hole plasma realized in semiconductors.

Thereby, the subjects of the cited works range from non-Markovian carrier-carrier scattering via sub-femtosecond relaxation processes, correlation-induced heating and the influence of initial correlations to a much-noticed numerical algorithm for propagating the nonequilibrium Green function for homogeneous fermion systems in the two-time domain, Ref. [KKY99]. From the theoretical perspective, advances such as the gauge-invariant formulation of the KBEs [KBBS99, BBK⁺99] or the derivation of highly-generalized non-Markovian Boltzmann equations [SKB00] have complemented and enriched the numerical approaches.

Being closer to specific experimental setups, the works of *H. Haug*, *P. Gartner* and *L. Bányai*, e.g., Refs. [HB96, GBH99], deal with the solution of two-time quantum kinetic equations for semiconductor electron-hole systems (the interband Kadanoff-Baym equations) including electron-phonon interaction. Furthermore, by modeling the optically excited carrier dynamics in quantum dots and wells¹², in particular, *F. Jahnke* and co-workers have generated insight into relaxation properties and carrier-phonon- as well as Coulomb interaction-induced dephasing mechanisms, see Refs. [GSJ06, LNS⁺06a, LNS⁺06b] and references therein.

For practical calculations, all aforementioned works consider the NEGF in momentum space, whereby, due to the (quasi) homogeneity of the systems, only a single momentum variable is required, i.e., $\mathcal{G}(1, \bar{1}) \rightarrow \mathcal{G}(\vec{p}, t, \bar{t})$. Then, owing to the non-Markovian integral structure of the Kadanoff-Baym equations (cf. Eq. (1.1)), the problem to be solved is of dimension $D_{\vec{p}} + 2$, where $D_{\vec{p}} = 1, 2$ or 3 , depending on the system's internal degrees of freedom. Hence, the problem is at least three-dimensional. On top of that, without further approximations¹³, the problem size grows quadratic with time, such that an unlimited integration of the equations of motion is inherently impossible. From this point of view, solving the two-time Kadanoff-Baym equations for spatially inhomogeneous systems does appear hardly feasible, because one has to account for $D_{\vec{p}}$ additional degrees of freedom leading to a dimensionality of $2(D_{\vec{p}} + 1) \geq 4$ (and less than 8).

Nevertheless, with continuously increasing computer power, NEGF methods have become more and more attractive also for the description of inhomogeneous systems. Again, it is due to the generality of the method that it has stimulated applications for a variety of finite systems such as electrons in atoms and small molecules [SDvL06, DvL07, DSvL06, DvLS06, DvLS06], few-electron quantum dots [BBvL⁺09, BB09], molecular junctions [Thy08], and quantum dot states coupled to leads [MSSvL08, MSSvL09]. In addition, also applications to lattice models in combination with the cluster-perturbation theory [BP11] and to bosons in optical lattices [GdSP11] have been reported. Moreover, the NEGF is used to compute the transport properties of one-dimensional nanoscale transistors [IKA05] and to simulate the collision of one-dimensional nuclear slabs [DRB10, RBBD11]—however, these works mainly focus on the mean-field dynamics.

In particular, in Refs. [PvFVA09, PvFVA10], a very systematic analysis of various many-body approximations ranging from the Hartree-Fock to the T-matrix has been presented, considering (in a time-dependent fashion) a strongly correlated one-dimensional Hubbard cluster¹⁴ consisting

¹²For an introduction to semiconductor quantum dots, see, e.g., Ref. [BK93]

¹³As, e.g., provided by the generalized Kadanoff-Baym ansatz [LŠV86].

¹⁴We note, that the Hubbard chain has open ends.

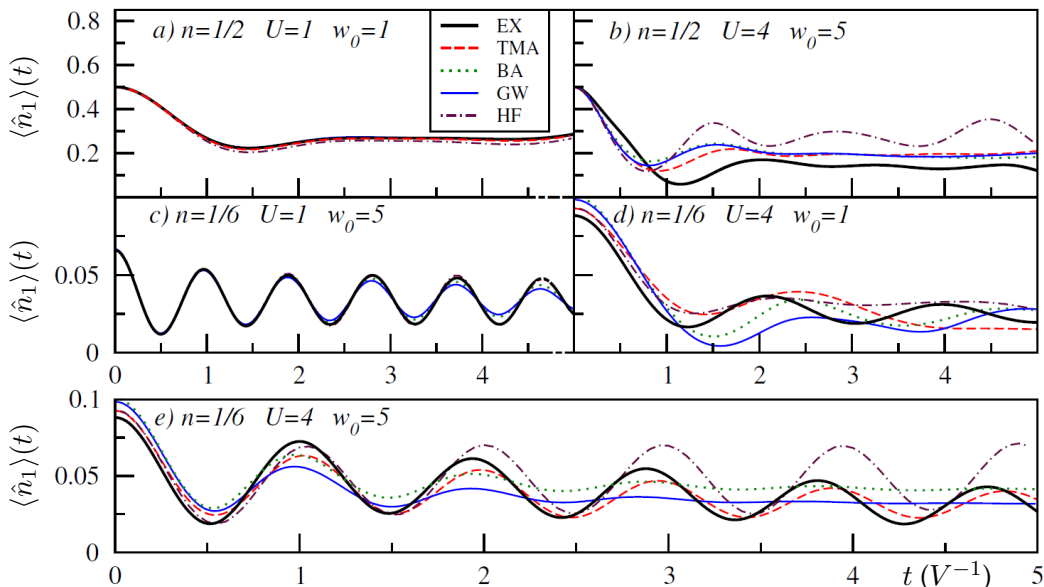


Figure 1.1: Electron dynamics of a one-dimensional Hubbard nanocluster involving six sites and, respectively, six (panels (a) and (b)) and two electrons (panels (c-e)). Shown is the evolution of the time-dependent density (or occupation) $\langle \hat{n}_1 \rangle(t)$ on the first lattice site after a field of form $w(t) = w_0 \theta(t)$ is switched on at site $R = 1$. The interaction strength U and w_0 are measured in units of the hopping parameter $V = 1$. While the black solid curve corresponds to the exact result, the others refer to the Hartree-Fock approximation (HF, brown dash-dotted), the second Born approximation (BA, green dotted), the GW approximation (blue solid) and the T-Matrix approximation (TMA, red dashed). Figure from *M. Puig von Friesen, C. Verdozzi, and C.-O. Almbladh* [PvFVA09].

of $R = 6$ sites and, respectively, $N = N_\uparrow + N_\downarrow = 2$ and 6 electrons ($N_\uparrow = N_\downarrow$). Thereby, the authors have solved the two-time Kadanoff-Baym equations (1.1) and, beyond an examination of the ground state spectral function, have investigated the electron dynamics under the influence of weak and strong external fields. Figure 1.1 (taken from Ref. [PvFVA09]) illustrates the response of the cluster for different interaction strengths U . Note that the system is initially in the ground state and that the electron density is measured in units of the number of electrons per site and per spin projection, i.e., $n = N(2R)^{-1}$.

In panel (a), one observes that, for, both, weak interaction ($U = 1$) and weak perturbation ($w_0 = 1$), all many-body approximations follow well the exact result for the time-dependent density $\langle \hat{n}_1 \rangle(t)$, compare the colored lines to the black line. On the contrary, in the adjacent panel (b), the simultaneous increase of U and w_0 leads to a situation where Hartree-Fock performs rather poorly while, when correlations are included (see the curves labeled GW, BA and TMA) consistently better results are obtained. For the Hubbard cluster with only two electrons (panels (c-e)), a similar trend is observed. In panel (d), it is difficult to compare approximate and exact occupation dynamics, and, in panel (e), the time-dependent T-matrix approximation appears to produce the

most accurate results. In summary, this example shows that (i) correlations play an important role in the dynamics of strongly interacting finite systems such that a beyond-Hartree-Fock treatment is necessary, and that (ii), along with system size and strength of perturbation, the quality of the applied many-body approximation can vary in favor of different excitation channels. For this reasons, differentiated studies also on other systems should be made.

Though it represents a finite system, the underlying Hamiltonian of the Hubbard cluster in Figure 1.1 is *relatively* simple (cf. Eq. (1) in Ref. [PvFVA09]). This is due to the fact, that, first, the electron-electron interaction is short-ranged and that, second, the electrons are assumed to move only between fixed lattice sites. The charge carriers themselves have no spatial extension¹⁵, and the time-dependent density is characterized by a set of on-site occupation numbers. Consequently, for the case discussed by Figure 1.1, the basis, in which the NEGF is expressed, has dimension 6.

Rather more complicated is the situation, when the concept of lattice sites is abandoned and a variable charge density distribution has to be resolved in space and time. To this end, the nonequilibrium Green function $\mathcal{G}(1, \bar{1})$ can, e.g., be represented on a spatial grid or can be expanded in an orbital basis that is adapted to the problem considered. When applying grid and, in turn, finite-difference methods¹⁶, an efficient way of integrating the two-time Kadanoff-Baym equations is difficult to realize in view of the fact that a large number of grid points (and a small mesh spacing) will be necessary. For this reason, so far, no numerical work in this direction has been reported which explicitly goes beyond the Hartree-Fock approximation and includes correlation effects. On the other hand, basis expansions of the NEGF according to $\mathcal{G}(1, \bar{1}) = \sum_{ij} \chi_i(\vec{r}) \chi_j^*(\vec{r}) \mathcal{G}_{ij}(t, \bar{t})$ are widely deployed: For atomic or molecular systems, the basis functions $\chi_i(\vec{r})$ are, e.g., constructed from Gauss- or Slater-type orbitals, see Ref. [DvLS06, DvL07], and, for quantum dots, it is a reasonable idea to apply eigenstates of the dot confinement [BBvL⁺09]. Furthermore, it is often possible to optimize the basis set by a separate Hartree-Fock calculation.

As a result of an orbital expansion, the Kadanoff-Baym equations (1.1) transform into a set of matrix equations for the elements $\mathcal{G}_{ij}(t, \bar{t})$. This directly promotes a numerical treatment. The drawback is, however, that rather complicated matrix elements for the binary interaction have to be provided before one can start to integrate the equations of motion. As these change with the system under investigation and enter the self-energy in a sophisticated manner, the solution of the KBEs involves a lot of precomputational analytical and/or numerical effort. In addition, an often repeated evaluation of the self-energy kernel $\Sigma[\mathcal{G}](1, \bar{1})$ for many-body approximations beyond Hartree-Fock will drastically slow down the two-time propagation algorithm [SDvL09]. Hence, within the context of those inhomogeneous systems where, to ensure convergence of the NEGF and derived observables, essentially more basis functions are needed than for (small- to moderately-sized) lattice models, a spatially and temporally extended solution of the KBEs is very demanding and limited by the available computer power.

In light of the above discussion, the question arises as to how a proper representation of the nonequilibrium Green function can be achieved that allows for an efficient solution of the two-time

¹⁵I.e., the inherent structure is neglected for simplicity of the model.

¹⁶To account for non-local operators that enter via $\hat{h}^{(1)}(1)$ in Eq. (1.1).

Kadanoff-Baym equations for inhomogeneous but non-lattice systems and that, at the same time, can be applied to a variety of different classes of (model) Hamiltonians. As a possible answer to this question, we, in this thesis, consider a hybrid method that combines the peculiar properties of the coordinate space with the sparse representation as offered by an orbital basis expansion. Together with the development of a highly parallelized code which overcomes hardware limitations, such an approach (at least for one-dimensional problems) promises a considerable advance towards extended full two-time solutions of the KBEs.

Finally, we emphasize that the availability of these solutions is, in particular, of relevance if, in a next step, further approximations such as the generalized Kadanoff-Baym (GKB) ansatz [LŠV86] are being applied. In this respect, these calculations serve as well-defined reference solutions. To follow this logical step will only be a marginal issue within this thesis.

1.3 Thesis Outline

The outline of this work is as follows.

CHAPTER 2 (Part I) sets the theoretical framework of this thesis and begins with a general introduction to quantum statistical mechanics and (non)equilibrium Green functions. Thereby, for a fermionic quantum system at finite temperatures, it presents the two-time Kadanoff-Baym equations and briefly reviews the concepts behind conserving many-body approximations. Particular focus is placed on avoiding the choice of a specific representation. The Chapter ends with the equations of motion for the individual Keldysh components of the one-particle NEGF.

In Part II, **CHAPTER 3** and **CHAPTER 4** deal with the numerical methods that are applied to efficiently solve the two-time Kadanoff-Baym equations including retardation, i.e., memory effects. The former introduces the finite element-discrete variable representation (FE-DVR) and shows how it is used at great advantage in the construction of the interaction matrix elements and the self-energies. The latter, implying FE-DVR notation, presents the method of how to integrate the equations of motion when the system is initially prepared in equilibrium and develops a well-scalable parallel distributed-memory algorithm for computing the NEGF in the two-time domain. In addition, the implementation of the generalized Kadanoff-Baym ansatz is discussed.

Then, in Part III, **CHAPTER 5** outlines the description of atomic and molecular systems in terms of one-dimensional models. To make the reader familiar with respective areas of application, a short (historic) literature overview is presented which covers the pathway from the one-dimensional hydrogen and the helium atom in (weak and strong) static and time-dependent external fields including ionization to multi-electron molecules in one dimension that undergo dissociation. Thereafter, the underlying model Hamiltonian is discussed in detail and the general situation is illustrated on the example of the diatomic molecule lithium hydride. At the end, the Chapter gives a brief overview on strong-field phenomena and shows that few-electron models being even simpler than that of helium can be worth studying to attack current issues regarding laser-matter interaction.

The thesis culminates in the Chapter last but one, **CHAPTER 6**, devoted to NEGF results on the

Table 1.1: Definition of atomic units [DE06], using the vacuum speed of light c , the electron mass (charge) m_e (e), the dielectric constant ϵ_0 and the inverse fine structure constant $\alpha^{-1} = 4\pi\epsilon_0\hbar c/e^2 \approx 137$.

Length (Bohr radius)	Time	Energy (Hartree)
$a_0 = \frac{4\pi\epsilon_0\hbar^2}{m_e e^2} = \frac{\hbar}{\alpha m_e c}$	$\tau_0 = \frac{16\pi^2\epsilon_0^2\hbar^3}{m_e e^4} = \frac{\hbar}{\alpha^2 c^2 m_e}$	$E_h = \frac{e^2}{4\pi\epsilon_0 a_0} = \alpha^2 c^2 m_e$
1 $a_0 \approx 0.529 \text{ \AA}$	1 $\tau_0 \approx 24.2 \text{ as}$	1 $E_h \approx 27.2 \text{ eV}$

static and dynamic properties of the one-dimensional models of helium (He), beryllium (Be), hydrogen (H_2), the molecular ion H_3^+ and lithium hydride (LiH). Thereby, all involved electrons are treated on the same footing, and correlations are included in the second(-order) Born approximation. Whereas, in the first part of this Chapter, the electronic ground state properties are computed for all mentioned systems from the Dyson equation, the second part covers, in particular, helium and the lithium hydride. Here, implying dipole and/or fixed-nuclei (Born-Oppenheimer) approximation, the central subject is the nonequilibrium behavior in the presence (non-)perturbative external fields. Overall, to assess the quality of the second Born approximation¹⁷, the results are compared to the Hartree-Fock approximation and to exact reference data obtained from the solution of the time-dependent Schrödinger equation. On top of that, to explore multi-electron excitations, the last part of the Chapter discusses on a slightly different model: four electrons in a one-dimensional quantum well.

Finally, in CHAPTER 7, some conclusions are drawn.

Unless stated otherwise, atomic units are used throughout the thesis, see Table 1.1.

¹⁷In nonequilibrium, this applies to, both, the full two-time evolution of the Green function and the single-time evolution under the generalized Kadanoff-Baym ansatz.

PART I

Theory

Quantum Statistical Mechanics

”... (E)quilibrium and nonequilibrium statistical mechanics are formally and structurally equivalent and ... this equivalence is demonstrated by introducing a contour ordering to play the role of the usual time ordering.” (Quotation from Ref. [RS86]).

This conclusion, drawn by *J. Rammer* and *H. Smith* in the Review [RS86], well delineates the situation when one proceeds from quantum field theory in thermodynamic equilibrium to the nonequilibrium case, and has the consequence that basically all fundamentals known from (equilibrium) Matsubara theory [FW71, Mah00], e.g., Feynman rules and diagram techniques, can be transferred and applied to the description of time-dependent processes.

The original work on nonequilibrium statistical mechanics and quantum kinetic equations was pioneered by *P.C. Martin* [MS59] and *J. Schwinger* [Sch61] and was developed further by *L.P. Kadanoff* and *G. Baym* [KB62] (in the USA) and, parallel, by *L.V. Keldysh* [Kel65a] and others (in the USSR). Regarding the boundary conditions of the kinetic equations, there exist mainly two approaches that define self-consistent, stationary initial states: (i) the formulation due to *Keldysh* [Kel65a] assuming an adiabatically switch-on of the interaction¹, and (ii) the use of the grand canonical ensemble which leads to an additional imaginary time path.

In the present thesis, we follow the latter approach.

2.1 Quantum Statistical Averages

Let us consider a quantum many-body system of identical particles at a finite temperature T ($\beta^{-1} = k_B T$, with Boltzmann’s constant k_B). The exact many-particle state of such a system is not known. This is a consequence of the system being connected to a bath of other particles, where, in addition, particles can eventually be exchanged with the reservoir (open system). The latter fact is well incorporated in the mixed state description of the grand canonical ensemble, which explicitly allows for variation of particle number.

¹The inclusion of initial correlations has become possible due to the work of *S. Fujita* [Fuj65], *A.G. Hall* [Hal75] and *P. Danielewicz* [Dan84a].

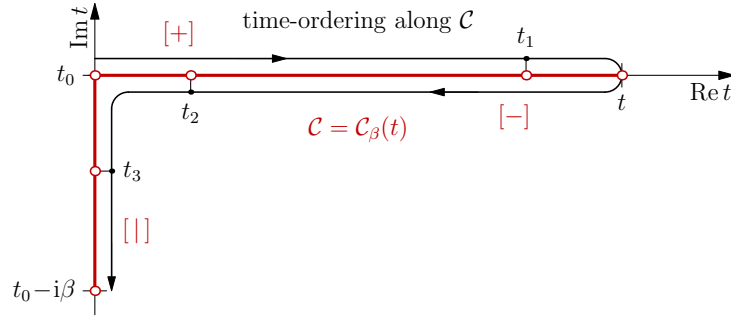


Figure 2.1: The complex Keldysh (Schwinger) time contour $\mathcal{C} = \mathcal{C}_\beta(t)$. Time t_2 is later on the contour than t_1 , and time t_3 is later on the contour than t_1 and t_2 .

In the grand canonical ensemble, the time-dependent observable of any operator \hat{O} is obtained from,

$$\langle \hat{O} \rangle(t) = \frac{1}{\Xi_0} \text{Tr} \left[e^{-\beta \hat{K}(t_0)} \hat{O} \right], \quad (2.1)$$

with the partition function $\Xi_0 = \text{Tr}[e^{-\beta \hat{K}(t_0)}]$ and the grand canonical Hamiltonian $\hat{K}(t) = \hat{H}(t) - \mu \hat{N}$ being time-independent for $t < t_0$. Further, $\hat{\rho} = \frac{1}{\Xi_0} e^{-\beta \hat{K}(t_0)}$ (\hat{N}) is just the equilibrium density (particle number) operator, and μ is the one-particle chemical potential. Due to the equality $\hat{U}(t_0 - i\beta, t_0) = e^{-\beta \hat{K}(t_0)}$ of the unitary time evolution operator $\hat{U}(t, t_0) = T_t e^{-i \int_{t_0}^t d\bar{t} \hat{K}(\bar{t})}$, with usual time-ordering guaranteed by T_t , we can rewrite² the above average as,

$$\begin{aligned} \langle \hat{O} \rangle(t) &= \frac{1}{\Xi_0} \text{Tr} \left[\hat{U}(t_0 - i\beta, t_0) \hat{U}(t_0, t) \hat{O} \hat{U}(t, t_0) \right] \\ &= \frac{1}{\Xi_0} \text{Tr} \left[T_{\mathcal{C}} \left\{ e^{-i \int_{\mathcal{C}} d\bar{t} \hat{H}(\bar{t})} \hat{O} \right\} \right]. \end{aligned} \quad (2.2)$$

Reading from right to left, Eq. (2.2) represents the starting point for the extension of the Matsubara technique [Mat55] to nonequilibrium situations, introducing a complex time variable $t_{\mathcal{C}} = t + i\tau$ and a corresponding time-ordering operator $T_{\mathcal{C}}$ (cf. second equality in Eq. (2.2)), that acts along the round-trip Keldysh contour $\mathcal{C} = \mathcal{C}_\beta(t)$, see Figure 2.1.

Despite the fact that Eq. (2.2) allows for calculating time-dependent properties of a quantum system from first principles, it has more consequences:

- (i) Formally, the presence of the contour \mathcal{C} , motivates a contour algebra for contour-ordered functions. Such an algebra has been described by *D.F. DuBois* [DuB67] and *D.C. Langreth* [Lan67], and finds its application in the Langreth rules [RS86], see Chapter 2.3.4.
- (ii) Particularly for two-time quantities³, such as the nonequilibrium Green function to be defined below, a (3×3) matrix representation is convenient [Wag91]. To this end, different contour branches can be labeled, ”+”, ”-”, and ”|”, cf. Figure 2.1.

²Using the cyclic invariance of the trace.

³In the extended Keldysh space, i.e., including the imaginary-time path from t_0 to $t_0 - i\beta$.

- (iii) Eq. (2.2) is, *a priori*, not restricted to the thermodynamic limit, where particle number N and volume V become macroscopic at $\frac{N}{V} = \text{const.}$, but is also applicable to finite systems as well as to the ground state ($\beta \rightarrow \infty$).

2.2 Dynamics of Creation and Annihilation Operators

For a many-fermion wave function $|\{n\}\rangle = |n_1, n_2, \dots\rangle$ with spin orbital [SO96] occupation numbers $n_i = 0, 1$, particle number $N = \sum_i n_i$ and inner product $\langle\{n\}|\{n'\}\rangle = \prod_i \delta_{n_i n'_i}$, the creation (annihilation) of an electron in a single-particle state $|i\rangle$ is described by an operator,

$$\hat{f}_i^\dagger \quad (\hat{f}_i) , \quad (2.3)$$

that acts in Fock space [Foc32], $\mathcal{F} = \bigoplus_{i=0}^{\infty} \mathcal{F}^{(i)}$, according to,

$$\begin{aligned} \hat{f}_i^\dagger |n_1, n_2, \dots, n_i, \dots\rangle &= (-1)^s (1 - n_i) |n_1, n_2, \dots, n_i + 1, \dots\rangle , \\ \hat{f}_i |n_1, n_2, \dots, n_i, \dots\rangle &= (-1)^s n_i |n_1, n_2, \dots, n_i - 1, \dots\rangle , \end{aligned} \quad (2.4)$$

where $s = \sum_{j=1}^{i-1} n_j$. Note that $\hat{f}_i |0\rangle = 0$ is just a special case of the annihilator action. As result of Eq. (2.4), one obtains a correctly antisymmetrized $(N \pm 1)$ -electron wave function. Thereby, the built-in state antisymmetrization is, in the Heisenberg picture, provided by the equal-time anticommutation relations⁴,

$$\begin{aligned} [\hat{f}_i(t), \hat{f}_j^\dagger(t)]_+ &= \delta_{ij} , \\ [\hat{f}_i^\dagger(t), \hat{f}_j^\dagger(t)]_+ &= [\hat{f}_i(t), \hat{f}_j(t)]_+ = 0 , \end{aligned} \quad (2.5)$$

where $\hat{f}_i(t)$ and $\hat{f}_j^\dagger(t)$ are canonically paired, e.g., [Hor10], and the number operator for particles in a state $|i\rangle$ reads,

$$\hat{n}_i(t) = \hat{f}_i^\dagger(t) \hat{f}_i(t) , \quad (2.6)$$

i.e., $\hat{N}(t) = \sum_i \hat{n}_i(t)$. The generalization of Eq. (2.6) is given by,

$$\hat{n}_{ij}(t, t') = \hat{f}_i^\dagger(t) \hat{f}_j(t') , \quad (2.7)$$

which is connected to the one-particle density operator, $\hat{\rho}_{ij}^{(1)}(t) = \hat{n}_{ij}(t, t')|_{t=t'}$.

Using the creation and annihilation operators (we neglect a superscript "H" that indicates the Heisenberg picture), the Hamiltonian for a quantum many-body system including a two-body

⁴For bosons, creation and annihilation operators, \hat{b}_i^\dagger and \hat{b}_i , obey corresponding commutation relations and have actions, $\hat{b}_i^\dagger(t) |n_1, n_2, \dots, n_i, \dots\rangle = \sqrt{n_i + 1} |n_1, n_2, \dots, n_i + 1, \dots\rangle$ and $\hat{b}_i(t) |n_1, n_2, \dots, n_i, \dots\rangle = \sqrt{n_i} |n_1, n_2, \dots, n_i - 1, \dots\rangle$.

interaction $\hat{h}^{(2)}$ can be expressed in the *second-quantized* form,

$$\begin{aligned}\hat{H}(t) &= \hat{H}^{(1)}(t) + \hat{H}^{(2)}(t) \\ &= \sum_{i,j} \langle i | \hat{h}^{(1)}(t) | j \rangle \hat{f}_i^\dagger(t) \hat{f}_j(t) \\ &\quad + \frac{1}{2!} \sum_{i,j,i',j'} \langle i, j | \hat{h}^{(2)} | i', j' \rangle \hat{f}_i^\dagger(t) \hat{f}_j^\dagger(t) \hat{f}_{j'}(t) \hat{f}_{i'}(t).\end{aligned}\tag{2.8}$$

The first line divides the Hamiltonian into a non-interacting and an interacting part, where, in the second line, $\hat{h}^{(1)}(t)$ denotes the single-particle contribution, containing kinetic plus potential energy, and $|i, j\rangle = |i\rangle \otimes |j\rangle$.

For a given $\hat{H}(t)$, the dynamics of the creation and annihilation operator follow from the Heisenberg equation,

$$\frac{\partial}{\partial t} \hat{f}_i(t) = i \left[\hat{H}(t), \hat{f}_i(t) \right]_- ,\tag{2.9}$$

which yields,

$$\left(i \frac{\partial}{\partial t} \delta_{ij} - \langle i | \hat{h}^{(1)}(t) | j \rangle \right) \hat{f}_j(t) = \langle i, k | \hat{h}^{(2)} | j, l \rangle \hat{f}_k^\dagger(t) \hat{f}_l(t) \hat{f}_j(t) .\tag{2.10}$$

Here, any double occurrence of indices implies an additional summation over all states (Einstein notation). Moreover, Eq. (2.10) depicts the most general form of the equation of motion as it is not limited to a specific quantum mechanical representation. The usual representation of $\hat{H}(t)$, and, respectively, of Eq. (2.10), using electron field operators $\hat{\psi}^\dagger(1)$ ($\hat{\psi}(1)$) with $1 = (x, t)$ and spin included in variable x , is obtained with the transformation to a coordinate basis $\{|x\rangle\}$,

$$\hat{\psi}^\dagger(1) = \sum_i \langle i | x \rangle \hat{f}_i^\dagger(t) , \quad \left(\hat{\psi}(1) = \sum_i \langle x | i \rangle \hat{f}_i(t) \right) .\tag{2.11}$$

One, then, recovers [KB62],

$$\left(i \frac{\partial}{\partial t} - \hat{h}^{(1)}(1) \right) \hat{\psi}(1) = \int d\bar{1} \hat{h}^{(2)}(1 - \bar{1}) \hat{\psi}^\dagger(\bar{1}) \hat{\psi}(\bar{1}) \hat{\psi}(1) ,$$

with, usually, $\hat{h}^{(1)}(1) = \hat{h}^{(1)}(x_1, -i \frac{\partial}{\partial x_1}, t_1)$ and $\hat{h}^{(2)}(1 - \bar{1}) = \delta(t_1 - t_{\bar{1}}) \hat{h}^{(2)}(|x_1 - x_{\bar{1}}|)$.

Below, instead of the field operators, we use the operators $\hat{f}_i(t)$ in order to emphasize the general structure. This is of relevance for the basis representation applied in Chapter 3.

2.3 Nonequilibrium Green Functions (NEGFs)

2.3.1 Definitions

Without applying a specific representation, the one-particle nonequilibrium Green function (NEGF) is defined as,

$$\mathcal{G}_{i_1 i_{\bar{1}}}^{(1)}(t_1, t_{\bar{1}}) = -i \left\langle T_C \{ \hat{f}_{i_1}(t_1) \hat{f}_{i_{\bar{1}}}^\dagger(t_{\bar{1}}) \} \right\rangle ,\tag{2.12}$$

which, according to Eq. (2.2), equals

$$\mathcal{G}_{i_1 i_{\bar{1}}}^{(1)}(t_1, t_{\bar{1}}) = -\frac{i}{\Xi_0} \text{Tr} \left[\hat{U}(t_0 - i\beta) T_{\mathcal{C}} \{ \hat{f}_{i_1}(t_1) \hat{f}_{i_{\bar{1}}}^\dagger(t_{\bar{1}}) \} \right].$$

Note that, due to the presence of the time-ordering operator $T_{\mathcal{C}}$, all times⁵ vary on the full Keldysh contour \mathcal{C} (cf. Figure 2.1), and that we, therefore, can define Green functions related to different domains in Keldysh space. Moreover, the Green function contains the one-particle (reduced) density matrix in the limit of equal times ($\eta > 0$),

$$\mathcal{F}_{i_1 i_{\bar{1}}}^{(1)}(t) = \lim_{\eta \rightarrow 0} \left(-i \mathcal{G}_{i_1 i_{\bar{1}}}^{(1)}(t, t + \eta) \right) \stackrel{\text{def.}}{=} -i \mathcal{G}_{i_1 i_{\bar{1}}}^{(1)}(t, t^+), \quad (2.13)$$

and, hence, is directly connected to many physically relevant observables⁶. For the two-particle nonequilibrium Green function, it is,

$$\mathcal{G}_{i_1 i_2, i_{\bar{1}} i_{\bar{2}}}^{(2)}(t_1, t_2; t_{\bar{1}}, t_{\bar{2}}) = (-i)^2 \left\langle T_{\mathcal{C}} \{ \hat{f}_{i_1}(t_1) \hat{f}_{i_2}(t_2) \hat{f}_{i_{\bar{2}}}^\dagger(t_{\bar{2}}) \hat{f}_{i_{\bar{1}}}^\dagger(t_{\bar{1}}) \} \right\rangle. \quad (2.14)$$

Any n -particle Green function with $n > 2$ is defined likewise taking a prefactor of $(-i)^n$.

2.3.2 The Kadanoff-Baym Equations

The equation of motions for the NEGFs follow directly from the time evolution of the creation and annihilation operators. $\mathcal{G}^{(1)}$ obeys the following pair of coupled integro-differential equations—the Kadanoff-Baym equations⁷ [KB62]:

(KBE I.)

$$\begin{aligned} & \left(i \frac{\partial}{\partial t_1} \delta_{i_1 i_2} - \langle i_1 | \hat{h}^{(1)}(t_1) | i_2 \rangle \right) \mathcal{G}_{i_2 i_{\bar{1}}}^{(1)}(t_1, t_{\bar{1}}) \\ &= \delta_{\mathcal{C}}(t_1 - t_{\bar{1}}) \delta_{i_1 i_{\bar{1}}} - i \int_{\mathcal{C}} dt_2 \langle i_1, i_2 | \hat{h}^{(2)}(t_1 - t_2) | i_3, i_4 \rangle \mathcal{G}_{i_4 i_3, i_{\bar{1}} i_2}^{(2)}(t_1, t_2; t_{\bar{1}}, t_2^+), \end{aligned} \quad (2.15)$$

(KBE II.)

$$\text{adjoint of Eq. (KBE I.) with } t_1 \leftrightarrow t_{\bar{1}}. \quad (2.16)$$

Here, again, summation is implied over all indices appearing twice. A few remarks are in order:

- (i) On the right hand side (r.h.s.) of Eq. (KBE I.), we have introduced the short notation $\hat{h}^{(2)}(t_1 - t_2) = \delta_{\mathcal{C}}(t_1 - t_2) \hat{h}^{(2)}$ for the generalized two-body interaction.
- (ii) The boundary and initial conditions for Eqs. (KBE I.) and (KBE II.) can be summarized in the Kubo-Martin-Schwinger (KMS) conditions⁸ [Kub57],

$$\mathcal{G}_{i_1 i_{\bar{1}}}^{(1)}(t_0, t_{\bar{1}}) = -\mathcal{G}_{i_1 i_{\bar{1}}}^{(1)}(t_0 - i\beta, t_{\bar{1}}), \quad \mathcal{G}_{i_1 i_{\bar{1}}}^{(1)}(t_1, t_0) = -\mathcal{G}_{i_1 i_{\bar{1}}}^{(1)}(t_1, t_0 - i\beta), \quad (2.17)$$

where $\hat{H}(t)$ is assumed to be time-independent for $t < t_0$.

⁵We neglect the subscript \mathcal{C} in $t_1, t_{\bar{1}}$, cf. Eq. (2.2).

⁶One-body quantities follow from $\langle \hat{O}^{(1)} \rangle(t) = \sum_{ij} \mathcal{F}_{ij}^{(1)}(t) \langle j | \hat{O}^{(1)} | i \rangle$.

⁷For a bosonic system, the contour integral in (KBE I.) and (KBE II.) has a prefactor of $+i$.

⁸Consider Eq. (2.12) at $t_1, t_{\bar{1}} = t_0 - i\beta$ and use the cyclic property of the trace.

- (iii) The Kadanoff-Baym equations for the one-particle Green function are not closed: Generally, the equation of motion for $\mathcal{G}^{(n)}$ requires information from $\mathcal{G}^{(n-1)}$ and $\mathcal{G}^{(n+1)}$, see, e.g., Refs. [KSK05, Hor10]. Therefore, Eqs. (KBE I.) and (KBE II.) indicate only the first equations of a complete hierarchy known as the Martin-Schwinger (MS) hierarchy [MS59].
- (iv) A perturbation expansion of $\mathcal{G}^{(1)}$ can be performed in the same manner as that of quantum field theory of equilibrium using a generalized S-matrix $\mathcal{S}_{\mathcal{C}}$ [Kit10]. Equivalently, a formal closure of the MS hierarchy is obtained by replacing the contour integral $-i \int_{\mathcal{C}} dt_2 \dots$ on the r.h.s. of Eq. (KBE. I) by,

$$\int_{\mathcal{C}} dt_2 \Sigma_{i_1 i_2}^{(1)}(t_1, t_2) \mathcal{G}_{i_2 i_1}^{(1)}(t_2, t_1), \quad (2.18)$$

with the two-time self-energy $\Sigma^{(1)}$, being a functional of $\mathcal{G}^{(1)}$ and $\hat{h}^{(2)}$.

- (v) Self-consistent approximations for $\Sigma^{(1)}$ in point (iv) obey conservation laws and preserve particle number, momentum and energy. This issue has been investigated first by *J.M. Luttinger* and *J.C. Ward* [LW60] analyzing the thermodynamic potential in terms of the exact self-energy. Later, a sufficient condition was given by *G. Baym* [Bay62]. It states that, if $\Sigma^{(1)}$ is generated from the Luttinger-Ward functional Φ as⁹,

$$\Sigma_{i_1 i_2}^{(1)}(t_1, t_2) = \frac{\delta \Phi[\mathcal{G}^{(1)}]}{\delta \mathcal{G}_{i_2 i_1}^{(1)}(t_2, t_1)}, \quad \Phi = \ln \langle \mathcal{S}_{\mathcal{C}} \rangle, \quad (2.19)$$

the over-all conservation laws are automatically fulfilled¹⁰. For this reason, approximations for the self-energy according to Eq. (2.19) are called Φ -*derivable* and can be constructed by diagram technique. The topologically distinct diagrams¹¹ for Φ up to second order (leading to the second Born approximation of $\Sigma^{(1)}$) are shown in Figure 2.2.

- (vi) For completeness, we present the explicit structure of the Kadanoff-Baym equations in coordinate representation. Replacing the states $|i\rangle$ by (spin) orbitals $|x\rangle$ and using,

$$\begin{aligned} \delta_{i_1 i_2} &\rightarrow \delta(x_1 - x_2), \\ \langle x_1 | \hat{h}^{(1)}(t) | x_2 \rangle &\rightarrow \delta(x_1 - x_2) \hat{h}^{(1)}(1), \\ \sum_{i_2} &\rightarrow \int dx_2, \end{aligned}$$

the first equation of motion (2.15) attains the closed form [Kit10, Hor10],

$$\left(i \frac{\partial}{\partial t_1} - \hat{h}^{(1)}(1) \right) \mathcal{G}(1, \bar{1}) = \delta_{\mathcal{C}}(1 - \bar{1}) + \int_{\mathcal{C}} d2 \Sigma(1, 2) \mathcal{G}(2, \bar{1}), \quad (2.20)$$

with $\mathcal{X}(1, \bar{1}) = \mathcal{X}_{x_1, x_{\bar{1}}}^{(1)}(t_1, t_{\bar{1}})$ ($\mathcal{X} = \mathcal{G}, \Sigma$), and notational simplifications $\delta_{\mathcal{C}}(1 - \bar{1}) = \delta_{\mathcal{C}}(t_1 - t_{\bar{1}}) \delta(x_1 - x_{\bar{1}})$ and $\int_{\mathcal{C}} d2 \stackrel{\text{def.}}{=} \int_{\mathcal{C}} dt_2 \int dx_2$.

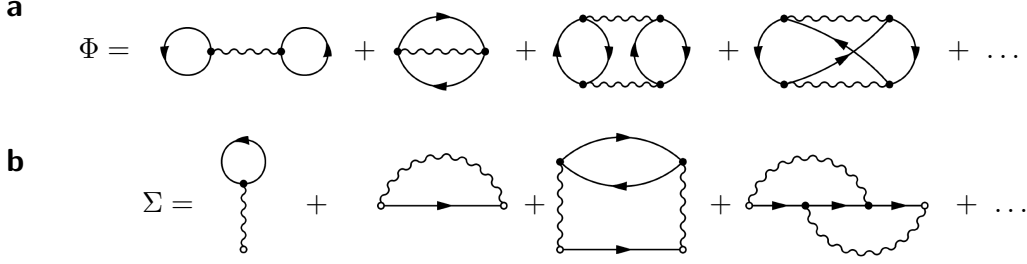


Figure 2.2: Topologically distinct first- and second-order (skeleton) diagrams for (a) the Luttinger-Ward functional $\Phi[\mathcal{G}^{(1)}]$ and (b) the derived self-energy $\Sigma[\mathcal{G}^{(1)}]$. Arrows denote NEGFs, wavy lines mark two-body interactions $\hat{h}^{(2)}$. The first two diagrams (being of first-order in the interaction) lead to the Hartree-Fock approximation, the two subsequent diagrams are added for the second(-order) Born approximation.

An important quantity subject to a conserving approximation is the average total energy, cf. definition (2.8). Thereby, in terms of the NEGF, the average one-body energy $\langle \hat{H}^{(1)} \rangle$ is—as all one-body observables—given by¹²,

$$\langle \hat{H}^{(1)} \rangle(t) = -i \mathcal{G}_{ij}^{(1)}(t, t^+) \langle j | \hat{h}^{(1)}(t) | i \rangle, \quad (2.21)$$

whereas the determination of the average two-body interaction energy $\langle \hat{H}^{(2)} \rangle$ is somewhat more involved ($\eta > 0$),

$$\begin{aligned} \langle \hat{H}^{(2)} \rangle(t) &= \frac{1}{2!} \langle i, j | \hat{h}^{(2)} | i', j' \rangle \langle \hat{f}_i^\dagger(t) \hat{f}_j^\dagger(t) \hat{f}_{j'}(t) \hat{f}_{i'}(t) \rangle \\ &= -\frac{i}{2!} \lim_{\eta \rightarrow 0} \int_{\mathcal{C}} d\bar{t} \Sigma_{ij}^{(1)}(t, \bar{t}) \mathcal{G}_{ji}^{(1)}(\bar{t}, t + \eta) \\ &\stackrel{\text{def.}}{=} -\frac{i}{2!} \int_{\mathcal{C}} d\bar{t} \Sigma_{ij}^{(1)}(t, \bar{t}) \mathcal{G}_{ji}^{(1)}(\bar{t}, t^+). \end{aligned} \quad (2.22)$$

The second equality, including the contour integral, is obtained by comparing the expression of Eq. (2.22) to the self-energy definition (at $t_{\bar{1}} > t_1$ on \mathcal{C}):

$$\begin{aligned} &\int_{\mathcal{C}} dt_2 \Sigma_{i_1 i_2}^{(1)}(t_1, t_2) \mathcal{G}_{i_2 i_{\bar{1}}}^{(1)}(t_2, t_{\bar{1}}) \\ &= -i \int_{\mathcal{C}} dt_2 \langle i_1, i_2 | \hat{h}^{(2)}(t_1 - t_2) | i_3, i_4 \rangle \mathcal{G}_{i_4 i_3, i_{\bar{1}}, i_2}^{(2)}(t_1, t_2; t_{\bar{1}}, t_2^+) \\ &= i \int_{\mathcal{C}} dt_2 \delta_{\mathcal{C}}(t_1 - t_2) \langle i_1, i_2 | \hat{h}^{(2)} | i_3, i_4 \rangle \langle T_{\mathcal{C}} \{ \hat{f}_{i_4}(t_1) \hat{f}_{i_3}(t_2) \hat{f}_{i_2}^\dagger(t_2^+) \hat{f}_{i_1}^\dagger(t_{\bar{1}}) \} \rangle \\ &= i \langle i_1, i_2 | \hat{h}^{(2)} | i_3, i_4 \rangle \langle \hat{f}_{i_{\bar{1}}}^\dagger(t_{\bar{1}}) \hat{f}_{i_2}^\dagger(t_{\bar{1}}^+) \hat{f}_{i_4}(t_1) \hat{f}_{i_3}(t_1) \rangle. \end{aligned} \quad (2.23)$$

⁹An explicit expression for Φ is given, e.g., in Ref. [DSvL06].

¹⁰This is a direct consequence of the (symmetry) conditions (A) and (B) for a conserving approximation formulated by *G. Baym* and *L.P. Kadanoff* in Ref. [BK61].

¹¹The terms "irreducible" and "proper" are often used as synonyms in conjunction with the resulting self-energy.

¹²Note that Einstein's notation is applied.

2.3.3 The Dyson Equation; Equilibrium Limit

The Kadanoff-Baym equations (KBE I.) and (KBE II.) include the usual Dyson equation for the equilibrium Matsubara Green function [Mah00] as the special case of $\mathcal{G}_{i_1 i_1}^{(1)}(t_1, t_1)$ having purely imaginary time arguments: $t_1, t_1 \in \{t_0 - i\tau | 0 \leq \tau \leq \beta\}$. In our notation, the Dyson equation has the form [DvL05],

(DE I.)

$$\left(-\frac{\partial}{\partial \tau} \delta_{i_1 i_2} - \langle i_1 | \hat{h}^{(1)} | i_2 \rangle \right) \mathcal{G}_{i_2 i_1}^M(\tau) = \delta(\tau) \delta_{i_1 i_1} + \int_0^\beta d\bar{\tau} \Sigma_{i_1 i_2}^M(\tau - \bar{\tau}) \mathcal{G}_{i_2 i_1}^M(\bar{\tau}), \quad (2.24)$$

in which we have applied the transformation rule¹³,

$$\mathcal{X}_{i_1 i_1}^M(\tau_1 - \tau_1) = -i \mathcal{X}_{i_1 i_1}^{(1)}(t_0 - i\tau_1, t_0 - i\tau_1), \quad \mathcal{X} = \mathcal{G}, \Sigma, \quad (2.25)$$

and the Matsubara self-energy Σ^M functionally depends upon \mathcal{G}^M and $\hat{h}^{(2)}$. The one-particle equilibrium density matrix is¹⁴, then ($\eta > 0$),

$$\mathcal{F}_{i_1 i_1}^{(1)}(t \leq t_0) = \lim_{\eta \rightarrow 0} \mathcal{G}_{i_1 i_1}^M(-\eta) \stackrel{\text{def.}}{=} \mathcal{G}_{i_1 i_1}^M(0^-). \quad (2.26)$$

Any self-consistent $\mathcal{G}^M(\tau)$ that satisfies Dyson's equation and the KMS conditions¹⁵ (2.17), for a specific choice of the self-energy, serves as an appropriate initial state for the time evolution of a quantum system subject to the Kadanoff-Baym equations and the time-dependent Hamiltonian $\hat{H}(t)$ of Eq. (2.8). Due to this significance, we want to outline the solution of Eq. (2.24) for three different situations.

First, consider the noninteracting Green function that describes an ideal Fermi system. Here, the r.h.s. of Eq. (2.24) vanishes due to $\Sigma^M \equiv 0$. The formal solution of the Dyson equation, then, reads,

$$\mathcal{G}^M(\tau) \propto \exp(-\hat{h}^{(1)} \tau). \quad (2.27)$$

The proportionality factor is obtained from the comparison of $\langle \hat{H}^{(1)} \rangle = \langle i | \hat{h}^{(1)} | j \rangle \mathcal{G}_{ji}^M(0^-)$ with the textbook result [Mah00],

$$\langle \hat{H}^{(1)} \rangle = -\frac{\partial}{\partial \beta} \ln \Xi_0 \Big|_{\xi_0, V} = \sum_{i=0}^{\infty} \epsilon_i \bar{n}(\beta, \epsilon_i - \mu), \quad (2.28)$$

at constant fugacity $\xi_0 = e^{\beta\mu}$ and volume V , where $\Xi_0 = \prod_{i=0}^{\infty} [1 + e^{-\beta(\epsilon_i - \mu)}]$ is the ideal partition function, $\bar{n}(\beta, \epsilon) = [1 + \exp(\beta\epsilon)]^{-1}$ denotes the Fermi-Dirac distribution, and the energies ϵ_i are

¹³In equilibrium quantum field theory, the Hamiltonian is time-independent which means that Green functions and self-energies become functions of time-differences only.

¹⁴In agreement with Eq. (2.13).

¹⁵The KMS conditions require $\mathcal{G}_{ij}^M(\tau)$ to be antiperiodic in β , i.e., $\mathcal{G}_{ij}^M(\tau + \beta) = -\mathcal{G}_{ij}^M(\tau)$.

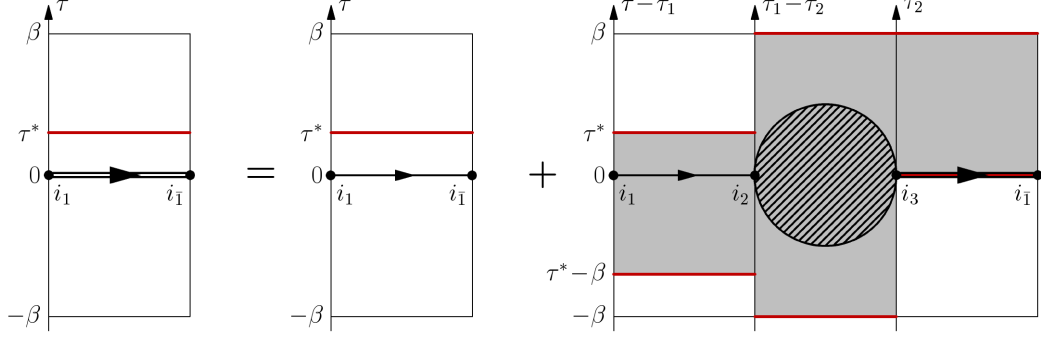


Figure 2.3: Diagrammatic representation of the Dyson equation (2.32) and integration region (gray) for fixed $\tau = \tau^*$ in $\mathcal{G}^M(\tau)$. Plain arrows denote \mathcal{G}^0 , double plain arrows indicate \mathcal{G}^M . The shaded circle represents the self-energy kernel Σ^K constructed from Σ^M and Σ^0 .

eigenvalues of $\langle i | \hat{h}^{(1)}(t_0) | j \rangle$. Consequently, if the states $\{|i\rangle\}$ together with the energies $\{\epsilon_i\}$ form an eigensystem of Hamiltonian $\hat{H}^{(1)}$, the Matsubara Green function is diagonal,

$$\mathcal{G}_{i_1 i_1}^M(\tau) = \delta_{i_1 i_1} \bar{n}(\beta, \epsilon_i - \mu) e^{-(\epsilon_i - \mu)\tau}. \quad (2.29)$$

If, instead of μ , the particle number is fixed, the chemical potential follows from inversion of equation $N = \sum_{i=0}^{\infty} \bar{n}(\beta, \epsilon_i - \mu)$.

Second, consider the Dyson equation under the constraint of the self-energy being time-local, i.e., when $\Sigma^M(\tau) = \delta(\tau)\Sigma^0$. This holds true for any first-order perturbation expansion of the Green function where correlations are being neglected. We write \mathcal{G}^0 for \mathcal{G}^M , and readily obtain the Dyson equation as¹⁶,

(DE II.)

$$\left(-\frac{\partial}{\partial \tau} \delta_{i_1 i_2} - \langle i_1 | \{ \hat{h}^{(1)} + \Sigma^0 \} | i_2 \rangle \right) \mathcal{G}_{i_2 i_1}(\tau) = \delta(\tau) \delta_{i_1 i_1}. \quad (2.30)$$

A consistent way to omit the delta function $\delta(\tau)$ is to restrict the Green function to $[-\beta, \beta] \setminus \{0\}$, see, e.g., Ref. [BF07]. With the above consideration, it is clear that the solution is also of form (2.29) including renormalized energies and, if necessary, a different chemical potential. However, we note, that in Eq. (2.30), Σ^0 functionally depends upon the solution (more precisely, on the one-body density matrix $\mathcal{G}^M(0^-)$) such that the Dyson equation must be iterated up to self-consistency¹⁷. In addition, the average total energy is not of form (2.28) but,

$$\langle \hat{H} \rangle = \left\{ \langle i | \hat{h}^{(1)} | j \rangle + \frac{1}{2} \Sigma_{ij}^0 \right\} \mathcal{G}_{ji}^0(0^-). \quad (2.31)$$

This is a direct consequence of Eq. (2.22).

¹⁶The expressions Σ_{ij}^0 and $\langle j | \Sigma^0 | j \rangle$ are equivalent.

¹⁷For weakly to moderately interacting systems, a suitable starting point may be the noninteracting Green function.

In the third and most general case, the self-energy Σ^M may have a non-trivial τ -dependence. In this situation, we can use Eq. (2.30) to transform the Dyson equation into integral form,

(DE III.)

$$\begin{aligned}\mathcal{G}_{i_1 i_{\bar{1}}}^M(\tau) &= \mathcal{G}_{i_1 i_{\bar{1}}}^0(\tau) + \int_0^\beta d\tau_1 \int_0^\beta d\tau_2 \mathcal{G}_{i_1 i_2}^0(\tau - \tau_1) \Sigma_{i_2 i_3}^K(\tau_1 - \tau_2) \mathcal{G}_{i_3 i_{\bar{1}}}^M(\tau_2), \\ \Sigma_{i_1 i_{\bar{1}}}^K(\tau) &= \Sigma_{i_1 i_{\bar{1}}}^M(\tau) - \delta(\tau) \Sigma_{i_1 i_{\bar{1}}}^0,\end{aligned}\quad (2.32)$$

which has the diagrammatic representation as shown in Figure 2.3. Further, it is to be noted that Σ^0 is a functional of \mathcal{G}^0 only (in first order), while the self-energy Σ^M involves first- and higher-order diagrams expressed by the full propagator \mathcal{G}^M . For self-consistency, Eq. (2.32) is, again, solved by iteration with $\mathcal{G}^M = \mathcal{G}^0$ as the natural starting point. Moreover, as the Matsubara Green function is antiperiodic in β , cf. Fn. 15 (footnote), it is sufficient to solve the Dyson equation on either the half interval $[-\beta, 0)$ or $(0, \beta]$ ¹⁸. Finally, with Eqs. (2.21) and (2.22), the average total energy reads,

$$\langle \hat{H} \rangle = \left\{ \langle i | \hat{h}^{(1)} | j \rangle + \frac{1}{2} \Sigma_{ij}^{M,0} \right\} \mathcal{G}_{ji}^M(0^-) + \frac{1}{2} \int_0^\beta d\tau \Sigma_{ij}^{M,1}(-\tau) \mathcal{G}_{ji}^M(\tau), \quad (2.33)$$

where we have introduced $\Sigma^M(\tau) = \delta(\tau) \Sigma^{M,0} + \Sigma^{M,1}(\tau)$. It is important to realize that the first-order contributions to the interaction energy extracted from Σ^0 and $\Sigma^{M,0}$ are not identical.

2.3.4 Matrix Formulation and Properties

Generally, the one-particle NEGF can be written as a linear combination of two functions with fixed contour-ordering. These are called correlation functions and are defined by (for simplicity, we neglect the state indices i_1 and $i_{\bar{1}}$),

$$\begin{aligned}\mathcal{G}^{(1)}(t_1, t_{\bar{1}}) &= \theta_C(t_1 - t_{\bar{1}}) g^>(t_1, t_{\bar{1}}) - \theta_C(t_{\bar{1}} - t_1) g^<(t_1, t_{\bar{1}}), \\ g^>(t_1, t_{\bar{1}}) &= -i \langle \hat{f}(t_1) \hat{f}^\dagger(t_{\bar{1}}) \rangle, \\ g^<(t_1, t_{\bar{1}}) &= i \langle \hat{f}^\dagger(t_{\bar{1}}) \hat{f}(t_1) \rangle,\end{aligned}\quad (2.34)$$

where $\theta_C(t)$ is the step function along the Keldysh contour. For practical calculations, it is often more convenient to unambiguously specify the position of the time arguments on \mathcal{C} , i.e., the affiliation to a unique branch of the contour, cf. Figure 2.1. To this end, the nonequilibrium Green function can be seen as a (3×3) matrix¹⁹ in Keldysh space, e.g., [Wag91, MR99],

$$\mathcal{G}^{(1)}(t_1, t_{\bar{1}}) \rightarrow \left(\begin{array}{cc|c} g^{++} & g^{+-} & g^{+|} \\ g^{-+} & g^{--} & g^{-|} \\ \hline g^{|+} & g^{|-} & g^{||} \end{array} \right), \quad (2.35)$$

¹⁸The former interval is more convenient as it includes the density matrix $\mathcal{F}_{ij}^{(1)} = \mathcal{G}_{ij}^M(0^-)$. Sometimes, also the symmetric interval $[-\frac{1}{2}\beta, \frac{1}{2}\beta] \setminus \{0\}$ is being considered, e.g., [PvFVA10].

¹⁹There are nine possibilities to distribute t_1 and $t_{\bar{1}}$ along the contour branches "+", "-", and "|".

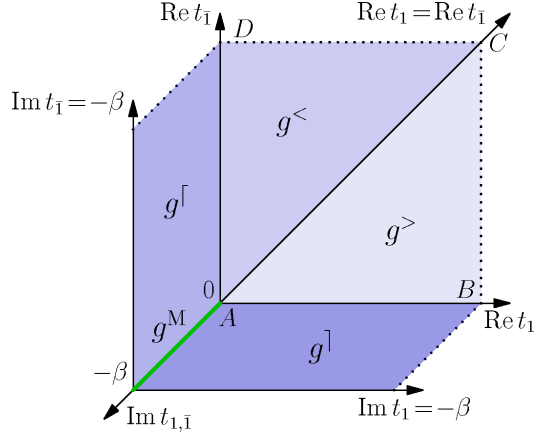


Figure 2.4: Matrix representation of $\mathcal{G}^{(1)}$ with components g^M (green), g^r , g^l , $g^>$ and $g^<$. Note that g^r and g^l can be converted into each other, see Eq. (2.38), and that $g^>$ ($g^<$) on the upper (lower) triangle ACD (ABC) can be expressed by $g^>$ ($g^<$) on the lower (upper) triangle.

in which time t_1 ($t_{\bar{1}}$) is attributed to the rows (columns). The following notations [BSE06, SDvL09] are commonly used ($\gamma \in \{+, -\}$),

$$\begin{aligned} g^< &= g^{+-}, & g^> &= g^{-+}, & g^c &= g^{++}, & g^a &= g^{--}, \\ g^r &= g^{\gamma r}, & g^l &= g^{\gamma l}, & g^M &= g^{\parallel}. \end{aligned} \quad (2.36)$$

In the stated order, we have the lesser and greater correlation function, the causal and anti-causal Green function, two (so-called) mixed Green functions²⁰, and the Matsubara Green function, cf. Figure 2.4. Four of them are completely independent, either g^M , g^r , $g^<$, and $g^>$ or g^M , g^l , g^c , and g^a , since,

$$g^{c/a}(t_1, t_{\bar{1}}) = \theta_C(\pm[t_1 - t_{\bar{1}}]) g^>(t_1, t_{\bar{1}}) + \theta_C(\pm[t_{\bar{1}} - t_1]) g^<(t_1, t_{\bar{1}}). \quad (2.37)$$

Further, we find ($t, t_1, t_{\bar{1}} \in [t_0, \infty]$ and $\tau \in [-\beta, 0]$),

$$\begin{aligned} g^M(0^-) &= -i g^<(t_0, t_0), \\ g^M(\tau) &= -i g^r(t_0 - i\tau, t_0), \\ g^r(t_0 - i\tau, t) &= [g^l(t, t_0 - i(\beta - \tau))]^\dagger, \\ g^{\geq}(t_1, t_{\bar{1}}) &= -[g^{\geq}(t_{\bar{1}}, t_1)]^\dagger, \\ g^>(t, t) &= -i + g^<(t, t), \end{aligned} \quad (2.38)$$

where the first two lines represent the initial conditions for calculating the NEGF by time propagation, cf. Chapter 4, and the last two properties (as indicated by Figure 2.4) allow one to restrict

²⁰Generally, one does not distinguish the origin of the real-time argument.

	Multiplication	Convolution
Component	$c(t_1, t_{\bar{1}}) = a(t_1, t_{\bar{1}}) b(t_{\bar{1}}, t_1)$	$c(t_1, t_{\bar{1}}) = \int_{\mathcal{C}} dt_2 a(t_1, t_2) b(t_2, t_{\bar{1}})$
c^M	$a^M b^M$	$a^M \star b^M$
c^{\lceil}	$a^{\lceil} b^{\lceil}$	$a^{\lceil} \circ b^A + a^M \star b^{\lceil}$
c^{\rceil}	$a^{\rceil} b^{\lceil}$	$a^R \circ b^{\rceil} + a^{\lceil} \star b^M$
$c^>$	$a^> b^<$	$a^R \circ b^> + a^> \circ b^A + a^{\lceil} \star b^{\lceil}$
$c^<$	$a^< b^>$	$a^R \circ b^< + a^< \circ b^A + a^{\rceil} \star b^{\rceil}$
c^R	$a^R b^> + a^> b^A$	$a^R \circ b^R$
c^A	$a^A b^< + a^< b^R$	$a^A \circ b^A$

Table 2.1: Langreth rules for multiplication and convolution of two contour-ordered functions a and b . The operations \circ and \star are defined by Eqs. (2.42) and (2.43).

the evaluation of $g^<(t_1, t_{\bar{1}})$ to $t_1 \leq t_{\bar{1}}$ and of $g^>(t_1, t_{\bar{1}})$ to $t_1 > t_{\bar{1}}$. Being equivalent to the usage of correlation functions, the dynamics can be described also in terms of retarded and advanced quantities defined as²¹,

$$\begin{aligned}
 g^{R/A}(t_1, t_{\bar{1}}) &= \pm \theta_{\mathcal{C}}(\pm[t_1 - t_{\bar{1}}]) \{g^>(t_1, t_{\bar{1}}) - g^<(t_1, t_{\bar{1}})\} . \\
 g^R &= g^c - g^< = g^> - g^a , \\
 g^A &= g^c - g^> = g^< - g^a .
 \end{aligned} \tag{2.39}$$

The partitioning into matrix components is virtually possible for any two-time function defined on the contour \mathcal{C} . Thus, the same representation (with identical nomenclature) proves valid for the self-energy $\Sigma^{(1)}$. In particular,

$$\Sigma^{\lceil}(t_0 - i\tau, t) = \left[\Sigma^{\lceil}(t, t_0 - i(\beta - \tau)) \right]^{\dagger} , \quad \Sigma^{\geq}(t_1, t_{\bar{1}}) = - \left[\Sigma^{\geq}(t_{\bar{1}}, t_1) \right]^{\dagger} . \tag{2.40}$$

Moreover, concerning the matrix structure (2.35), complex-time integrals (as they enter the equations of motions of the NEGF) are of great importance. Let us consider the convolution,

$$c(t_1, t_{\bar{1}}) = \int_{\mathcal{C}} dt_2 a(t_1, t_2) b(t_2, t_{\bar{1}}) , \tag{2.41}$$

of two contour-ordered functions a and b . The decomposition of c into parts is controlled by the Langreth rules²² [LW72], which are shown in Table 2.1 and comprise the following shorthand notation ($t_1, t_{\bar{1}} \in \mathcal{C}$ and $x, y \in \{\mathbf{R}, \mathbf{A}, >, <, \lceil, \rceil\}$),

$$[a^x \circ b^y](t_1, t_{\bar{1}}) = \int_{t_0}^{\infty} d\bar{t} a^x(t_1, \bar{t}) b^y(\bar{t}, t_{\bar{1}}) , \tag{2.42}$$

²¹These are formally obtained by performing a "Keldysh rotation", see, e.g., [RS86].

²²Synonymously with "analytic continuation" or "Langreth theorems".

for all quantities a^x (b^y) that allow for a real-time second (first) argument. To be conform with transformation (2.25), we present explicit results for those integrals in Table 2.1 that involve imaginary-time (Matsubara) quantities (here, $t, t_1, t_{\bar{1}} \in [0, \infty]$ and $\tau \in [-\beta, 0]$),

$$\begin{aligned}
[a^M \star b^M](\tau) &= \int_0^\beta d\bar{\tau} a^M(\tau - \bar{\tau}) b^M(\bar{\tau}) , \\
[a^M \star b^\rceil](t_0 - i\tau, t) &= \int_0^\beta d\bar{\tau} a^M(\tau - \bar{\tau}) b^\rceil(t_0 - i\bar{\tau}, t) , \\
[a^\lceil \star b^M](t, t_0 - i\tau) &= \int_0^\beta d\bar{\tau} a^\lceil(t, t_0 - i\bar{\tau}) b^M(\bar{\tau} - \tau) , \\
[a^\lceil \star b^\rceil](t_1, t_{\bar{1}}) &= -i \int_0^\beta d\bar{\tau} a^\lceil(t_1, t_0 - i\bar{\tau}) b^\rceil(t_0 - i\bar{\tau}, t_{\bar{1}}) .
\end{aligned} \tag{2.43}$$

Analogous rules are obtained for the multiplication of two Keldysh space functions (without intermediate integration), see the second column in Table 2.1.

Using the the matrix components of $\mathcal{G}^{(1)}$ and $\Sigma^{(1)}$, the two-time Kadanoff-Baym equations for can be summarized in compact form²³ [vLDdf, SDvL09],

(KBE III.)

$$\begin{aligned}
-\partial_{1-\bar{1}} g^M &= \delta + \Sigma^M \star g^M , \\
\partial_1 g^> &= \Sigma^R \circ g^> + \Sigma^> \circ g^A + \Sigma^\lceil \star g^\rceil \stackrel{\text{def.}}{=} i_1^> , \\
-g^< \partial_{\bar{1}} &= g^R \circ \Sigma^< + g^< \circ \Sigma^A + g^\lceil \star \Sigma^\rceil \stackrel{\text{def.}}{=} i_2^< , \\
\partial_1 g^\lceil &= \Sigma^R \circ g^\lceil + \Sigma^\lceil \star g^M \stackrel{\text{def.}}{=} i^\lceil , \\
-g^\rceil \partial_{\bar{1}} &= g^\rceil \circ \Sigma^A + g^M \star \Sigma^\rceil \stackrel{\text{def.}}{=} i^\rceil ,
\end{aligned} \tag{2.44}$$

with differential operators $\partial_{1-\bar{1}} = \frac{\partial}{\partial \tau} - \hat{h}^{(1)}(t_0)$ and $\partial_{1,\bar{1}} = i \frac{\partial}{\partial t_{1,\bar{1}}} - \hat{h}^{(1)}(t_{1,\bar{1}})$. The first equation is just the Dyson equation in short form, and we call the right hand sides of the remaining equations collision integrals i^x ($x = \gtrsim, \lceil \rceil$) as they account for the binary interactions. Thereby, the theta functions included in the retarded and advanced quantities, cf. Eq. (2.39), limit the integration regions to previous times.

2.4 Summary

In this Chapter, we have given a brief introduction to quantum statistical mechanics and its formulation by means of nonequilibrium Green functions. Thereby, the description is oriented towards the extended Keldysh contour \mathcal{C} (cf. Figure 2.1) which consistently depicts the transition from thermodynamic equilibrium to arbitrary nonequilibrium situations. Furthermore, generality of the presented formulas and equations is preserved by giving a representation-less formulation in terms of one-particle spin orbitals $|i\rangle$. Changing the basis is mediated by a linear transformation of type (2.11).

²³In line 2 and 4 of Eq. (2.44), the operators $\partial_{\bar{1}}$ are acting to the left.

The two-time Kadanoff-Baym equations for the different Keldysh components of the one-particle nonequilibrium Green function, see (KBE III.) on page 23, represent the central equations of this thesis. Starting from self-consistent initial states, their solution in Hartree-Fock and second Born approximation (cf. Figure 2.2) is the objective of Part III. Since the numerical treatment of g^x ($x = M, >, <, \rceil, \rfloor$) imposes strong challenges on the numerics especially when inhomogeneous quantum systems are being explored, the design of efficient solution strategies is in the center of Chapter 3 and Chapter 4 (Part II).

PART II

Numerical Methods

Representation of the Nonequilibrium Green Function

Although the theory of quantum statistical mechanics regarding systems far from equilibrium is well developed and great progress has been made on the basis of nonequilibrium Green functions (NEGFs) in the recent decade, see Refs. [BE00, BSE03, BFE06, BBE10] (as highlighted in Chapter 1), there are, from the numerical perspective, still great challenges related to the solution of the two-time Kadanoff-Baym equations in the presence of retardation effects. In addition, further evaluation and clarification of the performance of many-body approximations is claimed, particularly, for strongly correlated systems, see, e.g., Refs. [PvFVA09, PvFVA10].

As already outlined in the introduction of this thesis, the solution of the two-time Kadanoff-Baym equations for homogeneous fermion systems has been widely explored and the numerical treatment has been perfected, see Ref. [KKY99]. However, for inhomogeneous and finite quantum systems¹ including quite a number of discrete bound states, the NEGF approach is still far from being a standard tool for describing the correlated many-body dynamics. Although the available computer power is permanently increasing, this has to do with the increased computational complexity in comparison with the application of NEGFs on homogeneous systems. For this reason, we, in the present Chapter, want to establish a highly useful framework for representing the NEGF in numerical calculations with large inhomogeneity and spatial extend.

As seen in the previous Chapter, the one-particle NEGF $\mathcal{G}_{i_1 i_{\bar{1}}}^{(1)}(t_1, t_{\bar{1}})$ defined in Eq. (2.12) with spin orbitals $|j\rangle$ ($j = i_1, i_{\bar{1}}$), is in coordinate representation often abbreviated as $\mathcal{G}(1, \bar{1})$, where $1 = (x_1, t_1)$ stands for space, spin and time variables (spin is included in x_1). The main purpose of this Section is to develop an efficient representation regarding the spatial variables in the NEGF. More precisely, the goal is to set up a hybrid form of grid and basis method which offers additional advantages absent in a usual basis expansion, e.g., [BBvL⁺09]. This becomes possible by means of the finite element-discrete variable representation (FE-DVR) to be introduced in Chapter 3.2, which, at least in one spatial dimension², provides an easy-to-handle and well-adapted

¹These are subject of investigation in Part III of this thesis.

²We note that straight-forward generalizations to higher dimensionality are not ruled out.

representation of the nonequilibrium Green function.

But first of all, in the following Section, we discuss on the spin degrees of freedom.

3.1 Electron Spin Variables

In the zero-temperature limit ($\beta \rightarrow \infty$), the NEGF ansatz and the pure state description in terms of a many-body wave function merge into one another. This means that, for the N_e -electron ground state, the one-particle nonequilibrium Green function needs to be conform with the spin wave function $|S, M_S\rangle$ with predefined total spin S and $M_S = \sum_{n=1}^{N_e} m_{S_n} \in \{-S, -S+1, \dots, S-1, S\}$ which involves the spin z -components $m_{S_n} = \pm \frac{1}{2}$ of the individual electrons. Thereby, $|S, M_S\rangle$ obeys,

$$\begin{aligned} \hat{S}^2 |S, M_S\rangle &= S(S+1) |S, M_S\rangle, & \hat{S}_z |S, M_S\rangle &= M_S |S, M_S\rangle, \\ \hat{S}_{z,n} |S, M_S\rangle &= m_{S_n} |S, M_S\rangle, & \hat{S}_n^2 |S, M_S\rangle &= \frac{3}{4} |S, M_S\rangle, \end{aligned} \quad (3.1)$$

where $\hat{S} = \sum_{n=1}^{N_e} \hat{S}_n$ denotes the total spin operator.

For particle numbers $N_e \leq 5$, the resulting spin states are summarized in Table 3.1. The explicit form of $|S, M_S\rangle$ can be constructed, gradually, by using Clebsch-Gordan coefficients [Pau79, CS53], by applying generalized spin-ladder operators, see, e.g., Ref. [Mad04], or, directly, by diagonalizing the matrix of \hat{S}^2 in the basis $|m_{S_1} \dots m_{S_N}\rangle = |x_1 \dots x_{N_e}\rangle$ with $x_i \in \{\uparrow, \downarrow\}$. For $N_e = 2$, we obtain the well-known singlet spin wave function $|0, 0\rangle = \frac{1}{\sqrt{2}}(|\uparrow\downarrow\rangle - |\downarrow\uparrow\rangle)$, and the three triplet states $|1, -1\rangle = |\downarrow\downarrow\rangle$, $|1, 0\rangle = \frac{1}{\sqrt{2}}(|\uparrow\downarrow\rangle + |\downarrow\uparrow\rangle)$, and $|1, 1\rangle = |\uparrow\uparrow\rangle$ according to the multiplicity of $M = 2S + 1$. For $N_e > 2$, the number of states grows rapidly (with 2^{N_e}) and additional degeneracies may occur, see Table 3.1.

Of course, on the level of the many-body wave function, the introduction of $|S, M_S\rangle$ makes sense only for predefined total spin and situations where space and spin degrees of freedom can be separated³. The symmetry of the coordinate wave function is then adapted accordingly to get a completely antisymmetric state $|\{n\}\rangle$.

In the remainder of this thesis, we want to focus on the following two cases:

- (S1) singlet states for even particle number N_e , and,
- (S2) spin states with the largest possible value of S for N_e either even or odd.

According to Table 3.1, (S1) and (S2) represent spin configurations which indicate no additional degeneracy. Systems with configuration (S1) have an equal number of electrons of each spin and are usually referred to as closed-shell⁴ systems. In molecular orbital theory, also the term "spin-restricted" is used to denote the double occupancy of states. Electron ensembles with property (S2) are indicated as being spin-polarized. These include, e.g., the triplet states for $N_e = 2$ or the quintet states for $N_e = 4$.

³Realize that this is generally possible for spin-independent Hamiltonians.

⁴In contrast to open-shell systems that have, at least, one unpaired electron.

Table 3.1: Term classification for electronic systems with particle number N_e . In total, there exist 2^{N_e} spin states $|S, M_S\rangle$ of which, at fixed total spin, $M = 2S + 1$ are linear independent.

N_e	2^{N_e}	Terminology	Total spin S	Multiplicity M	Degeneracy ¹
1	2	singlet	$\frac{1}{2}$	2	n.d.
2	4	singlet	0	1	n.d.
		triplet	1	3	n.d.
3	8	doublet	$\frac{1}{2}$	2	two-fold
		quartet	$\frac{3}{2}$	4	n.d.
4	16	singlet	0	1	n.d.
		triplet	1	3	three-fold
		quintet	2	5	n.d.
5	32	doublet	$\frac{1}{2}$	2	five-fold
		quartet	$\frac{3}{2}$	4	four-fold
		sextet	$\frac{5}{2}$	6	n.d.

¹ n.d. means nondegenerate.

The advantage of the spin-state constraints is obvious. In both cases, the NEGF can be regarded as independent of the electron spin variables such that,

$$\mathcal{G}_{i_1 i_{\bar{1}}}^{(1)}(t_1, t_{\bar{1}}) \rightarrow \mathcal{G}_{p_1 p_{\bar{1}}}^{(1)}(t_1, t_{\bar{1}}), \quad (3.2)$$

where p_1 and $p_{\bar{1}}$ label spatial orbitals $|p_1\rangle$ and $|p_{\bar{1}}\rangle$, i.e., spin is excluded, and the creation and annihilation operators in Eq. (2.12) transform accordingly. The difference of the spin configurations (S1) and (S2) is then parametrically taken into account via the self-energy,

$$\Sigma_{i_1 i_{\bar{1}}}^{(1)}(t_1, t_{\bar{1}}) \rightarrow \Sigma_{\xi, p_1 p_{\bar{1}}}^{(1)}(t_1, t_{\bar{1}}), \quad (3.3)$$

with degeneracy factor ξ , and, again, basis indices p_1 and $p_{\bar{1}}$ referring to spatial orbitals. For the modeling of closed-shell singlet states, if N_e is even, we set $\xi = 2$ accounting for double occupancy of states. For any spin-polarized system, it is $\xi = 1$. The explicit construction of $\Sigma_{\xi, p_1 p_{\bar{1}}}^{(1)}$ is discussed in Chapter 3.3.3 including the respective interpretation of self-energy diagrams.

3.2 The Finite Element-Discrete Variable Representation (FE-DVR)

3.2.1 General Idea and Fields of Application

It is well-known that standard grid methods for solving (non-)linear partial differential equations usually require very small grid spacings⁵, if finite difference methods are used to approximate the

⁵To achieve adequate accuracy.

differential operators. On the other hand, expansions of the unknown in function space are often limited due to the number of elaborate matrix elements that (repeatedly) have to be computed.

In this dilemma, the finite element-discrete variable representation (FE-DVR) opens a compromise approach [CMK⁺04]. The general idea is to divide the space into a series of fixed finite elements, where, in each element, a few locally defined so-called DVR basis functions act as information carriers. Thereby, the DVR functions rely themselves on a subordinate grid based on a particular Gauss quadrature and, similarly to B-splines with compact support, have optimal interpolating character. In this sense, the FE-DVR method is a hybrid approach employing, both, finite elements (i.e., spatial grids) and, at intervals, a basis representation of the quantity of interest⁶. In anticipation of the following Sections, we note that the FE-DVR technique has the ability to preserve the best aspects of a grid and a basis and leads to sparse representations of the kinetic and potential energy (cf. Chapter 3.3.1). This is primarily attributable to the DVR [LHL85] which is widely used in quantum chemistry [LC07].

Originally, the FE-DVR method has appeared as an alternative to basis set expansions of the multi-particle wave function entering the time-dependent Schrödinger equation (TDSE). Pioneering work in this direction is due to *T.N. Rescigno* and *C.W. McCurdy* (currently at Lawrence Berkeley National Lab, Berkeley, California, USA), see Ref. [RM00], as well as *B.I. Schneider* (National Science Foundation, USA), see Ref. [SCH06].

Further developments and employment of the method concern scattering problems in combination with time-dependent close coupling [Hu06] and the study of atoms and molecules in intense fields. For instance, the bound and continuum states of H_2^+ as well as its photoionization cross sections are addressed in Refs. [TMR09a, TMR09b]. The extension to neutral (i.e., molecular) hydrogen can be found in [TMR10]. Moreover, calculations for the strong-field ionization of molecular ions in circularly polarized light have been reported in Ref. [HC06b]. To date, combined FE and DVR schemes are also used in the implementation of multiconfiguration time-dependent Hartree-Fock (MCTDHF), see, e.g., [HLM11, HB11] and references therein.

One of the key properties of the FE-DVR method regarding the propagation of the TDSE, beyond its high accuracy at a minimum number of grid points and the avoidance of complicated matrix elements (see Chapter 3.3.3 below), is the possibility for a highly effective code parallelization when using the real-space product ansatz [SC05]. The achievable $\mathcal{O}(n)$ -scaling (where n is the total number of grid points) has been demonstrated on various two- and three-dimensional problems [SCH06] and leads to crucial computational speed-ups.

In our application of the method, however, these specific scaling properties are not important. Instead, we focus on the FE-DVR benefits regarding the treatment of the electron-electron interactions in the two-time self-energy which, seen individually, require much computational expense and many resources in NEGF calculations.

For our purpose, we discuss the FE-DVR method in one spatial dimension (1D). The generalization to 2D and 3D is straight forward, see, e.g., Ref. [SCH06].

⁶In our case, this will be the two-time NEGF.

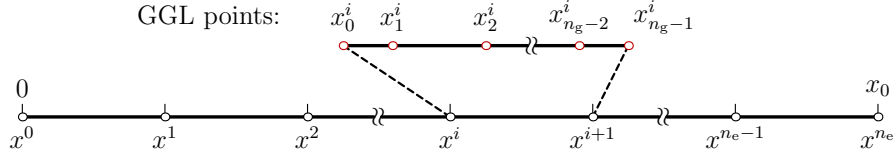


Figure 3.1: The interval \mathcal{S} as discretized in FE-DVR representation. The generalized Gauss-Lobatto (GGL) points x_m^i , with $m = 0, 1, \dots, n_g - 1$ in any finite element $[x^i, x^{i+1}]$, are used to construct a local DVR basis.

3.2.2 Definitions

We consider a one-dimensional interval $\mathcal{S} = [0, x_0]$ which, below and in Part III of this thesis, is also referred to as simulation box.

First, we arbitrarily partition the interval \mathcal{S} into a number of n_e finite elements $[x^i, x^{i+1}]$, $i \in \{0, 1, \dots, n_e - 1\}$, see Figure 3.1,

$$0 = x^0 < x^1 < x^2 < \dots < x^{n_e-1} < x^{n_e} = x_0 . \quad (3.4)$$

Second, in each finite element, we establish a pointwise representation of all data in terms of points that arise from a Gauss quadrature rule. This is the basic idea of the discrete variable representation and paves the way toward a local polynomial basis. In our case, the DVR is constructed from the Gauss-Lobatto quadrature, cf. Appendix A. However, the actual interval boundaries are not ∓ 1 as assumed by usual quadrature rules like Gauss-Legendre. Instead, they follow the FE arrangement of Eq. (3.4). For this reason, we have to consider generalized Gauss-Lobatto (GGL) points and similarly generalized attributed weights [RM00]. These (in element⁷ i) are defined by,

$$\begin{aligned} x_m^i &= \frac{1}{2} \left[(x^{i+1} - x^i)x_m + (x^{i+1} + x^i) \right] , \\ w_m^i &= \frac{1}{2} w_m(x^{i+1} - x^i) , \end{aligned} \quad (3.5)$$

where $m = 0, 1, \dots, n_g - 1$, cf. Figure 3.1. The standard Gauss-Lobatto points x_m (for fixed n_g) are defined as roots of the derivative of Legendre polynomials $\mathcal{L}_n(x)$ according to,

$$0 = \left. \frac{d\mathcal{L}_{n_g-1}(x)}{dx} \right|_{x=x_m} . \quad (3.6)$$

The corresponding weights w_m follow from,

$$w_m = \frac{2}{n_g(n_g - 1) [\mathcal{L}_{n_g-1}(x_m)]^2} . \quad (3.7)$$

⁷Whereas the first finite element is indicated by $i = 0$, the last is indexed $i = n_e - 1$.

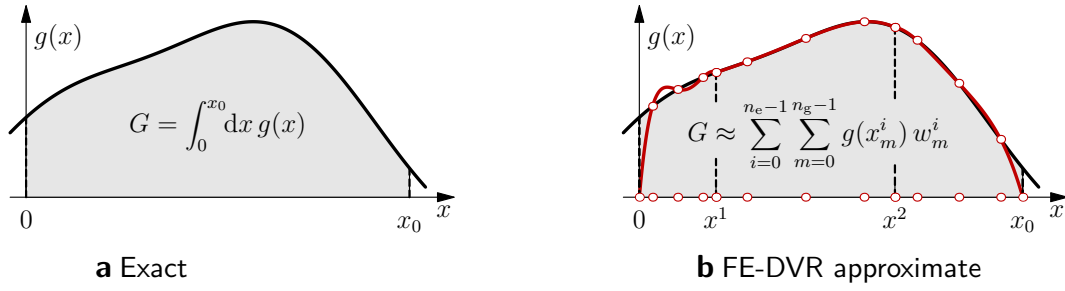


Figure 3.2: Integration of a function $g(x)$ in the context of a finite element-discrete variable representation of the interval $\mathcal{S} = [0, x_0]$ with $n_e = 3$ elements ($[0, x^1]$, $[x^1, x^2]$, and $[x^2, x_0]$) and $n_g = 5$ GGL points. In panel (b), the red curve demonstrates the integrand being expanded in the FE-DVR basis $\chi_m^i(x)$ of Eq. (3.13) which lacks of the DVR functions $f_0^0(x)$ and $f_{n_g-1}^{n_e-1}(x)$, cf. Chapter 3.2.3.

Once a specific set of points $\{x_m\}$ (with associated weights $\{w_m\}$) has been computed, we can approximate an integral G over a function $g(x)$ spanning the simulation box \mathcal{S} by segmentally applying the quadrature rule:

$$G = \int_0^{x_0} dx g(x) = \sum_{i=0}^{n_e-1} \int_{x^i}^{x^{i+1}} dx g(x) \approx \sum_{i=0}^{n_e-1} \sum_{m=0}^{n_g-1} g(x_m^i) w_m^i. \quad (3.8)$$

As the convergence of the right hand side of Eq. (3.8) to the exact result with respect to the number of grid points may be faster than polynomially, in many situations a relatively small value of $n_g \lesssim 10$ is sufficient for a highly accurate G . For an illustration with $n_e = 3$ and five GGL points per element, see Figure 3.2. Further, we emphasize that, by construction, the integration is exact for $g(x)$ being a polynomial of degree $2n_g - 1$ and less.

In each individual finite element i , the interpolating polynomials behind Eq. (3.8) are of Lagrange type and are usually referred to as DVR or Lobatto shape functions $f_m^i(x)$, see Figure 3.3 (a) and Refs. [RM00, MW88]. Their explicit definition reads,

$$f_m^i(x) = \begin{cases} \prod_{m' \neq m} \frac{x - x_{m'}^i}{x_m^i - x_{m'}^i}, & x^i \leq x \leq x^{i+1} \\ 0, & x < x^i \text{ and } x > x^{i+1} \end{cases}. \quad (3.9)$$

As all DVR functions equal zero outside their assigned interval $[x^i, x^{i+1}]$, they, as desired, define a local basis set. Moreover, we notice that the first (last) polynomial with $m = 0$ ($m = n_g - 1$) remains finite at the left (right) interval boundary x^i (x^{i+1}) whereas all the others vanish at both points, cf. the black dashed and dash-dotted lines in Figure 3.3 (a) and compare with the red curves for $m = 1, 2, \dots, n_g - 2$.

For further reference, we collect the most important mathematical properties of the Lobatto shape functions:

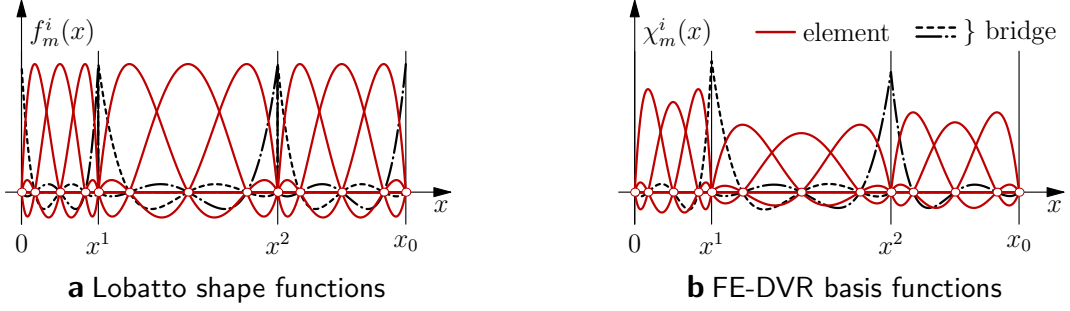


Figure 3.3: FE-DVR basis construction from the Lobatto shape functions $f_m^i(x)$ of Eq. (3.9) (see the red and black lines in panel (a)) with parameters $n_e = 3$ and $n_g = 5$. In panel (b), the first and the last DVR function is neglected in the orthonormal basis set $\{\chi_m^i(x)\}$, cf. Eq. (3.13), as any physical quantity is assumed to be zero at and beyond the simulation box boundaries 0 and x_0 . Further, the bridge functions (black) which extend over two adjacent FEs (element i has overlap with element $i + 1$) ensure communication between the different grid domains and guarantee spatial continuity of the expanded quantity. In the specific case shown, the basis has dimension $n_b = 11$.

(F1) identity of Lobatto shape functions at generalized Gauss-Lobatto points,

$$f_m^i(x_{m'}^{i'}) = \delta_{mm'}^{ii'}, \quad (3.10)$$

(F2) orthogonality,

$$\int_0^{x_0} dx f_m^i(x) f_{m'}^{i'}(x) = \delta_{mm'}^{ii'} w_m^i, \quad (3.11)$$

(F3) first derivative evaluated at generalized Gauss-Lobatto points,

$$\left. \frac{df_m^i(x)}{dx} \right|_{x=x_{m'}^{i'}} = \begin{cases} \frac{1}{x_m^i} \prod_{\bar{m} \neq m, m'} \frac{x_{m'}^{i'} - x_{\bar{m}}^i}{x_m^i - x_{\bar{m}}^i}, & m = m' \\ \frac{\delta_{m, n_g-1} + \delta_{m0}}{2w_m^i}, & m \neq m' \end{cases}. \quad (3.12)$$

Note that, for proving property (F2), the integral has to be evaluated under the usage of the generalized Gauss-Lobatto quadrature rule of Eq. (3.8).

3.2.3 FE-DVR Basis Functions

From property (F2) in Chapter 3.2.2, we see that, after normalization, the Lobatto shape functions enable the construction of an orthonormal basis set which spans the whole space $\mathcal{S} = [0, x_0]$ if the individual finite elements are properly joined together.

For simulation purposes, we want to assume that any physical quantity vanishes at the boundaries of the simulation box (i.e., at $x = 0$ and $x = x_0$) and, of course, outside \mathcal{S} . As a consequence,

we can neglect the DVR functions $f_0^0(x)$ and $f_{n_g-1}^{n_e-1}(x)$ in the construction of the basis, see Figure 3.3 (b). In addition, for continuity of the basis, we combine the last Lobatto shape function $f_{n_g-1}^i(x)$ of element i and the DVR function $f_0^{i+1}(x)$ of element $i+1$ into a single function which is referred to as "bridge" function, cf. the black lines in Figure 3.3 (b). The remaining basis functions are called "element" functions.

The resulting FE-DVR basis [RM00] is defined by,

$$\chi_m^i(x) = \begin{cases} \frac{f_{n_g-1}^i(x) + f_0^{i+1}(x)}{\sqrt{w_{n_g-1}^i + w_0^{i+1}}}, & m = 0 \quad (\text{bridge function}) \\ \frac{f_m^i(x)}{\sqrt{w_m^i}}, & \text{else} \quad (\text{element function}) \end{cases}, \quad (3.13)$$

where m is ranging from 0 to $n_g - 2$. Further, the FE-DVR basis has dimension,

$$n_b = n_e(n_g - 1) - 1, \quad (3.14)$$

and is orthonormal in the sense of the generalized Gauss-Lobatto quadrature, cf. Eq. (3.8).

Regarding the function $g(x)$ in Eq. (3.8), the removal of the two DVR basis functions mentioned above means that one assumes $\lim_{x \rightarrow 0} g(x) = \lim_{x \rightarrow x_0} g(x) = 0$. Consequently, $g(x)$ is not appropriately represented in the first and last element (and so is the integral), see the red curve in Figure 3.2 (b) which displays the integrand expanded in the corresponding FE-DVR basis, i.e., $g(x) \approx \sum_{im} c_m^i \chi_m^i(x)$ with $c_m^i = \int_0^{x_0} d\bar{x} g(\bar{x}) \chi_m^i(\bar{x})$. We note that this problem is directly related to the Gibbs phenomenon in Fourier series and concerns all quantities which are not continuously differentiable within the simulation box \mathcal{S} .

Although the indices i and m in Eq. (3.13) can be addressed with a single multi-index $p = (i, m)$, we, in the remainder of this work, keep this notation to avoid ambiguity. Computationally, it is convenient to use the following arrangement,

$$p = (0, 1), (0, 2), \dots, (0, n_g - 2), \underline{(0, 0)}, (1, 1), (1, 2), \dots, (1, n_g - 2), \underline{(1, 0)}, \dots, (n_e - 1, 1), \dots, (n_e - 1, n_g - 2), \quad (3.15)$$

where the bridge functions $\underline{(i, 0)}$ allocate the last position for fixed i , cf. Figure 3.3 (b).

Moreover, a generalization of the FE-DVR basis of Eq. (3.13) to a variable number of DVR functions in each element is straight forward, see Ref. [SCH06].

3.3 FE-DVR Hamiltonian; Matrix Elements and Self-energies

In FE-DVR representation, the creation (annihilation) operator $[\hat{f}_{m_1}^{i_1}]^\dagger (\hat{f}_{m_1}^{i_1})$ produces (deletes) a particle in (from) the state $|p_1\rangle = |(i_1 m_1)\rangle = \chi_{m_1}^{i_1}(x)$. Introducing the kinetic energy $\hat{t}^{(1)}$, the single-particle potential energy $\hat{v}^{(1)}$ as well as the notations,

$$\begin{aligned} \langle p_1 | \hat{h}^{(1)}(t) | p_2 \rangle &\rightarrow h_{m_1 m_2}^{i_1 i_2}(t) = t_{m_1 m_2}^{i_1 i_2} + v_{m_1 m_2}^{i_1 i_2}(t), \\ \langle p_1, p_2 | \hat{h}^{(2)} | p_3, p_4 \rangle &\rightarrow u_{m_1 m_2, m_3 m_4}^{i_1 i_2, i_3 i_4}, \end{aligned} \quad (3.16)$$

with $\hat{h}^{(1)}(t) = \hat{t}^{(1)}(-i\nabla) + \hat{v}^{(1)}(x, t)$, the Hamiltonian of Eq. (2.8) takes the form,

$$\begin{aligned} \hat{H}(t) = & \sum_{i_1 i_2} \sum_{m_1 m_2} h_{m_1 m_2}^{i_1 i_2}(t) [\hat{f}_{m_1}^{i_1}(t)]^\dagger \hat{f}_{m_2}^{i_2}(t) \\ & + \sum_{i_1 \dots i_4} \sum_{m_1 \dots m_4} u_{m_1 m_2, m_3 m_4}^{i_1 i_2, i_3 i_4} [\hat{f}_{m_1}^{i_1}(t)]^\dagger [\hat{f}_{m_3}^{i_3}(t)]^\dagger \hat{f}_{m_2}^{i_2}(t) \hat{f}_{m_4}^{i_4}(t). \end{aligned} \quad (3.17)$$

The matrix elements (the one- and two-electron integrals) defined by Eq. (3.16) have to be evaluated in the FE-DVR basis specified. Thereby, in contrast to an arbitrary (non-FE-DVR) basis⁸, it turns out that, for any partitioning of the simulation box according to Eq. (3.4), all matrix elements attain simple, semianalytical forms, cf. Ref. [CMK⁺04]. The results are discussed below.

Moreover, concerning the nonequilibrium Green function and the self-energy of Eq. (3.2) and Eq. (3.3), from now on, we notify the FE-DVR representation by,

$$\begin{aligned} \mathcal{G}_{p_1 p_{\bar{1}}}^{(1)}(t_1, t_{\bar{1}}) & \rightarrow g_{m_1 m_{\bar{1}}}^{i_1 i_{\bar{1}}}(t_1, t_{\bar{1}}), \\ \Sigma_{\xi, p_1 p_{\bar{1}}}^{(1)}[\mathcal{G}^{(1)}, \hat{h}^{(2)}](t_1, t_{\bar{1}}) & \rightarrow \Sigma_{\xi, m_1 m_{\bar{1}}}^{i_1 i_{\bar{1}}}[g, u](t_1, t_{\bar{1}}), \end{aligned} \quad (3.18)$$

where the coordinate representation is recovered by⁹,

$$\mathcal{G}^{(1)}(x_1 t_1, x_{\bar{1}} t_{\bar{1}}) = \sum_{i_1 m_1} \sum_{i_{\bar{1}} m_{\bar{1}}} \chi_{m_1}^{i_1}(x_1) \chi_{m_{\bar{1}}}^{i_{\bar{1}}}(x_{\bar{1}}) g_{m_1 m_{\bar{1}}}^{i_1 i_{\bar{1}}}(t_1, t_{\bar{1}}). \quad (3.19)$$

The (3×3) matrix structure on the Keldysh contour \mathcal{C} , cf. Chapter 2.3.4, is indicated by giving the appropriate index $x \in \{M, R, A, >, <, [,]\}$ in g^x and $\Sigma^x \xi$.

3.3.1 Single-particle Energy

In FE-DVR representation, the matrix of the single-particle contribution $\hat{v}^{(1)}$ to the potential energy is readily evaluated. Following property (F1), the matrix is completely diagonal with regard to element and DVR indices (cf. also Figure 3.4),

$$\begin{aligned} v_{m_1 m_2}^{i_1 i_2}(t) & = \int_0^{x_0} dx \chi_{m_1}^{i_1}(x) \hat{v}^{(1)}(x, t) \chi_{m_2}^{i_2}(x) \\ & = \delta_{m_1 m_2}^{i_1 i_2} \tilde{v}_{m_1}^{i_1}(t), \end{aligned} \quad (3.20)$$

where

$$\tilde{v}_{m_1}^{i_1}(t) = \begin{cases} \hat{v}^{(1)}(x_{n_g-1}^{i_1}, t), & m_1 = 0 \\ \hat{v}^{(1)}(x_{m_1}^{i_1}, t), & \text{else} \end{cases}. \quad (3.21)$$

The same expression holds for any other local operator, e.g., for the dipole operator $\hat{d}^{(1)}$.

⁸E.g., the basis of eigenstates of the potential $\hat{v}^{(1)}(x)$.

⁹The same expression holds for the self-energy $\Sigma_{\xi}^{(1)}(x_1 t_1, x_{\bar{1}} t_{\bar{1}})$.

3 Representation of the Nonequilibrium Green Function

Some care needs to be taken when evaluating the matrix elements of the kinetic energy, which, in atomic units, involves the operator $\hat{t}^{(1)} = -\frac{\nabla^2}{2}$:

$$t_{m_1 m_2}^{i_1 i_2} = \int_0^{x_0} dx \chi_{m_1}^{i_1}(x) \hat{t}^{(1)} \chi_{m_2}^{i_2}(x). \quad (3.22)$$

The reason for a careful analysis of Eq. (3.22) is the nonlocality caused by the second derivative and the fact that all basis functions¹⁰ $\chi_m^i(x)$ have discontinuous derivatives at the element boundaries $x^{\bar{i}}$ ($\bar{i} \in \{0, 1, \dots, n_e\}$), cf. definition (3.13). We note, that, usually, smooth orbitals are required to correctly define the kinetic energy.

Following Ref. [RM00], the consistent expression for the second derivative of a FE-DVR basis function considered under an integral is given by,

$$\nabla^2 \chi_m^i(x) = \begin{cases} \nabla^2 \chi_m^i(x), & x \neq x^{\bar{i}} \\ (\nabla \chi_m^i(x^+) - \nabla \chi_m^i(x^-)) \delta(x - x^{\bar{i}}), & x = x^{\bar{i}} \end{cases}, \quad (3.23)$$

where the second line takes into account that the first derivative is not continuously differentiable at the element boundaries. The indices "+" and "-" denote the right- and left-hand limit. Hence, we can write,

$$t_{m_1 m_2}^{i_1 i_2} = -\frac{1}{2} \sum_{\bar{i}} \lim_{\epsilon \rightarrow 0} \int_{x^{\bar{i}+\epsilon}^{x^{\bar{i}+1}-\epsilon} dx \chi_{m_1}^{i_1}(x) \nabla^2 \chi_{m_2}^{i_2}(x) \quad (3.24)$$

$$- \frac{1}{2} \sum_{\bar{i}} \int_0^{x_0} dx \chi_{m_1}^{i_1}(x) (\nabla \chi_{m_2}^{i_2}(x^+) - \nabla \chi_{m_2}^{i_2}(x^-)) \delta(x - x^{\bar{i}}) \\ = -\frac{1}{2} \sum_{\bar{i}} \lim_{\epsilon \rightarrow 0} [\chi_{m_1}^{i_1}(x) \nabla \chi_{m_2}^{i_2}(x)]_{x^{\bar{i}+\epsilon}^{x^{\bar{i}+1}-\epsilon} \quad (3.25)$$

$$+ \frac{1}{2} \sum_{\bar{i}} \lim_{\epsilon \rightarrow 0} \int_{x^{\bar{i}+\epsilon}^{x^{\bar{i}+1}-\epsilon} dx [\nabla \chi_{m_1}^{i_1}(x)] [\nabla \chi_{m_2}^{i_2}(x)] \\ - \frac{1}{2} \sum_{\bar{i}} \lim_{\epsilon \rightarrow 0} \chi_{m_1}^{i_1}(x) (\nabla \chi_{m_2}^{i_2}(x^{\bar{i}} + \epsilon) - \nabla \chi_{m_2}^{i_2}(x^{\bar{i}} - \epsilon)) \\ = \frac{1}{2} (\delta_{i_1 i_2} + \delta_{i_1, i_2 \pm 1}) \int_0^{x_0} dx [\nabla \chi_{m_1}^{i_1}(x)] [\nabla \chi_{m_2}^{i_2}(x)]. \quad (3.26)$$

Here, we have integrated by parts and, in Eq. (3.25), the first and the third term cancel. The last equality is due to the fact that the basis functions have non-vanishing overlap only in the same and adjacent elements, compare with Figure 3.3. Performing the integral in Eq. (3.26), we arrive

¹⁰Although they have no jump discontinuities, the basis functions are not *smooth* beyond element boundaries.

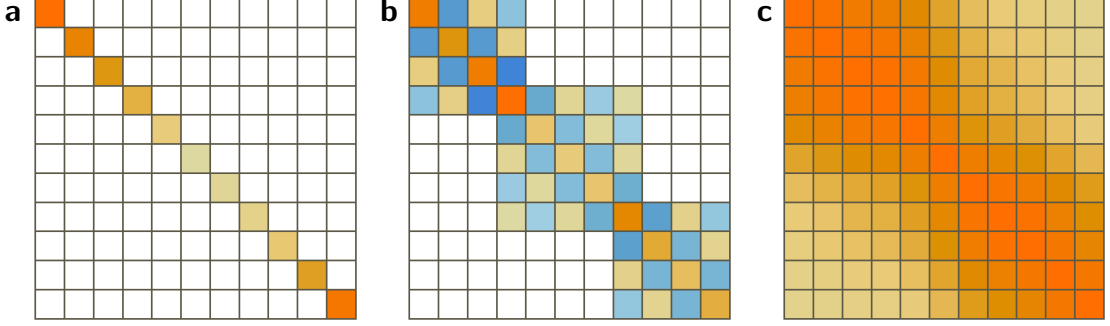


Figure 3.4: Matrix structure of the potential energy $v_{m_1 m_2}^{i_1 i_2}$, panel (a), the kinetic energy $t_{m_1 m_2}^{i_1 i_2}$, panel (b), and the interaction part $\tilde{u}_{m_1 m_2}^{i_1 i_2}$ of Eq. (3.31), panel (c), in finite element-discrete variable representation. The arrangement of multi-indices $p_{1,2} = (i_{1,2}, m_{1,2})$ is as in Eq. (3.15). Within the simulation box $\mathcal{S} = [0, x_0]$ with $x_0 = 3 a_0$, we, exemplarily, have chosen the potentials $\hat{v}^{(1)}(x) = \frac{1}{2}(x - \frac{3}{2})^2$ and $\hat{h}^{(2)}(|x - \bar{x}|) = [(x - \bar{x})^2 + 1]^{-1/2}$ in atomic units. The color coding ranges from negative values (blue) and zero (white) to positive values (orange). With non-equidistant subintervals and $n_b = 11$ basis functions, the FE-DVR basis is as in Figure 3.3. Moreover, the specific form of the interval partitioning is responsible for the broken symmetry and dominating matrix elements in the upper left corner, see in particular panel (b).

at the final result,

$$t_{m_1 m_2}^{i_1 i_2} = \frac{1}{2} \left\{ \begin{array}{l} \frac{\delta_{i_1 i_2} (\tilde{t}_{n_g-1, n_g-1}^{i_1} + \tilde{t}_{00}^{i_1+1}) + \delta_{i_1, i_2+1} \tilde{t}_{n_g-1, 0}^{i_1} + \delta_{i_1, i_2-1} \tilde{t}_{0, n_g-1}^{i_2}}{[(w_{n_g-1}^{i_1} + w_0^{i_1+1})(w_{n_g-1}^{i_2} + w_0^{i_2+1})]^{1/2}}, \quad m_1 = m_2 = 0 \\ \frac{\delta_{i_1 i_2} \tilde{t}_{n_g-1, m_2}^{i_1} + \delta_{i_1, i_2-1} \tilde{t}_{0 m_2}^{i_2}}{[w_{n_g-1}^{i_1} + w_0^{i_1+1}]^{1/2}}, \quad m_1 = 0, m_2 > 0 \\ \frac{\delta_{i_1 i_2} \tilde{t}_{m_1, n_g-1}^{i_1} + \delta_{i_1, i_2+1} \tilde{t}_{m_1 0}^{i_1}}{[w_{m_1}^{i_1} (w_{n_g-1}^{i_2} + w_0^{i_2+1})]^{1/2}}, \quad m_1 > 0, m_2 = 0 \\ \frac{\delta_{i_1 i_2} \tilde{t}_{m_1 m_2}^{i_1}}{[w_{m_1}^{i_1} w_{m_2}^{i_2}]^{1/2}}, \quad m_1, m_2 > 0 \end{array} \right. , \quad (3.27)$$

where the quantity \tilde{t} is connected to the first derivative of the Lobatto shape functions, cf. property (F3) in Chapter 3.2.2,

$$\tilde{t}_{m_1 m_2}^i = \sum_m \left[\nabla f_{m_1}^i(x_m^i) \right] \left[\nabla f_{m_2}^i(x_m^i) \right] w_m^i . \quad (3.28)$$

Moreover, from Eq. (3.26) and Eq. (3.27), we see, supposing the index arrangement of Eq. (3.15), that the kinetic energy matrix in FE-DVR representation has a block diagonal structure. A more detailed analysis yields that these blocks have a single element overlap at $t_{m_1 m_2}^{i_1 i_2}$ with $m_1 = m_2 = 0$, compare with Figure 3.4.

3.3.2 Interaction Energy

In nonequilibrium Green function theory, the interaction energy¹¹ is connected to the two-time self-energy $\Sigma_\xi[g, u]$ of Eq. (3.18), which, functionally, involves knowledge of the Green function g and the matrix elements u of the binary interaction potential (the two-electron integrals), cf. Eq. (3.16). In the FE-DVR picture and in the physicist's notation¹², using the pure form without anti-symmetrization, the two-electron integrals are defined by,

$$u_{m_1 m_2, m_3 m_4}^{i_1 i_2, i_3 i_4} = \int_0^{x_0} dx \int_0^{x_0} d\bar{x} \chi_{m_1}^{i_1}(x) \chi_{m_3}^{i_3}(\bar{x}) \hat{h}^{(2)}(|x - \bar{x}|) \chi_{m_2}^{i_2}(x) \chi_{m_4}^{i_4}(\bar{x}), \quad (3.29)$$

and are symmetric with respect to the interchange of $(i_1 m_1) \leftrightarrow (i_2 m_2)$, $(i_3 m_3) \leftrightarrow (i_4 m_4)$ and pairs $(i_1 m_1, i_2 m_2) \leftrightarrow (i_3 m_3, i_4 m_4)$. Evaluating the integrals in Eq. (3.29), we find a high degree of diagonality:

$$u_{m_1 m_2, m_3 m_4}^{i_1 i_2, i_3 i_4} = \delta_{m_1 m_2}^{i_1 i_2} \delta_{m_3 m_4}^{i_3 i_4} \tilde{u}_{m_1 m_3}^{i_1 i_3}. \quad (3.30)$$

We emphasize already at this point that it is this property which will greatly simplify the summation over parts of Feynman skeleton diagrams in Chapter 3.3.3, and, hence, will make the FE-DVR method favorable in comparison to other basis sets. Only in coordinate representation, a similar result is obtained.

The elements of matrix \tilde{u} defined in Eq. (3.30) are readily obtained with use of Eq. (3.20):

$$\tilde{u}_{m_1 m_3}^{i_1 i_3} = \begin{cases} \hat{h}^{(2)}(|x_{n_g-1}^{i_1} - x_{n_g-1}^{i_3}|), & m_1 = m_3 = 0 \\ \hat{h}^{(2)}(|x_{n_g-1}^{i_1} - x_{m_3}^{i_3}|), & m_1 = 0 \text{ and } m_2 > 0 \\ \hat{h}^{(2)}(|x_{m_1}^{i_1} - x_{n_g-1}^{i_3}|), & m_1 > 0 \text{ and } m_2 = 0 \\ \hat{h}^{(2)}(|x_{m_1}^{i_1} - x_{m_3}^{i_3}|), & m_1, m_2 > 0 \end{cases}. \quad (3.31)$$

We note, that \tilde{u} is symmetric but cannot be simplified any further in finite element-discrete variable representation, i.e., in comparison with the (block) diagonal potential (kinetic) energy of Chapter 3.3.1, all matrix elements have to be taken into account in practical calculations. However, in contrast to the full u of Eq. (3.29), the memory requirement of which scales as $\mathcal{O}(n_b^4)$, the matrix \tilde{u} is very memory-friendly.

Figure 3.4 (c) shows the structure of matrix $\tilde{u}_{m_1 m_2}^{i_1 i_2}$ for the case of a soft-Coulomb potential $\hat{h}^{(2)}(|x - \bar{x}|) = [(x - \bar{x})^2 + 1]^{-1/2}$ (in atomic units) and a FE-DVR basis of size $n_b = 11$.

3.3.3 Lowest-order Self-energies

Using the matrix elements of the interaction potential defined above by Eqs. (3.29) to (3.31), we can state explicit expressions for the self-energy. Here, we consider irreducible (topologically distinct)

¹¹For the corresponding expectation value, see Chapter 5.2.

¹²For the usual chemist's notation, see, e.g., Ref. [SO96].

Feynman diagrams up to the second Born approximation as depicted in Figure 2.2 of Chapter 2. Also, we assume, respectively, a spin-restricted (i.e., closed-shell) or a spin-polarized system, cf. the cases (S1) and (S2) outlined in Chapter 3.1.

Due to the high degree of diagonality found in the previous Section, in a FE-DVR basis, interaction lines are represented by elements of the matrix \tilde{u} which is of same dimension than the Green function g . Consequently, $\Sigma_\xi[g, u] = \Sigma_\xi[g, \tilde{u}]$ which signifies a drastic simplification (see the discussion below) [BBB10a]. In addition, according to the Feynman rules [BF07], any closed propagator loop is multiplied by a spin degeneracy factor of $\xi = 2$ (for electrons) to account for double occupancy of states if a closed-shell system is being described¹³. Otherwise, $\xi = 1$.

The (first-order) Hartree-Fock self-energy is then given by,

$$\begin{aligned} \Sigma_{\xi, m_1 m_2}^{\text{HF}, i_1 i_2}[g, \tilde{u}](t, t') &= \delta_C(t - t') \Sigma_{\xi, m_1 m_2}^{\text{HF}, i_1 i_2}[g, \tilde{u}](t) \\ &= \delta_C(t - t') \left(\Sigma_{\xi, m_1 m_2}^{\text{H}, i_1 i_2}[g, \tilde{u}](t) + \Sigma_{m_1 m_2}^{\text{F}, i_1 i_2}[g, \tilde{u}](t) \right), \end{aligned} \quad (3.32)$$

where,

$$\Sigma_{\xi, m_1 m_2}^{\text{H}, i_1 i_2}[g, \tilde{u}](t) = \begin{array}{c} \text{Diagram: A vertex } p \text{ with a loop above it and a wavy line below it labeled } \tilde{u}_{m_1 m}^{i_1 i} \text{ leading to a vertex } p_1. \end{array} = -i \xi \delta_{m_1 m_2}^{i_1 i_2} \sum_{im} \tilde{u}_{m_1 m}^{i_1 i} g_{mm}^{ii}(t, t^+), \quad (3.33)$$

$$\Sigma_{m_1 m_2}^{\text{F}, i_1 i_2}[g, \tilde{u}](t) = \begin{array}{c} \text{Diagram: A wavy line labeled } \tilde{u}_{m_1 m_2}^{i_1 i_2} \text{ connecting two vertices } p_1 \text{ and } p_2. \end{array} = i \tilde{u}_{m_2 m_1}^{i_2 i_1} g_{m_2 m_1}^{i_2 i_1}(t, t^+). \quad (3.34)$$

In the second(-order) Born approximation, we add the non-local expression,

$$\begin{aligned} \Sigma_{\xi, m_1 m_2}^{\text{2ndB}, i_1 i_2}[g, \tilde{u}](t, t') &= \begin{array}{c} \text{Diagram: Two vertices } p \text{ and } \bar{p} \text{ connected by two wavy lines labeled } \tilde{u}_{m_1 m}^{i_1 i} \text{ and } \tilde{u}_{\bar{m} m_2}^{i_2 i_2}. \end{array} + \begin{array}{c} \text{Diagram: A wavy line labeled } \tilde{u}_{m_1 \bar{m}}^{i_1 \bar{i}} \text{ connecting } p_1 \text{ to } \bar{p}, \text{ and another wavy line labeled } \tilde{u}_{\bar{m} m_2}^{i_2 i_2} \text{ connecting } \bar{p} \text{ to } p_2. \end{array} \\ &= \sum_{im} \sum_{\bar{i}\bar{m}} \tilde{u}_{m_1 m}^{i_1 i} \tilde{u}_{\bar{m} m_2}^{i_2 i_2} g_{m\bar{m}}^{i\bar{i}}(t', t) \\ &\quad \times \left(\xi g_{m_1 m_2}^{i_1 i_2}(t, t') g_{\bar{m} m}^{i\bar{i}}(t, t') - g_{m_1 \bar{m}}^{i_1 \bar{i}}(t, t') g_{\bar{m} m_2}^{i_2 i_2}(t, t') \right), \end{aligned} \quad (3.35)$$

which has a direct term, involving ξ , and an exchange contribution.

¹³For electrons, $\xi = 2\sigma + 1$ with spin magnitude $\sigma = \frac{1}{2}$ [Kit10].

In the general case (e.g., compare with Ref. [BBvL⁺09]), the calculation of a self-energy Σ_ξ involving M vertex points in its diagrammatic representation requires n_b^{2M-2} summations for each of the n_b^2 matrix elements. However, due to the specific form of u in FE-DVR representation, a lot of summations can be omitted. The reduction of complexity is considerable,

$$\mathcal{O}\left(n_b^{2M-2}\right) \rightarrow \mathcal{O}\left(n_b^{M-2}\right). \quad (3.36)$$

Hence, the evaluation of a single matrix element of the Hartree term scales linear in n_b rather than quadratically, and the scaling behavior of the exchange contribution¹⁴ is independent of n_b . Very significant improvement is obtained for second- and, principally, also for all higher-order self-energy contributions. Concerning the second Born term, cf. Eq. (3.35), for each element $\Sigma_{\xi, m_1 m_2}^{2\text{ndB}, i_1 i_2}(t, t')$, the effort is reduced from $\mathcal{O}(n_b^6)$ to a quadratic scaling, $\mathcal{O}(n_b^2)$. For clarification, we emphasize that, in Eqs. (3.32) to (3.35), any summation over $p = (i, m)$ is equivalent to summing over the total basis size n_b .

That the scaling of Eq. (3.36) is of great benefit to the practical implementation is elucidated by the following example: Suppose a typical basis size of $n_b = 50$. Then, concerning the Hartree self-energy (where $M = 2$), a number of 2500 summations have to be performed when a non-FE-DVR basis is used. On the contrary, in the FE-DVR case, only 50 summations are required. On top of that, the exchange term involves only the multiplication of two matrix elements (cf. Eq. (3.34)) instead of a full matrix multiplication consuming 2500 additional summations.

Of course, the reader may ask why a direct implementation of the above self-energy expressions is advantageous in the context of available, highly efficient linear algebra routines. Indeed, for the Hartree-Fock part, the scaling is less important. However, already at the level of the second-order self-energy (with $M = 4$), the situation becomes dramatic. Here, the number of summations is $50^6 = 1.5625 \times 10^{10}$ against 2500 per matrix element $\Sigma_{\xi, m_1 m_2}^{2\text{ndB}, i_1 i_2}(t, t')$. This means a computational reduction of more than six orders of magnitude when a FE-DVR basis is used. Particularly with reference to the fact that higher-order self-energies have to be computed for different time-arguments during the propagation of the NEGF (see Chapter 4), the FE-DVR scaling turns out to be highly favorable¹⁵.

3.4 Summary

In this Chapter, we have outlined the representation of the one-particle (two-time) nonequilibrium Green function $\mathcal{G}_{i_1 i_1}^{(1)}(t_1, t_1)$, cf. Eq. (2.12), in terms of a specifically designed basis in real space—the FE-DVR basis $\chi_m^i(x)$ introduced in Eq. (3.13). On the one hand, this one-dimensional basis is very special from the constructional point of view, but, on the other hand, it offers great flexibility due to its grid-based origin attributed to the partitioning of the simulation box into n_e finite elements

¹⁴Regarding a single matrix element $\Sigma_{m_1 m_2}^{F, i_1 i_2}(t)$.

¹⁵For algorithm speed-up, previous NEGF codes [BBvL⁺09] usually perform various tests for small self-energy contributions and neglect those in the high-dimensional summation. However, this is at the expense of accuracy, and can be fully avoided in the present FE-DVR formalism.

(FE). In addition, within the FEs, a number of $n_g - 1$ locally interpolating functions that arise from the discrete variable representation (DVR) enable excellent spatial resolution.

Further, spin is included into the formalism in terms of a degeneracy factor ξ allowing for the description of spin-polarized systems (with $\xi = 1$, e.g., H_2 in the triplet state, cf. Chapter 6) and closed-shell systems (with $\xi = 2$, comprising singlet states for even particle number). In order to simultaneously take both cases into account in the numerics¹⁶, the nonequilibrium Green function is normalized with respect to N_e/ξ , where N_e is the system's total particle number. Hence, the degeneracy factor only parametrically enters in the self-energies of Eqs. (3.32) and (3.35) and needs to be considered when calculating observables, see Chapter 5.

In FE-DVR representation, the matrix elements required in the equations of motion for the NEGF (see below) are obtained in simple semianalytic fashion. Thereby, in contrast to other basis sets, the FE-DVR method maintains the beneficial properties of the coordinate representation and reduces the four-indexed quantity u (the two-electron integrals, cf. Eq. (3.29)) to a two-indexed quantity \tilde{u} . By considerably improving the scaling with basis size, this has great advantages in the construction of the first-, second- and, principally, all higher-order self-energies (Chapter 3.3.3). Further, the only required input for a FE-DVR basis setup in an interval $[0, x_0]$ with defined FEs are Gauss-Lobatto points x_m and their assigned weights w_m (for details and a table of relevant sets $\{x_m, w_m\}$ with $n_g = 3$ to 15, see Appendix A).

In summary, the two-time Kadanoff-Baym equations read in FE-DVR representation¹⁷,

(FE-DVR I.)

$$\left(i \frac{\partial}{\partial t} \delta_{m_1 m_2}^{i_1 i_2} - \bar{h}_{m_1 m_2}^{i_1 i_2}[g, \tilde{u}](t) \right) g_{m_2 m_1}^{i_2 i_1}(t, t') = \delta_{\mathcal{C}}(t - t') \delta_{m_1 m_1}^{i_1 i_1} \quad (3.37)$$

$$+ \int_{\mathcal{C}} dt_2 \Sigma_{\xi, m_1 m_2}^{2\text{ndB}, i_1 i_2}[g, \tilde{u}](t, t_2) g_{m_2 m_1}^{i_2 i_1}(t_2, t'),$$

(FEDVR II.)

$$\text{adjoint of Eq. (FE-DVR. I.) with } t \leftrightarrow t', \quad (3.38)$$

where time-local self-energies are absorbed in the single-particle energy ($h_{m_1 m_2}^{i_1 i_2}(t) = t_{m_1 m_2}^{i_1 i_2} + v_{m_1 m_2}^{i_1 i_2}(t)$, cf. Eq. (3.16) and Chapter 3.3.1),

$$\bar{h}_{m_1 m_2}^{i_1 i_2}[g, \tilde{u}](t) = h_{m_1 m_2}^{i_1 i_2}(t) + \Sigma_{\xi, m_1 m_2}^{\text{HF}, i_1 i_2}[g, \tilde{u}](t). \quad (3.39)$$

For completeness, we also present the Dyson equation for the equilibrium Matsubara Green

¹⁶Details are presented in Chapter 4.

¹⁷As stated above, the notation implies summation over all indices that appear twice.

3 Representation of the Nonequilibrium Green Function

function in FE-DVR notation (cf. Eq. (2.32) and note transformation (2.25)),

(FE-DVR III.)

$$g_{m_1 m_{\bar{1}}}^{M, i_1 i_{\bar{1}}}(\tau) = g_{m_1 m_{\bar{1}}}^{0, i_1 i_{\bar{1}}}(\tau) + \int_0^\beta d\tau_1 \int_0^\beta d\tau_2 g_{m_1 m_2}^{0, i_1 i_2}(\tau - \tau_1) \Sigma_{\xi, m_2 m_3}^{K, i_2 i_3}[g^0, g^M, \tilde{u}](\tau_1 - \tau_2) g_{m_3 m_{\bar{1}}}^{M, i_3 i_{\bar{1}}}(\tau_2), \quad (3.40)$$

with,

$$\Sigma_{\xi, m_2 m_3}^{K, i_2 i_3}[g^0, g^M, \tilde{u}](\tau) = \Sigma_{\xi, m_2 m_3}^{2\text{ndB}, i_2 i_3}[g^M, \tilde{u}](\tau) - \delta(\tau) \Sigma_{\xi, m_2 m_3}^{\text{HF}, i_2 i_3}[g^0, \tilde{u}], \quad (3.41)$$

where the mean-field (Hartree-Fock) Green function $g^0(\tau)$ follows from (cf. Eq. (2.30); for times $t < t_0$, Hamiltonian (3.17) has no explicit time-dependence),

(FE-DVR IV.)

$$\left(-\frac{\partial}{\partial \tau} \delta_{m_1 m_2}^{i_1 i_2} - \bar{h}_{m_1 m_2}^{i_1 i_2}[g^0, \tilde{u}](t_0) \right) g_{m_2 m_{\bar{1}}}^{0, i_2 i_{\bar{1}}}(\tau) = \delta(\tau) \delta_{m_1 m_{\bar{1}}}^{i_1 i_{\bar{1}}}. \quad (3.42)$$

Solving the Two-time Kadanoff-Baym Equations

Primarily, in this thesis, we are aiming at solving the two-time Kadanoff-Baym equations without further approximations¹ except for the self-energy $\Sigma_{\xi}(t, t')$ which, however, remains a two-time quantity in a beyond-mean-field treatment, cf. Chapter 3.3.3. Thereby, as outlined in the previous Chapter, the FE-DVR method provides a flexible basis and an accurate representation of the NEGF. However, apart from greatly simplifying the construction of the self-energies and having, in general, the potential to reduce the necessary basis size, the use of finite elements and the discrete variable representation has no further advantages referring to the time evolution of the nonequilibrium Green function.

Whereas Hartree-Fock-type solutions of the Kadanoff-Baym equations (FE-DVR I.+II.)² are readily obtained by solely propagating the one-particle density matrix (or the lesser correlation function $g^{<}(t, t')|_{t=t'}$), full two-time solutions are still a challenging issue due to the computational cost which scales as t_{f}^2 , where t_{f} is the total simulation length (or time). For fast decaying integration kernels³, there exist computational techniques to improve the scaling behavior, see, e.g., Ref. [Zwo08]. However, for systems that are basically not connected to an environment (as the atomic and molecular models to be discussed in Part III of this thesis) such an approach is not applicable as, here, correlations are fairly persistent. Consequently, one has to account for the complete history of the non-Markovian dynamics.

For this reason, if further approximations such as the generalized Kadanoff-Baym ansatz (see Chapter 4.3) are to be avoided, an efficient two-time propagation algorithm is required that is able to handle *large* NEGF data without immense loss in performance. Applying state-of-the-art high-performance computing strategies, we, in Chapter 4.2, develop an advanced method of propagation on the basis of the (serial) propagation scheme described in Refs. [SDvL09, PvFVA10]

¹I.e., the present approach is distinct to the frequently used concept of utilizing the NEGF framework to derive single-time master (transport) equations.

²See the summary of the previous Chapter.

³The right hand sides of the Kadanoff-Baym equations (FE-DVR I.+II.).

(for a recapitulation see Chapter 4.1 and Appendix B). As a result of this development, we obtain a parallel algorithm which involves only small overhead due to inter-process communications and is ready for supercomputer usage.

4.1 Method of Propagation

4.1.1 Preparation of Initial States

According to Eq. (2.38) in Chapter 2, at time t_0 , any initial state is uniquely defined by,

$$\begin{aligned} g_{m_1 m_2}^{<, i_1 i_2}(t_0, t_0) &= i g_{m_1 m_2}^{x, i_1 i_2}(0^-), & g_{m_1 m_2}^{>, i_1 i_2}(t_0, t_0) &= -i g_{m_1 m_2}^{x, i_1 i_2}(-\beta), \\ g_{m_1 m_2}^{[, i_1 i_2}(t_0 - i\tau, t_0) &= i g_{m_1 m_2}^{x, i_1 i_2}(\tau), \end{aligned} \quad (4.1)$$

where, in FE-DVR notation, $g_{m_1 m_2}^{x, i_1 i_2}(\tau)$ is a Matsubara Green function on the imaginary part of the Keldysh contour \mathcal{C} . In order to ensure stationarity, for a given many-body approximation, g^x must be a self-consistent solution of the Dyson equation, i.e., $x=0, M$. Here, g^0 generally denotes the Matsubara Green function in Hartree-Fock approximation, and, with g^M , we refer to the second Born approximation, cf. Eqs. (FE-DVR III.) and (FE-DVR IV.) in the summary of Chapter 3.

The Hartree-Fock Green function is obtained in the form,

$$g_{m_1 m_2}^{0, i_1 i_2}(\tau) = c_{m m_1}^{i i_1} c_{m m_2}^{i i_2} g_m^i[g^0](\tau), \quad (4.2)$$

where,

$$g_m^i[g^0](\tau) = \bar{n}(\beta, \epsilon_m^i[g^0]) \exp\left(-\tau \epsilon_m^i[g^0]\right), \quad (4.3)$$

and $\bar{n}(\beta, \epsilon)$ is the Fermi-Dirac distribution. Further, ϵ_m^i are the eigenvalues of the real, symmetric matrix⁴ $\bar{h}[g^0, \tilde{u}]$ renormalized by the chemical potential μ , compare with Eq. (2.29) of Chapter 2. The components of the eigenvectors of \bar{h} are denoted $c_{m_1 m_2}^{i_1 i_2}$ and enter Eq. (4.2). We emphasize that the chemical potential μ is obtained implicitly by enforcing the correct normalization to $\bar{n}(\beta, \epsilon)$, i.e., $N_e \xi^{-1} = \sum_{im} \bar{n}(\beta, \epsilon_m^i)$.

Due to the dependence⁵ of \bar{h} on g^0 , the self-consistent initial state has to be determined iteratively such that \bar{h} and $g^0(\tau)$ become stationary. Thereby, an arbitrary symmetric density matrix $g_{m_1 m_2}^{0, i_1 i_2}(0^-)$ serves as starting point. Moreover, we note that the τ -dependence is steadily of exponential form, but, in comparison with the Hartree-Fock orbital picture represented through Eq. (4.3), cf. also [BBvL⁺09], in the FE-DVR basis (Eq. (4.2)), each matrix element of g^0 contains a superposition of many different exponentials.

In the zero-temperature limit ($\beta \rightarrow \infty$), the iterative procedure is similar to the self-consistent field (SCF) method [SO96] which allows for computation of the Hartree-Fock ground state wave function. In addition, the chemical potential is then situated within the HOMO-LUMO gap, i.e.,

⁴ \bar{h} is the Hartree-Fock energy defined in Eq. (3.39).

⁵To be precise, the dependence of Eq. (4.3) on the Green function g^0 is not fully functionally, because \bar{h} only depends on the one-particle density matrix $g_{m_1 m_2}^{0, i_1 i_2}(0^-)$.

in the energy interval between the highest occupied molecular orbital (HOMO) and the lowest unoccupied molecular orbital (LUMO). If we call the Hartree-Fock orbital energies⁶ $\epsilon_1, \epsilon_2, \dots, \epsilon_{n_b}$ and sort them by energy, the chemical potential is given by $\mu = \frac{1}{2}(\epsilon_{N_e \xi - 1} + \epsilon_{N_e \xi - 1 + 1})$.

If necessary, as in SCF calculations, different methods such as averaging (damping) or extrapolation schemes can be used to promote convergence, see, e.g., Ref. [Jen99].

To calculate the self-consistent initial state in the second Born approximation, the full Dyson equation (3.40) needs to be iterated starting from the Hartree-Fock Green function ($g^M \rightarrow g^0$ in the first evaluation of the right hand side):

$$g_{m_1 m_2}^{M, i_1 i_2}(\tau) = g_{m_1 m_2}^{0, i_1 i_2}(\tau) + i_{m_1 m_2}^{(2), i_1 i_2}[g^0, g^M, \tilde{u}](\tau), \quad (4.4)$$

where, cf. Ref. [BBB10b],

$$\begin{aligned} i_{m_1 m_2}^{(2), i_1 i_2}[g^0, g^M, \tilde{u}](\tau) &= \int_0^\beta d\bar{\tau} g_{m_1 m}^{0, i_1 i}(\tau - \bar{\tau}) i_{m m_2}^{(1), i_1 i_2}[g^0, g^M, \tilde{u}](\bar{\tau}), \\ i_{m_1 m_2}^{(1), i_1 i_2}[g^0, g^M, \tilde{u}](\tau) &= \int_0^\beta d\bar{\tau} \Sigma_{\xi, m_1 m}^K[g^0, g^M, \tilde{u}](\tau - \bar{\tau}) g_{m m_2}^{M, i_1 i_2}(\bar{\tau}), \end{aligned} \quad (4.5)$$

and the self-energy kernel Σ_{ξ}^K is defined as in Eq. (3.41). For the domain of integration for fixed τ in Eq. (4.4), remember Figure 2.3 in Chapter 2. With Eq. (4.5), the collision term has been divided into two separate convolution integrals which, in each iteration cycle, are solved consecutively. This approach, at least in the FE-DVR context, has been found to be more stable, controllable and substantially more efficient (for large n_b) than transforming the Dyson equation (3.40) into a set of linear equation systems, for details, see Refs. [BBvL⁺09, DvL05]. Moreover, it saves memory and allows for an easier code parallelization.

As in previous works [BBvL⁺09], we use a uniform power mesh [DvL05, KE02] to discretize all functions on the τ -interval $[-\beta, 0]$. Thereby, $\tau = 0$ means the limit $\tau \rightarrow 0^-$, and, as outlined in Chapter 2, the Matsubara Green function for positive τ can be obtained via the antiperiodicity property of g^x ($x = 0, M$). Generally, the uniform power mesh provides an accurate representation of the Green function⁷ which is peaked around $\tau = -\beta$ and $\tau = 0$, see Eqs. (4.2) and (4.3), and note that electron correlations will only lead to small deviations in the exponential decay or increase. Being adapted to this behavior, the mesh is chosen dense around both interval endpoints. It is constructed by $n_p - 1$ bisections of the lower (upper) part of the interval $[-\beta, -\frac{1}{2}\beta]$ ($[-\frac{1}{2}\beta, 0]$) and the introduction of an even-spaced grid of $n_u + 1$ points in each resulting subinterval. The total number of grid points is then $n_\tau = 2n_u n_p + 1$ and the smallest, respectively, largest mesh spacing reads $\beta(2^{n_p} n_u)^{-1}$ and $\beta(4n_u)^{-1}$. For the treatment of g^0 and Σ_{ξ}^K at the time differences $\tau - \bar{\tau}$ which not necessarily meet a mesh point, cf. Eq. (4.5), we linearly interpolate.

During the iteration of the Dyson equation (4.4), a very sensitive parameter is the particle number $N_e = \xi \sum_{im} g_{mm}^{M, ii}(0^-)$, the preservation of which may strongly depend on the specific choice of mesh parameters n_u and n_p . Further, as abort criterion, we recommend testing the

⁶These are the non-renormalized eigenvalues of matrix \bar{h} .

⁷For a different but equivalent numerical treatment of the Keldysh contour \mathcal{C} , see, e.g., Ref. [PvFVA10].

absolute norm⁸ of the one-particle density matrix *and* the correlation energy⁹ for convergence. Thereby, the correlation energy has the advantage of acting as a global convergence measure because it involves information of all τ , cf. Eq. (5.7).

4.1.2 Full Two-time Propagation of the NEGF

For integrating the Kadanoff-Baym equations (FE-DVR I.) and (FE-DVR II.) in the presence of external fields (included via $\bar{h}(t)$, cf. Eq. (3.39)) [KKY99], we straight forwardly discretize both time arguments of $g^{\gtrless}(t, t')$ in units of δ , where in atomic units $\delta\tau_0^{-1} \ll 1$. For a different approach using relative and center-of-mass variables see, e.g., Ref. [ZHWC03]. Further, we make use of the symmetry between $g^>$ and $g^<$, cf. Eq. (2.38), and arrive at the two-dimensional grid displayed in Figure 4.1, see the open and closed dots. Concerning the mixed Green functions $g^{\lceil}(-i\tau, t)$ (and $g^{\lceil}(t, -i\tau)$), we represent the variable t on the same equidistant grid, and, for the imaginary time argument $-i\tau$, we keep the uniform power mesh as introduced for the Matsubara Green function $g^M(\tau)$ in Chapter 4.1.1.

Explicitly, the propagation of the nonequilibrium Green function follows the method described in Refs. [SDvL09, PvFVA10] and is based on the earlier work of *S. Köhler et al.* [KKY99]. In an abstract form with $g^x(t)$ being either $g^x(t, \cdot)$ or $g^x(\cdot, t)$ ($x = >, <, \lceil, \rfloor$) and dropping the FE-DVR basis indices, the evolution of the NEGF is obtained from ($\delta\tau_0^{-1} \ll 1$),

$$g^x(t + \delta) = \mathcal{P}^x \{ g^x(t), \bar{h}[g^<, \tilde{u}](t), i^x[g, \tilde{u}](t) \} , \quad (4.6)$$

where, for the given situation, the other time argument (which is indicated by ” \cdot ” and may be real or complex) is fixed. The function \mathcal{P}^x determines the dependency of the unknown Green function $g^x(t + \delta)$ on its current value $g^x(t)$, the actual single-particle energy $\bar{h}(t)$ and the collision integral¹⁰ $i^x(t)$. Further, $\bar{h}(t)$ contains the Hartree-Fock self-energy and only depends on $g^<(t, t)$ (i.e., on the density matrix), compare with Eq. (3.39). The collision integral i^x incorporates the second-order Born terms¹¹, cf. Chapter 3.3.3.

We remark that, in the very first time step (where, without loss of generality, $t = 0$ in Eq. (4.6)), all collision terms $i^x(t)$ vanish, and $g^x(0)$ is defined by the initial and boundary conditions of Eq. (4.1). Moreover, for the special case of propagating $g^<$ along the time diagonal (compare with Figure 4.1), we have to extend Eq. (4.6) to,

$$g^<(t + \delta, t + \delta) = \mathcal{P}_{\text{diag}}^< \left\{ g^<(t, t), \bar{h}[g^<, \tilde{u}](t), i_{\text{diag}}^<[g, \tilde{u}](t, t) \right\} , \quad (4.7)$$

where,

$$i_{\text{diag}}^<[g, \tilde{u}](t, t) = i_1^>[g, \tilde{u}](t, t) - i_2^<[g, \tilde{u}](t, t) . \quad (4.8)$$

⁸The absolute norm of a matrix is defined as the sum of the absolute values of all entries.

⁹For the definition see Eq. (5.7) in Chapter 5.

¹⁰For the collision integral, which is a two-time quantity, we use the same notation than for the nonequilibrium Green function. In particular, $i^>(t) \equiv i_1^>(t, \cdot)$ and $i^<(t) \equiv i_2^<(\cdot, t)$.

¹¹Or, in general, all self-energy contributions that are of higher than first order in \tilde{u} .

The idea behind obtaining the right hand sides of Eqs. (4.6) and (4.7) is to treat $h(t)$ (the noninteracting Hamiltonian) and the time-local self-energy $\Sigma_\xi^{\text{HF}}[g^<, \tilde{u}](t)$ on the same footing in terms of a time evolution operator $u_t(t)$ which satisfies $i \partial_t u_{t-0}(t) = \bar{h}(t) u_{t-0}(t)$. Then, $u_t(t)$ allows for a unitary gauge transformation of the Green function (for details, see Ref. [SDvL09]) and, e.g., the expression for the greater correlation function in Eq. (4.6) becomes,

$$g^>(t + \delta) = u_\delta(t) g^>(t) - i u_{t+\delta}(t) \int_t^{t+\delta} d\bar{t} u_{\bar{t}}^\dagger(t) i_1^>(\bar{t}). \quad (4.9)$$

Similar formulas can be derived for the other Keldysh components $g^<(t)$, $g^\lceil(t)$ and $g^\rceil(t)$. Thereby, the remaining integrals (cf. the last term in Eq. (4.9)) are readily evaluated by assuming $i^x(t)$ to be stationary within the time interval $[t, t + \delta]$. The resulting expressions for \mathcal{P}^x and $\mathcal{P}_{\text{diag}}^<$ in Eqs. (4.6) and (4.7) are given in Appendix B together with a detailed overview of the algorithm and useful hints for algorithm tests¹². Finally, to reduce discretization errors, we emphasize that the arguments in \mathcal{P}^x and $\mathcal{P}_{\text{diag}}^<$ can be updated during the time stepping by a predictor-corrector method [SDvL09].

In the last part of this Section, we want to focus on the collision integrals, the structure of which is of great importance when establishing a parallel code as outlined in Chapter 4.2. Again, dropping all FE-DVR indices and implying matrix multiplication, $i_1^>$ and $i_2^<$ are defined by¹³,

$$\begin{aligned} i_1^>(t, t') &= \int_0^t d\bar{t} \Sigma_\xi^> <(t, \bar{t}) g^>(\bar{t}, t') + \int_0^{t'} d\bar{t} \Sigma_\xi^> <(t, \bar{t}) g^<->(\bar{t}, t') \\ &\quad + \Sigma_\xi^\lceil \star g^\lceil, \\ i_2^<(t', t) &= \int_0^{t'} d\bar{t} g^> <(t', \bar{t}) \Sigma_\xi^< <(\bar{t}, t) + \int_0^t d\bar{t} g^< <(t', \bar{t}) \Sigma_\xi^<->(\bar{t}, t) \\ &\quad + g^\lceil \star \Sigma_\xi^\lceil, \end{aligned} \quad (4.10)$$

where $X^{\gtrless-\lessgtr}$ is used to indicate the difference $X^{\gtrless} - X^{\lessgtr}$ ($X = g, \Sigma_\xi$). Thereby, we only write out the first two terms¹⁴, because the last term $\Sigma_\xi^\lceil \star g^\lceil$, respectively $g^\lceil \star \Sigma_\xi^\lceil$, involves only a trivial integration over the imaginary branch of the Keldysh contour (cf. Eq. (2.43)) and needs no further attention at this point.

Making use of the symmetry relations (2.38) and (2.40), Figure 4.1 (a) and (b) illustrate the composition of the collision integrals that are required for two representative time steps: $g^>(t, t') \rightarrow g^>(t + \delta, t')$ (see the red arrow in panel (a)) and $g^<(t', t) \rightarrow g^<(t', t + \delta)$ (panel (b)). Thereby, the red-bordered areas (cf. the solid, dashed and dash-dotted lines) indicate the required Green functions that directly enter either integral $i_1^>$ or $i_2^<$, and the black-bordered domains denote the

¹²The Hartree-Fock part of the algorithm, where $i^x(t) \equiv 0 \forall x \in \{>, <, \lceil, \rceil\}$, has been successfully tested on the breathing mode of 2 to 20 interacting fermions in a harmonic trap, cf. Refs. [BBHB09, BHBB10a]. For a discussion on the Kohn mode dynamics [BBvL07] including correlations and $i^x(t)$ treated in the second Born approximation, the reader is referred to Appendix B (page 115).

¹³Remind the Kadanoff-Baym equations in the compact form of Eq. (2.44).

¹⁴In full detail, the collision integrals are given in Appendix B.

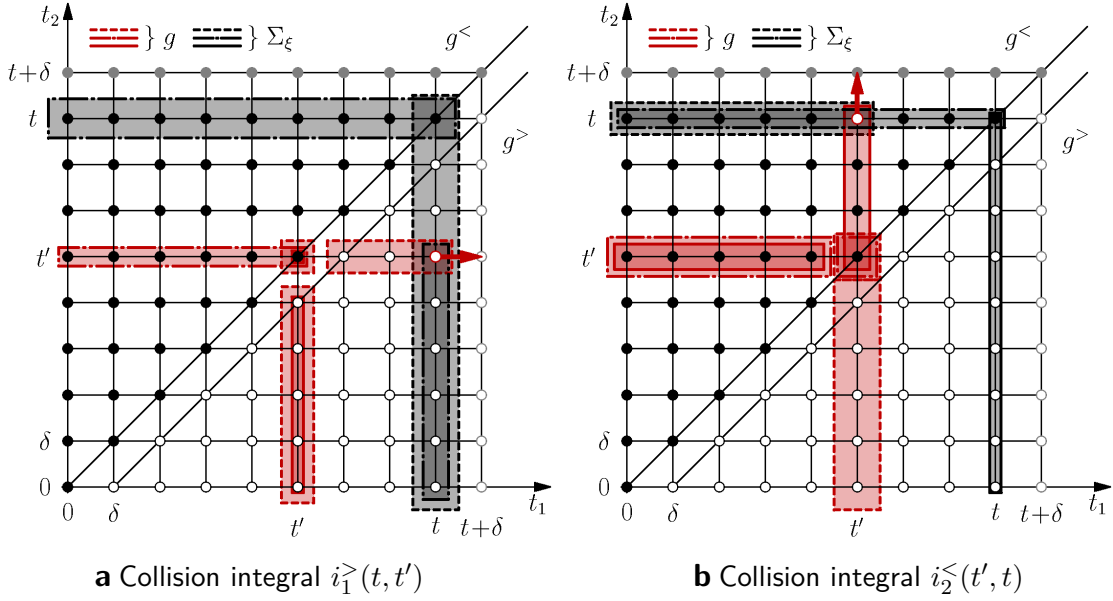


Figure 4.1: Construction of the collision terms $i_{1,2}^{\geq}$ of Eq. (4.10) as convolution integrals in the two-time domain. Panel (a) refers to the collision term $i_1^>(t, t')$ which is necessary to propagate $g^>$ from point (t, t') to point $(t + \delta, t')$, see the red arrow. Panel (b) shows the situation for $g^<$ being propagated from point (t', t) to point $(t', t + \delta)$. In both panels, open (closed) dots in the lower (upper) triangle represent the discretized correlation function $g^>$ ($g^<$), cf. Figure 2.4, and, on the time diagonal $t_1 = t_2$, we work with $g^<$, cf. Appendix B. While, the red-bordered areas reveal Green functions that directly enter the collision integral, the black-bordered areas denote Green functions that enter via the self-energies Σ_ξ^{\geq} . Note that the last integral $\Sigma_\xi^{\geq} \star g^{\square}$ ($g^{\square} \star \Sigma_\xi^{\geq}$) in $i_1^>$ ($i_2^<$) is not covered in this Figure, cf. Eq. (4.10).

NEGFs that enter via the self-energies $\Sigma_\xi^>$ and $\Sigma_\xi^<$ which each depend functionally on $g^>$ and $g^<$, compare with Eq. (3.35). In general, for fixed time “ \cdot ” in Eq. (4.6) (t' in Figure 4.1), the collision integrals involve the following Green functions in the two-dimensional plane of Figure 4.1: (i) those which are lying on the edge of the expanding square, i.e., which have time argument t , and (ii) those which depend on earlier time arguments and are situated on straight lines (parallel to the time axes) that intersect at point (\cdot, \cdot) . For the diagonal time step of Eq. (4.7), the regions (i) and (ii) become equal, compare with Figure 4.3 (a) further below.

According to the above discussion, in the practical calculation, the entire nonequilibrium Green function ($g^>$, $g^<$ and g^{\square} ; all being complex) needs to be stored to perform the collision integrals of Eq. (4.10). Thereby, the amount of data, being added in each time step, increases steadily because a number of $2t \delta^{-1} - 1$ correlation functions and $n_\tau t$ mixed Green functions (here, t is a multiple of δ) are newly computed when going from t to $t + \delta$ in either t_1 or t_2 direction, cf. Figure 4.1. Also, note that, in the FE-DVR representation, each Green function component $g^x(t, t')$ ($x = >, <, \square$) consists of a number of n_b^2 matrix elements.

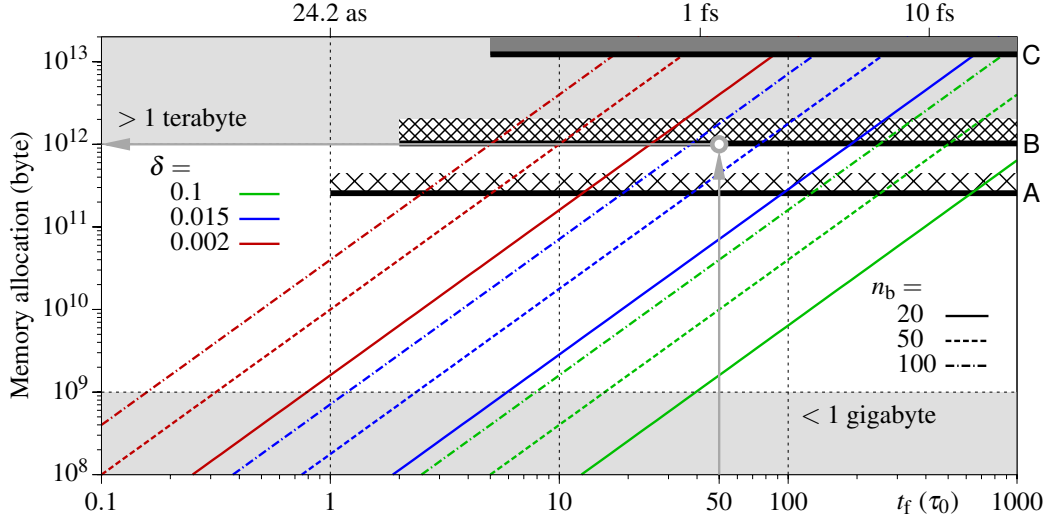


Figure 4.2: Memory required by $g^>$ and $g^<$ as function of final propagation time t_f (in units of τ_0) for full two-time NEGF calculations with FE-DVR basis size n_b and time step length δ . Whereas the line style distinguishes different values of n_b , the color coding refers to the indicated values of δ . Further, the gray arrows show the case where $t_f = 50 \tau_0$, $\delta = 0.02 \tau_0$ and $n_b = 100$. Hardware limitations: (A) "Fermion" (Linux) cluster of Institute of Theoretical Physics and Astrophysics of Kiel University: "fermion0x" nodes ($x = 40, 41, 42$), each with 32 cores and 256 gigabyte of shared memory, no wall time. (B) "ice1" ("xe") nodes at HLRN (the North-German Supercomputing Alliance): maximum resource request of 64 (16) nodes, each with 8 cores and 16 (64) gigabyte RAM, wall time: 12 h (24 h), Intel Xeon Harpertown E5472. (C) "ice2" nodes at HLRN: calculations limited to 256 nodes, each with 8 cores and 48 gigabyte RAM, wall time: 12 h, Intel Xeon Gainestown X5570.

Neglecting the mixed Green function¹⁵, the total memory demand scales as (in byte),

$$\mathcal{O}\left(16 n_b^2 (t_f \delta^{-1})^2\right), \quad (4.11)$$

where t_f denotes the final time of propagation and the prefactor accounts for a double-precision representation of complex numbers (where, per number, 2×8 byte are occupied). Note that, for Eq. (4.11), all symmetry properties have been borne in mind and only those parts of $g^>$ and $g^<$ are stored which are really needed (see the dots in Figure 4.1). Exemplarily, a two-time NEGF calculation of temporal length $t_f = 50 \tau_0$ with resolution $\delta = 0.02 \tau_0$ and $n_b = 100$ FE-DVR basis functions comprises one terabyte of data solely for the correlation functions. If g^Γ is being included with $n_\tau = 200$ mesh points, cf. Fn. 15, the memory increases by 80 gigabyte. Hence, g^{\gtrless} requires the dominant part of memory.

¹⁵The storage demand for g^Γ scales linear in the final propagation time t_f . In byte: $\mathcal{O}(16 n_b^2 n_\tau t_f \delta^{-1})$, where n_τ is the number of points on the uniform power mesh, cf. Chapter 4.1.1.

Focusing on the correlation functions, Figure 4.2 gives a more general overview of the scaling property (4.11) and displays the memory allocation for different values of n_b and δ in a double logarithmic plot—the example discussed above is indicated by the gray arrows. As can be seen, it is relatively easy—for various parameter settings—to reach the amount of data of one terabyte that has to be processed during the integration of the Kadanoff-Baym equations. Moreover, to reach the femtosecond time domain (10 fs correspond to $413 \tau_0$), one has to restrict oneself to small FE-DVR basis sets and/or to large time steps $\delta > 0.05$. In atomic (or molecular) applications, see Part III of this thesis, such a “hard” restriction will directly lead to non-converged results and an unstable propagation of the NEGF including divergent collision integrals and the violation of energy and momentum conservation. For this reason, we are generally limited to the simulation of the system’s short-time dynamics with t_f being essentially less than 10 fs. Then, simultaneously, an adequate time step and an accurate basis can be achieved.

Apart from the physical requirements of the modeled system, the numerical propagation of the NEGF according Eqs. (4.6) and (4.7) is, of course, likewise limited by the accessible computer hardware and power. The thick black lines labeled A-C in Figure 4.2 indicate the principal hardware limitations of (super) computers, with shared and/or distributed-memory configurations, that have been available during this work. For the computational specification and configuration, see the caption of Figure 4.2.

On the newest “Fermion” nodes¹⁶, two-time NEGF calculations with up to 256 gigabyte of shared memory are possible, see label A in Figure 4.2. For their usage, a parallel, shared-memory code has been established on the basis of OpenMP¹⁷ architecture [CJvdP08]. Beyond the “Fermion” compute resources, the supercomputing system at HLRN (the North-German Supercomputing Alliance¹⁸), provides plenty of flexibility regarding the number of available CPUs and the accessible RAM per node, see label B and C. Thus, more accurate and/or longer simulations are possible. However, for an efficient usage of the HLRN, reliable high-performance computing strategies with *message passing* paradigms (to account for the distributed-memory architecture and massive parallel computing) are indispensable to obtain results within the wall time limit, see Chapter 4.2. Threshold C in Figure 4.2 denotes the ultimate limit at HLRN (12.288 terabyte) which, however, cannot be reached in actual NEGF calculations¹⁹. Instead a memory allocation up to a few terabyte seems realistic.

4.2 Advanced Code Parallelization and Performance

In principle, the performance of the propagation algorithm outlined above can be directly improved by parallelizing all major loops in OpenMP. However, in such an approach, the nonequilibrium

¹⁶These have been available from autumn 2010.

¹⁷OpenMP stands for “Open Multi-Processing”.

¹⁸Computing time at the HLRN has been provided via Grant No. shp0006. For more information on the HLRN system (in German: “Norddeutscher Verbund zur Förderung des Hoch- und Höchstleistungsrechnens”), see <https://www.hlrn.de>.

¹⁹We expect that the algorithm performance will drop considerably when being close to this threshold.

Green function remains defined as a global shared-memory object, and one disregards the main problem in the propagation: the enormous amount of (dynamic) memory which must be provided to account for the non-Markovian structure of the Kadanoff-Baym equations. Thereby, the RAM requirements ($\gtrsim 1$ terabyte) discussed in Chapter 4.1.2 are usually beyond those offered by shared-memory computer architectures. For this reason, we, in this Section, develop a parallel algorithm which, on the one hand, is ready for large-scale distributed-memory computing²⁰ and, on the other hand, ensures an efficient time stepping. To completely avoid often-repeated and expensive accesses to non-local memory, we, in particular, put emphasis on a well-adapted distribution of the memory and exploit the specific structure of the collision integrals analyzed in the previous Section. Doing so leads to an algorithm which operates at minimum communication costs.

Below, the whole discussion on distributed-memory computing is based on the phraseology of the Message Passing Interface (MPI) [GLS99]. Thereby, MPI pursues a different strategy than OpenMP. Here, multiple copies of one and the same program are launched²¹, and the number of program copies defines the total number p of MPI processes (hereinafter also called MPI ranks). Parallelization is achieved by solving independent but synchronized subtasks on each rank, whereby information is exchanged by point-to-point and/or collective communications. The usual identification of a specific MPI process is as follows: The first MPI rank is labeled 0, the second is 1, the third is 2, etc., and the last MPI process (or rank) is $p - 1$.

Although the incorporation of the mixed Green function g^{\uparrow} is straightforward in the algorithm described below, we, for simplicity, focus on the propagation of the correlation functions and assume the system to be prepared initially in the Hartree-Fock state, cf. Eqs. (4.2) and (4.3).

4.2.1 Distribution of Memory

By Figure 4.1 of Chapter 4.1.2, it has been discussed in great detail how the correlation functions $g^>$ and $g^<$ enter the collision integrals, i.e., the right hand sides of the Kadanoff-Baym equations (3.37) and (3.38), cf. the summary of Chapter 3. From the computational point of view, regarding a parallel algorithm with many MPI instances, it is highly advantageous if all Green functions that are required by specific collision integrals $i_1^>$ and $i_2^<$ are directly accessible by the MPI process which is performing these integrals²². In this way, no Green function needs to be communicated between different MPI ranks, and, the collision integrals are readily evaluated.

For precomputed self-energies Σ_{ξ}^{\geq} , such a scheme is realized by a decomposition of the discretized two-time plane $\mathcal{T} = [0, t_f] \times [0, t_f]$ into arrays of different perpendicular blocks [BBB10c]. Depending on the number of MPI processes available, the memory is then distributed such that the nonequilibrium Green function in different domains is attributed to distinct MPI ranks. For the simplest case of $p = 2$ MPI processes, the required decomposition of \mathcal{T} is illustrated in Figure 4.3 (a) and (b), see the blue areas. In general, the desired situation is obtained when the Green function

²⁰A similar algorithm has been developed independently by *M. Garny* and *M.M. Müller*, see Ref. [GM10].

²¹On different compute nodes (i.e., CPUs) with either partly shared or separate RAM.

²²I.e., are available from the RAM of the corresponding compute node.

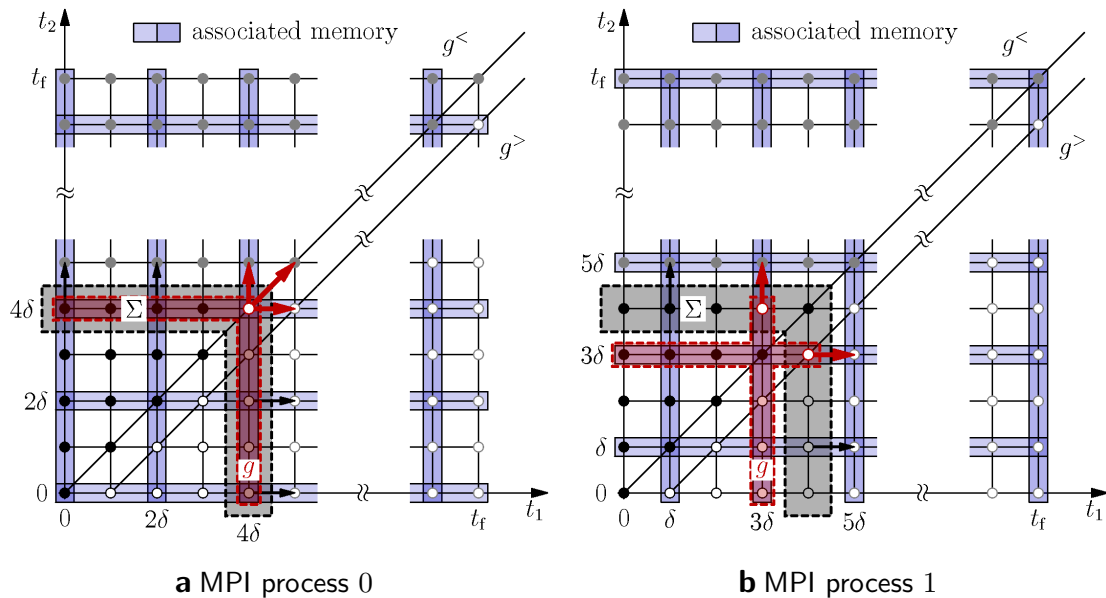


Figure 4.3: Distribution of memory (blue areas in panels (a) and (b)) for the simplest case of two MPI processes ($p=2$) involved in the two-time propagation of the nonequilibrium Green function. For $p > 2$, we arrive at a multicolored chessboard-like pattern which has a "primitive cell" of side length $(p-1)\delta$, cf. Ref. [BBB10c]. As in Figure 4.1, the open (closed) dots in the lower (upper) triangle represent $g^>$ ($g^<$). In the case shown, the final propagation time t_f is an odd multiple of δ . The black and red arrows indicate the propagation of the NEGF from $t_{1,2} = 4\delta$ to 5δ , which requires the self-energies at times $(4\delta, t_n)$ and $(t_n, 4\delta) \forall t_n \in \{0, \delta, 2\delta, 3\delta, 4\delta\}$, see the black-dashed-bordered area. Further, the time steps highlighted (as representative examples) by the red arrows involve the Green functions in the red-dashed-bordered domains which are directly accessible by the attributed MPI process.

at point $(t_m, t_n) \in \mathcal{T}$ is stored in the memory of two MPI processes, labeled r_1 and r_2 , where²³,

$$\begin{aligned} r_1 &= (t_m \delta^{-1}) \bmod p = m \bmod p, \\ r_2 &= (t_n \delta^{-1}) \bmod p = n \bmod p. \end{aligned} \quad (4.12)$$

If the memory is organized blockwise²⁴ according to the overlapping blue black-bordered horizontal and vertical arrays in Figure 4.3 (a) and (b), Eq. (4.12) implies that the entire NEGF is effectively stored twice. This, of course, is a compromise but goes along with essentially reduced communication effort and excellent computational performance and scalability (see below).

To avoid confusion on this issue, we remark that, for $m=n$, the compute nodes r_1 and r_2 are equal (i.e., they refer to the same MPI rank), and, consequently, some memory can be saved on

²³Note that $t_i = i\delta$ where $i \in \mathbb{N}_{\geq 0}$. Further, for $t_m > t_n$ ($t_m \leq t_n$), we refer to $g^>$ ($g^<$).

²⁴Usually, this is advantageous for the evaluation of the collision integrals $i_1^>$ and $i_2^<$, cf. Figures 4.1 and 4.3.

each rank²⁵. However, the associated memory proportion scales as²⁶ $1/p$, and, hence, the specific way of storing the nonequilibrium Green function on the individual nodes becomes less and less important the more MPI processes are being involved in the propagation. Note that, for cluster computations with $p > 32$, the percentage of avoidable duplicate storage is below 2%.

4.2.2 Inter-process Communications; Algorithm Overview

As outlined above, there exists an adequate distribution of memory that allows for a simple parallel-handling of the collision integrals. However, the above discussion has, so far, omitted the self-energies that also enter the collision integrals of Eq. (4.10). For an efficient treatment, it is a good idea to precompute Σ_{ξ}^{\geq} , in parallel, on the individual compute nodes and then to make them known to all other processes by a collective MPI communication, see the black-dashed-bordered areas in Figure 4.3 (a) and (b) and compare them to the local memory domains.

Beyond the self-energies, further communication is due to the single-particle energy $\bar{h}(t)$ which has to be constructed together with the deduced matrices $u_{\delta}(t)$ and $v_{\delta}(t)$, see Appendix B. As this task involves a diagonalization of $\bar{h}(t)$, only a single CPU is charged with this task, and, subsequently, $u_{\delta}(t)$ and $v_{\delta}(t)$ are transferred to all other compute nodes because both quantities are required in \mathcal{P}^x , ($x = >, <, \lceil$) and $\mathcal{P}_{\text{diag}}^<$ of Eqs. (4.6) and (4.7).

Once the self-energies, $u_{\delta}(t)$ and $v_{\delta}(t)$ are available on each MPI rank, the propagation of the nonequilibrium Green function can be carried out in t_1 and t_2 direction, see the black and red arrows in Figure 4.3. To this end, first, $i_1^>(t, \cdot)$ and $i_2^<(\cdot, t)$ are computed on the same CPU and, consequently, $g^>(t + \delta, \cdot)$ and $g^<(\cdot, t + \delta)$ are obtained in sequence but bunched on a single MPI process. Further, the propagation of $g^<$ on the time diagonal is prompted by the MPI process that computes $g^<(t, t + \delta)$. In the last step, all newly calculated data needs to be assigned to local and non-local storage sectors where the latter requires additional MPI communications. From Figure 4.3, it emerges that the destination of this communication is the same compute node for all determined Green functions.

To be specific, we want to give a detailed overview on the algorithm. The notes below indicate the individual steps to be performed, and Figure 4.4 accentuates the data that is exchanged between different compute nodes. When we discretize the time according to $t_n = n\delta$ and consider the case where a number of p MPI processes (ranks or copies of the code) are launched, the algorithm is structured as follows²⁷:

- (i) On each MPI rank (i.e., on process 0 to $p - 1$), set $n = 0$.
- (ii) On rank 0, use the Matsubara Green function of Eq. (4.2) to initialize $g^<(0, 0)$.
- (iii) On each rank, for reference, set $t_n = n\delta$.

²⁵This concerns the overlap of memory blocks at points $(ip+r, jp+r) \in \mathcal{T}$, where $i, j \in \mathbb{N}_{\geq 0}$ and $r \in \{0, 1, \dots, p-1\}$ denotes the MPI rank.

²⁶This, is readily obtained by assuming $t_f \delta^{-1}$ to be divisible by p .

²⁷Note that, for simplicity, we neglect g^{\lceil} and start from the Hartree-Fock Green function, cf. point (ii).

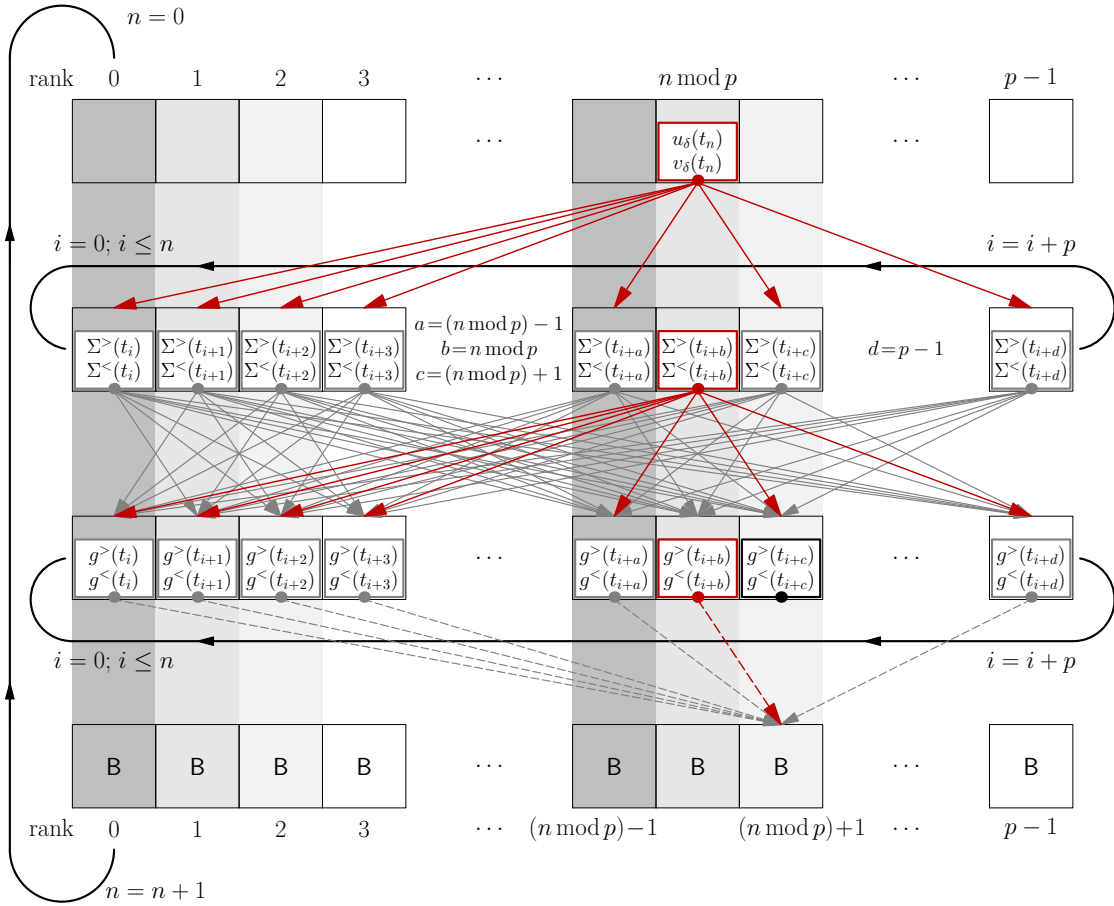


Figure 4.4: Parallelized propagation of the nonequilibrium Green function including a number of p MPI processes and distributed memory (cf. Chapter 4.2.1). Vertically aligned squares are attributed to the same MPI process, and the content of the gray and red boxes indicate the quantities that are computed and communicated. All tasks performed by process $(n \bmod p)$ are highlighted in red. Further, the black box in the third line refers to an internal assignment of the newly computed Green function, cf. point (vi.a) in the algorithm. The gray and red arrows show the direction of communication: Collective communications (implemented via `MPI_Bcast()` [GLS99]) are represented by solid lines, and non-blocking point-to-point communications (realized via `MPI_Isend()` and `MPI_IRecv()`) are given by dashed lines. Synchronization after the non-blocking communications is ensured by MPI barriers (`MPI_Barrier()`), see labels B. Note that, besides the main propagation loop (variable n), there appear internal loops (variable i) when n becomes larger than the number of processes available. If $n > p$, at least one MPI rank has to propagate more than one pair of correlation functions ($g^>$, $g^<$). Short notations: $\Sigma^>(t_i) = \Sigma_{\xi}^>(t_n, t_i)$, $\Sigma^<(t_i) = \Sigma_{\xi}^<(t_i, t_n)$, $g^>(t_i) = g^>(t_{n+1}, t_i)$, and $g^<(t_i) = g^<(t_i, t_{n+1})$. The lesser correlation function on the time diagonal, $g^<(t_{n+1}, t_{n+1})$, is treated together with $g^<(t_n, t_{n+1})$, compare with point (vi.a).

-
- (iv.a) On MPI rank $(n \bmod p)$, compute and diagonalize the Hartree-Fock energy $\bar{h}(t_n) = h(t_n) + \Sigma_{\xi}^{\text{HF}}[g^{\lessdot}, \tilde{u}](t_n)$. Using the eigenvalues and eigenvectors of $\bar{h}(t_n)$, calculate the matrices $u_{\delta}(t_n)$ and $v_{\delta}(t_n)$ according to Eq. (B.4) in Appendix B. Further, initiate a broadcast of $u_{\delta}(t_n)$ and $v_{\delta}(t_n)$ to all other MPI processes.
 - (iv.b) On each MPI rank except $(n \bmod p)$ receive $u_{\delta}(t_n)$ and $v_{\delta}(t_n)$.
 - (v.a) On the MPI ranks $(i \bmod p)$ for all $i \leq n$, compute the self-energies $\Sigma_{\xi}^{\gtrdot}(t_n, t_i)$ and $\Sigma_{\xi}^{\lessdot}(t_i, t_n)$. For each calculated self-energy Σ_{ξ} , initiate a broadcast and to all other processes.
 - (v.b) On each MPI rank $j \neq (i \bmod p)$ for all $i \leq n$, receive the self-energies $\Sigma_{\xi}^{\gtrdot}(t_n, t_i)$ and $\Sigma_{\xi}^{\lessdot}(t_i, t_n)$.
 - (vi.a) On each MPI rank $(i \bmod p)$ for all $i \leq n$, first, perform the collision integrals $i_1^{\gtrdot}(t_n, t_i)$ and $i_2^{\lessdot}(t_i, t_n)$ and, secondly, compute the new Green function $g^{\gtrdot}(t_{n+1}, t_i)$ and $g^{\lessdot}(t_i, t_{n+1})$ using Eq. (B.2). Thereby, MPI rank $(n \bmod p)$ also generates the new Green function on the time diagonal, i.e., $g^{\lessdot}(t_{n+1}, t_{n+1})$. Further, on each rank, that is involved, initiate a send of the computed Green functions to rank $((n+1) \bmod p)$ and store the Green functions in the local memory. Note that, thereby, process $((n+1) \bmod p)$ does not need to communicate, and that rank $(n \bmod p)$ has to transfer also the new time-diagonal Green functions.
 - (vi.b) On MPI rank $(n+1) \bmod p$, receive all the Green functions sent in step (vi.a).
 - (vii) As MPI rank $(n \bmod p)$ has knowledge of the time-diagonal collision integrals which enter the definition of the correlation energy (cf. Eq. (5.6)), it is responsible for computing all necessary observables.
 - (viii) Finally, on each rank, wait for all point-to-point communications to be completed (see the labels B in Figure 4.4), and, with n incremented by one, return to (iii).

Finally, in order to resume the propagation of the NEGF beyond the wall time limit of the batch-job system, we optionally allow each MPI rank to backup its data in binary format. However, we note, that the amount of data to be stored on the file system becomes very large for progressed time-evolution. This slows down the algorithm considerably and, particularly, consumes large resources on reinitialization.

4.2.3 Performance Tests

The implementation of the MPI-parallelized distributed-memory algorithm outlined in the previous Section has been intensively tested with varying numbers of processes and, in addition, has been compared to the serial implementation of Eqs. (4.6) and (4.7) (cf. also Appendix B) to ensure that exactly the same results are obtained. Thereby, it turned out that the overhead due to MPI communications and synchronizations is small and that an efficient propagation of the two-time nonequilibrium Green function is achieved.

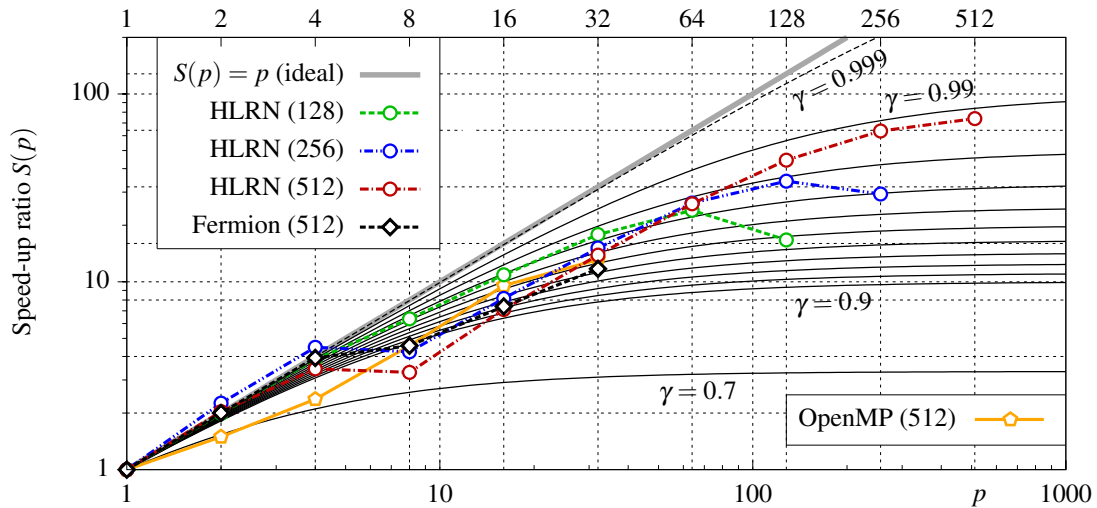


Figure 4.5: MPI-code performance: Speed-up ratio $S(p) = T_1/T_p$ as function of the number of processes p involved in the parallel algorithm of Chapter 4.2.2. As test system, we have considered the one-dimensional helium atom (cf. Part III of this thesis) including $n_b = 23$ FE-DVR basis functions. In the legend, the numbers in round brackets denote the number of time steps that are propagated using the HLRN batch system (green, blue and red curves) and the "Fermion" cluster (black). While the shortest HLRN-calculation has been performed by the "xe" nodes, the other calculations have been carried out by the "ice1" nodes. Further, the performance drop between $p = 4$ and 8 is caused by internal architecture differences. The thin black solid lines indicate a degree of parallelization between 90 and 99% (in steps of 1%) according to Amdahl's law $S_\gamma(p)$, cf. Eq. (4.13). For comparison, the yellow solid curve shows the performance of the shared-memory code that has been parallelized on the basis of OpenMP.

Figure 4.5 shows the result of systematic performance tests that are based on the propagation of the NEGF for the one-dimensional helium atom, see Chapter 5 and 6. To this end, runs of different temporal length (i.e., with a different number of total time steps at fixed $\delta = 0.025 \tau_0$) were performed on the "Fermion" cluster²⁸ and on the "xe" ("ice1") nodes at HLRN including up to 512 MPI processes. For details on the compute nodes, see the caption of Figure 4.2.

The degree of parallelization is measured in terms of the speed-up ratio $S(p) = T_1/T_p$, which compares the total computing (or run-) time T_p of a parallel program execution including p MPI ranks to the runtime T_1 consumed by the serial run ($p = 1$). For the performance tests displayed, the restriction to a relatively small number of FE-DVR basis functions ($n_b = 23$) is explained by the fact that the serial run had to complete within the time interval defined by the default wall time (12 h) of the HLRN batch system.

In the double logarithmic plot of Figure 4.5, the ideal speed-up is denoted by the gray straight

²⁸Here, for a MPI job, the maximum number of accessible CPUs is $p = 32$.

line. Regarding the test calculations, we observe, that the speed-up ratio is relatively close to the ideal case in all cases (see, also, the average gradient of the curves). Further, $S(p)$ does, generally, not collapse for large p , although the algorithm has the tendency to become inefficient if the number of propagated time steps equals the number of used processes, cf. the slight drop off in $S(p)$ at $p=128$ and 256 . However, this effect is reduced the more MPI ranks are involved, cf. the red curve in Figure 4.5. In addition, we note that the performance drop between 4 and 8 processes on the "Fermion" and "ice1" nodes²⁹ occurs for internal architectural reasons leading to changes in the program execution when more than 4 CPUs are being included. Thus, actually, some care needs to be taken when comparing T_1 and T_p with $p > 4$ in the speed-up ratio, and, eventually, the scaling is even better as indicated by the curves in Figure 4.5.

Moreover, Figure 4.5 compares the measured scalability to that of a simple speed-up predictor in parallel computing, Amdahl's law [HJS00] (see the thin black lines):

$$S_\gamma(p) = [(1 - \gamma) + \gamma/p]^{-1}, \quad (4.13)$$

where $\gamma \in [0, 1]$. Deviations from the ideal scaling ($S_1(p) = p$) are obtained through $\gamma < 1$, and the sequential fraction of the program is identified as $1 - \gamma$. From the Figure, we see that on both considered machines, our parallel code achieves good performance with a typical degree of parallelization of more than 95% ($\gamma > 0.95$). Hence, constituting less than 5%, the serial fraction of the code is pretty small.

Finally, the yellow solid curve in Figure 4.5, displays the speed-up ratio for the OpenMP-parallelized code mentioned in Chapter 4.1.2. Although this code reveals an equally good performance, it is very limited in application because it requires shared-memory architecture.

4.3 The Generalized Kadanoff-Baym (GKB) Ansatz

As practically all necessary information on the described quantum many-body system is contained in the one-particle density matrix $\rho^{(1)}(t) = -i g^<(t, t)$, it would computationally be highly advantageous if one only needs to propagate the lesser correlation function in the direction of the time diagonal $t_1 = t_2$, cf. Figure 4.3. Of course, in the time-local Hartree-Fock approximation, this is directly possible as the system's time evolution is Markovian ($i_{\text{diag}}^<(t, t) \equiv 0$ in Eq. (4.7)). However, when correlations are being included, such an approach is inhibited due to retardation, i.e., memory effects which explicitly require a non-Markovian treatment. Then, in Eq. (4.7), we have to incorporate the full collision integral $i_{\text{diag}}^<(t, t)$ which, neglecting initial correlations ($g^{\lceil} = g^{\lceil} = 0$ in Eq. (4.10)), reads,

$$i_{\text{diag}}^<[g, \tilde{u}](t, t) = \int_0^t d\bar{t} \left(\Sigma_\xi^>(t, \bar{t}) g^<(\bar{t}, t) - \Sigma_\xi^<(t, \bar{t}) g^>(\bar{t}, t) \right. \\ \left. + g^<(t, \bar{t}) \Sigma_\xi^>(\bar{t}, t) - g^>(t, \bar{t}) \Sigma_\xi^<(\bar{t}, t) \right), \quad (4.14)$$

²⁹Note that this behavior is not present for computations on the "xe" nodes at HLRN.

and includes many off-time-diagonal Green functions either directly or indirectly via $\Sigma_{\xi}^{\geq}(t, \cdot) = \Sigma_{\xi}^{\geq}[g, \tilde{u}](t, \cdot)$ and $\Sigma_{\xi}^{\leq}(\cdot, t) = \Sigma_{\xi}^{\leq}[g, \tilde{u}](\cdot, t)$. Usually, the collision term $i_{\text{diag}}^{\leq}(t, t)$ cannot be simplified any further. In particular, the introduction of a finite memory depth [BKS⁺96, VKŠ06] is inapplicable for the atomic and molecular systems under investigation in Part III of this thesis³⁰.

Nevertheless, from the perspective of theory, Eq. (4.14) can be simplified by additional approximations. The idea behind such a simplification is based on the fact that there exists an exact relation between the two-time correlation functions g^{\geq} and the single-time phase-space distribution function (or one-particle density matrix $\rho^{(1)}(t)$). Hence, in a procedure, the basis of which is similar to the Hohenberg-Kohn theorem [HK64] (which proves the existence of an unambiguous relation between the system's density and its many-body wave function), two-time Green functions at $t \neq t'$ can be reconstructed from their values on the time diagonal ($t = t'$).

The simplest form of such a reconstruction has found its way into the literature as the generalized Kadanoff-Baym (GKB) ansatz and is based on the pioneering work of *P. Lipavský, V. Špička* and *B. Velický*, see Ref. [LŠV86]. The GKB ansatz extends the common (or original) Kadanoff-Baym ansatz to arbitrary nonequilibrium situations. With f being the Wigner (distribution) function, the common Kadanoff-Baym ansatz reads [KB62, ŠVK05a],

$$g^{\leq}(t, t') \approx f((t+t')/2) \left(g^{\text{A}}(t, t') - g^{\text{R}}(t, t') \right), \quad (4.15)$$

where g^{R} and g^{A} are the retarded and advanced Green functions, cf. Eq. (2.39). Thereby, the applicability of Eq. (4.15) is limited to the quasi-particle picture and (temporally as well as spatially) slowly varying external perturbations [KB62].

Extending Eq. (4.15), the GKB ansatz³¹ is given by [BE00, BSE06],

$$\begin{aligned} g^{\geq}(t, t') &\approx \pm \left(g^{\text{R}}(t, t') \rho_{\geq}^{(1)}(t') - \rho_{\geq}^{(1)}(t) g^{\text{A}}(t, t') \right), \\ \rho_{\geq}^{(1)}(t) &= \pm i g^{\geq}(t, t) = 1 \pm i g^{\leq}(t, t), \end{aligned} \quad (4.16)$$

where $\rho_{\geq}^{(1)}(t)$ may be understood as a generalization of the one-particle density matrix.

Since its emergence, the generalized Kadanoff-Baym ansatz has been widely used in the generation of transport equations [HJ96, ŠVK05b, ŠVK05c, VKŠ06]. These are non-Markovian (quantum) kinetic equations for one-time quantities such as the Wigner function mentioned above. Moreover, including comparisons to full two-time calculations, the GKB ansatz has been tested, e.g., on interband Kadanoff-Baym equations for optically excited electron-hole plasmas [KBBK98], whereby also electron-phonon coupling has been taken into account [GBH99]. Concerning its application on the dynamics of small and spatially inhomogeneous systems, we emphasize that there is, so far, very little experience.

The generalized Kadanoff-Baym ansatz in form of Eq. (4.16) can be motivated and derived in different ways, see, e.g., Refs. [LŠV86, ŠVK05a]. To call for a causal time structure in the (acausal)

³⁰This is due to slow relaxations. Hence, even for large memory depths, energy conservation is heavily violated.

³¹Note that the GKB ansatz is sometimes also called the Lipavský ansatz, see, e.g., Ref. [Bon98], to emphasize the original publication. Moreover, slightly different expressions than Eq. (4.16) exist which differ in the prefactor convention of the one-particle nonequilibrium Green function [ŠVK05a].

original ansatz (4.15) thereby represents the most intuitive approach. More formally, Eq. (4.16) is obtained as the leading term in an iterative reconstruction process of the two-time correlation functions, for details see Ref. [LŠV86]. From this fact, it follows that the GKB ansatz is already approximate from the beginning. Nevertheless, it is in agreement with the conservation of density (particle number), energy and momentum.

Furthermore, we see from the definition, that the generalized Kadanoff-Baym ansatz depends on two propagators—the retarded and advanced Green functions. These have to be specified when making practical use of the ansatz. Principally, g^R and g^A obey similarly complex equations of motion as the correlation functions. Thus, application of the GKB ansatz is not possible with g^R and g^A on the same level of perturbation theory. Usually, one neglects all binary interactions and uses $g^{R/A}$ of the ideal (i.e., noninteracting) system as reference. In our approach, we will consider the retarded and advanced Green function in mean-field (Hartree-Fock) approximation. To this end, the time-dependent single-particle energy $\bar{h}(t) = h(t) + \Sigma_\xi^{\text{HF}}[g^<, \tilde{u}](t)$ is consistently taken into account in the construction of g^R and g^A (see below and Appendix C).

In conclusion, under the usage of the generalized Kadanoff Baym ansatz (4.16), the time-stepping procedure for the NEGF reduces to,

$$g^<(t + \delta, t + \delta) = \mathcal{P}_{\text{diag}}^< \left\{ g^<(t, t), \bar{h}[g^<, \tilde{u}](t), i_{\text{diag}}^<[g, \tilde{u}](t, t) \right\}, \quad (4.17)$$

where,

$$i_{\text{diag}}^<[g, \tilde{u}](t, t) \approx i_{\text{diag}}^<[g^{\geq}, g^R, g^A, \tilde{u}](t, t). \quad (4.18)$$

Thereby, on the right hand side of Eq. (4.18), the lesser and greater correlation functions g^{\geq} enter with equal time arguments, and the retarded and advanced Green functions, g^R and g^A , obey the following equations of motion (matrix notation is implied, and $a(t, t')$ denotes the corresponding spectral function $a(t, t') = i[g^>(t, t') - g^<(t, t')]$),

$$\left(i \frac{\partial}{\partial t} - \bar{h}(t) \right) g^{R/A}(t, t') = \delta(t - t') a(t, t'), \quad (4.19)$$

+ adjoint equation with $t \leftrightarrow t'$,

where the single-particle energy $\bar{h}(t)$ is defined outside of Eq. (4.19).

Details of the algorithm are compiled in Appendix C.

4.4 Summary

While the previous Chapter has focused on an advantageous and flexible grid-based representation of the NEGF using complementary features of the FE and DVR method, with this Chapter, we have laid the foundations for an efficient two-time propagation of the nonequilibrium Green function in the presence of external fields. Taken together, both strategies should facilitate more extended NEGF calculations on (strongly) inhomogeneous systems beyond the (time-local) Hartree-Fock

approximation—to demonstrate this *inter alia* for model atoms and molecules is the goal of Part III of this thesis.

Being based on a highly adapted distribution of memory over all compute nodes, the parallel algorithm developed in Chapter 4.2 permits the management of large computational resources. Thereby, the performance tests on the batch-job system of the North-German Supercomputing Alliance (HLRN) have shown that large cluster computations at a high degree of parallelization are possible. Note that the HLRN holds rank 77 and 78 (63 and 64) according to the June 2011 (November 2010) top 500 list of supercomputer sites³².

Beyond the realization of an efficient two-time propagation, we, in Chapter 4.3, have outlined the opportunity for NEGF calculations with drastically reduced computational effort. To this end, the off-time-diagonal Green functions are approximately reconstructed from their values on the time diagonal in terms of the generalized Kadanoff-Baym (GKB) ansatz, cf. Eq. (4.16). This method should enable larger simulations regarding, both, basis size and length. To present first GKB results and to assess their quality with regard to the description of correlation effects is one of the objectives of Chapter 6. With correlations treated in the second Born approximation, the GKB ansatz will be compared, on the one hand, to the Hartree-Fock approximation and, on the other hand, to full two-time NEGF and exact calculations.

³²See <http://www.top500.org> for the LINPACK benchmarking of supercomputers.

PART III

**Application to
Model Atoms and Molecules**

Model Description of Atoms and Molecules

”We will adopt the restriction that the electrons move along only one axis. The atom that results from this restriction to one dimension is only a shadow of real helium ... and cannot be expected to substitute for helium in any respect that involves more than one dimension—all questions regarding angular momentum, angular correlations, light polarization other than linear, etc., are out of range.” (Quotation from Ref. [HGE94]).

5.1 Introduction

Of course, the modeling of atomic (and, consequently, molecular) systems in reduced dimensionality leaves out the complex structure of our three-dimensional world, that indeed manifests itself quantum mechanically in the presence of the system’s angular momentum and its coupling to many other degrees of freedom. Hence, the level of abstraction is drastic and applications may be limited. However, precisely the arising simplicity thereof—not only with regard to historically restricted numerical scope—has provided the foundation for the success of one-dimensional models.

It all started with the publication of a thorough study of the hydrogen atom in one spatial dimension, Ref. [Lou59], including *hard* ($|r|^{-1}$), *soft* (rounded-off) and truncated Coulomb potentials. The corresponding single-electron Schrödinger equations are analytically solvable and exemplify that degeneracy may exist in one-dimensional systems, see Ref. [XDD97]. Later, many authors (e.g., Refs. [SEJ90, RKB91, SF94] and references given therein) have performed simulations on ionization and photoelectron spectra, numerically integrating the time-dependent Schrödinger equation. Thereby, the model H-atom turned out to be an ideal tool for studying a number of phenomena and applications.

Soon thereafter, the idea was also recognized for two-electron systems. In a series of early papers [JES88, PGB91, GE92, GE92, GE93, RTW93, HGE94, LCdAOdA96], the one-dimensional (1D) helium atom has been explored for its static and dynamic properties applying exact¹, approximate

¹Propagating the time-dependent Schrödinger equations on a two-dimensional lattice.

(e.g., TDHF) and semiclassical methods, for a detailed overview see Ref. [TRR00]. These investigations led to a solid understanding of the bound and continuum structure, identifying Rydberg series of singly excited states as well as series of autoionizing resonances—doubly excited states that can decay and lead to asymmetric line shapes as explained by *U. Fano* [Fan61]. Moreover, the mechanisms of different ionization processes have been analyzed in the strong-field regime (cf. Section 5.2.2 and Chapter 6). Overall, due to the presence of many features of the true helium atom, quite reliable qualitative results have been obtained in the one-dimensional context.

With a focus on laser fields and pulses, 1D helium has been further used to investigate rescattering and nonsequential ionization processes, e.g., Ref. [Bau97]. Beyond the fixed-nuclei (adiabatic or Born-Oppenheimer [SO96]) approximation², also ion recoil-momentum distributions have been calculated [LGE00]. Since then, the 1D helium atom has been revisited, e.g., within the time-dependent extended Hartree-Fock approximation [DvL01], or with the intention to derive and test improved exchange-correlation functionals in (time-dependent) density functional theory (DFT), see Refs. [RB09b, RB09a]. Today, the 1D helium model is still actively used, e.g., Ref. [CRB10], and serves as a "testing ground" for multi-electron calculations [ZKBS04, HBB10].

Finally, the success of the 1D two-electron model stimulated the description of molecules on a similar footing. There exist a number of intense-field applications to the hydrogenic molecules H_2 and H_3 as well as their positive ions in one dimension including soft-Coulomb [YZB96, KKB01, SKY07] and contact (δ -function) interaction [Lap81]. Again, also semiclassical studies [LC08] have been performed which, together with a semiclassical quantization [Gut90], have singled out periodic orbits that help to understand the chemical bond. In addition, the H_2 model has been coupled to quantized photon fields [NY00]. Recently, the hydrogen molecule (and its ion) drew particular interest in the field of attosecond physics exploring, e.g., Bohmian quantum trajectories [TB11]. More complex 1D systems have been subject to time-dependent multiconfiguration Hartree-Fock techniques [ZKF⁺03, CZK⁺05] (focusing on correlation effects in the ionization of molecular atom chains with several active electrons) and to DFT [TMM09] (revisiting the dissociation of monohydrides, examples of heteronuclear molecules).

Certainly, the author is aware of the fact that, during the recent decade, the theoretical investigation of field-matter interaction is more and more concerned with full three-dimensional calculations (e.g., [VS10]) and their comparison to experiment (see Refs. [BK00, KI09], to name only two reviews with regard to intense and ultra-short fields). However, as long as the explicit three-dimensional information is dispensable, few-electron models including even simpler potentials than that of 1D helium (as simple as the box potential, see Ref. [BBB10d]³) are able to give insight into topics of current interest. Often, such an approach goes along with some (severe) conceptual and/or computational advantages such as simplifying the problem of defining single and double ionization yields. On top of that, one-dimensional models may rapidly reveal the basic

²Due to the large mass difference between nuclei and electrons ($m_n/m_e > 1836$), the nucleus can be seen as infinitely heavy such that electronic and nuclear wave function can be separated.

³This work illuminates the influence of electron-electron correlations on the double ionization in a typical attosecond xuv-infrared pump-probe experiment.

influence of new field parameters (leading, eventually, to novel field effects) probing the electron dynamics triggered, e.g., by attosecond pulses [BS02] or by laser pulses with chirp Ref. [XNG09].

The objective of the present work is not to contribute to the understanding of multi-electron systems or to reveal even new physical findings. Instead, as a proof of principle, we demonstrate and examine the applicability of the two-time nonequilibrium Green function framework by reference to model atoms and molecules using a grid-based FE-DVR approach which allows for an efficient solution of the two-time Kadanoff-Baym equations. Furthermore, our results for the ground state and dynamic properties cannot be exact as the method of NEGFs is based on a systematic but approximate introduction of electronic correlations. However, in the long term perspective, the use of NEGFs may surpass other approaches with respect to the number of treatable electrons.

5.2 Model Hamiltonian for Atoms and Molecules; Observables

Generally, we are interested in the time-dependent, correlated motion of electrons in atoms or molecules including external electromagnetic fields which themselves can be treated classically.

The field-electron interaction is described by ($\hat{p}_i = -i\nabla_i$ is the momentum of electron i),

$$\hat{t}_i^{(1)} + \hat{v}_i^{(1,\text{field})} = \frac{1}{2} \left(\hat{p}_i + \frac{1}{c} \vec{A}_i(t) \right)^2 - \phi_i(t), \quad [\hat{p}_i, \vec{A}_i(t)]_- \neq 0, \quad (5.1)$$

where $\vec{A}_i(t) = \vec{A}(\vec{r}_i, t)$ is the vector potential and $\phi_i(t) = \phi(\vec{r}_i, t)$ denotes a scalar potential. Since the electric and magnetic fields (\vec{E} and \vec{B}) are invariant with respect to a gauge transformation⁴, one can work with different gauges in Eq. (5.1). The two most common ones are the length (field or longitudinal) gauge and the velocity (Coulomb, radiation or transversal) gauge.

In the electric-dipole approximation (EDA)⁵, the vector potential $\vec{A}_i(t) = \vec{A}(t)$ becomes independent of \vec{r}_i such that \hat{p}_i and $\vec{A}_i(t)$ commute (cf. Eq. (5.1)). Using the length gauge (i.e., applying the gauge function $\Lambda(\vec{r}, t) = -\vec{A}(t) \cdot \vec{r}_i$ in Eq. (5.1) and taking $\phi'_i = 0$, see footnote 4), we have,

$$\hat{t}_i^{(1)} + \hat{v}_i^{(1,\text{field})} = \frac{1}{2} \hat{p}_i^2 - \frac{\partial}{\partial t} \vec{A}(t) \cdot \vec{r}_i, \quad (5.2)$$

where the electric field is given by $\vec{E}(t) = -\frac{\partial}{\partial t} \vec{A}(t)$. The first term in Eq. (5.2) is the usual kinetic energy of electron i whereas the second term is responsible for the coupling to the field. In the (reduced⁶) velocity gauge one would obtain the second term as $-i\vec{A}(t) \cdot \nabla$.

Considering the external dipole-field $\vec{E}(t)$ linearly polarized along the x -direction, the Hamiltonian of the one-dimensional fixed-nuclei models for atoms and molecules reads in first quanti-

⁴I.e., with respect to the transformations $\vec{A}'_i = \vec{A}_i + \nabla \Lambda_i$ and $\phi'_i = \phi_i - \frac{1}{c} \frac{\partial}{\partial t} \Lambda_i$, where the gauge function $\Lambda_i = \Lambda(\vec{r}_i, t)$ is an arbitrary scalar.

⁵Assuming a field-matter interaction region of the order of $1 a_0$, the electric-dipole approximation is valid for photon energies (in atomic units) $\omega/c \ll 1$ or $\omega \ll 137$ (in atomic units). Hence, the EDA entirely captures the regime of visible light and continues to be applicable up to the uv (and soft xuv) regime.

⁶Neglecting the term which is quadratic in the vector potential.

zation (EDA, length gauge),

$$\begin{aligned}\hat{H}(t) &= \hat{H}^{(1)}(t) + \hat{H}^{(2)} \\ &= \sum_{i=1}^{N_e} \left(\hat{t}_i^{(1)} + \hat{v}_i^{(1,\text{field})}(t) + \hat{v}_i^{(1,\text{system})} \right) + \sum_{1 \leq i < j}^{N_e} \hat{h}_{ij}^{(2)},\end{aligned}\quad (5.3)$$

with (in atomic units),

$$\begin{aligned}\hat{t}_i^{(1)} &= -\frac{1}{2} \frac{\partial^2}{\partial x_i^2}, \\ \hat{v}_i^{(1,\text{field})}(t) &= E(t) x_i, \\ \hat{v}_i^{(1,\text{system})} &= -\sum_{n=1}^{N_n} \frac{Z_n}{\sqrt{(x_i - y_n)^2 + c_n}}, \\ \hat{h}_{ij}^{(2)} &= \frac{1}{\sqrt{(x_i - x_j)^2 + c}}.\end{aligned}\quad (5.4)$$

Here, x_i denotes the position of the i -th electron, $i \in \{1, \dots, N_e\}$, and the locations of the nuclei of atomic number (charge) Z_n are given by y_n with $n \in \{1, \dots, N_n\}$. If $N_n > 1$, the molecular bond lengths (the distances between nuclei m and n) are $d_b^{mn} = |y_n - y_m|$, $n \neq m \in \{1, \dots, N_n\}$. The parameters $c > 0$ (concerning the electron-electron interaction) and $c_n > 0$ (attributed to the nuclei) regularize the respective Coulomb potentials, see Section 5.2.1.

In the following, we want to denote the electronic ground state energy $\langle \hat{H}_{\text{gs}} \rangle$. Further, for molecules ($N_n > 1$), the binding energy $\langle \hat{H}_{\text{b}} \rangle$ is the sum of $\langle \hat{H}_{\text{gs}} \rangle$ and all unregularized nucleus-nucleus interactions,

$$\langle \hat{H}_{\text{b}} \rangle = \langle \hat{H}_{\text{gs}} \rangle + \sum_{1 \leq m < n}^{N_n} \frac{Z_m Z_n}{d_b^{mn}}. \quad (5.5)$$

The molecular ground state is characterized by the minimum binding energy with respect to variation of the nuclear geometry, i.e., $\langle \hat{H}_{\text{b}}^{\text{gs}} \rangle = \min_{d_b^{mn} \in \mathbb{R}} \langle \hat{H}_{\text{b}} \rangle$.

The general expression for the system's total energy is $\langle \hat{H} \rangle(t) = \langle \hat{h}^{(1)} \rangle(t) + \langle \hat{h}_{\text{hf}}^{(2)} \rangle(t) + \langle \hat{h}_{\text{corr}}^{(2)} \rangle(t)$, where, using the nonequilibrium Green function in FE-DVR representation, the one-particle energy, the Hartree-Fock energy and the correlation energy are given by⁷,

$$\begin{aligned}\langle \hat{h}^{(1)} \rangle(t) &= -i \xi \text{Tr}[\hat{h}^{(1)}(t) g^<(t, t)] = -i \xi \sum_{i_1 m_1} \sum_{i_2 m_2} \hat{h}_{m_1 m_2}^{(1), i_1 i_2}(t) g_{m_2 m_1}^{<, i_2 i_1}(t, t), \\ \langle \hat{h}_{\text{hf}}^{(2)} \rangle(t) &= -\frac{i \xi}{2} \text{Tr}[\Sigma_{\xi}^{\text{HF}}(t) g^<(t, t)], \\ \langle \hat{h}_{\text{corr}}^{(2)} \rangle(t) &= -\frac{i \xi}{2} \text{Tr}[i_1^>(t, t)].\end{aligned}\quad (5.6)$$

⁷ $\xi \in \{1, 2\}$ denotes the spin degeneracy factor.

The initial equilibrium ground state energy $\langle \hat{H}_{\text{gs}} \rangle$ is obtained by replacing the lesser (and greater) correlation functions in Eq. (5.6) by the Matsubara Green function $i g^M(0^-)$, cf. Eq. (2.38), and considering the limit $\beta \rightarrow \infty$ which is well satisfied for $\beta E_h \gg 1$. In particular, the collision integral term then reduces to (implicating the second Born approximation and the transformation rule of Eq. (2.25)),

$$\langle \hat{h}_{\text{corr}}^{(2)} \rangle = \sum_{i_1 m_1} \sum_{i_2 m_2} \int_0^\beta d\tau \Sigma_{\xi, m_1 m_2}^{2\text{ndB}, i_1 i_2}(-\tau) g_{m_2 m_1}^{M, i_2 i_1}(\tau). \quad (5.7)$$

For completeness, we also give the definition of the density and related quantities in terms of the NEGF. The one-electron density⁸ is computed according to,

$$\langle \hat{n}^{(1)} \rangle(x, t) = -i g^<(xt, xt) = -i \sum_{i_1 i_2} \sum_{m_1 m_2} \chi_{m_1}^{i_1}(x) \chi_{m_2}^{i_2}(x) g_{m_1 m_2}^{<, i_1 i_2}(t, t). \quad (5.8)$$

Again, the equilibrium ground state density follows from the insertion of the Matsubara Green function. The total number of electrons is $\langle \hat{N}_e \rangle(t) = \xi \int dx \langle \hat{n}^{(1)} \rangle(x, t) = -i \xi \sum_{i_1 m_1} g_{m_1 m_1}^{<, i_1 i_1}(t, t)$, which is the trace over the one-particle density matrix $\rho_{m_1 m_2}^{(1), i_1 i_2}(t) = -i g_{m_1 m_2}^{<, i_1 i_2}(t, t)$ times the spin degeneracy factor. The time-dependent dipole moment (being in atomic units equal to the average electron position) is given by,

$$\begin{aligned} \langle \hat{d}^{(1)} \rangle(t) &= -i \text{Tr}[\hat{x}^{(1)} g^<(t, t)] = -i \sum_{i_1 i_2} \sum_{m_1 m_2} \hat{x}_{m_1 m_2}^{(1), i_1 i_2} g_{m_2 m_1}^{<, i_2 i_1}(t, t), \quad (5.9) \\ \hat{x}_{m_1 m_2}^{(1), i_1 i_2} &= \int_0^{x_0} dx \chi_{m_1}^{i_1}(x) x \chi_{m_2}^{i_2}(x) \propto \delta_{m_1 m_2}^{i_1 i_2}. \end{aligned}$$

The explicit matrix elements of the operator $\hat{x}^{(1)}$ are obtained as a special case of Eq. (3.20) ($\hat{v}^{(1)}(x, t) = x$). Moreover, the evolution of the dipole moment is closely related to the field-induced (dynamic) polarizability α [Buc67],

$$\begin{aligned} \langle \hat{d}^{(1)} \rangle(t) &= \langle \hat{d}_0^{(1)} \rangle + \frac{1}{2} \alpha(t) E(t) + \dots, \quad (5.10) \\ \alpha(\omega) &= 2 \int_{-\infty}^{+\infty} dt \frac{[\langle \hat{d}^{(1)} \rangle(t) - \langle \hat{d}_0^{(1)} \rangle] e^{i\omega t}}{E(t)}, \end{aligned}$$

where, in the first line, $\langle \hat{d}_0^{(1)} \rangle$ denotes the permanent dipole moment and terms higher than first-order in the electric field (i.e., hyperpolarizabilities) have been neglected.

5.2.1 General Remarks

The model Hamiltonian of Eqs. (5.3) and (5.4) involves a number of parameters. While the particle numbers ($N_{e,n}$) and atomic numbers (Z_n) are generally predefined by the system of interest (e.g., $N_e = Z_1 = 2$ and $N_n = 1$ for 1D helium), the values for y_n , c_n and c have to be motivated.

⁸Being normalized to N_e/ξ .

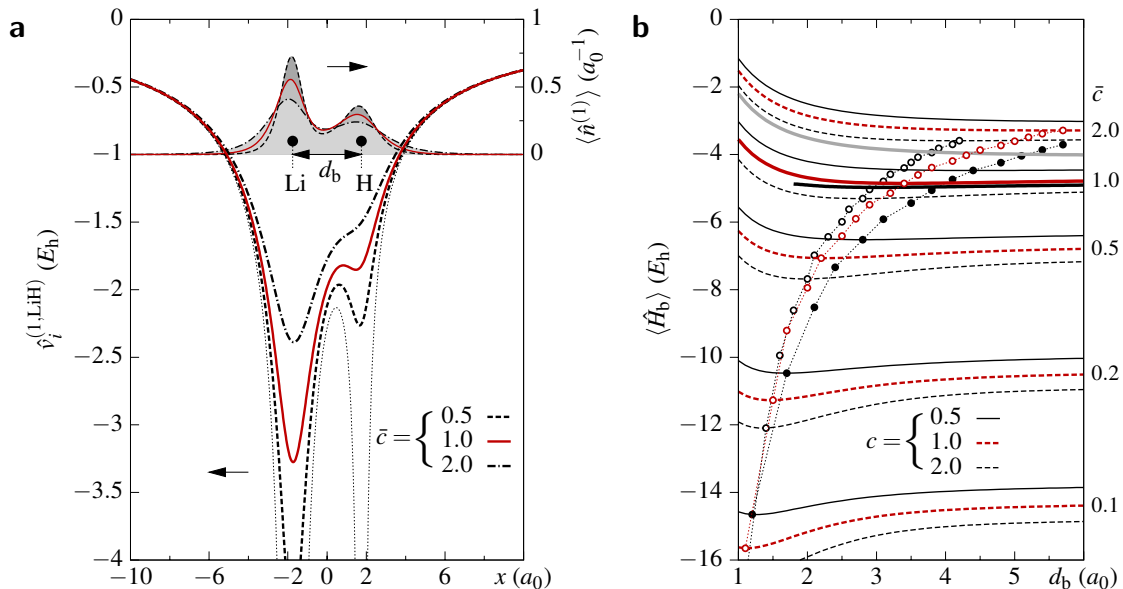


Figure 5.1: Heteronuclear molecule lithium hydride (LiH) modeled in one dimension. (a) One-electron potential $\hat{v}_i^{(1,\text{LiH})}$ for three different values of the regularization parameter $\bar{c} = c_1 = c_2$, see Eq. (5.4), and corresponding one-electron density $\langle \hat{n}^{(1)} \rangle(x)$ in Hartree-Fock approximation (singlet state). The bond length is fixed to $d_b = 3.5 a_0$. The dotted line refers to the pure Coulomb potential. (b) Influence of the regularization parameters \bar{c} and c on the binding energy $\langle \hat{H}_b \rangle$ as function of the bond length d_b (Hartree-Fock approximation). From bottom to top, \bar{c} (in a_0) is increased from 0.1 via 0.2, 0.5 and 1.0 to 2.0. The solid red line (with minimum $\langle \hat{H}_b \rangle$ at about $d_b = 3.5 a_0$) denotes the case $\bar{c} = c = 1$. The corresponding quintet state (represented by the gray line; cf. Table 3.1) has non-binding character. Further, the solid black (thick) line indicates the binding energy curve for the true LiH molecule [JKC06]. The connected dots mark the minima in the binding energy curves for \bar{c} -values of 0.1 to 2.0 in steps of 0.1.

For atoms, obviously, y_1 is irrelevant as long as the atomic extension in equilibrium and nonequilibrium is well covered by the simulation box $[0, x_0]$, cf. Section 3.2. For molecules⁹, the distances of the nuclei positions y_1, \dots, y_{N_n} define the bond lengths which themselves depend on the electronic structure. Thus, the relative positions $d_b^{mn} = |y_n - y_m|$ have to be computed self-consistently together with the electronic properties. In the fixed-nuclei approximation, the set $\{y_n\}$ corresponds to the ground state configuration and is not altered during the system's time evolution, see the example discussed below. Moreover, due to the reduction of dimensionality, the model Hamiltonian only allows for the description of molecules with linear geometry.

The parameters c_n and c remove the singularity of the Coulomb potential and soften the interaction between all charge carriers involved. This is necessary to avoid divergences in the FE-DVR matrix elements and, consequently, keeps the total energy finite. In Eq. (5.4), the asymptotic behav-

⁹For all calculations, we center the molecule at $x_0/2$.

ior of the soft-Coulomb potential $\hat{v}_i^{(1,\text{system})}$ as function of the distance $r_n = x_i - y_n$ is Coulombic ($\propto |r_n|^{-1}$) for $|r_n| \gg 1$ (in atomic units) and provides a harmonic cutoff at $r = 0$: $\hat{v}_i^{(1,\text{system})}(r_n) = -\frac{Z_n}{\sqrt{c_n}} + \frac{Z_n}{2\sqrt{c_n^3}}r_n^2 + \mathcal{O}(r_n^4)$ for $|r_n| \ll 1$. The same holds for the electron-electron repulsion $\hat{h}_{ij}^{(2)}$.

In a simple picture, the regularization of the Coulomb potential may be seen as simulating a transverse spread¹⁰ of the multi-electron wave function such that electrons may be able to pass each other. However, care needs to be taken with this interpretation as it does not apply simultaneously to the smoothing of the electron-nucleus interaction. Also, there is no straightforward mapping of the full three-dimensional Hamiltonian onto its 1D counterpart of Eqs. (5.3) and (5.4). A more fundamental argument for the removal of the singularities (besides the avoidance of numerical difficulties) is that, by changing the softening parameters, the ground-state and/or binding energy $\langle \hat{H}_{\text{gs/b}} \rangle$ and the ionization potentials I_P can be easily varied and adapted to the corresponding real 3D system without destroying the long-range character of the Coulomb potential [TMM09]. In Figure 5.1, this is demonstrated for the molecule lithium hydride (LiH) in one dimension, where $N_e = 4$, $N_n = 2$, $Z_1 = 3$ and $Z_2 = 1$. Thereby, all results are obtained in the Hartree-Fock approximation which gives the correct qualitative picture¹¹.

Figure 5.1 (a) shows how the one-electron potential changes with the softening of the electron-nucleus attraction and how this affects the electron density ($c = 1$) at fixed Li-H separation. Whereas the density directly at the lithium and the hydrogen atom strongly varies, it remains nearly constant in between. This is consistent with the overlap of molecular orbitals of different sites (or atoms) being essentially governed by the internuclear distances. In Figure 5.1 (b), the Li-H binding energy curve is depicted for different sets of parameters. With the increase of \bar{c} (for the definition see the Figure caption), a gradual transition from a very dense and strongly bound system to a weakly bound system with large bond length takes place. Thereby, the regularization of the electron-electron interaction only slightly shifts the binding energy and the resulting equilibrium bond length. For values about $c = c_n = 1$ (red solid line), one approaches the bond character of the real 3D LiH molecule (thick black line). Moreover, while all aforementioned findings have referred to the singlet state with closed-shell spin configuration, the gray curve in Figure 5.1 (b)—having no minimum—indicates that there exists no stable quintet state of total spin $S = 2$ for the 1D lithium hydride molecule.

In the remainder of this work, we focus on the case $c_n = c = 1$ ($\forall n$) which represents a reasonable choice and is also widely used in the literature for describing, both, atoms *and* molecules, e.g., Refs. [HGE94, KKB01].

Further, although being regularized, the soft-Coulomb potential provides bound states which follow the Rydberg scaling law [JES88], i.e., their asymptotic energy behavior is inverse to n^2 (for $n \gg 1 \in \mathbb{N}$). This leads to well-defined ionization thresholds—the ground states of the positively charged ions—and is responsible for the complex electronic structure of atoms and molecules. Con-

¹⁰An extension perpendicular to the x -direction.

¹¹At least for small to moderate internuclear distances. For $d_b \rightarrow \infty$, Hartree-Fock can fail in describing the dissociation and, hence, can lead to incorrect threshold energies. For a discussion on this point and for the inclusion of electron-electron correlations on the ground-state density and binding energy, see Chapter 6.

sequently, the atomic or molecular spectrum, also in 1D, comprises (i) one-electron excited states and (ii) series of multi-electron (autoionizing) resonances embedded in one- or more-electron continua [TRR00]. While the former states originate from transitions of individual electrons into energetically higher atomic or molecular orbitals, the latter exist solely due to binary correlations and point out the multi-electron nature.

The degree of correlation can be expressed, e.g., by means of the correlation energy,

$$\langle \hat{H}_{gs}^{\text{corr}} \rangle = \langle \hat{H}_{gs}^{\text{exact}} \rangle - \langle \hat{H}_{gs}^{\text{hf}} \rangle, \quad (5.11)$$

which is the difference of the exact total energy, $\langle \hat{H}_{gs}^{\text{exact}} \rangle$, and the total energy $\langle \hat{H}_{gs}^{\text{hf}} \rangle$ as obtained in Hartree-Fock approximation. Another option to describe the level of correlation is based on the information entropy (see Chapter 6.1.1).

5.2.2 A brief Overview on Strong-field Phenomena

In a static (or alternating) external electric field, the dc (ac) Stark effect leads to shifts and splittings of the atomic and molecular energy levels. However, standard perturbation theory for the linear or quadratic Stark effect¹² neglects the fact that, in the presence of intense fields, high-lying states are subject to a relatively fast decay in time. One of the corresponding strong-field phenomena is known as tunnel ionization (TI) for optical to infrared (ir) wavelengths and results from a large distortion of the nuclear potential which, at large intensities, is bend down and forms an oscillating potential barrier through which electrons may tunnel most effectively at maximum field amplitude in polarization direction [DE06]. At even larger intensities, TI merges into "over the barrier ionization" where the energy level of an electron is energetically above the tunnel barrier such that it can directly escape from the atom or molecule.

Another ionization channel is the absorption of several photons. If n photons of frequency or photon energy ω_{ph} are required for ionization, i.e., if $n\omega_{\text{ph}}$ becomes larger than the electron binding energy, the rate for multi-photon ionization (MPI) is proportional to $(I\omega_{\text{ph}}^{-1})^n$ [Kel65b]. Typical intensities for the absorption of two photons start from $I = 10^{14}$ W/cm². Of course, also more than the minimum number of photons that are actually needed to overcome the ionization potential can be absorbed. This process is known as "above threshold ionization" and leads to equidistant peaks (separated by ω_{ph}) in photoelectron spectra that measure the kinetic energy of the released electron [PAM88].

In contrast to a resonant excitation or a direct ionization (linear phenomena), TI and MPI are examples of nonlinear effects which can be classified by the Keldysh parameter $\gamma = \omega_{\text{ph}} \sqrt{2I_{\text{p}}} E_0^{-1}$ (in atomic units), see, e.g., Ref. [DE06], where I_{p} denotes the ionization potential of the system and E_0 is the electric field strength. Whereas for the multi-photon regime $\gamma \gg 1$, tunnel ionization dominates for $\gamma \ll 1$.

Moreover, strong-field ionization processes can be experimentally used to generate higher-harmonics radiation [BK00]. Here, the ionized electron is, by means of the laser field, driven back

¹²Note that the linear Stark shift vanishes for atoms and molecules with zero permanent dipole moment.

to the atom (or molecule) and, instead of undergoing interactions with residual bound electrons or nuclei¹³, it recombines by emission of electromagnetic radiation [YCAFE08]. As the frequencies of the emitted light are higher harmonics of the irradiated laser frequency¹⁴ the effect is called higher-harmonic generation (HHG). A typical HHG spectrum shows a well-formed plateau at intermediate photon energies and a classically motivated cut-off at $3.17 U_p + I_p$ (in atomic units where $U_p = E_0^2(4\omega_{ph}^2)^{-1}$ denotes the ponderomotive, cycle-averaged kinetic energy [Kel65b]) which is able to reach the soft x-ray regime.

Generally, all aforementioned intense-field phenomena are compatible with a single active electron (SAE) description, i.e., they do not involve the presence of other electrons in the atom or molecule. However, there are many strong-field situations where the SAE treatment fails and also a mean-field picture is insufficient. In these cases, dynamic correlation effects participate to a substantial level.

The most prominent indication of time-dependent electronic correlations is the "knee" structure observed in the double-ionization (DI) of noble gases [WSD⁺94, LTC98]. Here, up to certain threshold intensities (typically as large as 10^{15} W/cm²) the DI yield is several orders of magnitude larger than predicted from a sequential picture, where the second electron is assumed to escape from the singly charged ion. The underlying mechanism is well-investigated in full 3D [BF99, FLCC01] on the basis of the strong-field approximation and classical methods but has also been extensively studied in reduced dimensionality, for 1D helium see, e.g., Refs. [DvL01, WB06] and references therein.

Today, a still increasing number of experimental setups use sources of bright, coherent and ultra-short laser pulses (e.g., created by HHG techniques) and permit, in a time-dependent fashion, to resolve ultra-fast (sub-femtosecond) processes inside atoms or molecules, e.g., Ref. [UUS⁺07]. From the theoretical perspective, such experiments require accurate time-dependent modeling, particularly with a focus on correlation effects because their study is experimental reality. As representative example, where electron correlations are important and even have the ability to dominate the (ionization) dynamics, we want to, briefly, outline a typical attosecond pump-probe experiment [HC06a] that has been modeled in one spatial dimension by *S. Bauch et al.*, see Ref. [BBB10d].

In this TDSE study, a very simplified model of a helium-like atom is considered: two electrons with singlet spin configuration in a one-dimensional potential well with $v_i^{(1,\text{system})} = -1.6 E_h$ for $x_i \in [-2.8a_0, 2.8a_0]$ and zero outside the interval. Further, the electron-electron interaction is as in Eq. (5.4) ($c = 1$). Despite the simplicity of this model, it qualitatively captures the features of the 1D helium atom, including discrete (one- and two-electron) bound states and continuum states of the singly and doubly ionized system, for the energy levels and ionization potentials see inset of Figure 5.2 (a).

Aiming at the investigation of the single and double ionization, the model atom is exposed to a two-color (xuv-ir) laser field with Gaussian carrier envelopes, $E(t) = E_{xuv}(t) + E_{ir}(t) =$

¹³This would be a correlated process, e.g., leading to impact ionization.

¹⁴For symmetry reasons, only the odd harmonics are being emitted.

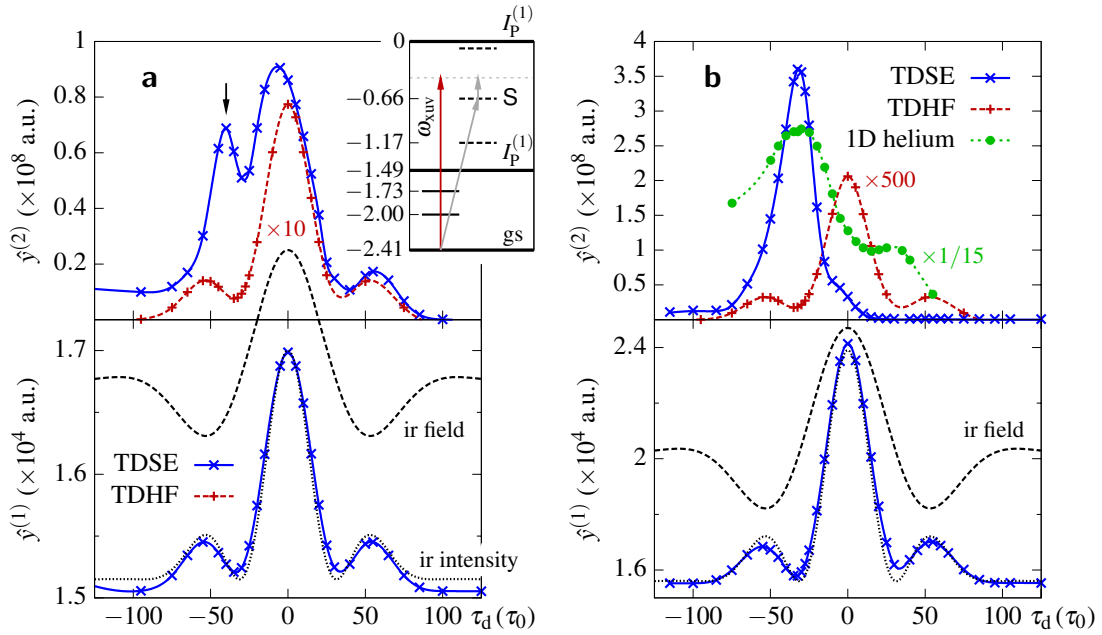


Figure 5.2: Single ($\hat{y}^{(1)}$) and double ionization yield ($\hat{y}^{(2)}$) as function of the pulse delay τ_d for a pump-probe experiment which involves a simple 1D two-electron model atom studied by the TDSE (blue lines) and TDHF (red dashed line in the upper panel). The inset in (a) shows the exact level diagram of the system, the ground state (gs), the ionization thresholds ($I_p^{(1,2)}$) and the xuv field (red arrow, $\omega_{\text{xuv}} = 1.99 E_h$, $\sigma_{\text{xuv}} = 10 \tau_0$). In (a), the intensity of the probing infrared pulse (black dashed line, $\sigma_{\text{ir}} = 45 \tau_0$) is $I = 8.8 \times 10^{13} \text{ W/cm}^2$, in (b), $I = 3.5 \times 10^{14} \text{ W/cm}^2$. The black dotted line in the lower panels depicts the instantaneous infrared intensity, $\propto |E_{\text{ir}}(t)|^2$. Moreover, the green dotted curve in (b) denotes respective results for the 1D helium model as defined in Chapter 5.2.1. Figures are according to *S. Bauch et al.*, cf. Ref. [BBB10d].

$E_{\text{xuv}}^0 \exp\left(-\frac{(t-\tau_d)^2}{2\sigma_{\text{xuv}}^2}\right) \cos(\omega_{\text{xuv}}(t - \tau_d)) + E_{\text{ir}}^0 \exp\left(-\frac{t^2}{2\sigma_{\text{ir}}^2}\right) \cos(\omega_{\text{ir}}t)$ in EDA, cf. Eq. (5.4). Thereby, τ_d denotes the time delay between both pulses, and, typically, $\sigma_{\text{xuv}} \ll \sigma_{\text{ir}}$. The xuv field acts as the pump pulse with a photon energy of $\omega_{\text{xuv}} = 1.99 E_h$, i.e., it promotes the system nonresonantly into the first continuum, cf. the red arrow in the inset of Figure 5.2 (a). Further, its relatively low intensity suppresses multi-photon absorption. On the other hand, the ir pulse ($\omega_{\text{ir}} = 900 \text{ nm}$) probes the atom but is not strong enough to produce significant strong-field tunneling or multi-photon ionization. For the specific pulse parameters, see the caption of Figure 5.2 or Ref. [BBB10d].

Figure 5.2 (a) and (b) resolve the single and double ionization yields (see the blue solid curves) for two different intensities of the probing ir pulse ((a) $8.8 \times 10^{13} \text{ W/cm}^2$ and (b) $3.5 \times 10^{14} \text{ W/cm}^2$) as function of the pump-probe delay. Note that, for negative τ_d , the maximum of the xuv pulse is rushing ahead, cf. $E(t)$ as given above. While in both cases the single ionization yield instanta-

neously follows the ir-field intensity¹⁵, the DI signal is strongly intensity-dependent forming an additional peak at negative delays (see the black arrow) and, in particular, does not at all follow a time-dependent Hartree-Fock description, see the red dashed line which is several orders of magnitude too small. The explanation is a highly non-linear process: The preceding xuv populates a shake-up state (see, e.g., Ref. [LLD⁺05], and the gray arrows in the level diagram) which, at about $\tau_d = -40 \tau_0$, is within reach of impact ionization induced by the probing ir field. Interestingly, Figure 5.2 (b) shows that, at intensities larger than 10^{14} W/cm², the release of electrons from the shake-up state becomes the dominant channel for DI. That the underlying mechanism is indeed due to a rescattering process (which, in the same manner, is responsible for the appearance of the "knee") can be understood by a semiclassical trajectory analysis, for details see Ref. [BBB10d].

In conclusion, this brief discussion on a pump-probe scenario emphasizes the role of electron correlations and shows that they can be the driving force in time-dependent strong-field phenomena. Thereby, in the present example, the complete failure of TDHF is due to the absence of the two-electron shake-up state (see label S in Figure 5.2 (a)), which only appears in a correlated treatment of the model system. Moreover, we also stress that for the 1D helium atom as defined in Chapter 5.2.1, i.e., including Coulomb-like potentials for the electron-nucleus interaction, one obtains similar results. These are depicted by the green dotted curve in Figure 5.2 (b).

5.3 Summary

In this Chapter, we, with Hamiltonian (5.3) and observables (5.5) to (5.11), have laid the foundation for the NEGF description of 1D atoms and molecules in the next Chapter. To this end, the discussion on LiH around Figure 5.1 has already given an idea how we will proceed in calculating the ground state properties. In Chapter 6, we extend these results and go beyond the mean-field (Hartree-Fock) treatment including correlations in the second(-order) Born approximation. Also, we present results for other atoms and molecules in one spatial dimension and discuss their correlated dynamics in the presence of time-dependent external fields (see $E(t)$ as introduced by Eq. (5.4)).

The brief discussion on the pump-probe experiment in Chapter 5.2.2 has motivated the inclusion of electron correlations in the nonequilibrium Green function approach. However, in the following, we do not aim at modeling the field-induced ionization of atoms (and molecules). This, on NEGF basis and by solving the two-time Kadanoff-Baym equations (3.37) and (3.38) without further approximations, turns out to be too expensive and complicated—we note that only a very few attempts have been made so far, see Refs. [HBBB10, BHBB10b]¹⁶. Instead, we, beyond the ground state properties of the considered models, primarily focus on the internal and short-time dynamics and, in this scope, investigate the role of dynamic correlations. In addition, the pur-

¹⁵This indicates the sequential process of xuv- and subsequent (respectively, preceding) ir-field perturbation.

¹⁶Due to lack of precision and temporal resolution, these works have not been successful in describing the correlated ionization dynamics. Particularly, we note that great care needs to be taken when applying the obscure approximation scheme established in Ref. [HBBB10].

pose is, of course, the benchmarking of the grid-based FE-DVR method developed in Part II of this thesis.

Equilibrium Properties and Nonequilibrium Behavior

6.1 Electronic Ground State Properties

As benchmarks for the efficient FE-DVR method developed in Part II of this thesis and as preparatory work for time-dependent (laser field) applications in Chapter 6.2, we, in this Section, present ground state (i.e., equilibrium) Green function results for the atomic/molecular model system discussed in Chapter 5.2, see Eqs. (5.3) and (5.4). Thereby, for thorough comparison and assessment of the Green function findings, exact reference data are computed from the full N_e -particle time-dependent Schrödinger equation (TDSE) using the method of imaginary time propagation¹. All approximate results follow from the Matsubara Green function $g^M(\tau)$, $\tau \in [-\beta, 0]$ in FE-DVR representation, where the Dyson equation (3.40)—as equilibrium limit of the two-time Kadanoff-Baym equations—is solved self-consistently in Hartree-Fock and second Born approximation, cf. Eqs. (4.2) and (4.4) in Chapter 4.1.1.

As examples of few-electron atoms, we focus on one-dimensional helium (He) and beryllium (Be; $N_e = Z_1 = 4$ and $N_n = 1$ in Eq. (5.4)). As molecular representatives, we study the one-dimensional hydrogen molecule (H_2 ; $N_e = N_n = 2$, $Z_{1,2} = 1$), the linear version of the molecular ion H_3^+ ($N_e = 2$, $N_n = 3$, $Z_n = 1 \forall n$) and the heteronuclear molecule lithium hydride (LiH). Further, all atoms and molecules are considered in the singlet (closed-shell) spin state with $|S, M_S\rangle = |0, 0\rangle$ unless noted otherwise, i.e., generally, $\xi = 2$ in all expressions.

Throughout, to account for the atomic and molecular ground state, we have chosen an inverse temperature of $\beta = 100 E_h^{-1}$, which requires the HOMO-LUMO gap (the energy spacing between the highest occupied molecular orbital and the lowest unoccupied molecular orbital in the context of Hartree-Fock, cf. Chapter 4.1.1) to be considerably larger² than $\frac{2}{\beta} \ln(3 + 2\sqrt{2}) \approx 0.04 E_h$. This is very well satisfied in all considered cases³. In addition, to ensure convergence, we have used simulation box widths ranging from 30 to 50 a_0 , cf. Eq. (3.4), and up to 231 FE-DVR basis functions

¹The code development and the production of most data are due to S. *Bauch*, e.g., Refs. [BBB10d, BHLE10].

²Estimated according to the FWHM (full width at half maximum) of the Fermi distribution's first derivative in order to ensure integer occupation of atomic or molecular orbitals.

³The size of the HOMO-LUMO gap is between 0.3 and 0.8 E_h .

which correspond to an interval partitioning into $n_e = 29$ finite elements and $n_g = 9$ local DVR basis functions per element (note that the basis has dimension $n_b = n_e(n_g - 1) - 1$, cf. Chapter 3.2). Generally, if the FEs do not follow an equidistant distribution, essentially more elements are placed in the center of the simulation box to support the large electron density and its modulation about the nuclei⁴.

6.1.1 Properties of He, Be, H₂, H₃⁺, and LiH

First, let us concentrate on the one-dimensional models of helium and beryllium. The helium atom is the most elementary closed-shell two-electron system and serves as convenient "testing ground" not only, as here, for NEGF calculations but also for other quantum many-body approaches such as multiconfiguration (time-dependent) Hartree-Fock [HBB10] or density functional theory [RB09a]. 1D beryllium acts as the next more sophisticated closed-shell system [BHBB10b].

Regarding the helium ground state, there exists (in Hartree-Fock theory) only a single orbital with energy⁵ $\epsilon_1 = -0.750 E_h$ that is occupied by two electrons. Beryllium—with four active electrons—possesses two doubly occupied orbitals ($\epsilon_1 = -1.371 E_h$ and $\epsilon_2 = -0.313 E_h$). The self-consistent approximate and exact ground state energies $\langle \hat{H}_{gs} \rangle$ are given in Table 6.1. In general, the inclusion of electron correlations must lower the ground state energy which is the manifestation of the Rayleigh-Ritz principle. For both atoms, we observe that the second Born approximation complies with this condition and accounts for 65-70% of the correlation energy, cf. Eq. (5.11), where, for beryllium, $\langle \hat{H}_{gs}^{corr} \rangle$ is more than three times larger than the value for helium. Overall, the second Born deviation to the exact ground state energy is less than $0.005 E_h$ ($0.014 E_h$) for He (Be) compared to $0.014 E_h$ ($0.045 E_h$) in Hartree-Fock approximation, i.e., the second Born results come relatively close to the exact ones. For the individual energy contributions to $\langle \hat{H}_{gs} \rangle$, the reader is referred to Appendix D (Table D.1 and Table D.2). We note, however, that, as soft Coulomb potentials are used for the electron-electron *and* electron-nucleus interaction ($c_n = c = 1$ in Eq. (5.4)), the virial theorem [Foc30] does not apply.

If necessary, ground state energies can be specified very accurately through the Dyson equation—including essentially more decimal places than are shown in Table 6.1. We want to illustrate this for the helium atom. To this end, we set up a simulation box with $x_0 = 50 a_0$ and divide the space into $n_e = 11$ finite elements that are arranged nonequidistantly. As function of the number of DVR basis functions n_g (given in brackets), one, at Hartree-Fock level, obtains the following converged decimal places: $-2.22 E_h$ ($n_g = 5$), $-2.224209 E_h$ (10), and $-2.2242095 E_h$ (15). The latter energy indicates a very precise value for the Hartree-Fock limit. In second Born approximation, $n_g = 15$ is needed for convergence in the sixth decimal place, then: $\langle \hat{H}_{gs} \rangle = -2.233419 E_h$ which has to be compared to the exact energy of $-2.2382578 E_h$. We note that, in the second

⁴An optimized FE-DVR basis with spatial extension of $200 a_0$ and non-equidistant interval segmentation has been discussed in Ref. [BBB10b] for the case of 1D helium.

⁵The orbital energies are obtained from a self-consistent field calculation. In compliance with Koopmans theorem, the negative energy of the HOMO predicts the first ionization energy. On the other hand, taking the LUMO energy (the energy of the first unoccupied orbital) as electron affinity is often a fairly poor assumption.

Table 6.1: Self-consistent ground state (binding) energies of the 1D model atoms (molecules).

Calculation	Ground state energy $\langle \hat{H}_{gs} \rangle (E_h)$		Binding energy $\langle \hat{H}_b \rangle (E_h)$		
	He	Be	H ₂	H ₃ ⁺	LiH
TDHF	-2.2242	-6.7394	-1.3531	-1.4710	-4.8534
TD2ndB	-2.2334	-6.7714	-1.3740	-1.5035	-4.8886
TDSE (exact)	-2.2383 ¹	-6.7852 ²	-1.391	-1.5324	-4.91

¹ e.g., Ref. [HGE94]; ² from Ref. [HBBB10].

Table 6.2: Self-consistent bond lengths of the molecules in Table 6.1.

Calculation	Bond length $d_b (a_0)$		
	H ₂	H ₃ ⁺ ($\times 2$)	LiH
TDHF	1.9925	4.3654	3.3860
TD2ndB	2.0561	4.5579	3.5053
TDSE (exact)	2.151	4.770	3.6

Born case, the convergence is complicated due to the nonanalytic τ -dependence of the Matsubara Green function, see the discussion below.

The one-electron ground state densities $\langle \hat{n}^{(1)} \rangle(x)$ of the helium and beryllium atom (obtained via Eq. (5.8) and being normalized to $N_e \xi^{-1}$) are displayed in the bottom graphs of Figure 6.1. For He, the density differences of Hartree-Fock (green dashed curve), second Born (blue solid curve) and TDSE (red dash-dotted line) are quite small and most dominant in the central region of $0.5 a_0$ about the He nucleus located at the origin. Along with increased electron number and correlation energy, a stronger deviation of approximate and exact densities is observed in the case of beryllium. However, as for He, the second Born density profile is situated well between the Hartree-Fock and the exact density, such that the second Born method produces coherently more accurate results than the mean-field calculation.

Now, let us turn over to the molecular examples and gather details on the models of H₂, H₃⁺ and LiH, the equilibrium properties of which, unlike in atoms, depend on additional parameters—the nuclei separations. In this work, we focus on the static case, i.e., no molecular vibrations are (e.g., thermally) excited. Then, whether or not individual atoms combine into molecules depends on the binding energy $\langle \hat{H}_b \rangle$ which appears as function of the interatomic distances d_b^{nm} , cf. Eq. (5.5). Figure 6.2 shows the corresponding potential energy curves (PECs) of the ground state. The color coding of the approximate and exact results is as in Figure 6.1, and our reference TDSE data for H₂ and H₃⁺ well coincide with those of Refs. [KKB01, YZB96].

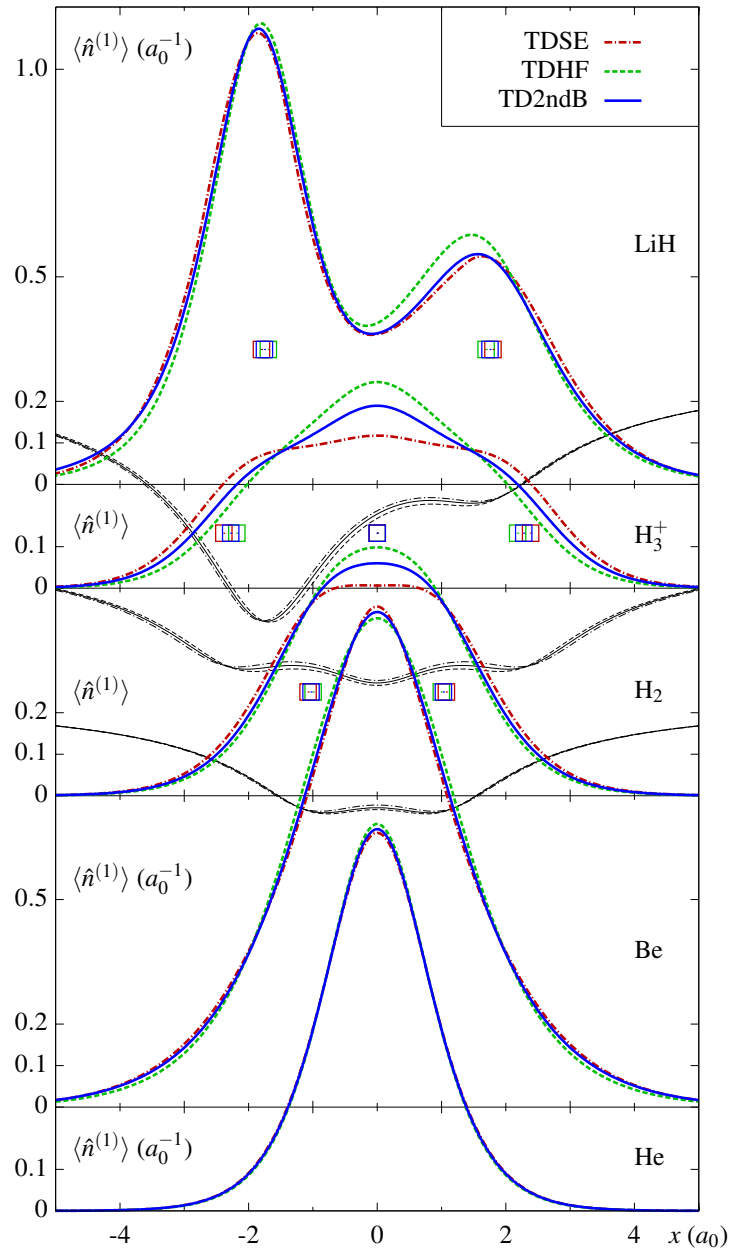


Figure 6.1: One-electron ground state density $\langle \hat{n}^{(1)} \rangle(x)$ for the one-dimensional models of helium (He), beryllium (Be), hydrogen (H_2), the molecular ion H_3^+ , and lithium hydride (LiH) in Hartree-Fock (TDHF, green dashed line) and second Born approximation (TD2ndB, blue solid line). The exact ground state density (TDSE, red dash-dotted line) is obtained from propagating the Schrödinger equation in imaginary time. For the molecules, the density profiles correspond to the self-consistent bond lengths d_b specified in Table 6.2. The squares (color-coded according to the legend) mark the nuclei positions and the thin black lines outline the resulting total core potentials which have been scaled by factor 0.2 and shifted (the squares have ordinate zero).

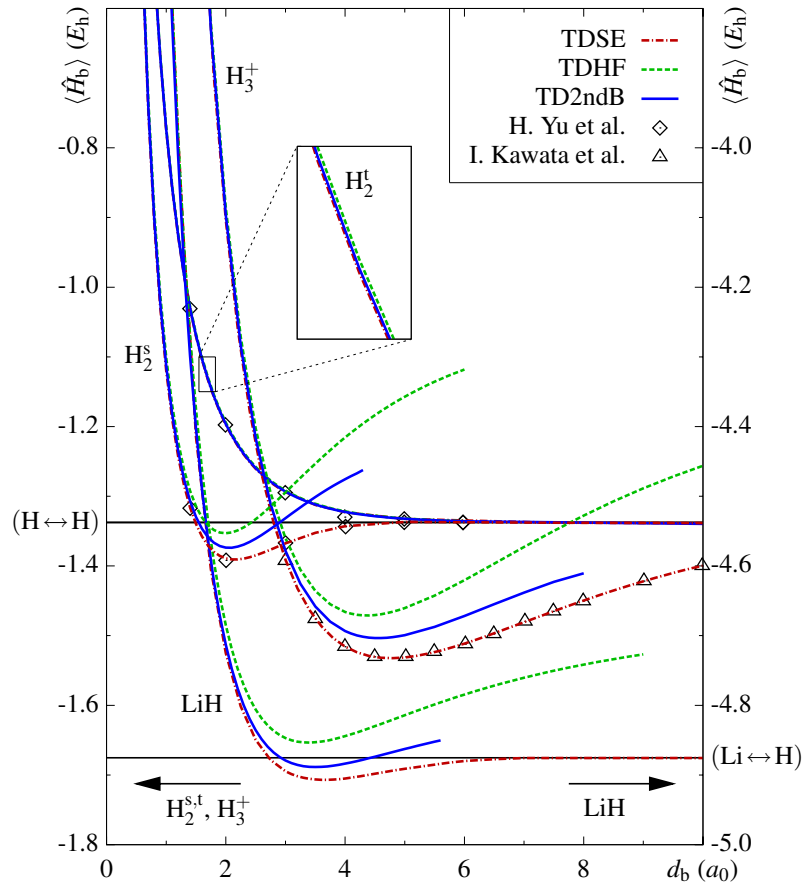


Figure 6.2: Potential energy curves, i.e., binding energy $\langle \hat{H}_b \rangle$ as function of interatomic distance d_b , for the models of hydrogen ($H_2^{s,t}$; s: singlet, t: triplet), the molecular ion H_3^+ , and lithium hydride (LiH). For H_3^+ , d_b corresponds to the distance of both outermost hydrogen atoms. The thresholds for complete fragmentation (dissociation thresholds) are labeled $(H \leftrightarrow H)$ at $-1.340 E_h$ and $(Li \leftrightarrow H)$ at $-4.880 E_h$. The inset refers to H_2 in the triplet (i.e., spin-polarized) electron configuration with nonbinding character. For the equilibrium bond lengths, i.e., the position of the minima in $\langle \hat{H}_b \rangle$, see Table 6.2. The diamonds and triangles indicate TDSE data from Refs. [KKB01] and [YZB96].

For hydrogen, Figure 6.2 considers, both, the singlet (H_2^s) and the triplet ground state (H_2^t with $\xi = 1$ and, e.g., $|S, M_S\rangle = |1, 1\rangle$). Regarding the singlet state, the exact PEC is of Morse-potential type and shows a minimum at about $2 a_0$ and a well-defined dissociation threshold indicated as $(H \leftrightarrow H)$. Similarly, the Hartree-Fock and second Born approximation confirm substantial hydrogen-hydrogen bonding, where the latter leads to an improvement of $\langle \hat{H}_b \rangle$ that measures 55% of the Hartree-Fock energy discrepancy about the PEC minimum. However, neither the Hartree-Fock nor the second Born approximation can accurately resolve the dissociation process.

This is due to the fact that the closed-shell H_2 molecule dissociates into open-shell fragments, i.e., individual neutral hydrogen atoms. Such a transition cannot be described within the semilocal (spin-restricted) approximations involved in the NEGF ansatz⁶. For the same reason, convergence becomes difficult at large interatomic distances⁷. However, the ground state properties at equilibrium bond length are not affected by this failure of the many-body approximation (cf. Table 6.1 and Table 6.2), and, as long as the fixed-nuclei approximation is applied, this also holds true in nonequilibrium situations. In contrast to the singlet state, the triplet variant of H_2 does not undergo molecular binding and all potential energy curves behave correctly in the limit $d_b a_0^{-1} \rightarrow \infty$. In addition, as it is typical for spin-polarized systems, correlations play a minor role such that the PEC is well approximated within Hartree-Fock. Nevertheless, second Born corrections improve the Hartree-Fock result, see the inset in Figure 6.2.

Like helium is the most elementary two-electron atom, H_3^+ (e.g., Ref. [ACK⁺09]) is the simplest representative of a triatomic molecule. For the PEC in Figure 6.2, we assume relaxed bonds with equal H-H spacing. Thereby, H_3^+ has the same dissociation threshold for complete fragmentation than the hydrogen molecule, but leaves behind a positively charged proton in addition to two neutral H atoms. The approximate and exact equilibrium bond lengths are slightly larger than in H_2 (compare with Table 6.2 and note that, for the molecular ion, d_b measures the distance between the outermost hydrogen atoms). Regardless of the above mentioned failure of the NEGF ansatz referring to the dissociation process, the nuclei positions are again consistently reproduced, and the correct trend is observed when correlations are being included: The equilibrium bond length shifts to larger nuclear separations.

The approximate PEC calculations for the lithium hydride molecule reveal similar features as observed for H_2 or H_3^+ . Here, we only point out that the degree of electron correlations is, in second Born approximation, slightly larger and that the corresponding minimum in $\langle \hat{H}_b \rangle$ is situated below the (Li \leftrightarrow H)-threshold which is not realized in Hartree-Fock approximation.

Summarizing the foregoing, the self-consistent binding energies and bond lengths obtained from Figure 6.2 are listed in Table 6.1 and Table 6.2, and the corresponding ground state densities for the di- and triatomic molecules are shown in the upper three panels of Figure 6.1. Concerning the densities, the molecular models universally indicate significantly larger differences among approximate and exact results than observed for the atomic examples, see the regions of high density. Hence, in all cases, the second Born approximation (blue solid lines) leads to considerable improvements of $\langle \hat{n}^{(1)} \rangle(x)$. For LiH, the second Born ground state density is even in surprisingly good agreement with the exact result. Moreover, the thin black curves in Figure 6.1 delineate the one-particle potentials $\hat{v}^{(1)}(x)$, cf. Eq. (5.4), that slightly vary with the equilibrium positions of the nuclei that are indicated by squares. In this context, we emphasize that the density differences are mainly based on correlation effects and that the influence of the bond length variation⁸ is secondary, for a discussion on H_3^+ see Ref. [BBB10b].

⁶We note that the same problem is encountered in density functional theory, e.g., Ref. [RPC⁺06].

⁷Although $\langle \hat{H}_b \rangle(d_b)$ does not diverge as it occurs in Møller-Plesset perturbation theory.

⁸Induced by the specific many-body approximation.

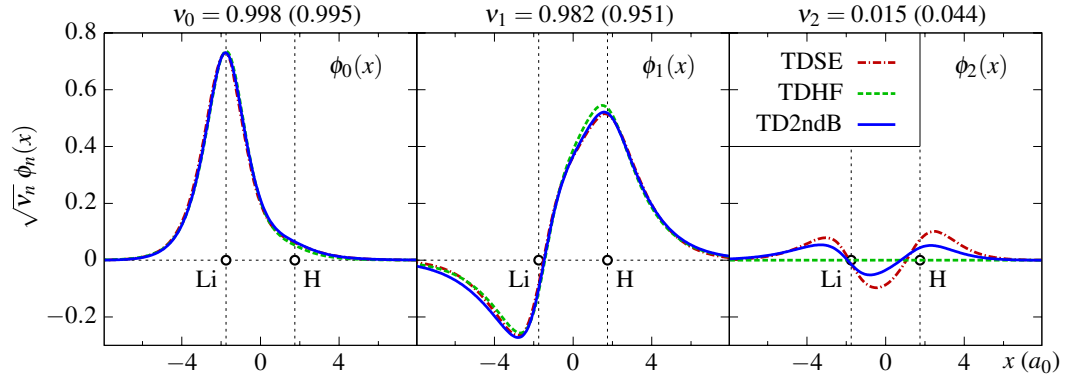


Figure 6.3: The three most relevant approximate and exact natural orbitals (NOs) $\phi_0(x)$, $\phi_1(x)$ and $\phi_2(x)$ for the lithium hydride molecule in its ground state obtained from Eq. (6.1) and weighted by $\sqrt{\nu_n}$; ν_n are the NO occupation numbers. The result of the Hartree-Fock (second Born) approximation is given by green dashed lines (blue solid lines) and the TDSE data are shown by red dashed-dotted curves. The numbers on top of each panel indicate the occupation number ν_n for the second Born (TDSE) calculation.

Natural Orbitals

A more precise identification of the electronic structure and the second Born-type deviations from the mean-field (TDHF) picture is possible by means of natural orbitals (NOs), e.g., [HTR10]. Generally, the accessible set of natural orbitals $\phi_n(x)$ ($n = 0, 1, \dots, n_b - 1$ where n_b denotes the FE-DVR basis size) is obtained from the eigenvalue problem,

$$\int dx' \rho_{\text{gs}}^{(1)}(x, x') \phi_n(x') = \xi \nu_n \phi_n(x), \quad (6.1)$$

with the one-electron ground state density matrix $\rho_{\text{gs}}^{(1)}(x, x') = \xi g^{\text{M}}(0^-)$ and natural orbital occupation numbers $0 \leq \nu_n \leq 1$ where $\sum_n \nu_n = N_e \xi^{-1}$. In FE-DVR representation, the NOs are constructed directly as $\phi_n(x) = \sum_{im} c_m^{(n),i} \chi_m^i(x)$ where the expansion coefficients $c_m^{(n)}$ are the eigenvectors of the Matsubara Green function $g_{mm'}^{\text{M},ii'}(0^-)$ (ν_n are the respective eigenvalues). In Hartree-Fock approximation, natural and Hartree-Fock orbitals are identical and, at least for $\beta \rightarrow \infty$, integral occupations ($\nu_n = 1$ for $n = 0, 1, \dots, N - 1$ and zero otherwise; N is the number of electrons with same spin projection) reflect the non-correlated character of the many-body wave function which is just a Slater determinant of all occupied NOs.

In the case of LiH, there exist two fully occupied natural orbitals that contribute to the Hartree-Fock ground state, see ϕ_0 and ϕ_1 in Figure 6.3, and note the scaling by $\sqrt{\nu_n}$. For the first, nodeless orbital $\phi_0(x)$, which is mainly situated at the lithium atom, approximate and exact results are lying almost on top of each other. This is the clear sign that the core electrons are less affected by electronic correlations⁹. In comparison to Hartree-Fock ($\nu_0 = 1$), the occupation numbers are

⁹Note that, at Hartree-Fock level, ascending orbital energies can be assigned to the NOs.

Table 6.3: Information entropy S as a correlation measure (cf. Eq. (6.2)). In Hartree-Fock approximation, it is $S = -N_e \log \xi$ with spin degeneracy factor ξ . Electronic correlations, generally, raise the entropy.

Calculation	Information entropy				
	He	Be	H ₂	H ₃ ⁺	LiH
TDHF	-1.3863	-2.7726	-1.3863	-1.3863	-2.7726
TD2ndB	-1.3327	-2.5372	-1.2319	-1.1073	-2.4793

changed by less than 0.6% for TD2ndB and TDSE.

For the second natural orbital, which, at Hartree-Fock level, represents the two valence electrons, correlation-induced deviations are larger. In addition, ϕ_1 is shared between both nuclei and extends over several bond lengths. Due to second Born corrections ν_1 decreases by about 2% in favor of the occupation of energetically higher orbitals, compare with Ref. [BBvL⁺09]. This represents the fact that the correlated many-body wave function for LiH cannot be expressed by a single Slater determinant. Moreover, in correspondence with the one-electron density in Figure 6.1, the explicit form of $\phi_1(x)$ is well approached in the second Born approximation.

For TD2ndB and TDSE, also the third natural orbitals ϕ_2 , being occupied by less than 5%, are similar in shape, although the occupation for TD2ndB is less than half the TDSE value (TDHF: $\nu_2 = 0$). Finally, all remaining natural orbitals (those which are not shown in Figure 6.3) are occupied by less than 1%.

Information Entropy

A unified measure of the degree of electron correlation which allows for comparison of different atoms and molecules is the information (or correlation) entropy, see, e.g., Ref. [NY00]. It is defined by ($\rho^{(1)}$ is the one-electron density matrix and ν_n denote natural orbital occupations, cf. Eq. (6.1)),

$$S = -\text{Tr}[\rho^{(1)} \log \rho^{(1)}] = -\xi \sum_n \log(\xi \nu_n) , \quad (6.2)$$

and describes the entanglement between a single electron in the system and the entirety of the remaining $N_e - 1$ electrons [HTR10]. In the case of integral (non-fractional) natural orbital occupations, i.e., in Hartree-Fock approximation, the information entropy adopts the value of $S = -N_e \log(\xi)$. For a spin-polarized and, respectively, for a closed-shell system the lower bound is $S = 0$ and $S = -N_e \log(2)$. Fractional occupation numbers generated by correlations lead to an entropy increase which is consistent with the usual entropy perception.

For the closed-shell model atoms and molecules under investigation in this Chapter, Table 6.3 summarizes the values of the information entropy in Hartree-Fock and second Born approximation. Focusing first on the two-electron systems He, H₂ and H₃⁺, we observe that the presence of

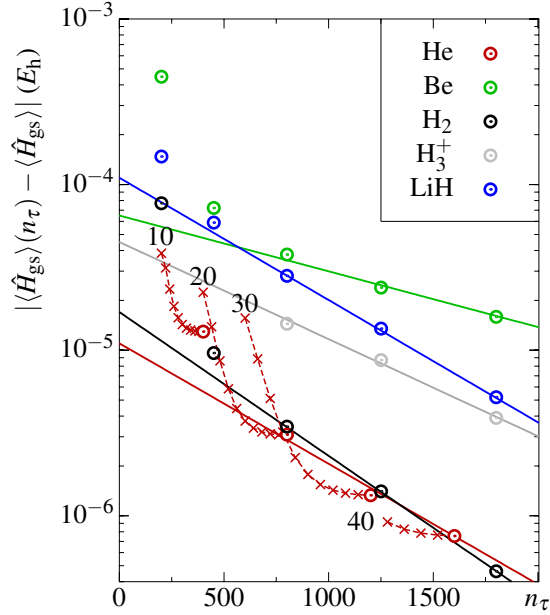


Figure 6.4: Second Born approximation: Convergence of the ground state energy $\langle \hat{H}_{gs} \rangle$ for models of helium (red), beryllium (green), hydrogen (black), the molecular ion H_3^+ (gray) and lithium hydride (blue) as function of the number of τ -grid points $n_\tau = 2n_u n_p + 1$ (red lines). The red dashed curves show the convergence behavior for helium as function of n_p only. Parameter n_u is fixed as indicated by the numbers.

more than one atomic core potential reveals a gradual growth in the degree of correlation. While for helium $S = -1.3327$ is close to the non-correlated (Hartree-Fock) result of $S = -1.3863$, it increases by about 0.1 for hydrogen and is largest for the molecular ion H_3^+ , where the two negative charges are shared between three hydrogen atoms. Secondly, referring to the four-electron examples (Be and LiH), the electrons are more strongly correlated in the diatomic lithium hydride molecule than in beryllium.

For completeness, we note that the same trend as specified by the entropy can be extracted also from the correlation energies which are listed in Appendix D, see Tables D.1 and D.2.

Second(-order) Born Convergence Behavior

In the last part of this Section, we want to present some additional computational details concerning the second Born calculations for He, Be, H_2 , H_3^+ and LiH. These relate to the time-argument τ in the Matsubara Green function $g^M(\tau)$ where $\tau \in [-\beta, 0]$ ($\beta = 100 E_h^{-1}$), cf. Eq. (2.25).

While, for Hartree-Fock, the τ -dependence of the Matsubara Green function is known (there is an exponential decay (growth) as function of τ for orbital energies above (below) the chemical potential, cf. Eqs. (4.2) and (4.3)), it is nontrivial for many-body approximations that include

electron-electron correlations, i.e., for which the self-energy is nonlocal in time, see the Dyson equation (4.4). Thereby, strong deviations from exponential behavior can be expected, in particular, about the interval endpoints $\tau = -\beta$ and $\tau = 0$ [BBvL⁺09]. Moreover, when a representation other than the Hartree-Fock orbital basis is applied (note that we work in the FE-DVR picture), the τ -discretization is more elaborate due to mixing of Hartree-Fock orbitals. For these reasons, an adequate τ -grid and a thorough convergence analysis with respect to the grid parameters is required.

As outlined in Chapter 4.1.1, we, for discretization of the interval $[-\beta, 0]$, adopt a uniform power mesh [BBvL⁺09, DvL05] that depends on two parameters, n_u and n_p . Figure 6.4, shows the convergence of the atomic and molecular ground state energies against the total number of grid points $n_\tau = 2n_u n_p + 1$, where a steady state is typically obtained after 10 to 20 iterations of the Dyson equation. As we see, generally, a grid with $n_\tau > 500$ yields errors that are less than $10^{-4} E_h$. In addition, how fast the energy converges depends on the number of electrons (compare helium and beryllium) as well as on the molecular geometry (see H_2 in comparison to H_3^+). On top of that, a dense grid around $\tau = 0$ is also relevant for particle number preservation. We note that, during the iteration process, the particle number $N_e = \xi \text{Tr}[g^M(0^-)]$ can be an unstable observable with respect to grid parameter variations (on that account, the trace over the second term on the r.h.s. of Eq. (4.4) must vanish).

Overall, relatively large τ -grids with more than a thousand grid points are necessary to obtain satisfactory ground state results as they are displayed in Tables 6.1 and 6.2. As a consequence, similarly large grids must be taken into account in nonequilibrium situations when initial correlations are non-negligible¹⁰ (turn to the following Chapter 6.2).

6.2 Nonequilibrium Behavior in External Fields

In this Section, we perform explicitly time-dependent second-order Born calculations for the model atoms and molecules treated in the previous Section for their (non-)correlated ground state properties. To this end, we solve the full two-time Kadanoff-Baym equations, as it is outlined in Chapter 4.1, in FE-DVR representation starting from the system's ground state. In the presence of external fields, cf. Eq. (5.4), we deploy the numerical methods developed in Part II including the dynamic self-energies of Eqs. (3.32) and (3.35), and, in particular, prove the applicability of the parallel, distributed-memory code described in Chapter 4.2. Moreover, we want to test the generalized Kadanoff-Baym ansatz for the dynamics of one-particle observables.

Regarding the physics, we focus on two central topics: (i) the linear response properties of He which are of relevance for the ground state excitation spectrum, and (ii) the correlated short-time electron dynamics in He and LiH being exposed to strong, non-perturbative laser fields in the (extreme) ultraviolet ((x)uv) regime, i.e., we make use of photon energies $10 \text{ eV} \leq \omega_{\text{ph}} \leq 120 \text{ eV}$ and field intensities larger than 10^{14} W/cm^2 .

¹⁰Maybe, a good idea—in future NEGF calculations—is to proceed from a time-grid representation to a basis expansion similar to a FE-DVR that is applied for the spatial coordinates of the Green function.

6.2.1 Linear Response Properties of He

Under a weak, i.e., perturbative, and spectrally broad dipole excitation, described by (cf. Eq. (5.4), t_0 denotes the time instant when the field acts),

$$\hat{v}_i^{(1,\text{field})}(t) = E(t) x_i, \quad E(t) = E_0 \delta(t - t_0), \quad (6.3)$$

where the field strength is typically $E_0 \ll 1$ a.u. (such that the intensity is well below 10^{14} W/cm²), the atom or molecule performs electric dipole transitions from the ground state into the excited state manifold. Thereby, the small field strength makes sure that all kind of ionization and multi-photon processes and excitations of higher order are negligibly small. Numerically, the dipole excitation of Eq. (6.3) is realized by letting the constant field E_0 act for a single time step (or a few) if its length is of the order of $10^{-2} \tau_0$ or, otherwise, by using an extremely short (e.g., Gaussian) pulse ($E(t) \propto \exp(-\frac{1}{2}(\frac{t-t_0}{\sigma_0})^2)$, $\sigma_0 \tau_0^{-1} \ll 1$). The infinitesimal temporal shortness ensures that, at least principally, all excited states¹¹ are accessible.

The carrier of the spectral information is the time-dependent dipole moment $\langle \hat{d}^{(1)} \rangle(t)$, see Eq. (5.9), from which one can extrapolate to the internal electronic structure and to the complete ground state dipole spectrum, the polarizability $\alpha(\omega) \propto \int_{-\infty}^{+\infty} dt e^{-i\omega t} \langle \hat{d}^{(1)} \rangle(t)$, cf. Eq. (5.10), and the response function [DvLS06].

In Figure 6.5, we compare the evolution of the dipole moment for the one-dimensional He atom in Hartree-Fock (TDHF, green dashed line) and second Born approximation (TD2ndB, blue solid line) to the exact result of the time-dependent Schrödinger equation (TDSE, red dash-dotted line). In addition, we present the dipole moment for the single-time second Born calculation (black dash-dash-dotted curve) that uses the generalized Kadanoff-Baym (GKB) ansatz for reconstructing the collision integral on the time diagonal, cf. Chapter 4.3. Thereby, the differences in user memory are huge: While the two-time evolution of the Green function consumes about one terabyte of memory (the simulation parameters are $x_0 = 70$, $n_b = 83$, and $\delta = 0.025$), the GKB calculation gets along with only about one to two gigabyte RAM (here, $x_0 = 40$, $n_b = 59$, and $\delta = 0.01$).

Following the δ -kick at $t = 0$, the dipole moment, generally, starts to oscillate about the position of the He nucleus (note that symmetry inhibits a permanent dipole moment). Thereby, we clearly identify differences between the mean-field and partly (fully) correlated results. In second Born approximation, the time-dependent dipole moment reasonably well approaches the TDSE result where, in comparison to TDHF, a general shift towards a larger main oscillation period is observed. The corresponding frequency roughly agrees with the excitation frequency of the first excited state (cf. Figure 6.6: $\omega_{01} = 0.533 E_h$, which gives a period of $11.8 \tau_0$). In addition, Figure 6.5 shows that the GKBA curve, particularly at the initial stage of propagation, well follows the TD2ndB result.

However, we remark that, in all approximate calculations of Figure 6.5 (thick lines), the initial state is non-correlated, i.e., of Hartree-Fock type. This, if dynamic correlations are included in the calculation, can become noticeable in form of additional (collective) excitations of non-dipole character, for details, see also the laser-induced electron dynamics discussed in Chapter 6.2.2 as

¹¹Of course, only those which are accessible from the ground state by a dipole transition.

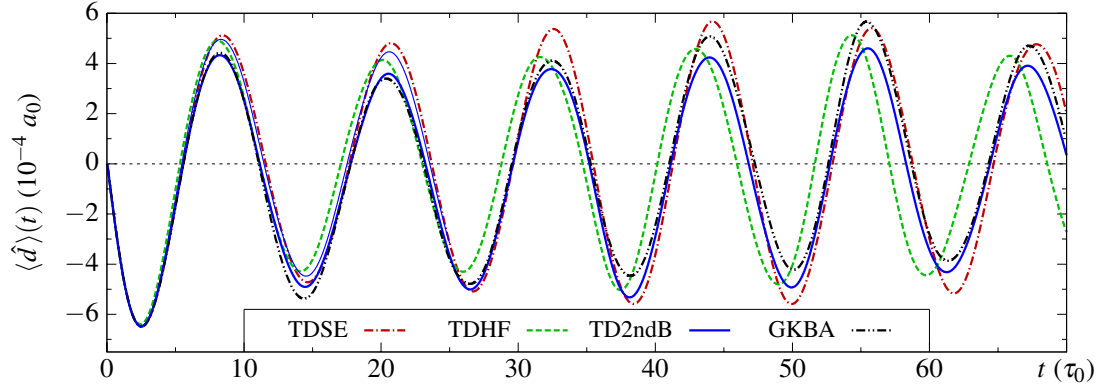


Figure 6.5: Time-dependent dipole moment $\langle \hat{d}^{(1)} \rangle(t)$ of the one-dimensional helium atom following a perturbative dipole δ -kick excitation at $t_0 = 0$, cf. Eq. (6.3). Whereas the green dashed (blue solid) curve indicates the Hartree-Fock (second Born) result, the TDSE data are given by the red dash-dotted curve. The black dash-dash-dotted line corresponds to the usage of the generalized Kadanoff-Baym ansatz (GKBA). In all approximate curves except for the thin blue line (which corresponds to the usage of the self-consistent correlated initial state, plotted up to $t = 25 \tau_0$) the helium atom is, for $t \leq 0$, prepared in the Hartree-Fock ground state of energy $-2.2242 E_h$, cf. Chapter 6.1.1.

well as Chapter 6.3. Thus, some care needs to be taken when comparing to the full TDSE result. We emphasize that the usage of self-consistent initial states further improves $\langle \hat{d}^{(1)} \rangle(t)$. For times $t < 25 \tau_0$, the reader is referred to the thin blue solid line¹² in Figure 6.5 or may compare with Ref. [BBB10c].

The 1D He model has, just like real helium, discrete, Rydberg-like arranged energy levels (bound states) *and* continuum states that represent the singly- or doubly-ionized atom, cf. Chapter 5.2.1. The schematic level diagram of the singlet system is displayed in Figure 6.6 including a couple of one- and two-electron excitation energies. Principally, as mentioned before, a detailed analysis of the time-dependent dipole moment obtained in linear response, should—in terms of its Fourier transform—give direct access to the excited states. In the following, we want to report on respective results which are achievable in the second Born approximation.

The dipole spectrum as computed from the TDSE¹³ is given by the black dash-dotted line in Figure 6.7 (a). It clearly indicates the series of singly- and doubly excited states outlined in Figure 6.6. However, to arrive at this result, the time-dependent dipole moment had to be recorded for several hundred atomic units, and, in addition, a very large simulation box ($x_0 \gg 50 a_0$) has been used in combination with absorbing potentials [BHLE10, VB92] to suppress spectral box artifacts, compare with Figure 6.7 (b). In full second Born approximation, such long and spatially

¹²Essentially longer full TD2ndB calculations are difficult to perform when the mixed Green function $g^\Gamma(-i\tau, t)$ ($\tau \in [-\beta, 0]$) is being included to account for initial correlations.

¹³Data from *S. Bauch*; solution of the two-electron time-dependent Schrödinger equation [HBB10].

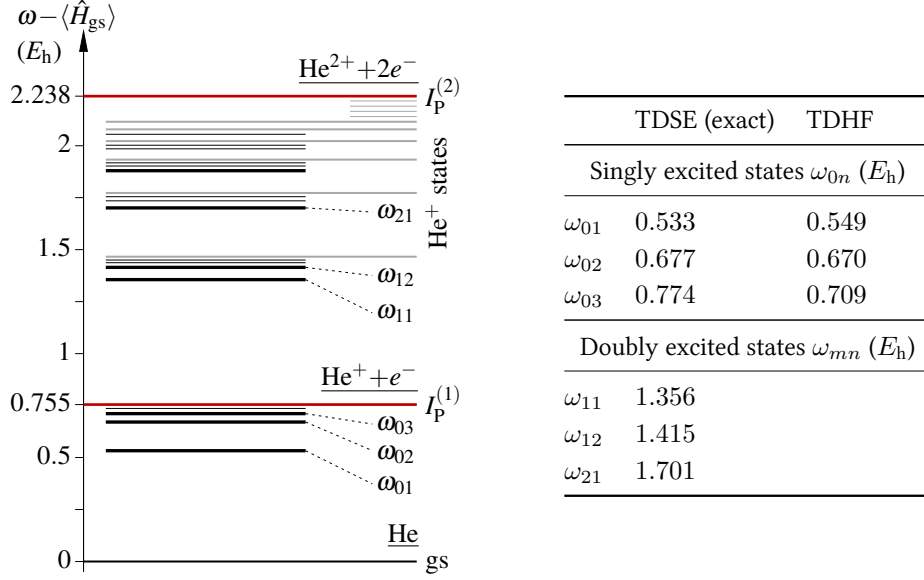


Figure 6.6: Level diagram of one-dimensional He from ground state (gs) to complete fragmentation, $\omega - \langle \hat{H}_{gs} \rangle > 2.238 E_h$. The gray lines indicate the excited states of the singly-charged ion, He^+ . The first and second ionization threshold, $I_p^{(1)} = 0.755$ and $I_p^{(2)} = 2.238$ (in units of Hartree, E_h), are marked by the red lines. The difference of the ionization potentials is $I_p^{(2)} - I_p^{(1)} = 1.483 E_h$. The excitation energies of the first singly excited states (black lines below $I_p^{(1)}$) and some autoionizing resonances (black lines between $I_p^{(1)}$ and $I_p^{(2)}$), computed from exact diagonalization and TDHF time series, are collected alongside in the Table.

extended calculations are (with present numerical capabilities) prohibited due to the two-time and non-Markovian structure of the Kadanoff-Baym equations. Instead, the propagation is limited to relatively short times even if the parallel algorithm of Chapter 4.2 is applied [BBB10c]. Hence, with a length of $t_f = 70 \tau_0$ (1.7 fs), the second Born data of the dipole moment displayed in Figure 6.5 are far too short to obtain complete spectral information by Fourier transform¹⁴ or harmonic inversion [MT97].

In order to gather at least some indications on the first and eventually on the second excited state, we have applied an autoregression (AR) spectral analysis [Mar87] which is appropriate for analyzing short time-series. Here, an autocorrelation model of order s is applied to the time-dependent dipole moment,

$$\langle \hat{d}^{(1)} \rangle(t) = \langle \hat{d}_0^{(1)} \rangle + \sum_{n=1}^s c_n \langle \hat{d}^{(1)} \rangle(t - n\Delta t), \quad \Delta t = \frac{t_f}{s}, \quad (6.4)$$

where $\langle \hat{d}_0^{(1)} \rangle$ denotes the permanent dipole moment, cf. Eq. (5.10), which is zero in the present case. Further, the AR coefficients c_n are obtained from the Yule-Walker equations, for details see

¹⁴Even if high-resolution windowing is used.

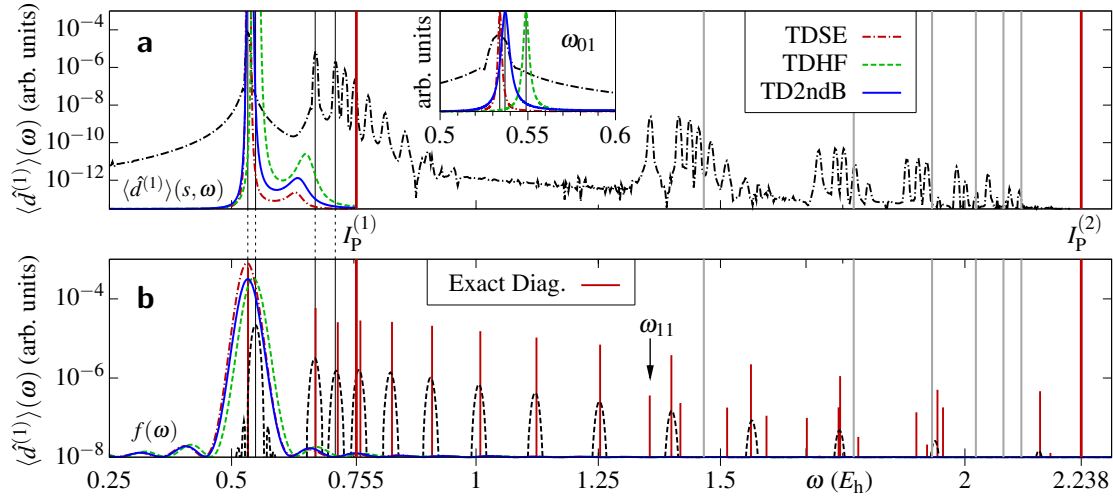


Figure 6.7: Ground state dipole spectrum for the one-dimensional He atom. (a) The black dash-dotted line represents $\langle \hat{d}^{(1)} \rangle(\omega)$ as computed from the solution of the TDSE using absorbing boundary conditions and a simulation box which is essentially larger than $x_0 = 50 a_0$, see Ref. [HBB10]. While the peaks situated energetically below the first ionization threshold $I_p^{(1)}$ are the singly excited bound states of He, the peaks between $\omega = 1.25 E_h$ and the second ionization threshold $I_p^{(2)}$ are the doubly excited states (i.e., resonances in the one-electron continuum). The gray vertical lines indicate the excited state energies of the singly-charged ion (He⁺), cf. Figure 6.6. Further, the colored curves (with nonlogarithmic scale) indicate the autoregression power spectral densities $\langle \hat{d}^{(1)} \rangle(s, \omega)$ obtained from Eq. (6.5) with model order $s = 1000$ and $t_f = 55 \tau_0$. In Hartree-Fock (second Born) approximation, the first excited state appears at frequency $\omega_{01}^{(1)} = 0.549 E_h$ ($\omega_{01}^{(2)} = 0.537 E_h$). The exact excitation frequency is $\omega_{01} = 0.533 E_h$, see the inset. (b) The black dashed line corresponds to the Fourier transform of $\langle \hat{d}^{(1)} \rangle(t)$ (plus Blackman window) in Hartree-Fock approximation where $t_f = 1000 \tau_0$ and $x_0 = 50 a_0$. Note that peaks beyond $I_p^{(1)}$ are artificial box states that are narrower and partially damped out in the case of the TDSE, compare with panel (a). The thin red vertical lines are the excited states as computed for the same simulation box width from exact diagonalization. Moreover, the colored lines in panel (b) show the integral $f(\omega) = |\int_0^{t_f} dt e^{-i\omega t} \langle \hat{d}^{(1)} \rangle(t)|^2$ where $t_f = 70 \tau_0$ as in Figure 6.5 (nonlogarithmic scale, arb. units).

Ref. [Mar87]. Once computed, the coefficients give access to the power spectral density via (δ is the time step size),

$$\langle \hat{d}^{(1)} \rangle(s, \omega) \propto \left| 1 - \sum_{n=1}^s c_n \exp(-in\omega\delta/2) \right|^{-2}. \quad (6.5)$$

We note that $\langle \hat{d}^{(1)} \rangle(s, \omega)$ is periodic in $\omega_s = 4\pi\Delta t^{-1}$, i.e., s must be larger than 4 to resolve frequencies below the first ionization threshold $I_p^{(1)} = 0.755 E_h$ which is close to the negative HOMO energy ϵ_1 given in Chapter 6.1.1 (Koopmans theorem).

The results of the AR spectral analysis for approximate and exact calculations of equal length $t_f = 55 \tau_0$ ($\Delta t \approx 0.05 \tau_0$) are shown in Figure 6.7 (a) by the colored lines. Overall, at relatively large model order s , we obtain good results for the first excited state, see also the inset plot which covers frequencies $0.5 \leq \omega \leq 0.6$ (in units of E_h). For TDHF (green dashed line), the well pronounced peak coincides with that obtained by discrete Fourier transform of $\langle \hat{d}^{(1)} \rangle(t)$ of a much longer TDHF calculation displayed in Figure 6.7 (b), see the black dashed line. As value for the Hartree-Fock excitation energy, we get $\omega_{01}^{(1)} = 0.549 E_h$ which equals the result of Ref. [RB09b]. Further, in second-order Born approximation (TD2ndB), we find $\omega_{01}^{(2)} = 0.537 E_h$. This corresponds to an improvement of the first excited state energy of 75% in the deviation of Hartree-Fock to exact. The TDSE result (red curve) reads $\omega_{01} = 0.533 E_h$, cf. Figure 6.6, and matches the peak position of the black dash-dotted curve. Moreover, in the AR power spectral density $\langle \hat{d}^{(1)} \rangle(s, \omega)$, also the second excited singlet state is resolved which is not the case for a direct Fourier transform of the time-dependent dipole moment, compare with the colored lines in Figure 6.7 (b). The shift toward smaller frequencies is thereby caused by the shortness of the time series. Although no physically useful data can be determined from the second peak in the AR data, we observe that the TD2ndB peak position is well situated in between the Hartree-Fock and the exact results.

From the above considerations, we conclude that concerning the excited state properties of the 1D helium atom, the second Born approximation is able to show correlation-induced features to a substantial level. However, the regime of large excitation energies was not accessible in the present calculations, i.e., unfortunately, we could not track the emergence of two-electron resonance states which are situated within the one-electron continuum (ranging from $I_p^{(1)}$ to $I_p^{(2)}$) and are the ultimate indication of a correlated quantum many-body state. Note that these states occur only for a correlated treatment of the electron-electron interaction. Hence, they first appear for self-energies that are of second-order in the Coulomb potential. Once, again, we emphasize that the present inability of the second Born calculation is neither due to the specific form of the many-body approximation¹⁵ nor related to the spatial resolution¹⁶. Instead, it is a consequence of the limited time of propagation. Using the generalized Kadanoff-Baym ansatz, one eventually may approach also the regime of doubly-excited resonance states. For a discussion on two-electron excitations in artificial atoms [Ash96], the reader is referred to Chapter 6.3 of this thesis.

6.2.2 Ultra-violet Field-induced Electron Dynamics in He and LiH

In order to describe situations, where the model atom (or molecule) is exposed to an external laser field, we, in EDA (electric dipole approximation, cf. Eq. (5.4)), consider,

$$\hat{v}_i^{(1,\text{field})}(t) = E(t) x_i, \quad E(t) = E_0 \theta(t - t_0) \cos(\omega_{\text{ph}}(t - t_0)). \quad (6.6)$$

¹⁵We expect the correlated two-electron features to be included in second Born approximation on a similar level.

¹⁶The exact diagonalization data shown in Figure 6.7 (b) indicates that, for a simulation box of $50 a_0$ length, the two-electron states appear as additional peaks in the spectrum, see the arrow and compare with the time-dependent Hartree-Fock result.

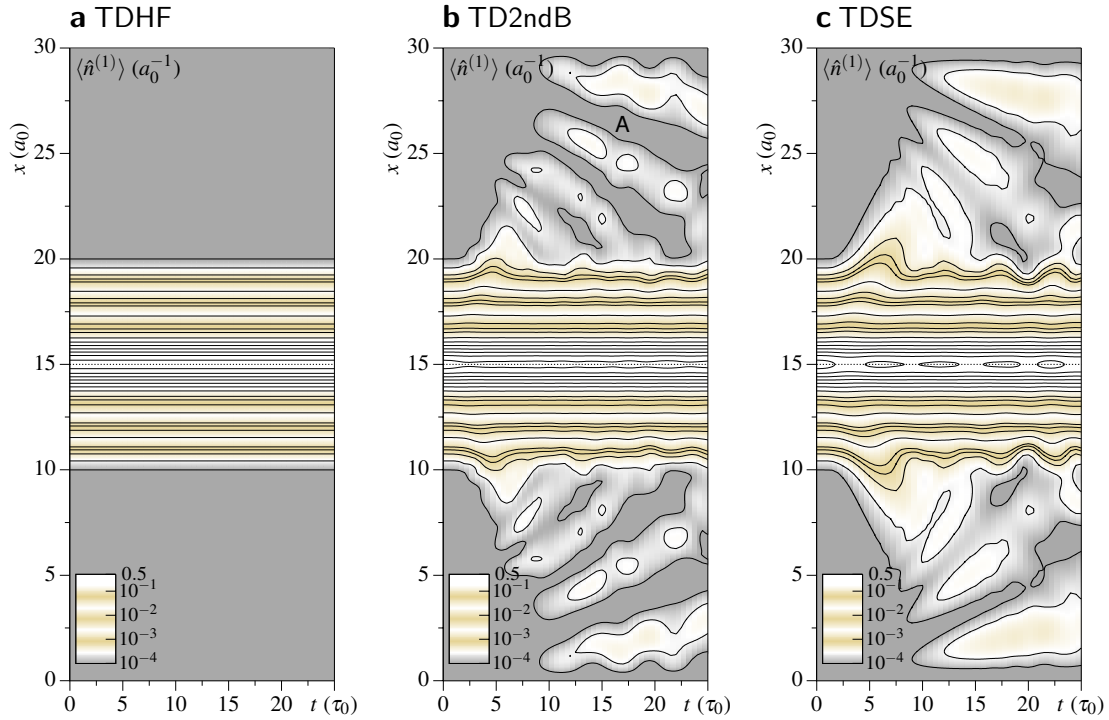


Figure 6.8: Combined contour-density plot (logarithmic) showing the time-dependent one-electron density $\langle \hat{n}^{(1)} \rangle(x, t)$ for the 1D helium atom initially (at $t_0 = 0$) prepared in the Hartree-Fock ground state. In none of the three panels (a-c) an external field is applied to the system. (a) Hartree-Fock approximation (TDHF), (b) second Born approximation (TD2ndB), and (c) solution of the two-electron time-dependent Schrödinger equation (TDSE: exact, but with Hartree-Fock initial state). The contour lines cover a density range from 10^{-4} to $0.5 a_0^{-1}$, including four contour lines in each decimal power between 10^{-1} and 0.1 , and contours between 0.1 and $0.5 a_0^{-1}$ each $0.05 a_0^{-1}$.

Here, ω_{ph} denotes the photon energy, and, instead of applying a laser pulse with a specific time-dependent carrier envelope, the theta-function in Eq. (6.6) simulates an instantaneous, i.e., sudden switch-on of the field which, for non-perturbative intensities (or field strengths E_0), will induce a highly nonlinear electron dynamics.

As a first strong-field example, we study the He atom in a field of $E_0 = 0.1$ a.u. (intensity: 3.5×10^{14} W/cm²). To this end, we represent the nonequilibrium Green function within a simulation box of width $x_0 = 30 a_0$ and use up to 49 FE-DVR basis functions. The photon energy $\omega_{\text{ph}} = 0.54 E_h$ (being equivalent to 84 nm uv radiation or 14.7 eV¹⁷) is chosen such that the laser is near resonant to the first excited singlet state of the atom, compare with ω_{01} in Figure 6.6. The short-time field response resolved in terms of the time-dependent density $\langle \hat{n}^{(1)} \rangle(x, t)$ and its initial state dependence is subject to Figures 6.8 to 6.10, cf. also Ref. [BBB10c].

¹⁷1 E_h (1 Hartree) is equivalent to 27.2 eV.

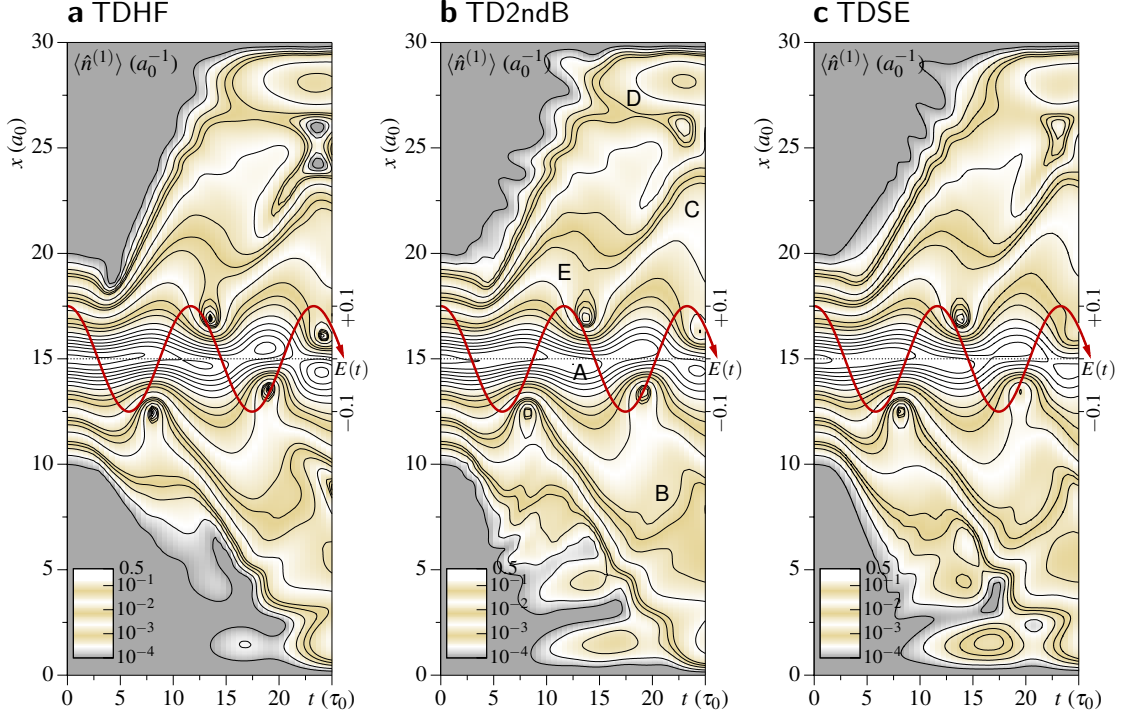


Figure 6.9: Same as in Figure 6.8, but including a non-perturbative uv laser field $E(t) = E_0 \theta(t) \cos(\omega_{\text{ph}} t)$ with parameters $E_0 = 0.1$ (3.5×10^{14} W/cm²) and $\omega_{\text{ph}} = 0.54$ (84 nm). Again, in all panels, the helium atom is prepared in the Hartree-Fock ground state.

First, Figure 6.8 shows the density dynamics in the absence of the laser field ($E_0 = 0$ in Eq. (6.6)) in form of logarithmic density plots including contour lines to guide the eye. In the time-dependent Hartree-Fock approximation (TDHF), panel (a), the initial Hartree-Fock ground state remains an eigenstate of the Hamiltonian. Thus, the initial density does not change in time, $\langle \hat{n}^{(1)} \rangle(x, t) \equiv \langle \hat{n}^{(1)} \rangle(x, 0)$. However, if the Hartree-Fock initial state evolves under the influence of electron-electron correlations (see panel (b), that shows the situation for the second Born approximation (TD2ndB)) the electrons start to move. Precisely, a dynamics is initiated that is conform with a collective, correlated oscillation of the two electrons in the attractive potential of the helium nucleus. Of course, such an excitation may lead to ionization of the atom. However, in the present example, outgoing wave packets are suppressed due to the finite simulation box. Instead, we observe the onset of reflection including interference pattern formation (see, e.g., region A). In comparison to the exact TDSE result with Hartree-Fock initial state¹⁸, panel (c), these time-dependent features are well covered by the second Born approximation.

In Figure 6.9, the non-perturbative laser field as parametrized above is switched on at time

¹⁸The Hartree-Fock ground state of the 1D helium atom suitable for the TDSE as initial condition (i.e., the wave function on a complex 2D lattice) is obtained from a two-electron TDHF code based on the Crank-Nicolson method, see, e.g., *S. Bauch et al.* in Ref. [BHLE10].

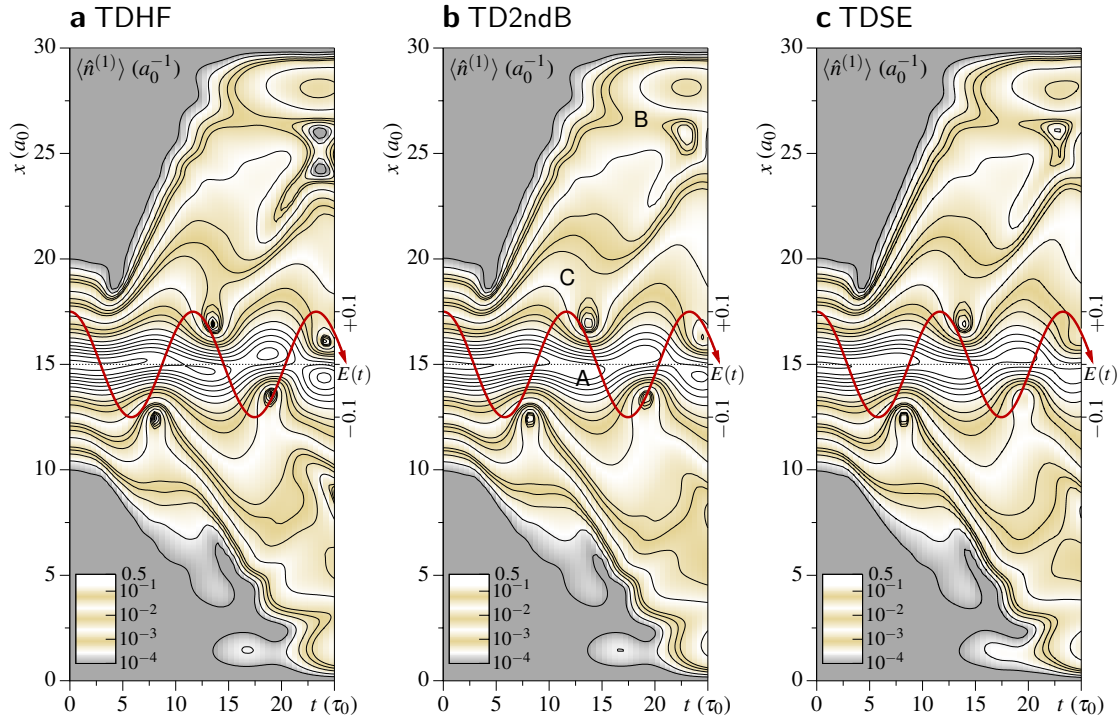


Figure 6.10: Same short-time response as in Figure 6.9, but for the case of self-consistent initial ground states in (b) and (c). Panel (a) is identical to Figure 6.9 (a).

$t_0 = 0$, see the red curves, and, again, the time-dependent simulations start out of the Hartree-Fock ground state. As can be seen in panel (a-c), the external field drives the system out of equilibrium leading to strong density deformations which reveal that both electrons begin to oscillate in the cumulative field of the uv light and the helium core¹⁹. Thereby, many temporal details in $\langle \hat{n}^{(1)} \rangle (x, t)$ at high and low density (see, e.g., the domains labeled A to E in Figure 6.9 (b)) are well resolved in the TD2ndB calculation but are not captured by the TDHF result. Moreover, in Figure 6.9 (b) and (c), the internal oscillatory density behavior of Figure 6.8 is superimposed on the external field response.

Figure 6.10 shows the density response after the preparation of initial states which are consistent with the applied many-body approximation. For the TDSE (Figure 6.10 (c)), this means that the fully correlated ground state is used²⁰. For TDHF and TD2ndB, we take the respective self-consistent ground states as discussed in Chapter 6.1.1, i.e., the propagation of the NEGF in the second Born approximation involves the mixed Green function $g^\square(-i\tau, t)$ (with $-i\tau$ on the imaginary branch on the Keldysh contour \mathcal{C}) which can be omitted in the case of TDHF. Comparing approximate to exact calculations in great detail, we see that TD2ndB performs reasonably well and complies essentially better with the TDSE density than with TDHF. This trend is observed

¹⁹Again, note, that ionization is suppressed and that reflections occur at the interval boundaries.

²⁰Obtained by propagation of the TDSE in imaginary time.

at high density about $x = 15 a_0$ (see label A) as well as for moderate- and low-density domains, where $\langle \hat{n}^{(1)} \rangle(x, t)$ is spatially more extended in the second Born approximation, see labels B and C. In addition, the oscillatory behavior being present in Figures 6.8 and 6.9 vanishes due to the self-consistency. For a difference plot quantifying $\langle \delta \hat{n}^{(1)} \rangle = |\langle \hat{n}_{\text{approx}}^{(1)} \rangle - \langle \hat{n}_{\text{exact}}^{(1)} \rangle|$ and for the same situation with the different contour lines plotted on top of each other, see Ref. [BBB10c].

Using the two-time NEGF, it is, of course, possible to describe other atomic or molecular model systems in nonequilibrium the electronic structure of which is more complex than that of helium. As a proof of principle, we consider the neutral LiH molecule of Chapter 6.1.1 in an (x)uv field of intensity 2.0×10^{16} W/cm² ($E_0 = 0.75$ a.u.) and frequency $\omega_{\text{ph}} = 1.3 E_{\text{h}}$ (35.5 eV). Prior to excitation, we have fixed the Li-H bond length d_{b} , within the fixed-nuclei approximation, to the self-consistent values given in Table 6.2. We emphasize that resolving the exact electron dynamics in the LiH molecule from the TDSE including all four spatial coordinates is, in contrast to helium (with only two electron coordinates), already ambitious but barely feasible. In contrast, going from 1D helium to the lithium hydride model solving the Kadanoff-Baym equations for the one-particle NEGF is conceptually and computationally very simple because the increase of the number of electrons only affects the normalization of the Green function.

Figure 6.11 reveals the picture of the field-induced electron dynamics in LiH over three laser cycles (see the red arrow for the field) as obtained from TDHF (panel (a)), full TD2ndB (panel (b)), second Born approximation plus the generalized Kadanoff-Baym ansatz (panel (c)) and the TDSE (panel (d)). Thereby, we have used an extended FE-DVR basis of size $n_{\text{b}} = 71$ and a simulation box of width $x_0 = 40 a_0$. Note that, in Figure 6.11, only the central part covering $20 a_0$ is shown. As general trend, we, from $\langle \hat{n}^{(1)} \rangle(x, t)$, observe that the full second Born calculation is superior to TDHF. This, in particular, manifests itself in the distinct density between the lithium and the hydrogen atom which, periodically, is considerably too large for TDHF, see the density about $x = 10$ for times $t = 9 \tau_0$ and $t = 13 \tau_0$ indicated by the arrows. This failure is essentially corrected in the second Born calculation, see the smoother density in panel (b).

Moreover, we find that the single-time second Born calculation with the generalized Kadanoff-Baym ansatz produces reasonable results (in comparison to, both, TD2ndB *and* TDSE) although the initial state is of Hartree-Fock type, i.e., is equal to that in panel (a). Hence, we can confirm that the weakness of the TDHF result in (a) is not related to the initial state preparation or the reduced Li-H bond length in Hartree-Fock (cf. Table 6.2) but is clearly due to the neglect of electron correlations which, as Figures 6.11 (a-d) show, are very important regarding the electron dynamics in molecules being exposed to strong fields.

6.3 Revisiting Few-electron Spectra

From tracking the short-time linear response behavior of atoms (as done in Chapter 6.2.1) or molecules, it is nearly impossible to resolve spectral features over the broad energy range of sev-

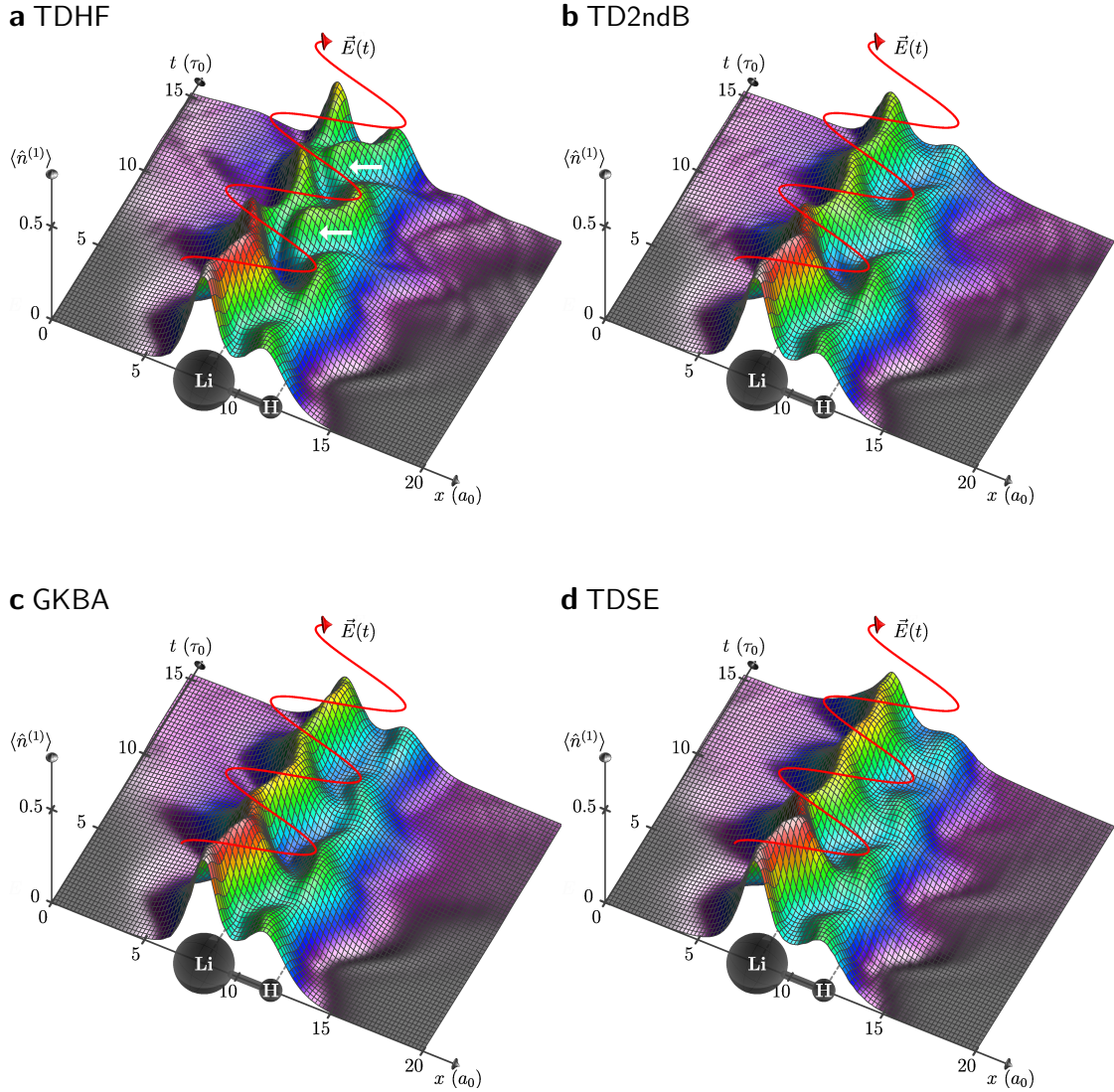


Figure 6.11: Time-dependent one-electron density $\langle \hat{n}^{(1)} \rangle(x, t)$ for the one-dimensional lithium hydride molecule (LiH) in a strong laser field $E(t) = E_0 \cos(\omega_{\text{ph}} t)$ in EDA with self-consistent initial states and bond lengths. The field intensity is $E_0 = 0.75$ a.u. (2.0×10^{16} W/cm²) and the photon energy is $\omega = 1.3 E_h$ (35.5 eV). Panel (a) shows the result of the time-dependent Hartree-Fock approximation (TDHF), panel (b) the dynamics in the fully self-consistent time-dependent second Born approximation (TD2ndB), and the density in panel (c) is obtained by using the generalized Kadanoff-Baym ansatz (GKBA; note that, here, the initial state is of Hartree-Fock type and correlations are treated in second Born approximation). Panel (d) displays the exact density that follows from the solution of the full, four-electron time-dependent Schrödinger equation (TDSE). Overall, panel (b) and (c) are in essentially better agreement with (d) than panel (a): The arrows in (a) indicate particularly strong deviations of TDHF compared to TDSE. For a comparison of the density profiles at specific points in time, see also Ref. [BBB10c].

eral tens of eV²¹ with excellent frequency resolution and inclusion of correlated transitions²². To this end, the extended and accurate evolution of the system has to be recorded over a great many oscillation cycles following a perturbative (e.g., dipole-kick) excitation. However, in a NEGF approach that includes electron correlations, full two-time second Born calculations are limited in length. In addition, in atoms, autoionizing states and resonances are typically well separated in energy—and also in space—from the single-electron part of the spectrum (they are situated above the lowest ionization threshold) which makes numerical access to these states even more difficult. For these reasons, in order to demonstrate the TD2ndB performance with regard to correlation-induced transitions, we want to restrict ourselves in the following to a system which lacks the long-range core potential and, hence, can be treated with less numerical effort²³.

A suitable system is to consider electrons in quantum dots (QDs), synonymously also called *artificial atoms* [Ash96]. Such systems are realized on semiconductor interfaces and, in small islands of material, confine the quantum motion of charge carriers (e.g., electrons or excitons) in all three spatial directions. Pairs of QDs and clusters or lattices of individual dots²⁴ are consequently the equivalent of real molecules. Here, charge carriers may tunnel quantum mechanically from one dot to another giving rise to interesting collective, optical and transport properties [BK93]. Moreover, the coupling of the electronic motion to phonons has great influence on the optical absorption spectra of QDs, e.g., Ref. [LNS⁺06a]. Beyond (nonlinear) optics and laser applications, contacted QDs can act as devices, e.g., as a single-electron transistor due to the Coulomb blockade effect [Kas92], and have also been proposed for quantum gates [LD98].

Although being in some aspects simpler than real atoms, few-electron QDs reveal a similarly rich electronic structure, see, e.g., Ref. [RM02] and references therein. Thereby, with an extent on the nanometer length scale, QDs can have a lot of different geometries [SPBA04] and can trap charges over a large density regime—from single- or few-electron dots to systems with mesoscopic or macroscopic ensembles of charge carriers. Very interesting for theory and nanotechnology applications is the fact that the QD properties can be controlled directly through fabrication²⁵ or, from outside, by applying electric and/or magnetic fields.

Theoretically, QDs are well-suited candidates to study finite size effects and many calculations are available in the literature based on different numerical methods which include self-consistent field (Hartree-Fock) calculations [YL07], configuration interaction [SPBA04, RCBG06], exact diagonalization [JHK93, CF06, KHJN07], and quantum Monte Carlo [EHMG99, FBL01]. An application of the NEGF framework can be found in Ref. [BBvL⁺09].

The QD confinement is often modeled by the potential of an (an)isotropic harmonic-oscillator. For our purpose, we, instead, consider a quantum well potential and neglect wetting layer (con-

²¹Cf. the 1D helium states in Figure 6.6.

²²These appear as correlation satellites in photoelectron spectra, see, e.g., Ref. [SES⁺99].

²³Referring to the size of the one-dimensional FE-DVR basis.

²⁴Referred to as quantum dot molecules.

²⁵Using, e.g., etching techniques, lithographic patterning, or letting QDs epitaxially self-assemble on substrates.

tinuum) states [LNS⁺06b]. The N_e -electron Hamiltonian reads (in SI units),

$$\hat{H} = \sum_{i=1}^{N_e} \left(-\frac{\hbar^2}{2m} \frac{\partial^2}{\partial x_i^2} + v(x_i) \right) + \sum_{1 \leq i < j}^{N_e} \frac{e^2}{4\pi\epsilon_0\epsilon \sqrt{(x_i - x_j)^2 + c}}, \quad (6.7)$$

$$v(x_i) = \begin{cases} 0, & 0 \leq x_i \leq L_0 \\ \infty, & \text{else} \end{cases},$$

where, m denotes the effective electron mass, $\epsilon_0\epsilon$ is the material specific dielectric constant²⁶ and L_0 represents the quantum well width. Further, c (here, in SI units) indicates softening of the electron-electron interaction.

Measuring the total energy in units of the characteristic quantum dot (or quantum well) energy $E_0 = \frac{\hbar^2}{m} \left(\frac{l_0^2}{L_0^2} \right)$, where l_0 is a dimensionless auxiliary parameter, Hamiltonian (6.7) transforms into a form similar to Eqs. (5.3) and (5.4) in Chapter 5.2. Using a simulation box $[0, l_0]$, we have to replace the one-particle potential by $\hat{v}_i^{(1, \text{system})} \rightarrow 0$ for $0 \leq x_i \leq l_0$ and have to change the interaction part according to $\hat{h}_{ij}^{(2)} \rightarrow \lambda[(x_i - x_j)^2 + c]^{-1/2}$. Note that lengths are now measured in multiples of L_0/l_0 . Moreover, the coupling (or Wigner) parameter,

$$\lambda = \frac{e^2 m L_0}{4\pi\epsilon_0\epsilon \hbar^2 l_0}, \quad (6.8)$$

denotes the relative interaction strength, the ratio of the Coulomb energy $E_C = \frac{e^2 l_0}{4\pi\epsilon_0\epsilon L_0}$ to the dot energy E_0 , and is dimensionless. With variation of the coupling parameter, the quantum dot's electronic state can be tuned from Fermi gas- or liquid-like at $\lambda \ll 1$ to Wigner molecule or crystal behavior [EHMG99] at $\lambda \gg 1$. The crossover to $\lambda \rightarrow \infty$ goes along with the appearance of (quasi) classical motion of the individual electrons.

The effect of $l_0 \neq 1$ in Eq. (6.8) is only to scale the characteristic length and quantum dot energy. In the following, we set $l_0 = 5$ and consider the case of moderate coupling $\lambda = 1$. For a GaAs-based semiconductor heterostructure with effective electron mass $m = 0.067m_e$ and dielectric constant $\epsilon = 12.9$, this corresponds to a $L_0 = 51$ nm wide quantum well, which is a realistic assumption. In addition, we consider a four-electron quantum dot ($N_e = 4$ in Eq. (6.7)) and focus on the excitation properties of the singlet (zero-temperature) ground state. For the case of thermodynamic equilibrium, harmonic confinement and different particle numbers, the finite temperature regime has been explored in Ref. [BBvL⁺09].

In comparison to real atoms, no Rydberg-like behavior is assigned to the energy spectrum of artificial atoms. Instead, QDs exhibit purely finite (and possibly divergent) level spacing and clear energy gaps which increase with decreasing dot size. In addition, the absence of electron continua causes states that are only accessible by multi-electron transitions to be non-degenerate. As a consequence, (i) these states (the resonances in the case of real atoms) do, generally, not decay radiationless by autoionization and (ii) appear not as isolated series but are energetically embedded within the single-electron part of the spectrum [HRB03]. On top of that, QDs often

²⁶With ϵ_0 being the usual dielectric constant.

show level bunching, i.e., narrow, nearly degenerate levels which cross or avoid the crossing as function of the coupling strength λ , cf. A in Figure 6.12. In higher dimensionality, such grouping of states goes along with the onset of shell formation [RM02].

6.3.1 Approximate Excitation Level

To clearly distinguish between singly, doubly and other multiply excited states of the quantum dot system, we can call on a metric introduced by *J.F. Stanton* and *R.J. Bartlett* [SB93] for atoms and molecules. This metric is called approximate excitation level (AEL) and acts as a measure of the number of electrons that are excited relative to the system's ground state,

$$A_n = \frac{1}{2} \text{Tr} \left| \rho_n^{(1)}(x, x') - \rho_{\text{gs}}^{(1)}(x, x') \right|. \quad (6.9)$$

Here, the ground ($\rho_{\text{gs}}^{(1)}$) and the excited-state reduced density matrix ($\rho_n^{(1)}$) are expressed in the natural orbital basis which diagonalizes the FE-DVR ground state density matrix, cf. Eq. (6.1). Further, $n_{\geq 0} \in \mathbb{N}$ sorts the N_e -electron levels by their total energy.

In our case, the density matrices entering the AEL are constructed as,

$$\rho_n^{(1)}(x, x') = \sum_{i_1 i_1'} \sum_{i_2 \dots i_{N_e}} c_{i_1 i_2 \dots i_{N_e}}^{(n)} c_{i_1' i_2 \dots i_{N_e}}^{(n)} \phi_{i_1}(x) \phi_{i_1'}(x'), \quad (6.10)$$

after exactly diagonalizing the full Hamiltonian, i.e., $\phi_i(x) = |i\rangle$ denote infinite square well potential eigenfunctions ($\phi_i(x) = \sqrt{\frac{2}{l_0}} \sin(i\pi x/l_0)$, $i = 1, 2, \dots$) and $c_{\vec{i}}^{(n)} = c_{i_1 \dots i_{N_e}}^{(n)}$ are the components of the n -th eigenvector of matrix,

$$H_{\vec{i} \vec{i}'} = \langle \vec{i} | \hat{H} | \vec{i}' \rangle, \quad |\vec{i}\rangle = |i_1 i_2 \dots i_{N_e}\rangle = \bigotimes_{j=1}^{N_e} |\phi_{i_j}\rangle. \quad (6.11)$$

As a specific eigenvector of $H_{\vec{i} \vec{i}'}$ does not automatically lead to a correctly antisymmetrized singlet ground or excited state, only those configurations n are permitted for which the total wave function ($\Lambda_{1 \dots N_e}^-$ is the N_e -particle antisymmetrization operator, e.g., [Bon98]),

$$\begin{aligned} |\Psi_n\rangle &= \Lambda_{1 \dots N_e}^- |S, M_S\rangle |\psi_n\rangle, \\ |S, M_S\rangle &= |0, 0\rangle, \\ |\psi_n\rangle &= \sum_{\vec{i}} c_{\vec{i}}^{(n)} |\vec{i}\rangle, \end{aligned} \quad (6.12)$$

does not vanish and is indeed fully antisymmetric, cf. the configurations indicated in Table D.4 (Appendix D).

6.3.2 One- and Multi-electron Transitions

In this section, we report on the spectral features of the four-electron quantum dot specified above²⁷. Thereby, we want to compare results in time-dependent second Born approximation to

²⁷The inset of Figure 6.12 delineates the corresponding ground state density profile $\langle \hat{n}^{(1)} \rangle(x)$, $x \in [0, l_0]$.

TDHF, on the one hand, and to the exact solution of the time-(in)dependent Schrödinger equation, on the other hand.

The exact excitation energies relative to the QD's ground state are given by $\omega = \omega^{(n)} - \langle \hat{H}_{\text{gs}} \rangle$, where $\omega^{(n)}$ are the relevant eigenvalues of matrix $H_{\vec{i}\vec{i}}$, (Eq. (6.11)) and $\langle \hat{H}_{\text{gs}} \rangle = 5.5278$ is the exact singlet ground state energy in units of E_0 (TDHF: 5.5384, TD2ndB: 5.5306, see also Table D.3 in Appendix D; $E_0 = 11$ meV for the material GaAs). The resulting excitation spectrum is shown by the dots in Figure 6.12 where ordinate position and dot shape characterize the type of transition. While open dots indicate dipole transitions that have dipole strengths (transition rates),

$$D^{(\text{gs} \leftrightarrow n)} \propto \left| \langle \Psi_n | \sum_{i=1}^{N_e} x_i | \Psi_{\text{gs}} \rangle \right|^2 > 0, \quad (6.13)$$

and are highlighted by additional vertical lines in the Figure, closed dots denote transitions of non-dipole type, $D^{(\text{gs} \leftrightarrow n)} \equiv 0$. The left-handed ordinate gives the AEL. Throughout, its variation from an integer has been found to be less than $\Delta A_n = 0.21$. The gray area indicates an interval of width 0.5 about the respective integral number. As there are four electrons confined in the QD, there exist excitations of four kinds: Single ($A_n \approx 1$), double ($A_n \approx 2$), triple ($A_n \approx 3$) and quadruple transitions ($A_n \approx 4$). Further, as indicated by the numbers, the QD has increasing threshold energies at which these transitions (of specific order) appear for the first time.

Figure 6.12 includes the dipole spectrum as obtained by Fourier transform of $\langle \hat{d}^{(1)} \rangle(t)$ from the TDSE, see the red curve referring to the right ordinate. It underlines the dipole transitions found by exact diagonalization and gives information on the dipole strengths which vary over many orders of magnitude. Together with the excitation of the first excited state (at energy separation $\omega = 1.145 E_0$), which indicates the most prominent dipole excitation channel, all one-electron transitions have relatively large rates which decrease as function of energy. In contrast, multi-electron transitions ($A_n > 1$) reveal comparably small rates. However, for $\omega E_0^{-1} > 4$, a transition type distinction based on $D^{(\text{gs} \leftrightarrow n)}$ becomes extremely difficult. In this regime, an unambiguous characterization is only possible through the AEL which provides a clear picture.

So far, we have concentrated on the exact excitation spectrum of the quantum dot. In the following, it will serve as reference for approximate considerations. But before outlining the result of explicitly time-dependent Hartree-Fock and second Born calculations, let us focus on the spectral information that a ground state self-consistent field (Hartree-Fock) calculation can yield.

A ground state Hartree-Fock calculation provides a number of (spin) orbitals φ_i which minimize the total energy functional $\langle \hat{H}_{\text{gs}} \rangle[\varphi_i]$. However, in the optimization procedure, there appear more orbitals than are actually occupied in the system's ground state. From this total set $\{\varphi_i\}$ of orbitals, approximate excited states can be constructed as Slater determinants where one or more electrons are lifted into energetically higher, unoccupied (i.e., virtual) orbitals. This is the frozen orbital approximation of Koopmans [Koo34]. We do not give a detailed description here—to this end, the reader is referred to the textbook [SO96]. Though, concerning our four-electron QD, the resulting excitation energies are given by the black squares in Figure 6.12 and, by construction, have integer AEL, $A_n \in \{1, 2, 3, 4\}$. Due to, both, the neglect of electron correlations and the

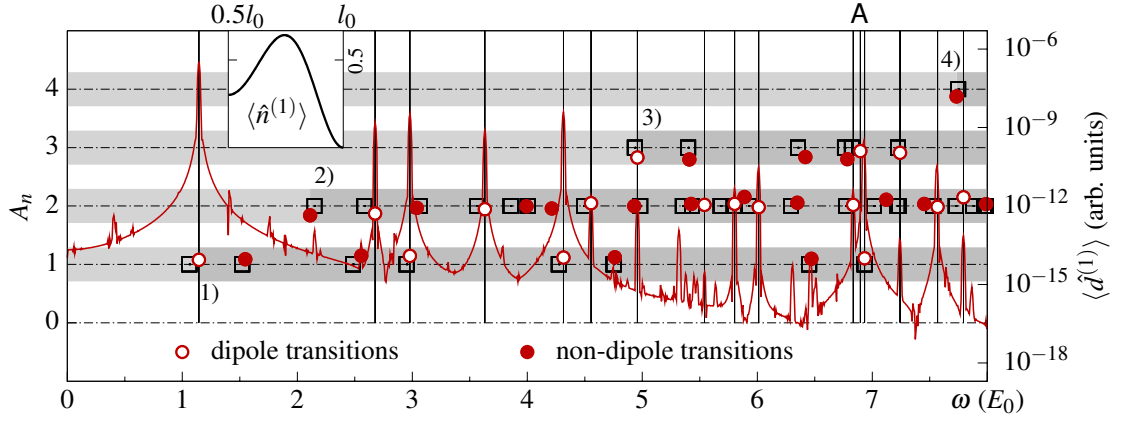


Figure 6.12: Excitation spectrum of a four-electron artificial atom with $l_0 = 5$ and $\lambda = 1$ in Eq. (6.7); for GaAs $E_0 = 11$ meV. The inset shows the singlet ground state density $\langle \hat{n}^{(1)} \rangle$ being symmetric about $l_0/2$. The dots (red) mark the value of the approximate excitation level A_n as obtained from Eq. (6.9). Dipole-allowed transitions are indicated by open dots, dipole-forbidden excitations are represented by full dots. The red curve (assigned to the right ordinate) denotes the dipole spectrum as obtained from the TDSE. The black squares show the excitation energy of single ($A_n \equiv 1$), double (2), triple (3) and quadruple transitions (4) as computed—in the frozen-orbital or Koopmans’ approximation [Koo34]—from the ground state Hartree-Fock orbitals, for details see Ref. [SO96].

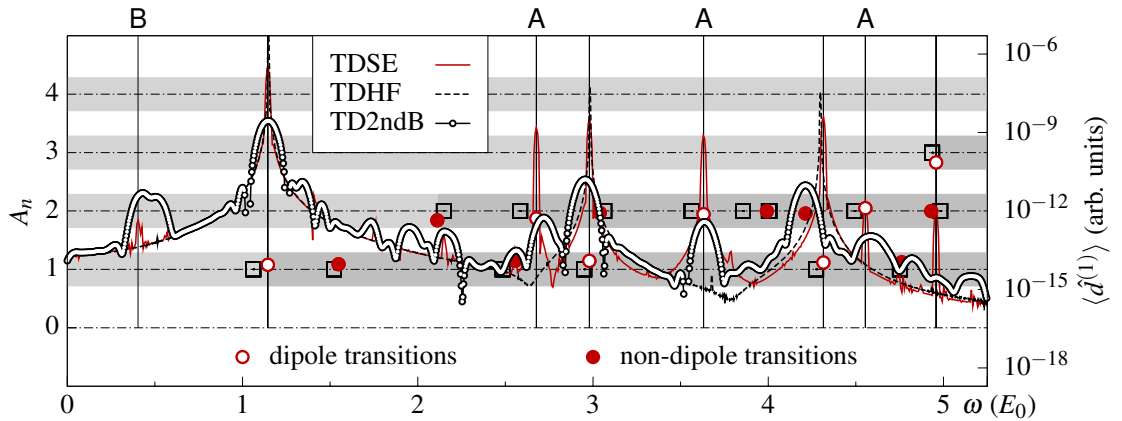


Figure 6.13: Same excitation spectrum as in Figure 6.12, but including the results of TDHF (dashed) and the TD2ndB calculation (dots). While in Hartree-Fock approximation only singly excited states are present, the second Born approximation well reproduces the peak positions (A) of the correlated, two-electron transitions. Note that, for the TD2ndB result (obtained by Fourier transform of the time-dependent dipole moment recorded for $175 \hbar E_0^{-1}$ (10.5 ps)), the initial state was of Hartree-Fock type. This fact explains the additional peak structure (e.g., B) indicating dipole transitions of higher order (cf. situation in Figures 6.8 and 6.9).

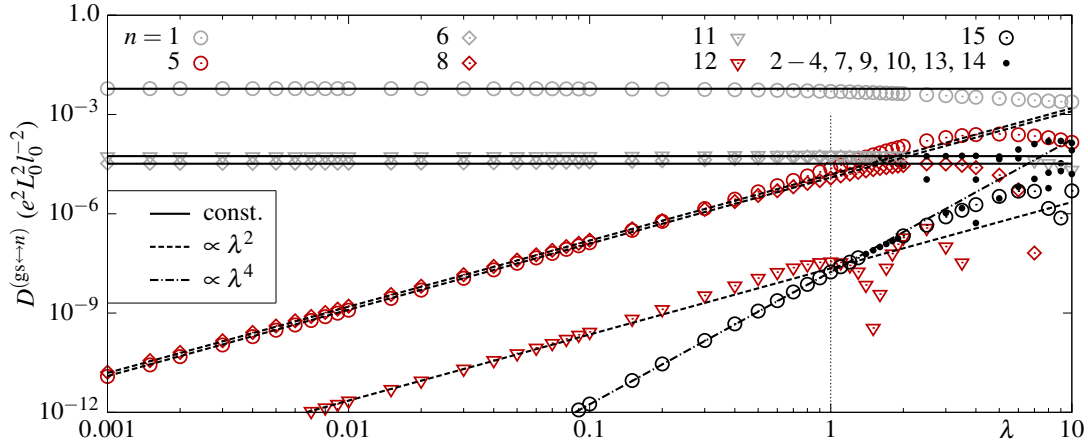


Figure 6.14: Dipole strengths $D^{(\text{gs} \leftrightarrow n)}$ of the four-electron quantum dot ($l_0 = 5$) as function of the coupling parameter λ , Eq. (6.8), which can be tuned by the quantum well width L_0 , see Eq. (6.7). All data are obtained by exact diagonalization and the states n are labeled as in Table D.4 (Appendix D). In the weakly interacting regime, $\lambda < 1$, each N -electron transition shows a $\lambda^{2(N-1)}$ -scaling, i.e., correlated transitions vanish for $\lambda \rightarrow 0$ (non-interacting case). At moderate to strong coupling, $\lambda \gtrsim 1$, the treatment of doubly excited states (red points) is important as their dipole strengths become comparable to those of single-electron transitions (gray). Note that quadruple transitions are not shown.

static (or frozen) orbitals, the spectrum does not coincide with the exact one. However, in contrast to atoms and molecules where Koopmans ansatz is generally considered a bad approximation for resonance states, principally all transitions are captured. Nevertheless, larger deviations are present, e.g., at frequencies $\omega \approx 4$ and $\omega > 7$ (in units of E_0).

Now, we proceed with the comparison to the linear response spectrum as obtained in TDHF and TD2ndB approximation. The results are shown in Figure 6.13 for excitation energies below $\omega E_0^{-1} = 5.25$. In the case of TDHF (see the black dashed curve), we recover all one-electron dipole transitions and the absence of doubly excited states²⁸ provides clear indication that these are induced by electron-electron correlations only. Moreover, due to the fact that natural orbitals are permitted to relax, the peak positions for TDHF are essentially more accurate than those of the respective ground state calculation (cf. the squares). In addition, as correlation shifts in the one-electron part of the spectrum are relatively small, time-dependent Hartree Fock is an adequate approximation for coupling strengths $\lambda \lesssim 1$ as long as the mean-field electron dynamics is concerned.

However, suppose the case where the QD is irradiated by a terahertz laser [UHS⁺11] the typical bandwidth of which is about 10 meV ($0.91 E_0$ ²⁹) or slightly less in QD applications [KTB⁺02].

²⁸Of course, likewise, neither three- nor four-electron transitions appear in TDHF.

²⁹All explicit data refer to GaAs.

Then, at a laser frequency of 8×10^{12} Hz ($3.0 E_0$), electron correlations are non-negligible since the bandwidth covers the second singly excited *as well as* the adjacent (first) doubly excited state³⁰. Thus, an additional, correlated excitation channel is activated which is not taken into account in the TDHF approximation. As the ratio of both transition rates is roughly $\frac{D^{(4 \leftrightarrow 69)}}{D^{(4 \leftrightarrow 83)}} = 0.4$ (cf. Table D.4 in Appendix D), both channels will simultaneously affect the electron dynamics. To support the discussion, Figure 6.14 shows the strengths of the energetically lowest dipole transitions as function of the coupling parameter λ . On top of that, non-marginal population of the correlated shake-up state at $\omega E_0^{-1} = 2.28$ may enable other, similarly effective excitation channels that contribute in subsequent (follow-up) transitions. For these reasons, a correlated treatment of the laser-quantum dot system is definitely necessary in order to account for the multi-electron nature of the artificial atom.

Principally, a full TD2ndB calculation—although approximate—should be capable to describe these correlation-induced processes. However, due to the self-energy being only of second order in the electron-electron interaction, cf. Eq. (3.35), we cannot expect TD2ndB to account for dipole transitions with an excitation level $A_n > 2$. Nevertheless, the time-dependent second Born approximation should well capture the dynamics since doubly excited states are the predominant multi-electron excited states (being separated by several orders of magnitude in dipole strength from three- and four-electron excitations, compare with Figures 6.12 and 6.14). As a prove of principle, we, in Figure 6.13, show the respective dipole spectrum (see the black dotted curve) which has been computed with large numerical effort³¹ starting from the non-correlated Hartree-Fock ground state. Indeed, we observe that peaks of doubly excited states emerge and that they are situated at the expected positions (see labels A in Figure 6.13). In addition, the ratio of the peak heights relative to each other and to the one-electron transitions are in good agreement with the exact TDSE result (red curve). Also, we note that the dynamic determination of doubly excited states in second Born approximation yields better results than the static fixed-orbital approximation (squares) based on the Hartree-Fock method.

Moreover, we need to understand the spectral substructure obtained in the case of TD2ndB. This originates from the fact that the initial state is not self-consistent in terms of the many-body approximation but is of Hartree-Fock type. This, under influence of dynamic electron correlations, leads to an intrinsic density oscillation that triggers additional transitions. Bear in mind that the Hartree-Fock ground state can be understood as a superposition of exact quantum dot eigenstates, i.e., in terms of the many-body wave function, the system is initially not in the ground state. This is the physical explanation for the appearance of higher-order transitions. For instance, the first peak at small energies (labeled B) is responsible for the transition $21 \leftrightarrow 34$, cf. Table D.4. This excitation also shows up in the TDSE calculation if the four-electron initial wave function is not

³⁰Here and in the remainder of this Section, we count only dipole transitions.

³¹To be exact, the nonequilibrium Green function has been propagated up to $t_f = 175 \hbar E_0^{-1}$ in steps of $\delta = 0.02 \hbar E_0^{-1}$ ($n_t = 8750$ time steps). Thereby, $n_b = 23$ FE-DVR basis functions have been included and the distributed memory was approximately $2 \cdot 0.65$ terabyte. The calculation was performed on the HLRN "ice2"-batch system with 2048 MPI processes and several restarts.

fully converged, i.e., not perfectly relaxed into the ground state by imaginary time propagation. A clear assignment of most peaks in the TD2ndB calculation is possible on the basis of the exact diagonalization result but goes beyond the goal of the present discussion.

Finally, we mention that the peak positions of the second and third singly excited state are slightly shifted and appear energetically not in between the results of TDHF and TDSE as one would expect. Eventually, this may indicate of hybridization effect which occurs when two states become close in energy; see the close by doubly excited states and compare with the first one- and the second two-electron transition which are not affected as they are well separated in energy from other states.

6.4 Summary

In this Chapter, using the NEGF, we have investigated (i) the equilibrium, i.e., ground state properties—inter alia the self-consistent energies, densities, potential energy curves and bond lengths—of fundamental two- and four-electron atoms and molecules which obey the one-dimensional model Hamiltonian introduced in Chapter 5, cf. Eqs. (5.3) and (5.4), and (ii) have focused on the (spatially resolved) correlated short-time electron dynamics induced by weak and strong time-dependent external fields. Concerning the self-energy, cf. Chapter 3.3.3, the NEGF results are obtained in the (first-order) Hartree-Fock and the second-(order) Born approximation.

The reason for the restriction to two- and four-electron systems is based on a proof of principle argument and stems from the availability of exact reference data that can be computed from the time-dependent Schrödinger equation (TDSE). We stress that full solutions of the TDSE for $N_e \approx 4$ in 1D, are currently at the limit of numerically attainable spatial resolution (even, if all kind of symmetries of the N_e -electron wave function are being exploited). In contrast, the power of the NEGF approach is affirmed by its basic insensitiveness on the particle number³². However, the price to pay for this promising property is threefold: (i) the two-time non-Markovian structure of the Kadanoff-Baym equations, (ii) the reduced system description in terms the one-particle NEGF, and (iii) the only-approximate treatment of electron correlations (although the self-energies are derived in a conserving manner, cf. Chapter 2).

The former shortcoming of the NEGF approach, which—in practical calculations—limits the simulation time, can be, at least, partly pushed back by an efficient numerical implementation. To this end, for the considered atomic and molecular models of He, Be, H₂, H₃⁺ and LiH, we have applied the grid-based method of Chapter 3. Thereby, the present analysis has shown that a one-dimensional FE-DVR expansion of the Green function allows for a very accurate solution of the Dyson equation (cf. the first part of this Chapter) and is also extremely useful for propagating the Kadanoff-Baym equations in the two-time domain if, in the full second Born approximation, a parallelized and distributed-memory code (as outlined in Chapter 4) is used.

Regarding the presented NEGF results for He and LiH, it has turned out that correlation effects

³²Far-from-equilibrium Green function calculations for more than four electrons are demonstrated in Appendix D in connection with the Kohn mode of interacting electrons in a harmonic trap.

are included to a substantial and valuable level in the case of TD2ndB, which, being of second-order in the electron-electron interaction, reflects the simplest approximation beyond Hartree-Fock. After a discussion on the linear response properties of He in Chapter 6.2.1, we have also put emphasis on the initial state dependence of the dynamics. Further, the discussion on LiH in Chapter 6.2.2 has revealed that, in the presence of strong fields, a beyond-mean-field treatment for molecules is indispensable and that relatively good results are obtained already in the context of the generalized Kadanoff-Baym ansatz. Finally, the four-electron quantum dot system discussed in Chapter 6.3 has provided access to correlated excitations of two-electron type which, so far, could not be investigated for the atomic or molecular examples due to the numerical complexity.

Conclusions

In this thesis, we addressed the description of quantum few-body systems utilizing the method of nonequilibrium Green functions (NEGFs). Thereby, apart from a four-electron quantum dot system (discussed in Chapter 6.3), we mainly focused on the atoms (molecules) He and Be (H_2 , H_3^+ and LiH) modeled in one spatial dimension (Chapter 6.1 and 6.2). To determine the equilibrium ground state properties, we iteratively solved the Dyson equation for the Matsubara Green function, and, to study the correlated electron dynamics in the presence of (non-)perturbative external fields, we numerically integrated the full two-time Kadanoff-Baym equations as far as it has been possible using the means at disposal. Except for the model character and the restriction of the electron motion to one dimension, the analysis was carried out *ab initio*, i.e., no assumptions on the electronic structure and the dynamical processes were made. Hence, all equilibrium and nonequilibrium properties arose self-consistently from the model Hamiltonian (Chapter 5) which involves long-range soft-Coulomb interactions between the charge carriers and describes the coupling to the external field in the electric dipole approximation. Throughout the analysis, electron-electron correlations were treated on the level of the second(-order) Born approximation, and, beyond single-time Hartree-Fock calculations, also the generalized Kadanoff-Baym ansatz was applied to a certain extent.

Irrespective of illustrative purposes, the reasons for applying the NEGF formalism to atomic and molecular models were manifold. Firstly, model atoms and molecules represent natural generalizations of one-dimensional lattice systems [PvFVA10] in the context of which—instead of (a few) on-site occupation numbers—an extended density distribution has to be resolved in space and time. Secondly, the fact that electron-electron correlations play a substantial role in these systems¹ [BBB10d] motivated the inclusion of retardation, i.e., memory effects in the Kadanoff-Baym equations from the beginning. Thirdly, the possibility that, in reduced dimensionality, exact reference data can be obtained from the solution of the time-(in)dependent Schrödinger equation allowed us to discuss on the performance of the second Born approximation, i.e., to detect the degree to which electron-electron correlation effects are described.

¹This particularly applies to the case where the electrons are in the singlet spin configuration.

Furthermore, the reason to study model atoms and molecules was associated with the general interest on far-from-equilibrium processes in atoms and molecules exposed to intense (laser) fields [BK00, KI09]. In this direction, among other methods such as time-dependent density functional theory [Bau97, RB09b] or density matrix renormalization group [WF04], the use of nonequilibrium Green functions represents an alternative approach where, in contrast to wave function-based methods, the many-body dynamics are described by means of reduced quantities—the two-time correlation functions. However, along with previous works [DvLS06, DvL07] and the computational advances presented in the thesis at hand, it remains to be seen whether or not two-time NEGFs become truly important for time-dependent *first-principle* investigations in the field of atomic and molecular physics.

The main objective of this thesis was to show that, on the basis of the finite element-discrete variable representation (FE-DVR), at least in 1D, efficient solutions of the two-time Kadanoff-Baym equations for inhomogeneous systems become possible². Thereby, the expansion of the nonequilibrium Green function in terms of FE-DVR basis functions is favorable because (i) it allows for a very flexible combination of grid and basis methods, where the basis can be well adapted to the problem considered, and where, eventually, the basis dimension can be reduced to a minimum [BBB10b], (ii) it goes along with simple semianalytical matrix elements for the kinetic and the one-particle potential energy [RM00], and (iii) it is highly advantageous with respect to the treatment of binary interactions introducing a high degree of diagonality into the respective matrix elements [BBB10a], which are then readily evaluated from the underlying set of FE-DVR grid points (i.e., from the generalized Gauss-Lobatto points defined in Chapter 3.2).

Point (iii) in the above enumeration is particularly responsible for the fact that Feynman diagrams for the self-energy are easily interpreted in FE-DVR representation. To be exact, one finds that, for a basis dimension n_b and a skeleton diagram with M vertex points, instead of $\mathcal{O}(n_b^{2M-2})$ only $\mathcal{O}(n_b^{M-2})$ summations are required in the evaluation of a single self-energy matrix element (cf. Chapter 3.3.3). Hence, regarding the solution of the Dyson equation as well as the two-time Kadanoff-Baym equations, an often repeated computation of the self-energy kernel in the second Born approximation ($M=4$) is no longer a demanding issue for larger basis dimensions.

As a consequence, several hundred FE-DVR basis functions can easily be incorporated to determine highly accurate solutions of the Dyson equation (Chapter 4.1.1). Principally, the finite element-discrete variable representation leads to similar advances in spatial resolution when the non-Markovian time evolution of the NEGF is concerned. But since here the memory requirement in the numerics grows quadratically with, both, basis dimension and final propagation time (and since the computational resources are limited), in general, a compromise has to be found between a reasonable basis size and the target simulation time (Chapter 4.1.2).

Further, in order to raise the possibility of extended two-time calculations, we, in the thesis at hand, developed a code that allows to integrate the two-time Kadanoff-Baym equations very efficiently on multi-processor machines. Thereby, the established parallel program can not only be

²So far, the FE-DVR has not been used in the context of nonequilibrium Green functions calculations.

used on shared-memory computers but is particularly suitable for large-scale distributed-memory computing. This was realized by a well-organized distribution of the correlation functions $g^>$ and $g^<$ over the compute nodes (Chapter 4.2), and benchmark calculations on the HLRN system³ have shown that load-balanced nonequilibrium Green function calculations can be achieved at a degree of parallelization of 95% and more. We emphasize that without such a distributed-memory code, it would not have been possible to calculate the dipole excitation spectrum of the four-electron quantum dot (discussed in Chapter 6.3) in the full (i.e., two-time) second Born approximation.

Turning back to the application of the NEGF method on model atoms and molecules, we, in Chapter 6.1, studied the spin-singlet ground states of the two-electron systems He, H₂ and H₃⁺, and likewise of the four-electron systems Be and LiH. Thereby, all electrons were treated on the same footing and the zero-temperature properties were extracted from the (non)correlated Matsubara Green function $g^M(\tau)$ in FE-DVR representation. Regarding the total (binding) energies, the self-consistent bond-lengths and the one-electron densities, the inclusion of electron-electron correlations in the second Born approximation yielded satisfactory results. Throughout, the comparison of the results to the mean-field (Hartree-Fock) findings, on the one hand, and to the exact ground states, on the other hand, indicated that correlations are being described to a substantial level such that the main features of the fully correlated ground states were correctly reproduced. According to the total energies, we found that the second Born approximation accounts for about 60% of the correlation energy (the energy contribution missing in the mean-field picture). In addition, by exploring the internal electronic structure by means of natural orbitals and their occupations, we observed full consistency in the results. In summary, although being the simplest conserving approximation beyond the level of Hartree-Fock, the second Born approximation turned out to perform reasonably well.

After the discussion on the equilibrium properties, we solved the two-time Kadanoff-Baym equations under two aspects: (i) to explore the linear response properties of the one-dimensional helium atom in Hartree-Fock and second Born approximation, and (ii) to assess the second Born approximation on the basis of the short-time electron dynamics induced by strong laser fields (at ultraviolet excitation conditions). Concerning the latter, we again focused on the helium atom but, in addition, presented results for the lithium hydride molecule. Furthermore, initial correlations were treated in the mixed Green function approach which involves the full (or extended) round-trip Keldysh contour (Chapter 2).

From the behavior of the time-dependent dipole moment of the one-dimensional helium atom exposed to a perturbative dipole δ -kick excitation, we observed that the second Born approximation performs just as well in explicitly time-dependent situations than in equilibrium (Chapter 6.2.1). Thereby, as had been expected, systematically better results were obtained when initially the atom is prepared in the ground state that is self-consistent to the applied many-body approximation. Moreover, by a thorough spectral analysis of the dipole moment time series, we found that the energy of the first excited state is improved by 75% (related to the energy difference between the

³I.e., on the machines of the North-German Supercomputing Alliance (<https://www.hlrn.de>).

Hartree-Fock and the exact result) in the second Born approximation.

Generally, the time-dependent dipole moment contains much information about the electronic structure. However, owing to the limited simulation time and consequent low spectral resolution, the extraction of the complete dipole spectrum turned out to be very difficult. Therefore, we could only discuss on the energetically lowest one-electron excitation channel. The autoionizing resonance states—clear signs of electronic correlations—appeared to be out of reach at least in a full two-time treatment of the problem. This means that to access them in a time-dependent NEGF framework will require further approximations as, e.g., provided through the generalized Kadanoff (GKB) ansatz. Concerning the time-dependent dipole moment of the He model, the GKB ansatz led to adequate results. To extend the GKB calculations such that, eventually, the complete spectrum becomes accessible, is subject of ongoing work. Along with this intention, however, the problem of preparing an initial state consistent with the GKB ansatz has to be solved [HBB11]. Otherwise, the excitation spectrum will be heavily overlaid by additional peaks of (non-ground state) transitions.

The findings in Chapter 6.2.2 allow us to conclude that the second Born approximation performs well also in the presence of strong laser fields⁴, i.e., in situations where the field intensity is larger than 10^{14} W/cm². Thereby, the discussion on the helium atom accentuated the importance of a consistent initial state for modeling the system's time evolution, and, the lithium hydride example indicated that the second Born approximation, on, both, the full two-time and the GKB level, is capable of correcting considerable deficiencies in the mean-field dynamics. Of course, generally, the considered field strengths will lead to non-negligible ionization of the model atoms and molecules. However, on the short time scales that have been considered ionization processes were irrelevant.

Finally, to demonstrate that the second Born approximation can, principally, well describe purely correlation-induced transitions was subject to the last part of Chapter 6. Here, we concentrated on the ground state excitation spectrum of a four-electron 1D quantum dot where the peaks of two-electron excitations (the resonance states in the case of helium) were much easier accessible from the time-dependent dipole moment as, computationally, a smaller FE-DVR basis allowed for longer two-time calculations and, in addition, no continuum states exist in the considered model of the quantum dot.

”Cui bono?”⁵—Of course, this question is particularly reasonable in light of the fact that full two-time solutions of the Kadanoff-Baym equations remain costly for inhomogeneous and strongly interacting quantum systems even if the techniques developed here can be successfully applied.

At this point, an entire or definite answer to this question cannot be given. But we believe that, in the perspective, the thesis at hand will stimulate further investigations on the basis of the nonequilibrium Green function which instead of being methodical are motivated by a concrete

⁴In the examples presented, the photon energy was comparable to typical (one-electron) excitation energies.

⁵Latin for ”Whom does it serve?”.

physical far-from-equilibrium problem. In the course of this, certainly, the NEGF methods' full potential can be utilized as the system to be described does not need to be closed or at zero-temperature.

While the developed distributed-memory algorithm should be of general interest in the field of (quantum) kinetic equations that deal with retardation, the advances due to the FE-DVR representation of the nonequilibrium Green function should be of relevance for specific applications which require excellent spatial resolution at relatively low numerical cost. Furthermore, we emphasize that the FE-DVR approach is very attractive also for other classes of many-body approximations such as GW or T-matrix, because the generation of the corresponding self-energies will notably simplify just as in the case of the second Born approximation.

Further, the grid-based representation of the nonequilibrium Green function makes the presented FE-DVR approach particularly interesting for the investigation of quantum scattering and collision processes. In this context, a promising potential application of the developed techniques could be the modeling of nuclear reactions⁶ such as the collision of one-dimensional nuclear slabs [DRB10]. While, here, so far only results on the mean-field level have been reported [RBBBD11], the use of an FE-DVR basis could allow for efficient (brute-force) NEGF simulations that include correlations.

⁶According to *A. Rios et al.* (Ref. [RBBBD11]), the method of nonequilibrium Green functions is "underutilized in nuclear physics".

The Gauss-Lobatto Quadrature Rule

The quadrature rule introduced by Eq. (3.8) in Chapter 3.2.2 is a generalization of the standard Gauss-Lobatto quadrature¹ defined on the interval $[-1, 1]$ (n_g abscissas),

$$\int_{-1}^{+1} dx g(x) = w_0 g(-1) + \sum_{m=1}^{n_g-2} w_m g(x_m) + w_{n_g-1} g(1), \quad (\text{A.1})$$

$$x_0 = -1,$$

$$x_{n_g-1} = 1.$$

Thereby, the extension to arbitrary interval boundaries is achieved by the linear transformation of Eq. (3.5).

With the quadrature points x_m and weights w_m defined by ($\mathcal{L}_n(x) = \frac{1}{2^n n!} \frac{d^n}{dx^n} [(x^2 - 1)^n]$ are the Legendre polynomials),

$$0 = \left. \frac{d\mathcal{L}_{n_g-1}(x)}{dx} \right|_{x=x_m}, \quad (\text{A.2})$$

$$w_m = \begin{cases} \frac{2}{n_g(n_g-1)}, & m = 0 \text{ and } m = n_g-1 \\ \frac{2}{n_g(n_g-1) [\mathcal{L}_{n_g-1}(x_m)]^2}, & \text{else} \end{cases},$$

Eq. (A.1) is accurate for polynomials of degree $2n_g-1$ or less. The abscissas are symmetric about the origin and the same applies to the weights,

$$x_m = x_{n_g-1-m}, \quad w_m = w_{n_g-1-m}, \quad m = 0, 1, \dots, n_g-1. \quad (\text{A.3})$$

In Table A.1 (see page 112), we collect the numerical values of the Gauss-Lobatto points and weights for different n_g . If less than nine decimal places are given, the values are exact².

¹The Gauss-Lobatto rule is also known as the Radau quadrature [Cha60].

²Note that, besides computing the Gauss-Lobatto points directly as roots according to Eq. (A.2) and Newton's method [PTVF07], there exist other methods, e.g., the Golub-Welsch algorithm [GW69].

Table A.1: Numerical values of the precomputed and tabulated Gauss-Lobatto points x_m and weights w_m for $n_g=3$ up to $n_g=15$ ($m=0, 1, \dots, n_g - 1$ with the symmetries of Eq. (A.3)).

n_g	x_m	w_m	n_g	x_m	w_m
3	0	1.333333333	11	0	0.300217595
	± 1	0.333333333		± 0.295758136	0.286879125
4	± 0.447213595	0.833333333	± 0.565235327	0.248048104	
	± 1	0.166666667	± 0.784483474	0.187169882	
5	0	0.711111111	± 0.934001430	0.109612273	
	± 0.654653671	0.544444444	± 1	0.018181818	
	± 1	0.1	12	± 0.136552933	0.271405241
6	± 0.285231516	0.554858377		± 0.399530941	0.251275603
	± 0.765055324	0.378474956		± 0.632876153	0.212508418
	± 1	0.066666667	± 0.819279322	0.157974706	
7	0	0.487619048	± 0.944899272	0.091684517	
	± 0.468848793	0.431745381	± 1	0.015151515	
	± 0.830223896	0.276826047	13	0	0.251930849
	± 1	0.047619048		± 0.249286930	0.244015790
8	± 0.209299218	0.412458795		± 0.482909821	0.220767794
	± 0.591700181	0.341122692		± 0.686188469	0.183646865
	± 0.871740149	0.210704227	± 0.846347565	0.134981927	
	± 1	0.035714286	± 0.953309847	0.077801687	
9	0	0.371519274	± 1	0.012820513	
	± 0.363117464	0.346428511	14	± 0.116331869	0.231612794
	± 0.677186280	0.274538713		± 0.342724013	0.219126253
	± 0.899757995	0.165495362		± 0.550639403	0.194826149
	± 1	0.027777778		± 0.728868599	0.160021852
10	± 0.165278958	0.327539761		± 0.867801054	0.116586656
	± 0.477924950	0.292042684	± 0.959935045	0.066837284	
	± 0.738773865	0.224889342	± 1	0.010989011	
	± 0.919533908	0.133305991	15	0	0.217048116
	± 1	0.022222222		± 0.215353955	0.211973586
		± 0.420638055		0.196987236	
		± 0.606253205		0.172789647	
		± 0.763519690		0.140511700	
		± 0.885082044	0.101660070		
		± 0.965245927	0.058029893		
		± 1	0.009523810		

Two-time Propagation of the NEGF; Algorithm and Tests

Collision Integrals

In detail, the collision integrals relevant for the time evolution of the nonequilibrium Green function, cf. Eq. (2.44) in Chapter 2, read ($\xi \in \{1, 2\}$ denotes the spin degeneracy factor and without loss of generality $t_0 = 0$),

$$\begin{aligned}
i_1^>(t, \bar{t}) &= \int_0^t dt' \Sigma_\xi^{><}(t, t') g^>(t', \bar{t}) + \int_0^{\bar{t}} dt' \Sigma_\xi^{>}(t, t') g^{<->}(t', \bar{t}) \\
&\quad - i \int_0^\beta d\tau' \Sigma_\xi^{\lceil}(t, -i\tau') g^{\lceil}(-i\tau', \bar{t}), \\
i_2^<(\bar{t}, t) &= \int_0^{\bar{t}} dt' g^{><}(\bar{t}, t') \Sigma_\xi^{<}(t', t) + \int_0^t dt' g^{<}(\bar{t}, t') \Sigma_\xi^{<->}(t', t) \\
&\quad - i \int_0^\beta d\tau' g^{\lceil}(\bar{t}, -i\tau') \Sigma_\xi^{\lceil}(-i\tau', t), \\
i^{\lceil}(t, -i\bar{\tau}) &= \int_0^t dt' \Sigma_\xi^{><}(t, t') g^{\lceil}(t', -i\bar{\tau}) + \int_0^\beta d\tau' \Sigma_\xi^{\lceil}(t, -i\tau') g^M(\tau' - \bar{\tau}), \\
i^{\lceil}(-i\bar{\tau}, t) &= \int_0^t dt' g^{\lceil}(-i\bar{\tau}, t') \Sigma_\xi^{<->}(t', t) + \int_0^\beta d\tau' g^M(\bar{\tau} - \tau') \Sigma_\xi^{\lceil}(-i\tau', t),
\end{aligned} \tag{B.1}$$

where, concerning the FE-DVR representation, the notation implies matrix multiplication and $X^{\gtrless} (X = g, \Sigma_\xi)$ means $X^{\gtrless} - X^{\lesseqgtr}$ with the same time arguments for both expressions. Further, the self-energies Σ_ξ^x ($x = >, <, \lceil, \rceil$) do not include the time-local Hartree-Fock part as it is absorbed in the single-particle energy \bar{h} , compare with Eq. (3.39) in Chapter 3.

For completeness, we collect the symmetry properties: $i_1^{\gtrless}(t_1, t_{\bar{1}}) = -[i_2^{\gtrless}(t_{\bar{1}}, t_1)]^\dagger$ and, on the time diagonal, $i_{1,2}^>(t, t) = i_{1,2}^<(t, t)$. In addition, it is $i^{\lceil}(-i\tau) = [i^{\lceil}(t, -i(\beta - \tau))]^\dagger$.

Algorithm Overview

Including initial correlations via the Matsubara Green function $g^M(\tau)$, per time step $\delta \ll 1$ (in units of τ_0), we have to propagate the greater and lesser correlation functions, $g^>(t, \bar{t})$ and $g^<(\bar{t}, t)$, as well as the mixed Green functions, $g^{\lceil}(-i\bar{\tau}, t)$ and $g^{\lceil}(t, -i\bar{\tau})$, cf. Figure 2.4. Thereby, as outlined in Chapter 2, it is sufficient to compute $g^>(t, \bar{t})$ for $t > \bar{t}$ and $g^<(\bar{t}, t)$ for $t \geq \bar{t}$.

Following the method described by *A. Stan, N.E. Dahlen* and *R. van Leeuwen* in Ref. [SDvL09], one has to take into account five distinct propagation steps (note that, below, all Green functions are known for all times less than and equal to t):

$$\begin{aligned} g^>(t + \delta, \bar{t}) &= u_\delta(t) g^>(t, \bar{t}) - v_\delta(t) i_1^>(t, \bar{t}) , \\ g^<(\bar{t}, t + \delta) &= g^<(\bar{t}, t) u_\delta^\dagger(t) - i_2^<(\bar{t}, t) v_\delta^\dagger(t) , \\ g^<(t + \delta, t + \delta) &= u_\delta(t) \left(g^<(t, t) + \sum_{n=0}^{\infty} c^{(n)}(t) \right) u_\delta^\dagger(t) , \quad (\text{time diagonal}) \end{aligned} \quad (\text{B.2})$$

and,

$$\begin{aligned} g^{\lceil}(t + \delta, -i\bar{\tau}) &= u_\delta(t) g^{\lceil}(t, -i\bar{\tau}) - v_\delta(t) i^{\lceil}(t, -i\bar{\tau}) , \\ g^{\lceil}(-i\bar{\tau}, t + \delta) &= g^{\lceil}(-i\bar{\tau}, t) u_\delta^\dagger(t) - i^{\lceil}(-i\bar{\tau}, t) v_\delta^\dagger(t) , \end{aligned} \quad (\text{B.3})$$

where,

$$u_\delta(t) = \exp(-i \bar{h}(t) \delta) , \quad v_\delta(t) = \frac{1}{\bar{h}(t)} (1 - \exp(-i \bar{h}(t) \delta)) , \quad (\text{B.4})$$

are constructed from the energy $\bar{h}(t) = \bar{h}[g, \tilde{u}](t) = h(t) + \Sigma_\xi^{\text{HF}}[g^<, \tilde{u}](t)$ (single-particle plus Hartree-Fock energy), and, recursively,

$$c^{(n)}(t) = \frac{i \delta}{n+1} \left[\bar{h}(t), c^{(n-1)}(t) \right]_- , \quad c^{(0)}(t) = -i \delta i_{\text{diag}}^<(t, t) , \quad (\text{B.5})$$

with, on the time diagonal, $i_{\text{diag}}^<(t, t) = i_1^<(t, t) - i_2^<(t, t) = i_1^>(t, t) - i_2^>(t, t)$. In Eq. (B.5), as a general rule, $0 < n < 5$ is known to yield sufficient accuracy, e.g., [SDvL09].

In the practical calculation, the following steps are processed in sequence:

- (i) Provide the self-consistent (equilibrium) Matsubara Green function $g_{m_1 m_{\bar{1}}}^{M, i_1 i_{\bar{1}}}(\tau)$ as obtained from the Dyson equation, cf. Eqs. (4.4) and (4.5) in Chapter 4.1.1.
- (ii) Initialize the Green functions $g_{m_1 m_{\bar{1}}}^{x, i_1 i_{\bar{1}}}(\cdot, \cdot)$ ($x = <, \lceil, \rceil$) with time argument $t_0 = 0$ according to Eq. (4.1).
- (iii) Compute $\bar{h}_{m_1 m_{\bar{1}}}^{i_1 i_{\bar{1}}}(t)$ as sum of $h_{m_1 m_{\bar{1}}}^{i_1 i_{\bar{1}}}(t)$ and $\Sigma_{\xi, m_1 m_{\bar{1}}}^{\text{HF}, i_1 i_{\bar{1}}}[g^<, \tilde{u}](t)$.
- (iv) Diagonalize $\bar{h}(t)$ and construct the matrix elements $u_{\delta, m_1 m_{\bar{1}}}^{i_1 i_{\bar{1}}}(t)$ and $v_{\delta, m_1 m_{\bar{1}}}^{i_1 i_{\bar{1}}}(t)$ defined by Eq. (B.4).

-
- (v) Evaluate all the self-energies $\Sigma_{\xi, m_1 m_{\bar{1}}}^{x, i_1 i_{\bar{1}}}(\cdot, \cdot)$ ($x = >, <, \lceil, \rfloor$) that enter the collision integrals.
 - (vi) Perform the collision integrals $i_{1, m_1 m_{\bar{1}}}^{>, i_1 i_{\bar{1}}}(\cdot, \cdot)$, $i_{2, m_1 m_{\bar{1}}}^{<, i_1 i_{\bar{1}}}(\cdot, \cdot)$ and $i_{m_1 m_{\bar{1}}}^{x, i_1 i_{\bar{1}}}(\cdot, \cdot)$ ($x = \lceil, \rfloor$) with the time arguments as required by Eqs. (B.2) and (B.3).
 - (vii) Propagate all necessary Green functions¹, $g_{m_1 m_{\bar{1}}}^{\geq, i_1 i_{\bar{1}}}(\cdot, \cdot)$ and $g_{m_1 m_{\bar{1}}}^{\lceil, i_1 i_{\bar{1}}}(\cdot, \cdot)$, using, respectively, Eq. (B.2) and Eq. (B.3).
 - (viii) Return to (ii) with t incremented by δ .

Conservation of Particle Number

The particle number at a time t is obtained from the NEGF by,

$$N_e = -i \xi \text{Tr}[g^<(t, t)] , \quad (\text{B.6})$$

where $\xi \in \{1, 2\}$ denotes the degeneracy factor.

Taking Eq. (B.6) at $t = t + \delta$ and inserting the third line of Eq. (B.2) yields,

$$N_e = -i \xi \text{Tr} \left[u_\delta(t) g^<(t, t) u_\delta^\dagger(t) \right] - i \xi \text{Tr} \left[u_\delta(t) \sum_{n=0}^{\infty} c^{(n)}(t) u_\delta^\dagger(t) \right] .$$

The first term on the right hand side just gives N_e (the particle number at time t) since the trace is invariant under cyclic permutation and $u_\delta(t)$ is unitary. Consequently, the second term has to vanish, i.e., $\sum_{n=0}^{\infty} \text{Tr}[c^{(n)}(t)] = 0$. In fact, each single trace must disappear separately as the time-stepping scheme remains valid when adding the matrices $c^{(n)}(t)$ term by term. Due to the recursive definition, it follows (case $n = 0$),

$$\text{Tr}[i_{\text{diag}}^{<}(t, t)] = 0 , \quad (\text{B.7})$$

which is an important property to satisfy in the implementation—its violation² provides indications to potential errors.

Invariance of the Kohn Mode in a Conserving Theory

Another sensitive test for the numerics is to consider an ensemble of electrons in a harmonic confinement ($\hat{v}^{(1)}(x) = \frac{1}{2}\omega^2 x^2$ in Eqs. (5.3) and (5.4) (Chapter 5.2); trap frequency ω) and to observe and record the form of the Kohn (center of mass or sloshing) mode.

Generally, the so-called *Kohn theorem*³ [BJH89, Koh61] states that, for an interacting classical or quantum system in a harmonic trap⁴ and initially in the ground state (or in equilibrium), the application of a homogeneous time-dependent dipole field $E(t)$ induces a center of

¹Due to symmetry reasons, one may skip calculating one of the mixed Green functions and keep either g^{\lceil} or g^{\rfloor} , see the third line in Eq. (2.38) of Chapter 2.

²By values larger than the computational accuracy.

³Also known as the *generalized Kohn theorem*.

⁴Of arbitrary dimensionality.

mass (c.m.) dynamics that coincides with that of a noninteracting system: The c.m. coordinate $X(t) = N_e^{-1} \sum_i x_i(t)$ performs the motion of a forced harmonic oscillator.

Mathematically, the theorem can be expressed by means of collective ladder operators [BJH89] $\hat{c}^\pm = \sum_i \omega \hat{x}_i \mp i \hat{p}_i$ (in atomic units; \hat{p}_i denotes the momentum operator of particle i) which create (annihilate) states with excess (loss) energy ω . Realizing that $[\hat{H}^{(2)}, \hat{c}^\pm]_- = 0$, where $\hat{H}^{(2)}$ is the exact pair interaction Hamiltonian, cf. Eq. (2.8), the dynamics of \hat{c}^\pm are obtained from the Heisenberg equation as [BBvL07],

$$\frac{d}{dt} \hat{c}^\pm = \pm i \omega \hat{c}^\pm \mp i N_e E(t). \quad (\text{B.8})$$

With the definition of the center of mass $\hat{X} = (2N_e)^{-1}(\hat{c}^+ + \hat{c}^-)$, one, in Eq. (B.8), recovers the driven oscillation,

$$\frac{d^2}{dt^2} \hat{X} + \omega^2 \hat{X} = E(t). \quad (\text{B.9})$$

Strictly speaking, the Kohn theorem holds only for an exact treatment of the pair interactions with the result that the commutator above vanishes (leading over to Eq. (B.8)), i.e., it not necessarily remains true, if the interaction part $\hat{H}^{(2)}$ is being approximated. However, the validity of the Kohn theorem can be extended to an important class of approximate (zero and finite temperature) theories [BBvL07]. It can be proven that the Kohn theorem is obeyed for any approximation that preserves particle number and total momentum. Because this is nothing but the sufficient criterion formulated by Baym and Kadanoff for a conserving theory, any Φ -derivable approximation—as is the Hartree-Fock and second Born approximation—fulfills the Kohn theorem.

Concerning simulation tests, the Kohn theorem is applied with the implication that any equilibrium (one-electron) density profile $\langle \hat{n}^{(1)} \rangle(x, t \equiv 0)$ retains its shape when initially only the c.m. mode (of eigenfrequency ω) was excited. This behavior can be accurately tested along with the time-dependence of the c.m. coordinate $X(t)$ (the dipole-moment $\langle \hat{d}^{(1)} \rangle(t)$) and the kinetic and single-particle potential energy.

As example, we, in Figure B.1, consider the Kohn mode dynamics of ten spin-restricted electrons ($\xi = 2$) in four different approximate cases: time-dependent Hartree-Fock (TDHF, green dashed curves), fully self-consistent time-dependent second Born (TD2ndB 2, blue solid curves), time-dependent second Born with non-correlated Hartree-Fock initial state (TD2ndB 1, blue dotted curves) and time-dependent second Born under usage of the generalized Kadanoff-Baym ansatz plus Hartree-Fock initial state (GKBA, black dash-dotted curves). All these approximate calculations are known to preserve particle number and momentum, and, in all cases, we observe exact sinusoidal oscillation of the time-dependent dipole moment with frequency $\omega = 1$ (i.e., with confinement frequency), see Figure B.1 (a).

However, we emphasize that, despite the uniform sloshing mode behavior observed in all calculations, there is great diversity in the temporal evolution of the energies, see Figure B.1 (b). After the dipole-kick excitation, the kinetic and potential energies start to oscillate. Thereby, TDHF and TD2ndB 2, indicate clear harmonic oscillation with twice the confinement frequency and a

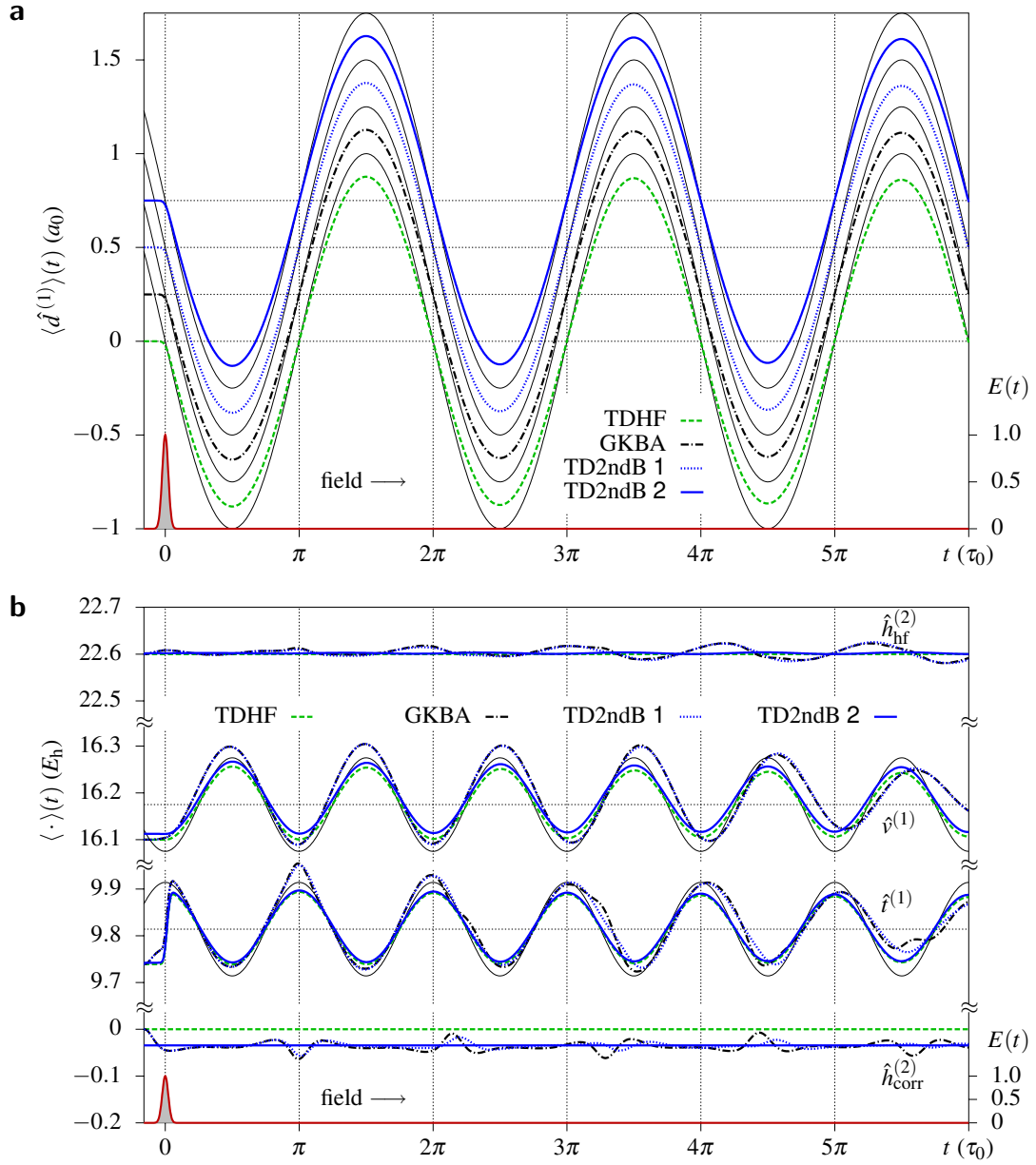


Figure B.1: Kohn mode dynamics of ten spin-restricted electrons in a one-dimensional harmonic trap of frequency $\omega = 1$. Initially, for $t \leq -\frac{1}{2}$ (in units of τ_0), the system is in the singlet ground state (FE-DVR basis size $n_b = 41$). (a) Time evolution of the dipole moment $\langle \hat{d}^{(1)} \rangle(t)$ for different approximations following a non-perturbative dipole-kick (red) at field strength $E_0 = 1$. For better visibility, lines have been separated vertically by $0.25 a_0$. (b) Temporal behavior of the different energy contributions: the kinetic energy ($\langle \hat{t}^{(1)} \rangle(t)$), the one-electron part of the potential energy ($\langle \hat{v}^{(1)} \rangle(t)$), the Hartree-Fock energy ($\langle \hat{h}_{\text{hf}}^{(2)} \rangle(t)$) and the correlation energy ($\langle \hat{h}_{\text{corr}}^{(2)} \rangle(t)$) in second Born approximation. In both figures, the thin solid lines (black) are sinusoidal curves to guide the eye; the respective frequency in (a) is $\omega = 1$, in (b), $\omega = 2$ since the kinetic and potential energy oscillate with twice the confinement frequency (the phase shift is $\frac{\pi}{2}$).

constant phase shift of $\frac{\pi}{2}$ between $\langle \hat{t}^{(1)} \rangle(t)$ and $\langle \hat{v}^{(1)} \rangle(t)$ as is required for the Kohn mode. Further, note, that the energy offset in TD2ndB 2 is due to inclusion of electron correlations. In contrast, TD2ndB 1 and GKBA do not show a harmonic oscillation in the kinetic and potential energy. This is caused by the non-correlated initial state and the dynamic built-up of correlations. Hence, although the c.m. motion is of Kohn mode type, we cannot observe a purely rigid translation of the equilibrium density profile $\langle \hat{n}^{(1)} \rangle(x)$ in these two cases.

Next, let us consider the Hartree-Fock energy $\langle \hat{h}_{\text{hf}}^{(2)} \rangle(t)$. For, both, TDHF and TD2ndB 2, it is constant⁵ although not exactly equal due to the presence of distinct initial states (we note that the difference is virtually not extractable from Figure B.1 (b)). On the contrary, $\langle \hat{h}_{\text{hf}}^{(2)} \rangle(t)$ starts to oscillate about its initial value for TD2ndB 1 and the GKBA. Finally, the correlation energy $\langle \hat{h}_{\text{corr}}^{(2)} \rangle(t)$ (being zero for TDHF) remains constant for the full second Born calculation while it reveals nontrivial time-dependence—being initially zero—for the cases where the system is prepared (at $t \leq \frac{1}{2}\tau_0$) in the Hartree-Fock ground state (i.e., for TD2ndB 1 and GKBA).

In conclusion, only those calculations including self-consistent initial states (hence, TDHF and the full second Born calculation) demonstrate all dynamic features that are consequences of the Kohn theorem.

⁵In the case of TD2ndB 2, small deviations from a constant value (especially for later times) are attributed to the finite time step δ .

The GKB Ansatz; Retarded/Advanced Green Function and Algorithm

Treatment of the Retarded and Advanced Green Functions

From Eq. (4.16) in Chapter 4.3, we see that the generalized Kadanoff-Baym (GKB) ansatz for reconstructing off-time-diagonal Green functions still involves double-time propagators, namely g^R and g^A (for their definition in terms of g^{\gtrless} , see Eq. (2.39)). These propagators must be provided as additional input before one can make practical use of the ansatz. For the description of homogeneous systems, it is often a good idea to consider the noninteracting Hamiltonian as reference for constructing g^R and g^A . In this work, however, we want to include the propagators on the mean-field (Hartree-Fock) level. This, in the collision terms of the Kadanoff-Baym equations, guarantees consistency with regard to the separation of time-local and -nonlocal parts of the self-energy.

When the mean-field, i.e., $\Sigma_{\xi}^{\text{HF}}(t)$, is self-consistently obtained from the one-particle density matrix during the GKB time-evolution, the equations of motion for the retarded/advanced Green function read (in FE-DVR representation),

$$\left(i \frac{\partial}{\partial t} \delta_{m_1 m_2}^{i_1 i_2} - \bar{h}_{m_1 m_2}^{i_1 i_2}(t) \right) g_{m_2 m_1}^{R/A, i_2 i_1}(t, t') = \delta_C(t - t') a_{m_1 m_1}^{i_1 i_1}(t, t'), \quad (\text{C.1})$$

+ adjoint equation with $t \leftrightarrow t'$,

where $\bar{h}(t)$ is defined by ($\xi \in \{1, 2\}$),

$$\bar{h}_{m_1 m_2}^{i_1 i_2}(t) = h_{m_1 m_2}^{i_1 i_2}(t) + \Sigma_{\xi, m_1 m_2}^{\text{HF}, i_1 i_2}[g^<, \tilde{u}](t),$$

and,

$$a(t, t') = i [g^>(t, t') - g^<(t, t')] = \begin{cases} i g^R(t, t'), & t \geq t' \\ -i g^A(t, t'), & t < t' \end{cases},$$

denotes the spectral function, e.g., [Bon98].

Formally, using relative and center-of-mass variables, $T = \frac{1}{2}(t + t')$ and $\tau = t - t'$, Eq. (C.1) has the solution,

$$g^{\text{R/A}}(T, \tau) = \mp i \theta_C(\pm\tau) \exp\left(-i \int_{T-\tau/2}^{T+\tau/2} dt \bar{h}(\bar{t})\right) \\ \stackrel{\text{def.}}{=} \mp i \theta_C(\pm\tau) y(t, t'), \quad (\text{C.2})$$

where $g^{\text{A}}(T, \tau) = [g^{\text{R}}(T, -\tau)]^*$, and,

$$y(t, t') = [y(t', t)]^\dagger, \quad (\text{C.3}) \\ y(t, t) = 1.$$

Note that, in the second line of Eq. (C.3), in any basis representation, the 1 stands for the identity matrix, i.e., in FE-DVR representation, $y_{m_1 m_2}^{i_1 i_2}(t, t) = \delta_{m_1 m_1}^{i_1 i_1}$.

Reconstruction of the Collision Integral

Using the retarded and advanced Green functions in the form of (C.2), the GKB ansatz of Eq. (4.16) can be reformulated as,

$$g^{\geq}(t, t') \approx \theta_C(t - t') y(t, t') g^{\geq}(t', t') + \theta_C(t' - t) g^{\geq}(t, t) y(t, t'), \quad (\text{C.4})$$

where, for $t = t'$, we (due to the second property in Eq. (C.3)) exactly recover the Green function on the time diagonal.

For the time-propagation of the nonequilibrium Green function under the GKB ansatz, we now apply Eq. (C.4) in the collision integral $i_{\text{diag}}^<(t, t)$ which becomes¹,

$$i_{\text{diag}}^<(t, t) = \int_0^t dt \left(\Sigma_\xi^>[y, \tilde{u}](t, \bar{t}) g^<(\bar{t}, \bar{t}) y(\bar{t}, t) - \Sigma_\xi^<[y, \tilde{u}](t, \bar{t}) g^>(\bar{t}, \bar{t}) y(\bar{t}, t) \right), \quad (\text{C.5}) \\ + y(t, \bar{t}) g^<(\bar{t}, \bar{t}) \Sigma_\xi^>[y, \tilde{u}](\bar{t}, t) - y(t, \bar{t}) g^>(\bar{t}, \bar{t}) \Sigma_\xi^<[y, \tilde{u}](\bar{t}, t) \right).$$

Here, the quantity y enters in many facets. Precisely, we need $y(\bar{t}, t)$ for all times² $\bar{t} \leq t$. However, for $\bar{t} \neq t$ (the case $\bar{t} = t$ is trivial), it is not a good idea to compute y directly from Eq. (C.2). Doing so, would, for each pair (\bar{t}, t) , require a diagonalization of the matrix $H(\bar{t}, t) = \int_t^{\bar{t}} dt' \bar{h}(t')$, cf. the definition of y in Eq. (C.2). As a consequence, for progressed propagation times, a large number of diagonalizations would have to be performed in each time step. This makes the algorithm highly inefficient.

In order to circumvent this problem, we reduce the computation of y to a simple recurrence

¹Neglecting initial correlations ($g^\top = g^\dagger = 0$).

²Note that y with interchanged time arguments is readily obtained from the second line in Eq. (C.3).

relation which is justified for small $\delta \ll 1$ (in atomic units):

$$\begin{aligned}
y(\bar{t}, t) &= \exp\left(-i \int_t^{\bar{t}} dt' \bar{h}(t')\right) \approx \exp\left(-i \int_{t-\delta}^{\bar{t}} dt' \bar{h}(t') + i \delta \bar{h}(t - \delta)\right) \\
&= \exp\left(-i \int_{t-\delta}^{\bar{t}} dt' \bar{h}(t')\right) \exp(i \delta \bar{h}(t - \delta)) \\
&= y(\bar{t}, t - \delta) u_\delta^\dagger(t - \delta) \\
&= u_\delta(t - \delta) y^\dagger(\bar{t}, t - \delta) .
\end{aligned} \tag{C.6}$$

Here, to arrive at the third equality, the Baker-Campbell-Hausdorff formula, $e^{a+b} = e^a e^b e^{-\frac{1}{2}[a,b]}$, has been used (in which the commutator vanishes). Further, $u_\delta(t - \delta)$ is just the time-evolution operator of the previous time step, cf. Eq. (B.4), and $y(0, 0) = 1$.

Algorithm Overview

Ignoring initial correlations ($g^\lceil = g^\lrcorner = 0$ in the collision integrals of Eq. (B.1)), the propagation of the Kadanoff-Baym equations (FE-DVR I.+II.) under the GKB ansatz confines itself to (cf. Eq. (B.2) in Appendix B and note the matrix notation),

$$g^<(t + \delta, t + \delta) = u_\delta(t) \left(g^<(t, t) + \sum_{n=0}^{\infty} c^{(n)}(t) \right) u_\delta^\dagger(t) , \tag{C.7}$$

$$\begin{aligned}
c^{(n)}(t) &= \frac{i \delta}{n+1} [\bar{h}(t), c^{(n-1)}(t)]_- , \\
c^{(0)}(t) &= -i \delta i_{\text{diag}}^<(t, t) , \\
u_\delta(t) &= \exp(-i \bar{h}(t) \delta) ,
\end{aligned} \tag{C.8}$$

where $\delta \ll 1$ (in units of τ_0), and, in the first line, the sum is typically truncated at $0 < n < 5$ as the quantity $c^{(n)}(t)$ is of the order $\mathcal{O}(\delta^{n+1})$.

Compared to the diagonal time step of the full propagation scheme (see Appendix B), the GKB propagation only differs in the evaluation of the collision integral $i_{\text{diag}}^<(t, t)$, which is obtained from Eq. (C.5) with all off-diagonal nonequilibrium Green functions being reconstructed according to Eq. (C.4). We emphasize that, to this end, all previous Green functions, i.e., all $g^<(\bar{t}, \bar{t})$ with $\bar{t} \leq t$, are needed in the GKB ansatz (see Eq. (C.5)) and, thus, cannot be discarded after each propagation step as it is the case for the Hartree-Fock approximation³. However, in contrast to Eq. (4.11) in Chapter 4.1.2, the memory demand is essentially reduced as it scales linear (instead of quadratic) with the final propagation time t_f . In byte, the memory requirement⁴ is $\mathcal{O}(2 \cdot 16 n_b^2 t_f \delta^{-1})$.

³Note that the greater correlation functions on the time-diagonal are readily obtained from the relation $g^>(\bar{t}, \bar{t}) = -i + g^<(\bar{t}, \bar{t})$, cf. Eq. (4.16) in Chapter 4.3.

⁴While the factor of 2 takes into account that memory has to be reserved for $y(\bar{t}, t)$ and $g^<(\bar{t}, \bar{t})$ (with $\bar{t} \leq t \leq t_f$), the factor of 16 ensures complex-double precision in all matrix elements.

With the above considerations and the FE-DVR indices being restored, the algorithm involves the following steps:

- (i) Initialize the lesser correlation function⁵: $g_{m_1 m_{\bar{1}}}^{<, i_1 i_{\bar{1}}}(0, 0) = i g_{m_1 m_{\bar{1}}}^{0, i_1 i_{\bar{1}}}(0^-)$.
- (ii) If $t = 0$ (initial time), set $y_{m_1 m_{\bar{1}}}^{i_1 i_{\bar{1}}}(0, 0) = \delta_{m_1 m_{\bar{1}}}^{i_1 i_{\bar{1}}}$; else compute $y_{m_1 m_{\bar{1}}}^{i_1 i_{\bar{1}}}(\bar{t}, t)$ for all $\bar{t} < t$ according to the recurrence formula (C.6) using the time-evolution operator $u_{\delta}(t - \delta)$ of the previous time step and set $y_{m_1 m_{\bar{1}}}^{i_1 i_{\bar{1}}}(t, t) = \delta_{m_1 m_{\bar{1}}}^{i_1 i_{\bar{1}}}$.
- (iii) In the given many-body approximation, compute the self-energies $\Sigma_{\xi, m_1 m_{\bar{1}}}^{>, i_1 i_{\bar{1}}}[g^{<}, y, \tilde{u}](t, \bar{t})$ and $\Sigma_{\xi, m_1 m_{\bar{1}}}^{<, i_1 i_{\bar{1}}}[g^{<}, y, \tilde{u}](\bar{t}, t)$ for all $\bar{t} \leq t$ using the reconstructed nonequilibrium Green functions of Eq. (C.4).
- (iv) Perform the collision integral $i_{\text{diag}, m_1 m_{\bar{1}}}^{<, i_1 i_{\bar{1}}}(t, t)$ of Eq. (C.5).
- (v) Compute the matrix elements $\bar{h}_{m_1 m_{\bar{1}}}^{i_1 i_{\bar{1}}}(t) = h_{m_1 m_{\bar{1}}}^{i_1 i_{\bar{1}}}(t) + \Sigma_{\xi, m_1 m_{\bar{1}}}^{\text{HF}, i_1 i_{\bar{1}}}[g^{<}, \tilde{u}](t)$ and diagonalize $\bar{h}(t)$. From the eigenvalues and eigenvectors, construct the matrix elements $u_{\delta, m_1 m_{\bar{1}}}^{i_1 i_{\bar{1}}}(t)$ of the time-evolution operator, cf. Eq. (C.8). For $t > 0$, it is important to backup the old time-evolution operator, cf. step (ii).
- (vi) Get the new Green function $g_{m_1 m_{\bar{1}}}^{<, i_1 i_{\bar{1}}}(t + \delta, t + \delta)$ from Eq. (C.7).
- (vii) Increase t by δ and continue with (ii).

⁵Here, $g^0(0^-)$ is just the one-particle density matrix in Hartree-Fock approximation, cf. Eq. (4.2) in Chapter 4.1.

Supplement Tables

Table D.1: Ground state energy contributions of the model atoms (He, Be) and molecules (H_2 , H_3^+ and LiH) addressed in Chapter 6.1.1. Hartree-Fock approximation.

Energy (E_h)	He	Be	H_2	H_3^+	LiH
$\langle \hat{t}^{(1)} \rangle$	0.2904	1.1447	0.1503	0.1070	0.6779
$\langle \hat{v}^{(1)} \rangle$	-3.2383	-11.2561	-2.6434	-3.3071	-9.1863
$\langle \hat{h}_{\text{hf}}^{(2)} \rangle$	0.7237	3.3719	0.6382	0.5837	2.7690

Table D.2: Self-consistent ground state energy contributions of the model atoms (He, Be) and molecules (H_2 , H_3^+ and LiH) addressed in Chapter 6.1.1. Second(-order) Born approximation.

Energy (E_h)	He	Be	H_2	H_3^+	LiH
$\langle \hat{t}^{(1)} \rangle$	0.2878	1.1245	0.1491	0.1109	0.6741
$\langle \hat{v}^{(1)} \rangle$	-3.2266	-11.1646	-2.6029	-3.2235	-9.0838
$\langle \hat{h}_{\text{hf}}^{(2)} \rangle$	0.7240	3.3354	0.6366	0.5798	2.7414
$\langle \hat{h}_{\text{corr}}^{(2)} \rangle$	-0.0186	-0.0668	-0.0431	-0.0676	-0.0762

Table D.3: Ground state properties of the four-electron quantum dot of Chapter 6.3 in Hartree-Fock (second Born) approximation. The total energy is $\langle \hat{H}_{\text{gs}} \rangle = 5.5384 E_0$ ($\langle \hat{H}_{\text{gs}} \rangle = 5.5306 E_0$).

Energy (E_0)	Hartree-Fock	Second Born
$\langle \hat{t}^{(1)} \rangle$	2.0478	2.0525
$\langle \hat{v}^{(1)} \rangle$	0 ¹	0 ¹
$\langle \hat{h}_{\text{hf}}^{(2)} \rangle$	3.4906	3.4939
$\langle \hat{h}_{\text{corr}}^{(2)} \rangle$	0 ¹	-0.0158

¹ zero by definition.

Table D.4: Ground state excitation energies ω and values of the approximate excitation level A_n , Eq. (6.9), for the four-electron system discussed in Chapter 6.3 ($\lambda=1$). All data is obtained from the method of exact diagonalization. The exact ground state energy is $\langle \hat{H}_{\text{gs}} \rangle = 5.5278 E_0$.

n	Transition ¹	A_n	$\omega(E_0)$	Classification	n	Transition ¹	A_n	$\omega(E_0)$	Classification
1	4 ↔ 21	1.079	1.1445	dipole	19	4 ↔ 251	2.038	5.8032	dipole
2	4 ↔ 34	1.088	1.5478	non-dipole	20	4 ↔ 257	2.153	5.8882	non-dipole
3	4 ↔ 43	1.842	2.1118	non-dipole	21	4 ↔ 267	1.981	6.0119	dipole
4	4 ↔ 63	1.150	2.5559	non-dipole	22	4 ↔ 286	2.055	6.3480	non-dipole
5	4 ↔ 69	1.870	2.6769	dipole	23	4 ↔ 294	2.839	6.4185	non-dipole
6	4 ↔ 83	1.145	2.9794	dipole	24	4 ↔ 303	1.096	6.4711	non-dipole
7	4 ↔ 85	1.969	3.0394	non-dipole	25	4 ↔ 328	2.802	6.7825	non-dipole
8	4 ↔ 106	1.944	3.6314	dipole	26	4 ↔ 331	2.018	6.8345	dipole
9	4 ↔ 129	1.997	3.9928	non-dipole	27	4 ↔ 337	2.941	6.8966	dipole
10	4 ↔ 142	1.956	4.2129	non-dipole	28	4 ↔ 349	1.104	6.9333	dipole
11	4 ↔ 150	1.119	4.3150	dipole	29	4 ↔ 367	2.108	7.1216	non-dipole
12	4 ↔ 162	2.048	4.5544	dipole	30	4 ↔ 375	2.912	7.2410	dipole
13	4 ↔ 177	1.122	4.7619	non-dipole	31	4 ↔ 395	2.035	7.4516	non-dipole
14	4 ↔ 186	1.998	4.9300	non-dipole	32	4 ↔ 403	1.986	7.5683	dipole
15	4 ↔ 188	2.830	4.9575	dipole	33	4 ↔ 420	3.876	7.7324	non-dipole
16	4 ↔ 215	2.797	5.4099	non-dipole	34	4 ↔ 432	2.150	7.7932	dipole
17	4 ↔ 217	2.034	5.4250	non-dipole	35	4 ↔ 449	2.031	7.9891	non-dipole
18	4 ↔ 230	2.019	5.5413	dipole					

¹ State numbering in the full exact diagonalization context.

Bibliography

- [ACK⁺09] J.D. Alexander, C.R. Calvert, R.B. King, O. Kelly, L. Graham, W.A. Bryan, G.R.A.J. Nemeth, W.R. Newell, C.A. Froud, I.C.E. Turcu, E. Springate, I.D. Williams, and J.B. Greenwood. Photodissociation of D_3^+ in an intense, femtosecond laser field. *J. Phys. B: At. Mol. Opt. Phys.*, 42:141004, 2009.
- [Ann04] J.F. Annett. *Superconductivity, Superfluids, and Condensates*, Oxford University Press, New York, 2004.
- [Ash96] R.C. Ashoori. Electrons in artificial atoms. *Nature*, 379:413, 1996.
- [Bau97] D. Bauer. Two-dimensional, two-electron model atom in a laser pulse: Exact treatment, single-active-electron analysis, time-dependent density-functional theory, classical calculations, and nonsequential ionization. *Phys. Rev. A*, 56:3028, 1997.
- [Bay62] G. Baym. Self-consistent approximations in many-body systems. *Phys. Rev.*, 127:1391, 1962.
- [BB09] K. Balzer and M. Bonitz. Nonequilibrium properties of strongly correlated artificial atoms—a Green’s functions approach. *J. Phys. A: Math. Theor.*, 42:214020, 2009.
- [BBB10a] K. Balzer, S. Bauch, and M. Bonitz. Efficient grid-based method in nonequilibrium Green’s function calculations: Application to model atoms and molecules. *Phys. Rev. A*, 81:022510, 2010.
- [BBB10b] K. Balzer, S. Bauch, and M. Bonitz. Finite elements and the discrete variable representation in nonequilibrium Green’s function calculations. Atomic and molecular models. *J. Phys.: Conf. Ser.*, 220:012020, 2010.
- [BBB10c] K. Balzer, S. Bauch, and M. Bonitz. Time-dependent second-order Born calculations for model atoms and molecules in strong laser fields. *Phys. Rev. A*, 82:033427, 2010.
- [BBB10d] S. Bauch, K. Balzer, and M. Bonitz. Electronic correlations in double ionization of atoms in pump-probe experiments. *EPL*, 91:53001, 2010.

-
- [BBE10] M. Bonitz and K. Balzer (Eds.). Progress in Nonequilibrium Green's Functions IV. *J. Phys.: Conf. Ser.*, 220:011001–012023, 2010.
- [BBHB09] S. Bauch, K. Balzer, C. Henning, and M. Bonitz. Quantum breathing mode of trapped bosons and fermions at arbitrary coupling. *Phys. Rev. B*, 80:054515, 2009.
- [BBK⁺99] M. Bonitz, Th. Bornath, D. Kremp, M. Schlanges, and W.D. Kraeft. Quantum kinetic theory for laser plasmas. Dynamical screening in strong fields. *Contrib. Plasma Phys.*, 39:329, 1999.
- [BBvL07] M. Bonitz, K. Balzer, and R. van Leeuwen. Invariance of the Kohn center-of-mass mode in a conserving theory. *Phys. Rev. B*, 76:045341, 2007.
- [BBvL⁺09] K. Balzer, M. Bonitz, R. van Leeuwen, A. Stan, and N.E. Dahlen. Nonequilibrium Green's function approach to strongly correlated few-electron quantum dots. *Phys. Rev. B*, 79:245306, 2009.
- [BE00] M. Bonitz (Ed.). *Progress in Nonequilibrium Green's Functions*, World Scientific, Singapore, 2000.
- [BF99] A. Becker and F.H.M. Faisal. Interplay of electron correlation and intense field dynamics in the double ionization of helium. *Phys. Rev. A*, 59:R1742, 1999.
- [BF07] H. Bruus and K. Flensberg. *Many-Body Quantum Theory in Condensed Matter Physics*, Oxford University Press, New York, 2007.
- [BFB11] J. Böning, A. Filinov, and M. Bonitz. Crystallization of an exciton superfluid. *Phys. Rev. B*, 84:075130, 2011.
- [BFE06] M. Bonitz and A. Filinov (Eds.). Progress in Nonequilibrium Green's Functions III. *J. Phys.: Conf. Ser.*, 35:001–042, 2006.
- [BHBB10a] S. Bauch, D. Hochstuhl, K. Balzer, and M. Bonitz. Quantum breathing mode of interacting particles in harmonic traps. *J. Phys.: Conf. Ser.*, 220:012013, 2010.
- [BHBB10b] M. Bonitz, D. Hochstuhl, S. Bauch, and K. Balzer. Quantum kinetic approach to time-resolved photoionization of atoms. *Contrib. Plasma Phys.*, 50:54, 2010.
- [BHLE10] M. Bonitz, N. Horing, and P. Ludwig (Eds.). *Introduction to Complex Plasmas*, Springer, Berlin, 2010.
- [BJH89] L. Brey, N.F. Johnson, and B.I. Halperin. Optical and magneto-optical absorption in parabolic quantum wells. *Phys. Rev. B*, 40:10647, 1989.
- [BK61] G. Baym and L.P. Kadanoff. Conservation laws and correlation functions. *Phys. Rev.*, 124:287, 1961.

-
- [BK93] L. Bányai and S.W. Koch. *Semiconductor Quantum Dots*, World Scientific, Singapore, 1993.
- [BK00] Th. Brabec and F. Krausz. Intense few-cycle laser fields: Frontiers of nonlinear optics. *Rev. Mod. Phys.*, 72:545, 2000.
- [BKBK97] R. Binder, H.S. Köhler, M. Bonitz, and N. Kwong. Green's function description of momentum-orientation relaxation of photoexcited electron plasmas in semiconductors. *Phys. Rev. B*, 55:5110, 1997.
- [BKS⁺96] M. Bonitz, D. Kremp, D.C. Scott, R. Binder, W.D. Kraeft, and H.S. Köhler. Numerical analysis of non-Markovian effects in charge-carrier scattering: One-time versus two-time kinetic equations. *J. Phys.: Condens. Matter*, 8:6057, 1996.
- [BM90] W. Botermans and R. Malfliet. Quantum transport theory of nuclear matter. *Phys. Rep.*, 198:115, 1990.
- [Bon98] M. Bonitz. *Quantum Kinetic Theory*, Teubner, Stuttgart/Leipzig, 1998.
- [Bož97] P. Božek. Particle production in quantum transport theories. *Phys. Rev. C*, 56:1452, 1997.
- [BP11] M. Balzer and M. Potthoff. Nonequilibrium cluster perturbation theory. *Phys. Rev. B*, 83:195132, 2011.
- [BS02] A.D. Bandrauk and N.H. Shon. Attosecond control of ionization and high-order harmonic generation in molecules. *Phys. Rev. A*, 66:031401, 2002.
- [BSE03] M. Bonitz and D. Semkat (Eds.). *Progress in Nonequilibrium Green's Functions II*, World Scientific, Singapore, 2003.
- [BSE06] M. Bonitz and D. Semkat (Eds.). *Introduction to Computational Methods in Many Body Physics*, Rinton Press, New Jersey, 2006.
- [Buc67] A.D. Buckingham. Permanent and induced molecular moments and long-range intermolecular forces. *Adv. Chem. Phys.*, 12:107, 1967.
- [CF06] O. Ciftja and M.G. Faruk. Two interacting electrons in a one-dimensional parabolic quantum dot: Exact numerical diagonalization. *J. Phys.: Condens. Matter*, 18:2623, 2006.
- [Cha60] S. Chandrasekhar. *Radiative Transfer*, Dover, New York, 1960.
- [C]vdP08] B. Chapman, G. Jost, and R. van der Pas. *Using OpenMP. Portable Shared Memory Parallel Programming*, The MIT Press, Cambridge, Massachusetts, 2008.

-
- [CMK⁺04] L.A. Collins, S. Mazevet, J.D. Kress, B.I. Schneider, and D.L. Feder. Time-dependent simulations of large-scale quantum dynamics. *Phys. Scr.*, T110:408, 2004.
- [Coo56] L.N. Cooper. Bound electron pairs in a degenerate Fermi gas. *Phys. Rev.*, 104:1189, 1956.
- [CRB10] S. Chen, C. Ruiz, and A. Becker. Double ionization of helium by intense near-infrared and vuv laser pulses. *Phys. Rev. A*, 82:033426, 2010.
- [CS53] E.U. Condon and G.H. Shortley. *The Theory of Atomic Spectra*, Cambridge University Press, New York, 1953.
- [CW02] E.A. Cornell and C.E. Wieman. Nobel lecture: Bose-Einstein condensation in a dilute gas, the first 70 years and some recent experiments. *Rev. Mod. Phys.*, 74:875, 2002.
- [CZK⁺05] J. Caillat, J. Zanghellini, M. Kitzler, O. Koch, W. Kreuzer, and A. Scrinzi. Correlated multielectron systems in strong laser fields: A multiconfiguration time-dependent Hartree-Fock approach. *Phys. Rev. A*, 71:012712, 2005.
- [Dan84a] P. Danielewicz. Quantum theory of nonequilibrium processes I. *Annals of Physics*, 152:239, 1984.
- [Dan84b] P. Danielewicz. Quantum theory of nonequilibrium processes II. Application to nuclear collisions. *Annals of Physics*, 152:305, 1984.
- [DE06] G.W.F. Drake (Ed.). *Handbook of Atomic, Molecular and Optical Physics*, Springer, New York, 2006.
- [DRB10] P. Danielewicz, A. Rios, and B. Barker. Towards quantum transport for nuclear reactions. *Physica E: Low-dim. Syst. Nanostruct.*, 42:501, 2010.
- [DSvL06] N.E. Dahlen, A. Stan, and R. van Leeuwen. Nonequilibrium Green function theory for excitation and transport in atoms and molecules. *J. Phys.: Conf. Ser.*, 35:324, 2006.
- [DuB67] D.F. DuBois. *Lectures in Theoretical Physics*, (edited by W.E. Brittin) Gordon and Breach, New York, 1967.
- [DvL01] N.E. Dahlen and R. van Leeuwen. Double ionization of a two-electron system in the time-dependent extended Hartree-Fock approximation. *Phys. Rev. A*, 64:023405, 2001.
- [DvL05] N.E. Dahlen and R. van Leeuwen. Self-consistent solution of the Dyson equation for atoms and molecules within a conserving approximation. *J. Chem. Phys.*, 122:164102, 2005.

-
- [DvL07] N.E. Dahlen and R. van Leeuwen. Solving the Kadanoff-Baym equations for inhomogeneous systems: Application to atoms and molecules. *Phys. Rev. Lett.*, 98:153004, 2007.
- [DvLS06] N.E. Dahlen, R. van Leeuwen, and A. Stan. Propagating the Kadanoff-Baym equations for atoms and molecules. *J. Phys.: Conf. Ser.*, 35:340, 2006.
- [EHMG99] R. Egger, W. Häusler, C.H. Mak, and H. Grabert. Crossover from Fermi liquid to Wigner molecule behavior in quantum dots. *Phys. Rev. Lett.*, 82:3320, 1999.
- [Fan61] U. Fano. Effects of configuration interaction on intensities and phase shifts. *Phys. Rev.*, 124:1866, 1961.
- [FBL01] A.V. Filinov, M. Bonitz, and Yu.E. Lozovik. Wigner crystallization in mesoscopic 2D electron systems. *Phys. Rev. Lett.*, 86:3851, 2001.
- [FLCC01] L.-B. Fu, J. Liu, J. Chen, and S.-G. Chen. Classical collisional trajectories as the source of strong-field double ionization of helium in the knee regime. *Phys. Rev. A*, 63:043416, 2001.
- [Foc30] V. Fock. Bemerkung zum Virialsatz. *Z. Phys. A: Hadrons Nucl.*, 63:855, 1930.
- [Foc32] V. Fock. Konfigurationsraum und zweite Quantelung. *Z. Phys. A: Hadrons Nucl.*, 75:622, 1932.
- [Fuj65] S. Fujita. Thermodynamic evolution equation for a quantum statistical gas. *J. Math. Phys.*, 6:1877, 1965.
- [FW71] A.L. Fetter and J.D. Walecka. *Quantum Theory of Many-Particle Systems*, McGraw-Hill, San Francisco, 1971.
- [GBH99] P. Gartner, L. Bányai, and H. Haug. Two-time electron-LO-phonon quantum kinetics and the generalized Kadanoff-Baym approximation. *Phys. Rev. B*, 60:14234, 1999.
- [GdSP11] T.D. Graß, F.E.A. dos Santos, and A. Pelster. Excitation spectra of bosons in optical lattices from the Schwinger-Keldysh calculation. *Phys. Rev. A*, 84:013613, 2011.
- [GE92] R. Grobe and J.H. Eberly. Photoelectron spectra for a two-electron system in a strong laser field. *Phys. Rev. Lett.*, 68:2905, 1992.
- [GE93] R. Grobe and J.H. Eberly. Single and double ionization and strong-field stabilization of a two-electron system. *Phys. Rev. A*, 47:R1605, 1993.
- [GLS99] W. Gropp, E. Lusk, and A. Skjellum. *Portable Parallel Programming with the Message-Passing Interface*, The MIT Press, Cambridge, Massachusetts, 1999.

-
- [GM10] M. Garny and M.M. Müller. *High Performance Computing in Science and Engineering, Garching/Munich 2009*, Springer, Berlin, 2010.
- [GSJ06] P. Gartner, J. Seebeck, and F. Jahnke. Relaxation properties of the quantum kinetics of carrier-LO-phonon interaction in quantum wells and quantum dots. *Phys. Rev. B*, 73:115307, 2006.
- [Gut90] M.C. Gutzwiller. *Chaos in Classical and Quantum Mechanics*, Springer, Heidelberg, 1990.
- [GW69] G.H. Golub and J.H. Welsch. Calculation of gauss quadrature rules. *Math. Comp.*, 23:221, 1969.
- [GWR94] C. Greiner, K. Wagner, and P.-G. Reinhard. Memory effects in relativistic heavy ion collisions. *Phys. Rev. C*, 49:1693, 1994.
- [Hal75] A.G. Hall. Non-equilibrium Green functions: Generalized Wick's theorem and diagrammatic perturbation with initial correlations. *J. Phys. A: Math. Gen.*, 8:214, 1975.
- [HB96] H. Haug and L. Bányai. Improved spectral functions for quantum kinetics. *Solid State Commun.*, 100:303, 1996.
- [HB11] D. Hochstuhl and M. Bonitz. Two-photon ionization of helium studied with the multiconfigurational time-dependent Hartree-Fock method. *J. Chem. Phys.*, 134:084106, 2011.
- [HBB10] D. Hochstuhl, S. Bauch, and M. Bonitz. Multiconfigurational time-dependent Hartree-Fock calculations for photoionization of one-dimensional helium. *J. Phys.: Conf. Ser.*, 220:012019, 2010.
- [HBB11] S. Hermanns, K. Balzer, and M. Bonitz. *to be published*, 2011.
- [HBBB10] D. Hochstuhl, K. Balzer, S. Bauch, and M. Bonitz. Nonequilibrium Green function approach to photoionization processes in atoms. *Physica E: Low-dim. Syst. Nanostruct.*, 42:513, 2010.
- [HC06a] S.X. Hu and L.A. Collins. Attosecond pump probe: Exploring ultrafast electron motion inside an atom. *Phys. Rev. Lett.*, 96:073004, 2006.
- [HC06b] S.X. Hu and L.A. Collins. Strong-field ionization of molecules in circularly polarized few-cycle pulses. *Phys. Rev. A*, 73:023405, 2006.
- [HGE94] S.L. Haan, R. Grobe, and J.H. Eberly. Numerical study of autoionizing states in completely correlated two-electron systems. *Phys. Rev. A*, 50:378, 1994.

-
- [HJ96] H. Haug and A.-P. Jauho. *Quantum Kinetics in Transport and Optics of Semiconductors*, Springer, Heidelberg, 1996.
- [HJS00] M.D. Hill, N.P. Jouppi, and G.S. Sohi. *Readings in Computer Architecture*, Academic Press, San Diego, 2000.
- [HK64] P. Hohenberg and W. Kohn. Inhomogeneous electron gas. *Phys. Rev.*, 136:B864, 1964.
- [HLM11] D.J. Haxton, K.V. Lawler, and C.W. McCurdy. Multiconfiguration time-dependent Hartree-Fock treatment of electronic and nuclear dynamics in diatomic molecules. *Phys. Rev. A*, 83:063416, 2011.
- [Hor10] N.J.M. Horing. Quantum theory of solid state plasma dielectric response. *Contrib. Plasma Phys.*, 51:589, 2010.
- [HRB03] Th.M. Henderson, K. Runge, and R.J. Bartlett. Excited states in artificial atoms via equation-of-motion coupled cluster theory. *Phys. Rev. B*, 67:045320, 2003.
- [HTR10] N. Helbig, I.V. Tokatly, and A. Rubio. Physical meaning of the natural orbitals: Analysis of exactly solvable models. *Phys. Rev. A*, 81:022504, 2010.
- [Hu06] S.X. Hu. Quantum study of slow electron collisions with Rydberg atoms. *Phys. Rev. A*, 74:062716, 2006.
- [IKA05] K.M. Indlekofer, J. Knoch, and J. Appenzeller. Quantum kinetic description of Coulomb effects in one-dimensional nanoscale transistors. *Phys. Rev. B*, 72:125308, 2005.
- [Jen99] F. Jensen. *Introduction to Computational Chemistry*, John Wiley and Sons Ltd., Chichester, 1999.
- [JES88] J. Javanainen, J.H. Eberly, and Q. Su. Numerical simulations of multiphoton ionization and above-threshold electron spectra. *Phys. Rev. A*, 38:3430, 1988.
- [JHK93] K. Jauregui, W. Häusler, and B. Kramer. Wigner molecules in nanostructures. *EPL*, 24:581, 1993.
- [JKC06] E. Juarros, K. Kirby, and R. Côté. Laser-assisted ultracold lithium-hydride molecule formation: Stimulated versus spontaneous emission. *J. Phys. B: At. Mol. Opt. Phys.*, 39:S965, 2006.
- [Kas92] M.A. Kastner. The single-electron transistor. *Rev. Mod. Phys.*, 64:849, 1992.
- [KB62] L.P. Kadanoff and G. Baym. *Quantum Statistical Mechanics*, Benjamin, New York, 1962.

-
- [KBBK98] N.H. Kwong, M. Bonitz, R. Binder, and H.S. Köhler. Semiconductor Kadanoff-Baym equation results for optically excited electron-hole plasmas in quantum wells. *phys. stat. sol. (b)*, 206:197, 1998.
- [KBBS99] D. Kremp, Th. Bornath, M. Bonitz, and M. Schlanges. Quantum kinetic theory of plasmas in strong laser fields. *Phys. Rev. E*, 60:4725, 1999.
- [KE02] W. Ku and A.G. Eguiluz. Band-gap problem in semiconductors revisited: Effects of core states and many-body self-consistency. *Phys. Rev. Lett.*, 89:126401, 2002.
- [Kel65a] L.V. Keldysh. *Zh. Eksp. Teor. Fiz.*, 47:1515, 1964 [*Sov. Phys. JETP*, 20:1018, 1965].
- [Kel65b] L.V. Keldysh. Ionization in the field of a strong electromagnetic wave. *Sov. Phys. JETP*, 20:1307, 1965.
- [Ket02] W. Ketterle. Nobel lecture: When atoms behave as waves: Bose-Einstein condensation and the atom laser. *Rev. Mod. Phys.*, 74:1131, 2002.
- [KGU⁺04] R. Kienberger, E. Goulielmakis, M. Uiberacker, A. Baltuska, V. Yakovlev, F. Bammer, A. Scrinzi, Th. Westerwalbesloh, U. Kleineberg, U. Heinzmann, M. Drescher, and F. Krausz. Atomic transient recorder. *Nature*, 427:817, 2004.
- [KHJN07] S. Kvaal, M. Hjorth-Jensen, and H.M. Nilsen. Effective interactions, large-scale diagonalization, and one-dimensional quantum dots. *Phys. Rev. B*, 76:085421, 2007.
- [KI09] F. Krausz and M. Ivanov. Attosecond physics. *Rev. Mod. Phys.*, 81:163, 2009.
- [Kit10] T. Kita. Introduction to nonequilibrium statistical mechanics with quantum field theory. *Prog. Theor. Phys.*, 123:581, 2010.
- [KKB01] I. Kawata, H. Kono, and A.D. Bandrauk. Mechanism of enhanced ionization of linear H_3^+ in intense laser fields. *Phys. Rev. A*, 64:043411, 2001.
- [KKY99] H.S. Köhler, N.H. Kwong, and H.A. Yousif. A Fortran code for solving the Kadanoff-Baym equations for a homogeneous fermion system. *Comput. Phys. Commun.*, 123:123, 1999.
- [KM01] H.S. Köhler and K. Morawetz. Correlations in many-body systems with two-time Green's functions. *Phys. Rev. C*, 64:024613, 2001.
- [Koh61] W. Kohn. Cyclotron resonance and de Haas-van Alphen oscillations of an interacting electron gas. *Phys. Rev.*, 123:1242, 1961.
- [Koh99] W. Kohn. An essay on condensed matter physics in the twentieth century. *Rev. Mod. Phys.*, 71:S59, 1999.

-
- [Koo34] T. Koopmans. Über die Zuordnung von Wellenfunktionen und Eigenwerten zu den einzelnen Elektronen eines Atoms. *Physica*, 1:104, 1934.
- [KSB05] D. Kremp, D. Semkat, and M. Bonitz. Short-time kinetics and initial correlations in quantum kinetic theory. *J. Phys.: Conf. Ser.*, 11:1, 2005.
- [KSK05] D. Kremp, M. Schlanges, and W.D. Kraeft. *Quantum Statistics of Nonideal Plasmas*, Springer, Berlin, 2005.
- [KTB⁺02] R. Köhler, A. Tredicucci, F. Beltram, H.E. Beere, E.H. Linfield, A.G. Davies, D.A. Ritchie, R.C. Iotti, and F. Rossi. Terahertz semiconductor-heterostructure laser. *Nature*, 417:156, 2002.
- [Kub57] R. Kubo. Statistical-mechanical theory of irreversible processes. I. General theory and simple applications to magnetic and conduction problems. *J. Phys. Soc. Jpn.*, 12:570, 1957.
- [Kö95] H.S. Köhler. Memory and correlation effects in nuclear collisions. *Phys. Rev. C*, 51:3232, 1995.
- [Lan67] D.C. Langreth. *NATO Adv. Study Inst. Series B: Physics*, (edited by J.T. Devreese and V.E. Van Doren) Plenum, New York, 1967.
- [Lap81] I.R. Lapidus. One-dimensional hydrogen molecule revisited. *Am. J. Phys.*, 50:453, 1981.
- [LC07] J.C. Light and T. Carrington. Discrete-variable representations and their utilization. *Adv. Chem. Phys.*, 114:263, 2007.
- [LC08] A. López-Castillo. Semiclassical study of the one-dimensional hydrogen molecule. *Chaos*, 18:033130, 2008.
- [LCdAOdA96] A. López-Castillo, M.A.M. de Aguiar, and A.M. Ozorio de Almeida. On the one-dimensional helium atom. *J. Phys. B: At. Mol. Opt. Phys.*, 29:197, 1996.
- [LD98] D. Loss and D.P. DiVincenzo. Quantum computation with quantum dots. *Phys. Rev. A*, 57:120, 1998.
- [Leg99] A.J. Leggett. Superfluidity. *Rev. Mod. Phys.*, 71:S318, 1999.
- [LGE00] M. Lein, E.K.U. Gross, and V. Engel. Intense-field double ionization of helium: Identifying the mechanism. *Phys. Rev. Lett.*, 85:4707, 2000.
- [LHL85] J.C. Light, I.P. Hamilton, and J.V. Lill. Generalized discrete variable approximation in quantum mechanics. *J. Chem. Phys.*, 82:1400, 1985.

-
- [LLD⁺05] I.V. Litvinyuk, F. Légaré, P.W. Dooley, D.M. Villeneuve, P.B. Corkum, J. Zanghellini, A. Pegarkov, C. Fabian, and Th. Brabec. Shakeup excitation during optical tunnel ionization. *Phys. Rev. Lett.*, 94:033003, 2005.
- [LNS⁺06a] M. Lorke, T.R. Nielsen, J. Seebeck, P. Gartner, and F. Jahnke. Influence of carrier-carrier and carrier-phonon correlations on optical absorption and gain in quantum-dot systems. *Phys. Rev. B*, 73:085324, 2006.
- [LNS⁺06b] M. Lorke, T.R. Nielsen, J. Seebeck, P. Gartner, and F. Jahnke. Quantum kinetic effects in the optical absorption of semiconductor quantum-dot systems. *J. Phys.: Conf. Ser.*, 35:182, 2006.
- [Lou59] R. Loudon. One-dimensional hydrogen atom. *Am. J. Phys.*, 27:649, 1959.
- [LŠV86] P. Lipavský, V. Špička, and B. Velický. Generalized Kadanoff-Baym ansatz for deriving quantum transport equations. *Phys. Rev. B*, 34:6933, 1986.
- [LTC98] S. Larochelle, A. Talebpour, and S.L. Chin. Non-sequential multiple ionization of rare gas atoms in a Ti:Sapphire laser field. *J. Phys. B: At. Mol. Opt. Phys.*, 31:1201, 1998.
- [LW60] J.M. Luttinger and J.C. Ward. Ground-state energy of a many-fermion system II. *Phys. Rev.*, 118:1417, 1960.
- [LW72] D.C. Langreth and J.W. Wilkins. Theory of spin resonance in dilute magnetic alloys. *Phys. Rev. B*, 6:3189, 1972.
- [Mad04] L.B. Madsen. Correlated electrons in multiply excited states at and below threshold. *Phys. Scr.*, T110:144, 2004.
- [Mah00] G.D. Mahan. *Many-Particle Physics*, Kluwer Academic/Plenum Publishers, New York, 2000.
- [Mar87] S.L. Marple. *Digital Spectral Analysis with Applications*, Prentice-Hill, Englewood Cliffs, NJ, 1987.
- [Mat55] T. Matsubara. A new approach to quantum-statistical mechanics. *Prog. Theor. Phys.*, 14:351, 1955.
- [MR99] V.G. Morozov and G. Röpke. The "mixed" Green's function approach to quantum kinetics with initial correlations. *Annals of Physics*, 278:127, 1999.
- [MS59] P.C. Martin and J. Schwinger. Theory of many-particle systems I. *Phys. Rev.*, 115:1342, 1959.

-
- [MSSvL08] P. Myöhänen, A. Stan, G. Stefanucci, and R. van Leeuwen. A many-body approach to quantum transport dynamics: Initial correlations and memory effects. *EPL*, 84:67001, 2008.
- [MSSvL09] P. Myöhänen, A. Stan, G. Stefanucci, and R. van Leeuwen. Kadanoff-Baym approach to quantum transport through interacting nanoscale systems: From the transient to the steady-state regime. *Phys. Rev. B*, 80:115107, 2009.
- [MT97] V.A. Mandelshtam and H.S. Taylor. Harmonic inversion of time signals and its applications. *J. Chem. Phys.*, 107:6756, 1997.
- [MW88] D.E. Manolopoulos and R.E. Wyatt. Quantum scattering via the log derivative version of the Kohn variational principle. *Chem. Phys. Lett.*, 152:23, 1988.
- [NY00] M. Nakano and K. Yamaguchi. Electron-correlation dynamics of a one-dimensional H₂ model in a quantized photon field. *Chem. Phys. Lett.*, 317:103, 2000.
- [PAM88] G. Petite, P. Agostini, and H.G. Muller. Intensity dependence of non-perturbative above-threshold ionisation spectra: Experimental study. *J. Phys. B: At. Mol. Opt. Phys.*, 21:4097, 1988.
- [Pau79] R. Pauncz. *Spin Eigenfunctions, Construction and Use*, Plenum, New York, 1979.
- [PGB91] M.S. Pindzola, D.C. Griffin, and C. Bottcher. Validity of time-dependent Hartree-Fock theory for the multiphoton ionization of atoms. *Phys. Rev. Lett.*, 66:2305, 1991.
- [PTVF07] W.H. Press, S.A. Teukolsky, W.T. Vetterling, and B.P. Flannery. *Numerical Recipes*, Cambridge University Press, New York, 2007.
- [PvFVA09] M. Puig von Friesen, C. Verdozzi, and C.-O. Almbladh. Successes and failures of Kadanoff-Baym dynamics in Hubbard nanoclusters. *Phys. Rev. Lett.*, 103:176404, 2009.
- [PvFVA10] M. Puig von Friesen, C. Verdozzi, and C.-O. Almbladh. Kadanoff-Baym dynamics of Hubbard clusters: Performance of many-body schemes, correlation-induced damping and multiple steady and quasi-steady states. *Phys. Rev. B*, 82:155108, 2010.
- [RB09a] M. Ruggenthaler and D. Bauer. Local Hartree-exchange and correlation potential defined by local force equations. *Phys. Rev. A*, 80:052502, 2009.
- [RB09b] M. Ruggenthaler and D. Bauer. Rabi oscillations and few-level approximations in time-dependent density functional theory. *Phys. Rev. Lett.*, 102:233001, 2009.

-
- [RBBD11] A. Rios, B. Barker, M. Buchler, and P. Danielewicz. Towards a nonequilibrium Green's function description of nuclear reactions: One-dimensional mean-field dynamics. *Annals of Physics*, 326:1274, 2011.
- [RCBG06] M. Rontani, C. Cavazzoni, D. Bellucci, and G. Goldoni. Full configuration interaction approach to the few-electron problem in artificial atoms. *J. Chem. Phys.*, 124:124102, 2006.
- [RKB91] V.C. Reed, P.L. Knight, and K. Burnett. Suppression of ionization in superintense fields without dichotomy. *Phys. Rev. Lett.*, 67:1415, 1991.
- [RM00] T.N. Rescigno and C.W. McCurdy. Numerical grid methods for quantum-mechanical scattering problems. *Phys. Rev. A*, 62:032706, 2000.
- [RM02] S.M. Reimann and M. Manninen. Electronic structure of quantum dots. *Rev. Mod. Phys.*, 74:1283, 2002.
- [RPC⁺06] A. Ruzsinszky, J.P. Perdew, G.I. Csonka, O.A. Vydrov, and G.E. Scuseria. Spurious fractional charge on dissociated atoms: Pervasive and resilient self-interaction error of common density functionals. *J. Chem. Phys.*, 125:194112, 2006.
- [RS86] J. Rammer and H. Smith. Quantum field-theoretical methods in transport theory of metals. *Rev. Mod. Phys.*, 58:323, 1986.
- [RTW93] K. Richter, G. Tanner, and D. Wintgen. Classical mechanics of two-electron atoms. *Phys. Rev. A*, 48:4182, 1993.
- [SB93] J.F. Stanton and R.J. Bartlett. The equation of motion coupled-cluster method. A systematic biorthogonal approach to molecular excitation energies, transition probabilities, and excited state properties. *J. Chem. Phys.*, 98:7029, 1993.
- [SC05] B.I. Schneider and L.A. Collins. The discrete variable method for the solution of the time-dependent Schrödinger equation. *J. Non-Cryst. Solids*, 351:1551, 2005.
- [Sch61] J. Schwinger. Brownian motion of a quantum oscillator. *J. Math. Phys.*, 2:407, 1961.
- [Sch96] W. Schäfer. Influence of electron-electron scattering on femtosecond four-wave mixing in semiconductors. *J. Opt. Soc. Am. B*, 13:1291, 1996.
- [SCH06] B.I. Schneider, L.A. Collins, and S.X. Hu. Parallel solver for the time-dependent linear and nonlinear Schrödinger equation. *Phys. Rev. E*, 73:036708, 2006.
- [SDvL06] A. Stan, N.E. Dahlen, and R. van Leeuwen. Fully self-consistent GW calculations for atoms and molecules. *EPL*, 76:298, 2006.

-
- [SDvL09] A. Stan, N.E. Dahlen, and R. van Leeuwen. Time propagation of the Kadanoff-Baym equations for inhomogeneous systems. *J. Chem. Phys.*, 130:224101, 2009.
- [SE]90] Q. Su, J.H. Eberly, and J. Javanainen. Dynamics of atomic ionization suppression and electron localization in an intense high-frequency radiation field. *Phys. Rev. Lett.*, 64:862, 1990.
- [SES⁺99] R.C. Shiell, M. Evans, S. Stimson, C.-W. Hsu, C.Y. Ng, and J.W. Hepburn. Characteristics of correlation satellites below 25 eV in xenon probed by pulsed-field-ionization—zero-kinetic-energy photoelectron spectroscopy. *Phys. Rev. A*, 59:2903, 1999.
- [SF94] U. Schwengelbeck and F.H.M. Faisal. Ionization of the one-dimensional Coulomb atom in an intense laser field. *Phys. Rev. A*, 50:632, 1994.
- [SKB99] D. Semkat, D. Kremp, and M. Bonitz. Kadanoff-Baym equations with initial correlations. *Phys. Rev. E*, 59:1557, 1999.
- [SKB00] D. Semkat, D. Kremp, and M. Bonitz. Kadanoff-Baym equations and non-Markovian Boltzmann equation in generalized T-matrix approximation. *J. Math. Phys.*, 41:7458, 2000.
- [SKY07] N. Suzuki, I. Kawata, and K. Yamashita. Comparison of the mechanisms of enhanced ionization of H₂ and in intense laser fields. *Chem. Phys.*, 338:348, 2007.
- [SO96] A. Szabo and N.S. Ostlund. *Modern Quantum Chemistry*, Dover Publications, New York, 1996.
- [SPBA04] B. Szafran, F.M. Peeters, S. Bednarek, and J. Adamowski. Anisotropic quantum dots: Correspondence between quantum and classical Wigner molecules, parity symmetry, and broken-symmetry states. *Phys. Rev. B*, 69:125344, 2004.
- [ŠVK05a] V. Špička, B. Velický, and A. Kalvová. Long and short time quantum dynamics: I. Between Green's functions and transport equations. *Physica E: Low-dim. Syst. Nanostruct.*, 29:154, 2005.
- [ŠVK05b] V. Špička, B. Velický, and A. Kalvová. Long and short time quantum dynamics: II. Kinetic regime. *Physica E: Low-dim. Syst. Nanostruct.*, 29:175, 2005.
- [ŠVK05c] V. Špička, B. Velický, and A. Kalvová. Long and short time quantum dynamics: III. Transients. *Physica E: Low-dim. Syst. Nanostruct.*, 29:196, 2005.
- [TB11] N. Takemoto and A. Becker. Visualization and interpretation of attosecond electron dynamics in laser-driven hydrogen molecular ion using Bohmian trajectories. *J. Chem. Phys.*, 134:074309, 2011.

-
- [Thy08] K.S. Thygesen. Impact of exchange-correlation effects on the IV characteristics of a molecular junction. *Phys. Rev. Lett.*, 100:166804, 2008.
- [TMM09] D.G. Tempel, T.J. Martínez, and N.T. Maitra. Revisiting molecular dissociation in density functional theory: A simple model. *J. Chem. Theory Comput.*, 5:770, 2009.
- [TMR09a] L. Tao, C.W. McCurdy, and T.N. Rescigno. Grid-based methods for diatomic quantum scattering problems: A finite-element discrete-variable representation in prolate spheroidal coordinates. *Phys. Rev. A*, 79:012719, 2009.
- [TMR09b] L. Tao, C.W. McCurdy, and T.N. Rescigno. Grid-based methods for diatomic quantum scattering problems. II. Time-dependent treatment of single- and two-photon ionization of H_2^+ . *Phys. Rev. A*, 80:013402, 2009.
- [TMR10] L. Tao, C.W. McCurdy, and T.N. Rescigno. Grid-based methods for diatomic quantum scattering problems. III. Double photoionization of molecular hydrogen in prolate spheroidal coordinates. *Phys. Rev. A*, 82:023423, 2010.
- [TRR00] G. Tanner, K. Richter, and J.-M. Rost. The theory of two-electron atoms: Between ground state and complete fragmentation. *Rev. Mod. Phys.*, 72:497, 2000.
- [UHS⁺11] R. Ulbricht, E. Hendry, J. Shan, T.F. Heinz, and M. Bonn. Carrier dynamics in semiconductors studied with time-resolved terahertz spectroscopy. *Rev. Mod. Phys.*, 83:543, 2011.
- [UMD⁺97] J. Ullrich, R. Moshhammer, R. Dörner, O. Jagutzki, V. Mergel, H. Schmidt-Böcking, and L. Spielberger. Recoil-ion momentum spectroscopy. *J. Phys. B: At. Mol. Opt. Phys.*, 30:2917, 1997.
- [UUS⁺07] M. Uiberacker, Th. Uphues, M. Schultze, A.J. Verhoef, V. Yakovlev, M.F. Kling, J. Rauschenberger, N.M. Kabachnik, H. Schröder, M. Lezius, K.L. Kompa, H.-G. Müller, M.J.J. Vrakking, S. Hendel, U. Kleineberg, U. Heinzmann, M. Drescher, and F. Krausz. Attosecond real-time observation of electron tunnelling in atoms. *Nature*, 446:627, 2007.
- [VB92] A. Vibók and G.G. Balint-Kurti. Reflection and transmission of waves by a complex potential—a semiclassical Jeffreys–Wentzel–Kramers–Brillouin treatment. *J. Chem. Phys.*, 96:7615, 1992.
- [VKŠ06] B. Velický, A. Kalvová, , and V. Špička. Between Green’s functions and transport equations: Reconstruction theorems and the role of initial conditions. *J. Phys.: Conf. Ser.*, 35:1, 2006.
- [vLDdf] R. van Leeuwen and N.E. Dahlen. *An Introduction to Nonequilibrium Green Functions*, Lecture notes, unpublished, 2005 (<http://theochem.chem.rug.nl/research/vanleeuwen/literature/NGF.pdf>).

-
- [VS10] Y.V. Vanne and A. Saenz. Alignment-dependent ionization of molecular hydrogen in intense laser fields. *Phys. Rev. A*, 82:011403, 2010.
- [Wag91] M. Wagner. Expansions of nonequilibrium Green's functions. *Phys. Rev. B*, 44:6104, 1991.
- [WB06] F. Wilken and D. Bauer. Adiabatic approximation of the correlation function in the density-functional treatment of ionization processes. *Phys. Rev. Lett.*, 97:203001, 2006.
- [WF04] S.R. White and A.E. Feiguin. Real-time evolution using the density matrix renormalization group. *Phys. Rev. Lett.*, 93:076401, 2004.
- [WSD⁺94] B. Walker, B. Sheehy, L.F. DiMauro, P. Agostini, K.J. Schafer, and K.C. Kulander. Precision measurement of strong field double ionization of helium. *Phys. Rev. Lett.*, 73:1227, 1994.
- [XDD97] D. Xianxi, Jixin Dai, and Jiqiong Dai. Orthogonality criteria for singular states and the nonexistence of stationary states with even parity for the one-dimensional hydrogen atom. *Phys. Rev. A*, 55:2617, 1997.
- [XNG09] Y. Xiang, Y. Niu, and S. Gong. Above-threshold ionization by few-cycle nonlinear chirped pulses. *Phys. Rev. A*, 80:023423, 2009.
- [YCAFE08] K. Yamanouchi, S.L. Chin, P. Agostini, and G. Ferrante (Eds.). *Progress in Ultrafast Intense Laser Science III*, Springer, Berlin/Heidelberg, 2008.
- [YL07] C. Yannouleas and U. Landman. Symmetry breaking and quantum correlations in finite systems: Studies of quantum dots and ultracold bose gases and related nuclear and chemical methods. *Rep. Prog. Phys.*, 70:2067, 2007.
- [YZB96] H. Yu, T. Zuo, and A.D. Bandrauk. Molecules in intense laser fields: Enhanced ionization in a one-dimensional model of H₂. *Phys. Rev. A*, 54:3290, 1996.
- [ZHWC03] P. Zhao, N.J.M. Horing, D.L. Woolard, and H.L. Cui. Nonequilibrium Green's function formulation of quantum transport theory for multi-band semiconductors. *Phys. Lett. A*, 310:258, 2003.
- [ZKBS04] J. Zanghellini, M. Kitzler, Th. Brabec, and A. Scrinzi. Testing the multi-configuration time-dependent Hartree–Fock method. *J. Phys. B: At. Mol. Opt. Phys.*, 37:763, 2004.
- [ZKF⁺03] J. Zanghellini, M. Kitzler, C. Fabian, Th. Brabec, and A. Scrinzi. An MCTDHF approach to multielectron dynamics in laser fields. *Laser Phys.*, 13:1064, 2003.

-
- [Zwo08] M. Zwolak. Numerical ansatz for solving integro-differential equations with increasingly smooth memory kernels: Spin-boson model and beyond. *Comput. Sci. Disc.*, 1:015002, 2008.

List of the Author's Publications

Complete List of Peer-Reviewed Journal Publications

1. K. Balzer, S. Bauch, and M. Bonitz,
Time-dependent second-order Born calculations for model atoms and molecules in strong laser fields,
Phys. Rev. A **82**, 033427 (2010),
2. S. Bauch, K. Balzer, and M. Bonitz,
Electronic correlations in double ionization of atoms in pump-probe experiments,
EPL **91**, 53001 (2010),
3. K. Balzer, S. Bauch, and M. Bonitz,
Efficient grid-based method in nonequilibrium Green's function calculations. Application to model atoms and molecules,
Phys. Rev. A **81**, 022510 (2010),
4. K. Balzer, S. Bauch, and M. Bonitz,
Finite elements and the discrete variable representation in nonequilibrium Green's function calculations. Atomic and molecular models,
J. Phys.: Conf. Ser. **220**, 012020 (2010),
5. M. Bonitz, D. Hochstuhl, S. Bauch, and K. Balzer,
Quantum kinetic approach to time-resolved photoionization of atoms,
Contrib. Plasma Phys. **80**, 54 (2010),
6. D. Hochstuhl, K. Balzer, S. Bauch, and M. Bonitz,
Nonequilibrium Green functions approach to photoionization processes in atoms,
Physica E **42**, 513 (2010),
7. S. Bauch, D. Hochstuhl, K. Balzer, and M. Bonitz,
Quantum breathing mode of interacting particles in harmonic traps,
J. Phys.: Conf. Ser. **220**, 012013 (2010),

-
8. P. Ludwig, H. Thomsen, K. Balzer, A. Filinov, and M. Bonitz,
Tuning correlations in multi-component plasmas,
Plasma Phys. Control. Fusion **52**, 124013 (2010),
 9. K. Balzer and M. Bonitz,
Nonequilibrium properties of strongly correlated artificial atoms—a Green’s functions approach,
J. Phys. A: Math. Theor. **42**, 214020 (2009),
 10. K. Balzer, M. Bonitz, R. van Leeuwen, N.E. Dahlen, and A. Stan,
Nonequilibrium Green’s functions approach to strongly correlated few-electron quantum dots,
Phys. Rev. B **79**, 245306 (2009),
 11. S. Bauch, K. Balzer, C. Henning, and M. Bonitz,
Quantum breathing mode of trapped bosons and fermions at arbitrary coupling,
Phys. Rev. B **80**, 054515 (2009),
 12. P. Ludwig, K. Balzer, A. Filinov, H. Stolz, and M. Bonitz,
On the Coulomb-dipole transition in mesoscopic classical and quantum electron-hole bilayers,
New J. Phys. **10**, 083031 (2008),
 13. M. Bonitz, K. Balzer, and R. van Leeuwen,
Invariance of the Kohn (sloshing) mode in a conserving theory,
Phys. Rev. B **76**, 045341 (2007),
 14. K. Balzer, C. Nölle, M. Bonitz, and A. Filinov,
Energy spectrum of strongly correlated particles in quantum dots,
J. Phys.: Conf. Ser. **35**, 209 (2006),
 15. K. Balzer, C. Nölle, M. Bonitz, and A. Filinov,
Energy spectrum of strongly correlated electrons and indirect excitons in quantum dots,
phys. stat. sol. (c) **3**, 2402 (2006).

Contributions to Books and Newsletters

- M. Bonitz and K. Balzer (Eds.),
Progress in Nonequilibrium Green’s Functions IV,
J. Phys.: Conf. Ser. **220**, 011001-012023 (2010).

-
- S. Bauch, K. Balzer, P. Ludwig, A. Filinov, and M. Bonitz,
Introduction to Quantum Plasma Simulations,
Chapter in the book: M. Bonitz, N. Horing, and P. Ludwig (Eds.), *Introduction to Complex Plasmas*, Springer Series "Atomic, Optical and Plasma Physics", Volume 59, Berlin (2010).
 - K. Balzer, S. Bauch, T. Ott, and M. Bonitz,
Solving Two-time Quantum Kinetic Equations,
HLRN Newsletter 10 (December 2010),
Project report for the North German Super Computer Alliance (HLRN), Grant No. shp0006:
"First principle simulations of classical and quantum charged-particle systems".

Selected Contributions to International Conferences

- K. Balzer, S. Bauch, D. Hochstuhl, and M. Bonitz,
Correlated and ultrafast electron dynamics (in atoms and molecules) excited by uv radiation,
Invited symposium talk at DPG Spring Meeting of the divisions Plasma Physics and Short
Time-scale Physics, Kiel, Germany, 28-31 March 2011.
- K. Balzer and M. Bonitz,
*Solving the Kadanoff-Baym equations on spatial grids. Computational concepts and
parallelization*,
Talk at Workshop "Solving the Two-time Kadanoff-Baym Equations. Status and Open
Problems", Kiel, Germany, 23-25 March 2010.
- K. Balzer, D. Hochstuhl, S. Bauch, and M. Bonitz,
*Efficient grid-based method in non-equilibrium Green's function calculations for
inhomogeneous systems*,
Invited talk at Conference "Progress in Nonequilibrium Green's Functions IV", Glasgow,
United Kingdom, 17-21 August 2009.
- K. Balzer, R. van Leeuwen, and M. Bonitz,
Quantum dynamics of interacting electrons,
Lecture at Summer Institute "Complex Plasmas", Hoboken, New Jersey, United States, 30
July - 8 August 2008.
- K. Balzer, M. Bonitz, A. Filinov, and P. Ludwig,
Quantum kinetic theory for artificial atoms,
Talk at Conference Frontiers of Quantum and Mesoscopic Thermodynamics, Prague, Czech
Republic, 28 July - 2 August 2008.



Acknowledgements

At the first place, I would like to thank my supervisor Prof. Dr. Michael Bonitz (hereinafter referred to as M.B.) for giving me the possibility to prepare this thesis. Thereby, he accompanied the research with guiding remarks and constructive suggestions. Also, I would like to mention, that M.B. generously provided the opportunity to give presentations at various domestic and international workshops and conferences, whereby the present work in its early and advanced stage could reach a specialist audience and I could widen my horizon. Moreover, I wish to express gratitude to M.B. for letting me be coeditor of the volume "Progress in Nonequilibrium Green's functions IV", which has been published as *J. Phys.: Conf. Ser.* **220** (2010), and contains the Proceedings (a collection of 23 refereed articles) of the eponymous interdisciplinary conference held at the University of Glasgow, Scotland, from 17th to 21st August 2009.

Furthermore, I am indebted to my colleague Sebastian Bauch for stimulating discussions and the good cooperation without which this thesis would not have been possible. I always enjoyed the friendly office atmosphere and the numerous interesting conversations.

In addition, I would like to mention Dr. Patrick Ludwig with whom I was able to work in adjacent areas of research (see *P. Ludwig et al. New. J. Phys.* **10**, 083031 (2008)) and who has provided encouraging words during the final period of writing this dissertation.

Generally, without all my current and former colleagues—Sebastian Bauch, Dr. Henning Baumgartner, Dr. Jens Böning, Dr. Alexei Filinov, Kenji Fujioka, Dr. Christian Henning, David Hochstuhl, Hanno Kählert, Dr. Patrick Ludwig, Torben Ott, Lasse Rosenthal, Tim Schoof and Hauke Thomsen—my PhD studies, definitely, wouldn't have been half as much fun. Out of this group of people, I wish to acknowledge David Hochstuhl, Dr. Patrick Ludwig, Torben Ott and Hauke Thomsen for their commitment in proofreading. For the same reason, I thank Sebastian Hermanns.

Lastly, I offer my regards to my wife, my parents and all of those who supported me in any respect during the completion of this thesis.



Curriculum Vitae

Personal data

Karsten B a l z e r
Born 3 September 1980 in Kiel
German citizenship
Married



School education

8/1987 - 6/1991 Ganztagsgrundschule am Göteborgring, Kiel
(All-day elementary school)

8/1991 - 6/2000 Gymnasium im Bildungszentrum Mettenhof, Kiel;
since 2004: Thor-Heyerdahl-Gymnasium

- July 1999: Fachhochschulreife (advanced technical college certificate)
- June 2000: Allgemeine Hochschulreife (high school diploma)

Civilian service

9/2000 - 7/2001 Zivildienst, Kindertagesstätte Hasseldieksdamm, Kiel
(Community service in a day nursery)

Studies

10/2001 - 7/2007 Studium der Physik (Study of Physics),
Christian-Albrechts-Universität zu Kiel, Germany

- Since June 2004: Stipendiat der Studienstiftung des deutschen Volkes (Scholar of the German National Merit Foundation)
- July 2004 - January 2005: Semester abroad at the University of Western Australia, Perth, Australia
- November 2003: Vordiplom in Physik (Intermediate Diploma)
- July 2007: Physikdiplom (Diploma in Physics), Thesis:
Nonequilibrium Green's functions approach to artificial atoms

Postgraduate studies

Since 7/2007

Promotionsstudium (PhD studies),
Institut für Theoretische Physik und Astrophysik,
Christian-Albrechts-Universität zu Kiel, Germany

- June/July 2008: Participation in the 58th Meeting of Nobel Laureates as young researcher
- August/September 2010: Four-week stay at the Kavli Institute for Theoretical Physics, University of California, Santa Barbara, USA

Selbständigkeitserklärung

Hiermit versichere ich, dass diese Dissertationsschrift abgesehen von der Beratung durch den Betreuer, Herrn Prof. Dr. Michael Bonitz, nach Inhalt und Form die eigene Arbeit ist.

Außerdem erkläre ich, dass die vorliegende Arbeit weder ganz noch zum Teil bereits einer anderen Stelle im Rahmen eines Prüfungsverfahrens vorgelegen hat, sowie in dieser Form weder veröffentlicht worden ist noch zur Veröffentlichung eingereicht wurde.

Die im Rahmen der Arbeit entstandenen wissenschaftlichen Publikationen in Fachzeitschriften sind auf den Seiten 141 und 142 aufgeführt.

Weiterhin versichere ich, dass die Arbeit unter Einhaltung der Regeln guter wissenschaftlicher Praxis der Deutschen Forschungsgemeinschaft¹ entstanden ist.

Kiel,

(Ort)

(Datum)

(Unterschrift)

¹Deutsche Forschungsgemeinschaft, *Vorschläge zur Sicherung guter wissenschaftlicher Praxis. Empfehlungen der Kommission "Selbstkontrolle in der Wissenschaft"*, WILEY-VCH Verlag GmbH, Weinheim (1998).